Technische Universität München
TUM School of Medicine and Health

Deciphering the mechanism of a unique type of oncolytic virus-induced syncytial cancer cell death

Fabian Alexander Kortum

Vollständiger Abdruck der von der TUM School of Medicine and Health der Technischen Universität München zur Erlangung eines

Doctor of Philosophy (Ph.D.)

genehmigten Dissertation.

Vorsitz:	Priv.-Doz. Dr. Christian Sorg
Betreuerin:	Priv.-Doz. Dr. Jennifer Altomonte

Prüfer der Dissertation:

1. Prof. Dr. Philipp Jost
2. apl. Prof. Dr. Oliver Ebert

Die Dissertation wurde am 26.03.2024 bei der TUM School of Medicine and Health der Technischen Universität München eingereicht und durch die TUM School of Medicine and Health am 09.06.2024 angenommen.

The work presented herein was conducted at the Klinikum rechts der Isar der Technischen Universität München, Klinik und Poliklinik für Innere Medizin II, in the laboratory of PD. Dr. Jennifer Altomonte, in the period of October 2018 to March 2024.

Postal address:
Klinikum rechts der Isar
Klinik und Poliklinik für Innere Medizin II
Gastrolabor IV
Trogerstraße 32
81675 München

Content

ABSTRACT

Oncolytic viruses (OVs) represent a novel class of anti-cancer therapy, offering a dual attack on cancer cells. The direct oncolytic effect comprises the intrinsic ability of these viruses to selectively replicate in and destroy tumor cells while sparing adjacent healthy tissue. Concurrent induction of an immunogenic cell death (ICD) then lights up and empowers the patient's immune system to mount an anti-tumor immune response. The chimeric vector, rVSV-NDV, has been engineered to induce tumor-specific syncytia formation, an elegant way of OV dissemination in solid tumors via cell-to-cell spreading. Previous data characterized rVSV-NDV as a potent ICD inducer *in vitro* and *in vivo;* however, the cell death pathways underlying syncytial cancer cell death are yet unknown. To interrogate the molecular mechanism underlying viral oncolysis, the impact of cell fusion on the induction of apoptosis and necroptosis pathways and its immunogenic potential were characterized. To that end, oncolysis and cell death pathways induced by two fusion-competent rVSV-NDV variants, which mediate high versus intermediate levels of fusogenicity, were compared to those of non-fusogenic rVSV.

All three virus variants efficiently replicated and induced dose-dependent oncolysis in human lung adenocarcinoma cells (A549, H1437), but with a distinct virus- and cell-line-specific death phenotype. Western Blot and enzyme activity data pointed to a dynamic dependence of viral oncolysis on intrinsic and extrinsic apoptosis, which were; however, largely uninfluenced by viral fusogenicity. Interestingly, fusogenic OVs engaged necroptosis as a backup death mechanism, while rVSV preferred apoptosis. CRISPR/Cas9 knockouts of essential apoptosis or necroptosis regulators not only dynamically reworked the underlying oncolysis but also changed syncytia morphology. Collectively, a potentially pivotal role of effector caspase 3 and mixed-lineage kinase domain-like (MLKL) during syncytia destruction is discussed. Despite the complexity and apparent overlapping of apoptosis and necroptosis pathways induced by the OVs investigated in this work, an enhanced immunogenicity of cell death mediated by the fusogenic variants was observed. This was demonstrated by prominent ICD marker expression and syncytia-dependent activation of human dendritic cells (DCs) in an *ex vivo* co-culture system.

This work additionally represents a pilot evaluation of the oncolytic potential of rVSV-NDV in lung adenocarcinoma. The oncolytic effects of this vector were investigated in two syngeneic murine models of lung cancer by comparing intratracheal and intravenous routes of delivery. Even though rVSV-NDV treatment did not yield clear survival benefits in the presented studies, and the *in vivo* lung cancer models necessitate further optimization, this pilot scheme encourages follow-up preclinical research pursuing a future clinical translation of an rVSV-NDV-based viro-immunotherapy against lung cancer.

ZUSAMMENFASSUNG

Die Verwendung onkolytischer Viren (OV) beschreibt einen neuartigen Ansatz der Krebs-Immuntherapie, der sich einen zweistufigen Angriff auf Krebszellen zunutze macht. Durch intrinsische Tumorspezifität vermehren sich OV ausschließlich in malignem Gewebe und zerstören dieses durch Onkolyse, während angrenzende gesunde Zellen verschont werden. Ein mit der Onkolyse einhergehender immunogener Zelltod unterstützt dann das körpereigene Immunsystem zur Entwicklung einer gegen den Krebs gerichteten adaptiven Immunantwort. Der neuartige hybride onkolytische Vektor, rVSV-NDV, wurde entwickelt, um Krebszellen mittels eines einzigartigen Mechanismus der Zell-Zell Fusionierung, der sogenannten Synzytien Bildung, zu zerstören. In vorangegangenen *in vitro* und *in vivo* Experimenten wurde bereits gezeigt, dass dieser elegante Weg der Virusausbreitung im Tumor zu einem besonders immunogenen Zellsterben führt. Der molekulare Wirkmechanismus dieses Synzytien Absterbens ist allerdings bisher unbekannt. Folglich wurde in diesem Projekt die OV-vermittelte fusogene Onkolyse hinsichtlich ihres Einflusses auf die Immunogenität und die Beteiligung zweier bekannter Mechanismen des geregelten Zelltodes, Apoptose und Nekroptose, charakterisiert.

Im Vergleich zu nicht-fusogenem rVSV Virus, zeigten zwei fusogene rVSV-NDV Varianten ein zelllinien- und virus-spezifisches Infektionsverhalten und phänotypisch unterschiedliche Onkolyse in humanen A549 und H1437 Lungenkrebszellen. Western Blot und Enzymaktivitätsdaten ließen eine dynamische Beteiligung der intrinsischen und extrinsischen Apoptose erkennen, die jedoch kaum durch die Fusionseigenschaften der Viren beeinflusst wurde. Gleichzeitig zeigen die Ergebnisse, dass vor allem die fusogenen rVSV-NDV-basierten Vektoren Nekroptose als onkolytische Alternative aktivieren, während rVSV Apoptose bevorzugt. Über genetische Deletion wichtiger Regulatoren der Apoptose oder Nekroptose mittels CRISPR/Cas9, konnten die zusammenwirkenden Zelltodmechanismen flexibel umprogrammiert und sogar die Ausbildung der Synzytien beeinflusst werden. Es wird diskutiert, ob Caspase 3 und MLKL eine mögliche zentrale Rolle bei der Zerstörung von Synzytien einnehmen. Trotz der Komplexität und Verschachtelung der durch die OV induzierten Zelltodmechanismen, wurde beobachtet, dass eine erhöhte Immunogenität von Tumorzellen ausgeht, die zuvor einem synzytien-basierten Zelltod unterlegen sind. Nachdem ein synzytien-basierter Zelltod auch in einem *ex vivo* Ko-Kulturmodell zu signifikant besserer Aktivierung humaner dendritischer Zellen geführt hat, lässt sich abschließend betonen, dass ein rVSV-NDV-vermitteltes fusogenes Absterben von Krebszellen ein höheres und vielversprechenderes therapeutisches Potential zur Immunaktivierung hat, als ein nicht-fusogener Zelltod.

Darüber hinaus umfasst diese Arbeit eine Pilotstudie zur Beurteilung der therapeutischen Effektivität von rVSV-NDV in zwei unterschiedlichen syngenen murinen Lungenkrebsmodellen und unter Einsatz zweier OV-Applikationsrouten (intratracheal und intravenös). Obwohl die rVSV-NDV-Behandlung gegenüber der Kontrollgruppe keine eindeutigen Überlebensvorteile erzielte und die angewandten *in vivo* Lungenkrebsmodelle weitreichende Verbesserungen bedürfen, gilt diese Pilotstudie als wegweisend für weitere präklinische Studien mit rVSV-NDV, mit dem Ziel eine klinische Entwicklung einer rVSV-NDV-basierten Immuntherapie gegen Lungenkrebs weiter voranzutreiben.

1 INTRODUCTION

At the beginning of the 21st century, the cancer therapy landscape underwent a major shift from traditional treatments, like surgery, radiation, or chemotherapy, towards the development of targeted therapies, such as kinase inhibitors or tumor-associated antigen (TAA) targeting antibodies and the advent of immuno-oncology. With an ever-growing understanding of cancer immunosurveillance within the tumor microenvironment (TME) and the discovery of cancer immune evasion mechanisms, the approval of several immune checkpoint inhibitor (ICI) therapies leveraged the re-emergence of cancer immunotherapy [1]. Immunotherapy aims to harness and reactivate the body's immune response to target mutated cancer cells and develop a sustainable line of defense against relapsing or metastasizing tumors. Other branches of cancer immunotherapy with auspicious clinical performance, despite only a few drug approvals, comprise cytokine therapies, cancer vaccines, adoptive cell transfer, and oncolytic virus (OV) therapies [2]. Oncolytic virotherapy utilizes virus vectors with an intrinsic or engineered ability to specifically replicate in malignant cells and induce tumor cell killing (oncolysis) while sparing the surrounding healthy tissue (**Figure 1**). In healthy cells, virus pathogen-associated molecular patterns (PAMPs) are usually sensed by a panel of pattern recognition receptors (PRRs) that activate host antiviral immunity to clear the infection, primarily mediated by type I interferons (IFN), amongst other chemokines and cytokines to attract immune cells [3]. Tumor cells, however, acquire numerous mutations to sustain their growth, alter cell death signaling and metabolism, and suppress anti-tumoral and antiviral immunity [4], all in all, an environment conducive to viral infection by OVs. In addition to the direct oncolytic effect, a key aspect of OV therapy involves an immunogenic cell death (ICD) and sparking local inflammation that turns an immunologically "*cold*" tumor into a highly immune cell infiltrated, "*hot*", tumor [5], as will be further explained below. OV therapy thus implements a two-tiered attack on cancer: direct killing of malignant cells in an immunogenic fashion and empowering the patient's immune system to systemically fight the cancer, including metastatic sites, which is often referred to as the *in-situ* vaccination effect [6]. ICD is a superordinate concept that can comprise one or multiple regulated cell death mechanisms. OV infection triggers host antiviral sensing mechanisms which transmit death stimuli to closely interconnected multimodal cell death pathways as part of the lytic host defense. Hence, to harness that cancer cell killing effect in OV therapy, OVs must induce a proper type of cell death pathway in order to trigger ICD and shape a potent anti-tumor immune response [7].

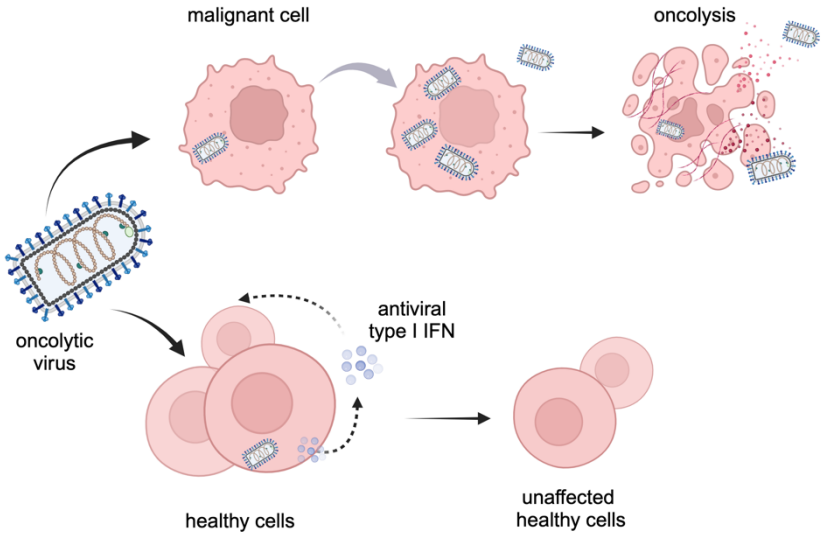

Figure 1. Concept of oncolytic virotherapy

Oncolytic viruses have an intrinsic or engineered tumor-specificity and only replicate in malignant cells. In healthy cells, the viral pathogen is eliminated by the host's innate antiviral immunity. In tumor cells however, antiviral mechanisms, such as virus sensing and type I IFN signaling, are often dysfunctional. This provides an ideal platform for OV replication and culminates in oncolysis. This rupture of cancer cells releases a cocktail of pro-inflammatory and immune-stimulating factors, including TAAs, that eventually reprogram the immune system to fight the cancer. Created with BioRender.com

1.1 Oncolytic viruses in clinical development

1.1.1 From early discovery to approved OV therapies

Long before modern virology research described the biological nature of a viral pathogen, naturally occurring viruses were pursued as potential treatment agents against cancer. Several case reports in the early 20th century mention occasional leukemia remission in patients experiencing acute infection with a pathogen presumed to be influenza or chickenpox virus [8]. Even though advancements in cell and tissue culture techniques and rodent models contributed to great leaps in molecular virology understanding from the 1950's to the 1990's, progress in virus-based therapies was impaired over several decades by serious, virus-related side effects, a lack of controlled and sterile virus production methods, and only short-lived tumor remission. Concurrent successes in chemo- and radiotherapy nearly eclipsed oncolytic virotherapy approaches until the 80's. Significant advances in reverse genetics and viral engineering in the early 1990's resurged interest in the development of non-pathogenic OV vectors with a cumulative understanding of oncolytic mechanisms and soon, several adapted vectors from diverse viral families; *Adeno-*, *Herpes-*, *Paramyxo-*, *Picorna-, Pox-* and *Rhabdoviridae;* were in the limelight of OV clinical research [8]. In 2005, Chinese regulators announced the world's first approval of a genetically modified oncolytic adenovirus, H101, for the treatment of head and neck cancer, showing enhanced response rates in combination with chemotherapy over chemotherapy alone, albeit with lacking survival data [9].

The first oncolytic virus approved by the Federal Drug Agency (FDA) and the European Medicines Agency (EMA) was a genetically modified, herpes simplex virus 1 (HSV-1) expressing the human granulocyte-macrophage colony-stimulating factor (GM-CSF), termed *Talimogene laherparepvec* (T-VEC), in 2015. T-VEC successfully demonstrated tumor-selectivity and promoted local and systemic anti-tumor immunity upon intratumoral treatment of patients with refractory malignant melanoma [10]. Six years later, another highlight in OV-based medicine was the approval of a mutated HSV-1 vector (*Teserpaturev*) for the treatment of malignant glioblastoma in Japan, followed by the approved gene therapy with a replication-incompetent, non-oncolytic adenovirus expressing human IFN-α-2B (*Nadofaragene firadenovec*) indicated for an invasive type of bladder cancer, in the United States in 2022 [6]. With numerous other vectors in all stages of clinical development and for diverse tumor indications, recent regulatory approvals and growing clinical data demonstrating evidence of immune activation and significant response rates, clearly attest to the treatment potential of OVs and mark the beginning of an oncolytic virotherapy era.

1.1.2 Choosing a suitable oncolytic vector

A key challenge in OV development is vector design. It requires an understanding of the basic molecular virology and mode of action of the OV, as well as identifying strategies to improve tumor specificity and intratumoral spreading, immunomodulation, and "*arming*" OVs with novel therapeutic or reporter transgenes [5]. Our group has a long history and expertise with two inherently oncolytic vectors: Vesicular stomatitis virus (VSV) and Newcastle disease virus (NDV), and recently presented a superior OV platform based on the chimeric vector, recombinant (r) VSV-NDV (rVSV-NDV). Basic concepts of their molecular virology, tumor specificity and unique mode of oncolysis of the parental and chimeric viruses are outlined below.

1.1.2.1 VSV virology

VSV is a prototypical negative, single-stranded RNA viruses (ss(-)RNA, ~11 kb) in the *Rhabdoviridae* family (order Mononegavirales) and causes Vesicular stomatitis disease in livestock (cattle, pigs, horses). It is considered apathogenic in human, with individuals rarely developing mild, flu-like symptoms [11]. VSV forms enveloped particles of approximately 180 x 75 nm in size with an iconic bullet shape due to the supercoiled helical RNA that is wrapped in a cylindrical nucleocapsid. VSV RNA sequentially encodes five proteins, namely the nucleoprotein (N), the viral phosphoprotein (P), matrix protein (M), surface glycoprotein (G), and the viral RNA-dependent RNA polymerase (L) (**Figure 2** A) [12].

For infection, VSV-G attaches to members of the ubiquitously expressed low-density lipoprotein (LDL) receptor family, explaining VSV's broad cell tropism [13], followed by receptor-mediated endocytosis and acidification of endosomes. To release its nucleocapsid to the host cytoplasm and release viral RNA, VSV-G induces fusion of its viral envelope with the endosomal membranes. Due to the negative-sensed viral RNA and absence of host cellular RNA-dependent RNA polymerases, VSV-L is co-packaged into every virion to synthesize viral mRNA transcripts. A switch from transcription mode to viral replication occurs when sufficient N and P proteins have been generated to guarantee nucleocapsid wrapping of nascent RNA. Viral glycoproteins are processed through the *trans*-Golgi network and reside in the host plasma membrane for virion assembly. Subsequent to cytoplasmic replication, M and G proteins interact to prepare nucleocapsids for the budding of new virions from the host plasma membrane, and the host cell succumbs under the induced death program (as further outlined in 1.2) [12, 14].

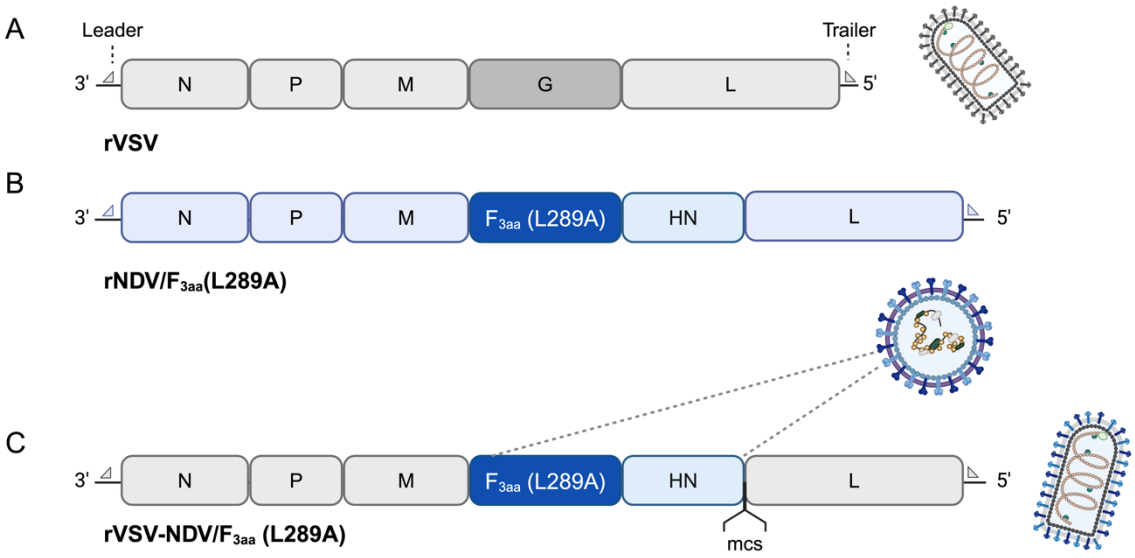

Figure 2. Viral genomes of rVSV, rNDV, and the hybrid virus rVSV-NDV

Visualized is the conserved gene order of (**A**) the recombinant rhabdovirus, rVSV, and (**B**) the recombinant paramyxovirus, rNDV, shown in its fusion-optimized vector rNDV/F_{3aa}(L289A). The triangle marks the 3' leader sequence, which is the start of viral mRNA transcription. Each gene transcription is terminated, polyadenylated and reinitiated at each of the intergenic junctions. These junctions are ignored for genome replication and copies of full-length viral genomes are generated by the RNA-dependent RNA polymerase (L) [12]. (**C**) Genome sequence of the engineered pseudotyped hybrid virus rVSV-NDV/F_{3aa}(L289A) (short: rVSV-NDV). In rVSV-NDV the rVSV glycoprotein (G) had been replaced with the structural proteins (HN and F_{3aa}(L289A)) of rNDV, marked by the dotted lines, and a multiple cloning site (mcs) had been inserted upstream of the L gene. Figure created in BioRender.com.

Upon infection, VSV is rapidly sensed by cell surface and cytoplasmic PRRs of the toll-like receptor (TLR) family or retinoic-acid-inducible gene-like receptor class (RLRs: RIG-I, MDA5), resulting in inflammation and antiviral type I IFN production. The latter then stimulates the activation of several interferon stimulated genes (ISG) in an autocrine or paracrine fashion and

mounts a broad innate immune response [15]. VSV is particularly susceptible to the antiviral effects of type I IFN. One of the mechanisms for the inherent oncotropism of VSV is the accumulated defects in antiviral sensing in tumor cells; thus, providing an ideal substrate for unimpeded VSV replication [14]. Another viral strategy to circumvent an antiviral state is mediated by the VSV M protein, which is known to shut down nuclear export of host antiviral transcripts. rVSV-MΔ51 and rVSV-M51R mutants, devoid of this ability, were generated as attenuated, safer OV vectors that restrict viral replication to tumor cells, while non-cancerous cells retain an unimpaired antiviral response [16, 17].

The VSV vector encompasses a broad flexibility in the expression of foreign therapeutic or reporter transgenes, for example, as an additional transcription unit between VSV-G and VSV-L, without affecting the virus life cycle [14]. A promising oncolytic candidate expressing human IFN-β to potentiate antiviral immunity in healthy cells and selectively replicate in IFN-defective tumor cells is named rVSV-IFN-β-NIS. This vector further encodes a sodium iodide symporter (NIS) to trace oncoselectivity *in vivo* and proved its safety and efficacy upon systemic administration in several cancer models [18, 19], leading to current advancement into phase I/II clinical studies [20].

Major safety concerns applying VSV as an oncolytic vector are due to severe neuro- and hepatotropic side effects observed in rodent and primate models, all of which are attributed to the indiscriminative cell tropism mediated by VSV-G [21, 22].

1.1.2.2 NDV virology

NDV is a member of the *Paramyxoviridae* family and forms characteristic, spherical (150 – 350 nm), enveloped particles with protruding glycoprotein spikes. NDV's natural hosts are birds, and epidemiologically, NDV is grouped into velogenic (highly virulent), mesogenic (intermediate virulent), and lentogenic (avirulent) strains. A major environmental risk and agricultural burden to the poultry industry is imposed by highly contagious and pathogenic strains (velo- and mesogenic), causing Newcastle disease with high mortality rates. This limits the use of these strains as OV vectors and necessitates the generation of safer NDV vectors, for example, by genetic engineering approaches (see next subchapter 1.1.2.3). Surface tropism of NDV relies on α2,3 and α2,6 N-linked sialic acid residues on glycolipids or glycoproteins, which are prevalent on many eukaryotic host cell membranes, including humans. However, NDV is not a human pathogen, and only (rarely) provokes influenza-like disease and conjunctivitis in human [23]. The reasons for NDV's inherent oncoselectivity are multifold (reviewed in detail in [24]), but like in VSV, they are primarily due to defects in the type I IFN pathway in tumor cells, whereas healthy cells efficiently clear NDV infection.

Being classified in the same order as VSV (Mononegavirales), its 15.2 kb ss(-)RNA genome encodes for a similar gene set of nucleoprotein (N), the viral phosphoprotein (P), matrix protein (M), surface hemagglutinin-neuraminidase (HN) and the viral fusion protein (F), as well as a viral RNA-dependent RNA polymerase (L) (**Figure 2** B) [12]. While the majority of the NDV life cycle (nucleocapsid uncoating, transcription, viral replication, virion assembly and budding) resembles that of VSV, the paramyxovirus entry mechanism via viral envelope-host cell fusion, as well as the feature of cell-cell fusion is quite distinct.

1.1.2.3 NDV-HN and NDV-F as mediators of virus-cell and cell-cell fusion

The NDV life cycle begins with the attachment of HN protein spikes to α2,3 and α2,6 N-linked sialic acid residues on the cell surface, followed by virus particle internalization in a unique mechanism of pH-independent fusion of the viral envelope with the host membrane, orchestrated by the viral F protein. As virus infected cells expose HN and F proteins on their surface, NDV can spread to neighboring uninfected cells via cell-to-cell fusion in a similar mechanism (**Figure 3**). Initially, F protein is expressed as an F_0 precursor that requires cleavage by host cell proteases at monobasic or polybasic cleavage sites to generate the fusion-competent F_1+F_2 heterodimer. The HN protein provides a trigger to undergo irreversible conformational changes leading to the exposure of the hydrophobic fusion peptide, which intrudes into the host cell membrane to ensure close proximity of virus and host or neighboring cells (in case of cell-cell fusion). The actual membrane fusion is then navigated by a series of conformational changes, bending of the opposing membranes, and culminates in forming of a fusion pore [12, 25, 26]. In virus-cell fusion, the nucleocapsid of the fused virion enters through the pore and is uncoated in the host cytoplasm to proceed with viral gene transcription. Infected cells can repeatedly undergo cell-cell fusions with neighboring cells, leading to merging of cytoplasmic contents and the formation of multinucleated giant cells, so-called syncytia [27].

In highly virulent strains of NDV, F_0 is cleaved at a polybasic cleavage site by the widely abundant endonuclease furin, which renders many cells easily infectible and co-determines virulence of paramyxoviruses. In contrast, most NDV strains suitable as vaccines or OV vectors are lento- or mesogenic and often encompass a monobasic cleavage site in the F protein that is only accessible by specific proteases, limiting the host range [25]. Therefore, the F protein cleavage site in the lentogenic NDV-Hitchner B1 strain was genetically modified to a polybasic cleavage site, resulting in a syncytia-competent vector (called rNDV-B1/F_{3aa}) with better replication and a broadened host range, now including rodents and human that do not require the addition of exogenous proteases [28].

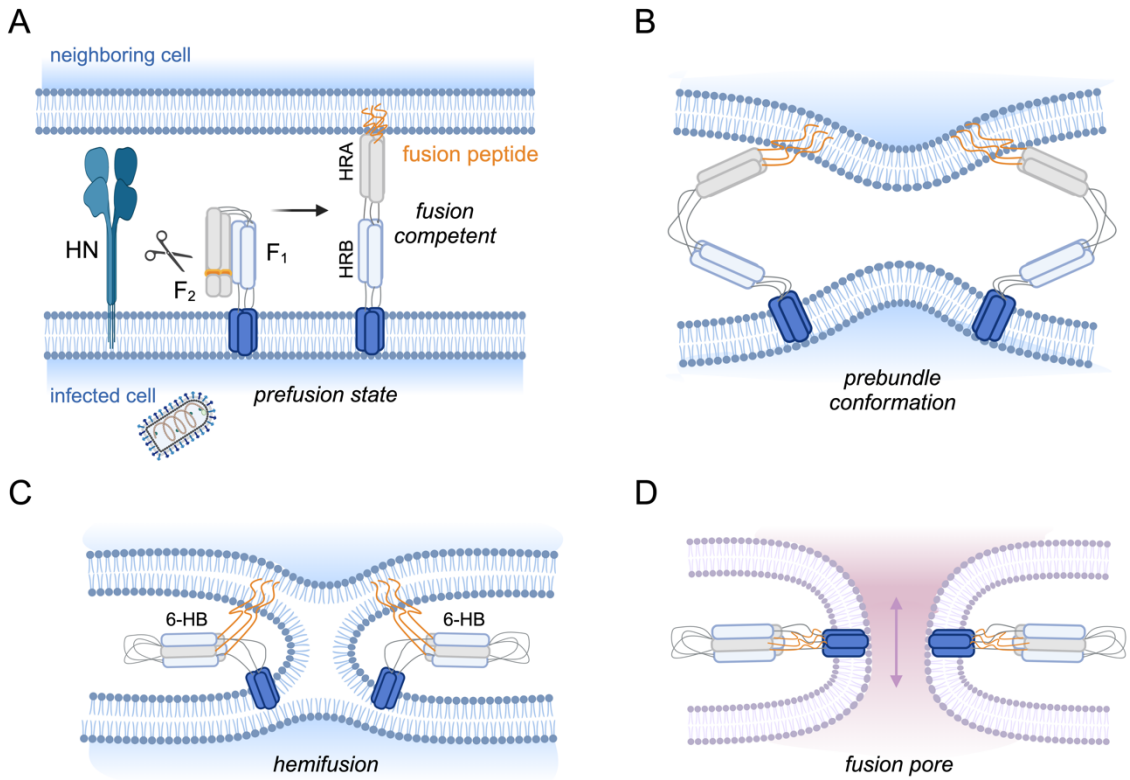

Figure 3. Model for the paramyxovirus-mediated cell-cell fusion

The fusion (F) protein is a type I integral membrane protein with a C-terminal transmembrane domain (in dark blue) and a long N-terminal domain projecting outside, consisting of two heptad repeat regions (HRA, HRB). (**A**) The F_0 precursor is cleaved into the membrane-anchored C-terminal F1 peptide and the N-terminal F2 peptide linked via disulfide bonds. The binding of HN to sialic acid residues (not shown) on neighboring cells triggers two events (indicated by the scissors): (i) the exposure of the N-terminal fusion peptide and (ii) conformational changes that allow the fusion peptide to intrude into the neighboring cell membrane at neutral pH. This achieves close proximity (~ 1 nm) of infected and uninfected neighboring cells. (**B**) Further conformational changes in HRA and HRB mediate the membrane fusion event via a prebundle conformation. (**C**) With a six-helix bundle (6HB), also called the hemifusion stage, cell-cell fusion progresses in an energy-intensive process and is completed with (**D**) opening of a fusion pore through which cytoplasm and cellular content of the two fused cells mix. Virus-cell fusion for viral entry is similarly controlled and leads to the release of the nucleocapsid into the host cytoplasm through the fusion pore. Figure created in BioReder.com under consultation of [12, 25, 26, 29].

In addition to the inherent fusion capacity of NDV, another main advantage of NDV over VSV is its remarkable safety profile, even at high intravenous or intratumoral doses, which was demonstrated in preclinical animal models and in human clinical studies over the last 60 years [30-32]. Efficient tumor reduction and immunomodulation, however, were only achieved by genetically engineered NDV vectors that optimize fusion, or express immune-stimulatory transgenes, or when administered in combination with ICI therapy [33]. A phase 1 clinical trial involving rNDV expressing human interleukin 12 (IL-12) as an immune-stimulatory cytokine in combination with ICI therapy is currently underway in patients with advanced and metastatic solid tumors [34].

1.1.3 rVSV-NDV: a hybrid oncolytic virus inducing cancer cell fusion on a next level

In a strategy to engineer a safer VSV vector, neurotropic VSV-G was replaced with the envelope G-protein of lymphocytic choriomeningitis virus (LCMV), resulting in a pseudotyped vector (called VSV-GP) with superior efficacy in glioma cells and eliminated neurotoxicity on healthy neurons [35]. Since VSV-GP demonstrated oncolysis, immune cell priming, and safety in a range of other preclinical models and upon various routes of administration, the OV recently entered first-in-human clinical trials in multiple tumor indications [36]. Albeit still in preclinical development, our group is currently exploring a likewise promising approach of pseudotyping VSV with fusion-optimized surface proteins of NDV.

Additional modification of the NDV fusion protein by a single amino acid substitution from lysine (L) to alanine (A) at amino acid 289 favored the switch into the fusion competent conformation and yielded a modified NDV vector with augmented fusion properties, termed rNDV/F_{3aa}(L289A), which allowed cell-cell fusion even in the absence of the HN protein [37, 38]. Evidence of improved fusion characteristics and tumor necrosis leading to survival prolongation was shown in an orthotopic hepatocellular carcinoma (HCC) model in rats, with no observed local or systemic toxicity [39]. However, considering the challenges related to environmental concerns associated with this vector, further development of a safe and fusion-competent vector was sought.

Under consideration of the assets and weaknesses of both VSV and NDV, a new oncolytic virus platform was established in our group, led by the novel fusogenic hybrid vector rVSV-NDV/F_{3aa}(L289A), referred to herein as rVSV-NDV. This novel OV is constructed of the backbone of rVSV in which the glycoprotein VSV-G had been eliminated and pseudotyped with both surface proteins (HN and F) of the modified rNDV/F_{3aa}(L289A) (**Figure 2** C). rVSV-NDV demonstrated rapid, VSV-like replication and tumor specific lysis under syncytia formation in HCC cells *in vitro.* By eliminating VSV-G, off-target toxicities in the liver or brain were eliminated, and systemic tail-vein injection into immunodeficient mice demonstrated superior safety of rVSV-NDV, wherein doses up to 1000-fold higher compared to rVSV were tolerated. The oncolytic potential of rVSV-NDV was then exposited by significant survival prolongation in a murine model of multifocal orthotopic HCC compared to buffer treatment [40]. In a subsequent study, evaluating synergistic effects of rVSV-NDV with immunotherapies, it was discovered that a combination of rVSV-NDV with adoptively transferred antigen-specific T cells efficiently stimulated major histocompatibility complex I (MHC-I)-mediated antigen presentation in B16 murine melanoma cells and stimulated a systemic immune-mediated therapeutic effect. Local treatment of bilateral implanted B16 tumors with rVSV-NDV or a combination of OV and antigen-specific T cells in mice resulted in

prolonged survival, pronounced tumor reduction, and T cell infiltration into the injected and distant tumors [41]. Marek and colleagues then demonstrated that rVSV-NDV can successfully sensitize B16 tumors to ICI therapy, which was dependent on active RIG-I-mediated viral sensing [42]. Taken together, previous and ongoing work highlights that rVSV-NDV is a potent oncolytic agent that kills cancer cells by syncytia formation and can modulate the TME to elicit a systemic anti-tumor immune response *in vitro* and *in vivo*.

1.1.4 Syncytia formation as unique and preferable mode of oncolysis

From an evolutionary perspective, the inherent feature of virus-induced cell-cell fusion enhances virus dissemination and sustains infection. As a matter of course, these beneficial amenities and the therapeutic potential of syncytia formation came to the fore of oncolytic virotherapy research [43]. Any cancer therapy, including OVs, is only efficient as it reaches its desired destination. A non-fusogenic virus is believed to be severely hampered in its ability to spread inside a tissue-dense TME, resulting in limited killing and poor immunogenicity due to the sparse release of TAAs and DAMPs. The great advantage of fusion-competent vectors is that they can induce a domino effect in viral spreading inside the tumor, involving neighboring non-infected tumor cells (also called bystander effect) [44] and thereby debulk a dense tumor mass. Secondary to the oncolytic effects, the concerted rupture of syncytia is believed to release a multitude of cancer neoantigens, DAMPs, and PAMPs. This so-called oncolysate is an ideal maturation and activation cocktail for innate antigen presenting immune cells (APCs) [44]. Thus, syncytial death can not only trigger local inflammation, but it can also augment a systemic tumor-specific immune response (see also section 1.2.5.2) [45, 46]. Although the oncolysate also contains viral antigens, and nascent OV particles still escape by classical budding, syncytial spreading is considered underrecognized by host antiviral surveillance, such as neutralizing antibodies or the complement system.

Syncytial infection and death are accompanied by a diverse and abnormal cellular phenotype [45]. As a newly developed OV hybrid, little is known about the underlying oncolytic mechanisms and the immunogenicity triggered by fusogenic rVSV-NDV. Thus, in light of the development of a safe and efficient OV therapy, there is a profound interest in clarifying the biology of syncytial spreading, bystander killing, as well as the immunogenic potential of fusogenic OVs. In this study, some of the above questions were addressed by generating a new vector with altered fusogenicity, termed rVSV-NDV/F_{3aa} (containing the modified proteolytic cleavage site but lacking the *hyperfusogenic* (L289A) modification in the fusion protein, see section 3.1.1) and comparing it with rVSV-NDV/F_{3aa}(L289A) and parental, non-fusogenic rVSV. With this research tool in hand, it was attempted to decipher the underlying cell death pathways and characterize the immunogenicity of the syncytia phenomenon.

1.2 Oncolytic virus-mediated cell death

OV-induced oncolysis displaces tumor cells into an invidious situation that is resolved with a unique and multimodal death program that is not unnoticed by host immunity. With an enormous versatility in viral vectors, cancer entities, and mutational landscape in cancer cells, oncolysis in one cell line might be disparate from oncolysis in another. Ma and colleagues, for example, characterized cell death modalities and immunogenicity of three distinct OVs (adenovirus, vaccinia virus (VV), Semliki Forest virus) and reported three individual death profiles involving one or more of the common programmed death pathways: apoptosis, necroptosis, pyroptosis and autophagy [47]. Oncolytic death mediated by engineered vectors, however, may further complicate the picture. Thus, it is hypothesized that rVSV-NDV triggers a unique type of programmed cell death that is, however, dissimilar to that induced by either of the parental viruses.

In 2002, Bateman and coworkers described tumor cell syncytia as initially highly ordered structures, that, however, quickly lead to cell death in a non-apoptotic fashion under release of vesicles, so-called syncytiosomes [44]. The death was specified to involve autophagic digestion, chromosome condensation, and nuclear fusion. Although these syncytia were not mediated by a replicating OV, but resulting from cells transfected with viral fusogenic membrane glycoproteins (FMGs; cytomegalovirus Gibbon ape leukemia virus; GALV or Measles virus (MV) F + HN protein), Bateman et al. demonstrated considerable immunogenicity of the syncytiosomes. Compared to non-fusing cells, the latter had a high potential to stimulate dendritic cells (DC) and superior antigen cross-presentation to cytotoxic T cells [44]. While much of the complexity of death pathway regulation was unknown in 2002, the study pinpoints unresolved mechanistic concepts on a syncytial death.

Accordingly, the unique cytopathic effect and syncytial death triggered by rVSV-NDV are mechanistically and immunologically poorly characterized. To decipher some of the complexity of a syncytial cell death, this study provides early, pioneering results on rVSV-NDV-induced cell death mechanisms, focusing on two well-characterized pathways: apoptosis and necroptosis.

1.2.1 Apoptosis

Apoptosis is one of the best-defined regulated cell death modalities that is classically divided into an extrinsic and intrinsic pathway. Cells undergoing apoptosis usually display a distinct morphology of cell rounding and shrinkage, fragmentation of nuclei, chromatin condensation, and plasma membrane blebbing. Another characteristic often seen in apoptotic cells is the secretion and secondary necrosis of apoptotic bodies due to a systematic vesicle-based disassembly of cellular organelles [48, 49]. Dismantled cells are recognized by the exposure of phosphatidylserine (PS) on their surface and phagocytosed by macrophages without arousing an inflammatory response. This explains why apoptosis, unlike lytic necroptosis or pyroptosis, is usually classified as "*immunologically silent*" [49]. On a molecular level, a hallmark of intrinsic and extrinsic apoptosis is the activation of downstream effector caspases that cleave and process myriad cellular death substrates and lead to the observed apoptotic morphology [49].

1.2.1.1 Survival signaling and switch to extrinsic apoptosis

Under physiological conditions, the decision for cell survival or death is in principle governed by members of the tumor necrosis factor (TNF) death receptor superfamily (among those TNF receptor 1 (TNFR1), FAS (also known as CD95), and TNF-related apoptosis-inducing ligand receptor (TRAIL-R) that, upon ligand engagement, transmit extracellular stimuli via their cytoplasmic death domain and induce the formation of a receptor-associated multi-protein death-inducing signaling complex (DISC) [50].

In the case of FAS and TRAIL-R, the DISC is composed of a FAS-associated via death domain (FADD), FLICE-like inhibitory protein (c-FLIP) and pro-caspase 8. Ligand binding to FAS and TRAIL-R predominantly leads to death signaling and activation of pro-apoptotic caspase 8, whereas TNF binding to TNFR1 initially leads to the formation of a pro-survival receptor-bound complex, termed Complex I (**Figure 4**). TNFR1 signaling involves (among other factors) recruitment of TNF receptor-associated death domain (TRADD), TNF-receptor associated factors 2/5 (TRAF 2/5), receptor-interacting serine/threonine protein kinase 1 (RIPK1) and cellular inhibitor of apoptosis (cIAP 1/2), which coordinate a series of ubiquitination and phosphorylation events that lead to nuclear factor kappa B (NF-κB)- driven pro-survival and pro-inflammatory gene expression. Among those genes are pro-survival B-cell lymphoma-2 (Bcl-2) family members (Bcl-2, Bcl-XL, and induced myeloid leukemia differentiation protein-1 (Mcl-1)) as well as c-FLIP. Under certain conditions, such as chemical inhibition of receptor-associated components, pathogen infection, or epigenetic factors, Complex I dissociates from the receptor and is internalized as a cytosolic pro-death Complex II [50, 51].

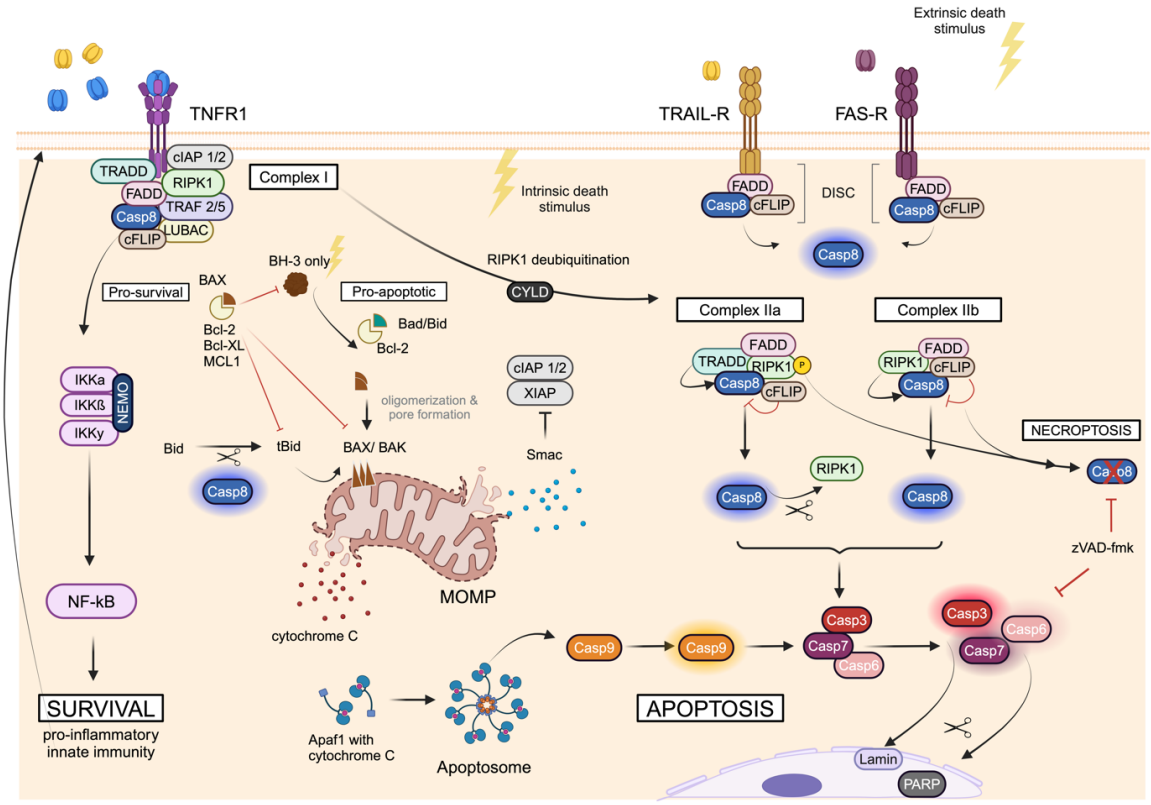

Figure 4. Schematic overview of extrinsic and intrinsic apoptosis signaling

In normal biology, ligand binding to TNFR1 recruits a set of factors to the cytoplasmic receptor domain to form a receptor-bound, pro-survival Complex I. Regulated by an intricate ubiquitination and phosphorylation cascade, Complex I induces NF-κB-driven pro-survival gene expression. Those genes can include further death receptor ligands TNF-α, TRAIL or FAS-ligand. Binding of TRAIL or FAS-ligand to their cognate receptors directly affects caspase 8 activation through the DISC. Pro-survival gene activation complexes resulting from these receptors are possible but are not shown for simplicity (see [50]). Anti-apoptotic Bcl-2 family members sequester several pro-apoptotic BH3-only proteins to support anti-apoptotic signaling cues. Extrinsic death stimuli and cellular stress (viral infection) can induce deubiquitination of RIPK1 by CYLD, leading to RIPK1 and TRADD dissociation from the TNFR1, forming cytosolic Complexes IIa and IIb. TRADD-dependent activation of caspase 8 in Complex IIa occurs independently of RIPK1, whereas in Complex IIb, TRADD is absent, and RIPK1 is required to activate caspase 8. Caspase 8 cleaves and activates Bid, RIPK1, and downstream effector caspases 3, 6, and 7. In intrinsic apoptosis signaling, pro-apoptotic Bad and Bid interact with anti-apoptotic BH3-only proteins, enabling BAX and BAK oligomers to insert themselves into the mitochondrial outer membrane to induce MOMP. This will result in the secretion of mitochondrial content and formation of the apoptosome (involving cytochrome C and Apaf-1), which serves as a caspase 9 activating hub. Similar to caspase 8, caspase 9 can activate effector caspases 3, 6, and 7. If caspase 8 is also active, Bid gets cleaved to tBid, and the latter supports BAX-BAK-mediated MOMP. Some of the effector functions of caspase 3, 6, and 7 include nuclear condensation, PS exposure and PARP cleavage. The glow surrounding caspases (abbreviated Casp) indicates their activation. The scissor symbol indicates cleavage activity and a red X or red arrow with a blunt end marks inhibition or absence of central regulators. Abbreviations: TRADD (TNF receptor-associated death domain); TRAF 2/5 (TNF-receptor associated factors 2/5); BAK (Bcl-2 homologous antagonist/killer). Figure created in BioRender.com under consultation of [51-55].

Crucial for the switch to Complex IIa and IIb is the ubiquitination status of RIPK1 and RIPK1-associated proteins. The deubiquitination of RIPK1 by cylindromatosis deubiquitinase (CYLD) promotes Complex II formation [55], as well as blocking of cIAP1/2 and X-linked inhibitor of apoptosis (XIAP) by second mitochondrial activator of caspases (SMAC) or SMAC mimetics, such as LCL-161 [53]. In essence, Complex II forms homodimers of activated initiator caspase 8 that promote apoptosis by two distinct routes: directly by cleavage and activation of downstream effector caspases 3, 6, and 7, or indirectly by cleavage of the BH3-only interacting domain death agonist (BID) into truncated BID (tBID), elegantly linking extrinsic with the intrinsic apoptosis pathway [49].

1.2.1.2 Intrinsic apoptosis and effector caspases

Intracellular stress, such as oxidative stress, endoplasmic reticulum (ER) stress, DNA damage or pathogens sensed by cytosolic PRRs, acts upon several pro- and anti-apoptotic members of the Bcl-2 protein family that eventually mediate mitochondrial outer membrane permeabilization (MOMP). The mitochondrial pores are generated by insertion of apoptogenic BAX and Bcl-2 homologous antagonist/killer (BAK) oligomers into the outer mitochondrial membrane, a process supported by tBID inhibitory activity on anti-apoptotic Bcl-2 proteins (Bcl-2, Bcl-XL, Mcl-1). As a result, SMAC, cytochrome C, and mitochondrial DNA are released as pro-apoptotic factors to the cytoplasm, where cytochrome C will interact with apoptotic peptidase activating factor 1 (Apaf-1). Apaf-1 multimerizes and attracts pro-caspase 9 into a macromolecular complex, the apoptosome, which will activate caspase 9 to additionally cleave effector caspases 3, 6, and 7 [52].

These effectors then shut down several ATP-consuming processes including translation, proteasomal degradation, and the activity of poly-(ADP-ribose) polymerase (PARP) family members, preparing the cellular demise [48]. Furthermore, caspases target the cytoskeleton, break down the protective lamin-layer on nuclear membranes and thereby bare open chromatin structures, which affects fragmentation of nuclei [54]. PS usually lines the inner leaflet of the plasma membrane, controlled by an ATP-dependent enzyme called flippase. During apoptosis, however, caspase 3 cleaves and activates scramblase enzymes that abrogate flippase function and PS architecture. PS is then exposed on the outside of apoptotic cells as an "*eat-me*" signal to macrophages [56].

1.2.2 Necroptosis

Necroptosis describes a regulated form of cellular necrosis, identified by organelle swelling, loss of cell membrane integrity leading to an inflow of water, and subsequent cell swelling until rupture. Necroptosis can be induced by a similar cascade of death receptor signaling as in apoptosis, but is independent of caspase activity. Because numerous pro-inflammatory DAMPs and cellular content are released concomitantly to cell burst, its outcome is much more inflammatory than during apoptosis (as further explained in 1.2.5.3) [48]. A central determinant for downstream necroptosis signaling originating from death receptor engagement is the inhibition of caspase 8 by, for example, c-FLIP or pan-caspase inhibitors, such as zVAD-fmk (shortened: zVAD) [57]. This enables a phosphorylation cascade of RIPK1, RIPK3 and the necroptosis executioner pseudokinase mixed-lineage kinase domain-like (MLKL), and the formation of the necrosome complex (consisting of RIPK1-RIPK3-MLKL). Eventually, phosphorylated MLKL oligomers translocate to the plasma membrane to mediate its permeabilization and cause the typical bursting phenotype of necroptosis (**Figure 5**) [58].

Necroptosis can limit viral replication and was therefore often described as a host suicide response to viral pathogens [57]. As part of this host antiviral defense, necroptosis can alternatively be activated in a RIPK1-independent manner [59]. A major contribution to host antiviral immunity emanates from viral nucleic acid sensing by a set of specialized PRRs: TLRs, RLRs, cGMP-AMP synthase (cGAS), and Z-DNA binding protein 1 (ZBP1). PRR signaling starts an antiviral inflammatory transcription program, leading to the expression of various death receptor ligands and type I IFN.

Additionally, PRRs can directly interact with regulators of apoptosis and necroptosis to stimulate a programmed cell death [60]. When TLR3 and TLR4 bind foreign viral double-stranded RNA in endosomes and interact with their adaptor protein TIR-domain-containing adapter-inducing IFN-β (TRIF), RIPK3 is recruited and binds TRIF via the RIP homotypic interaction motif (RHIM) domain. Similarly, ZBP1 can sense foreign Z-shaped RNA intermediates and bind RIPK3. Either of the complexes then triggers autophosphorylation of RIPK3 and stimulate MLKL phosphorylation in the absence of upstream death receptor signaling and RIPK1 [61-63].

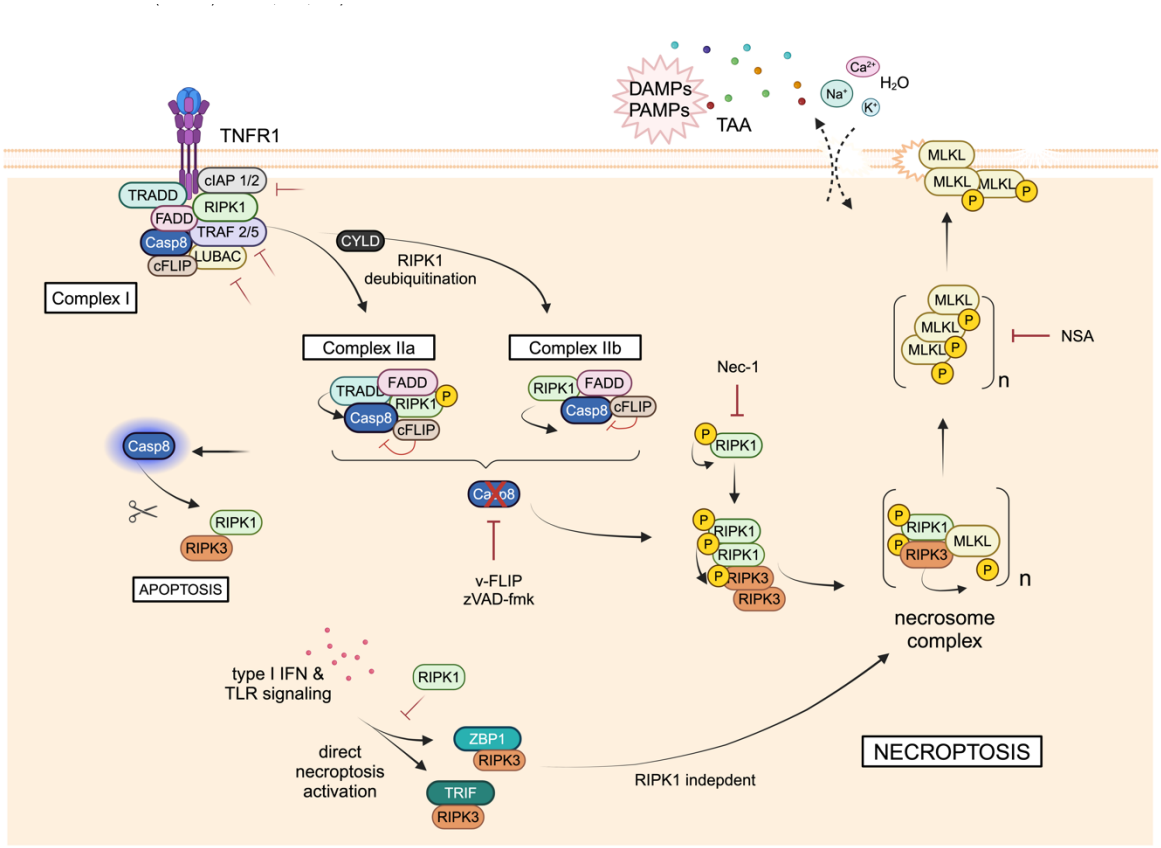

Figure 5. Schematic overview of necroptosis signaling

Similar to apoptosis, death ligand binding to their cognate receptors (here only shown for TNFR1) results in the assembly of caspase 8 containing Complex I. In situations of inhibition of cIAP1/2, TRAF 2/5, or linear ubiquitin chain assembly complex (LUBAC), the phosphorylation and ubiquitination pattern on RIPK1 and TRADD change and cytosolic Complex II forms. In necroptosis, however, initiator caspase 8 is inhibited by c-FLIP, zVAD-fmk, or viral analogs of FLIP (v-FLIP). TAK-mediated hyperphosphorylation of RIPK1 and polyubiquitination by PELI1 (not shown here) allow for interaction with RIPK3 through their RHIM domains and RIPK3 phosphorylation. RIPK3, in turn, phosphorylates and recruits MLKL to build the necrosome complex. Oligomerization of phospho-MLKL and translocation to the outer membrane results in MLKL-mediated membrane pore formation. Water inflow causes cell and organelle swelling and eventually lyses the cell, releasing several DAMPs, PAMPs, and cellular antigens. Alternatively, in a RIPK1-independent manner, RIPK3 interacts with the viral danger sensors ZBP1 or TRIF, respectively, and gets autocatalytically activated. RIPK3 signaling complexes phosphorylate MLKL to trigger necrosome complex formation. Pharmacologically, necroptosis was blocked in this study by using necrostatin-1 (Nec-1) that specifically blocks RIPK1 autophosphorylation [64], or using necrosulfonamide (NSA) which blocks MLKL tetramer polymerization [65]. The glow surrounding caspases (abbreviated Casp) indicates their activation. The scissor symbol indicates cleavage activity and a red X or red arrow with a blunt end marks inhibition or absence of central regulators. Abbreviations: TRADD (TNF receptor-associated death domain); TRAF 2/5 (TNF-receptor associated factors 2/5); PELI1 (pellino E3 ubiquitin ligase 1). Figure created in BioRender.com under consultation of [48, 57, 63].

1.2.3 Mutual regulators of survival signaling, apoptosis, and necroptosis

Survival signaling, apoptosis, and necroptosis are interconnected pathways that share several mutual regulators (RIPK1, caspase 8, c-FLIP, RIPK3), which determine the predominance of one or the other pathway and help to back each other up in response to viral perturbations [50]. Heterodimers of caspase 8 and the long isoform of pseudo-caspase c-FLIP$_L$ curtail caspase 8 activity to a level where RIPK1 and RIPK3 are still being cleaved but caspase 8 activity is insufficient to activate apoptosis; thus, promoting cell survival. This balance can be shifted to either caspase 8-mediated apoptosis (low levels of c-FLIP$_L$) or RIPK1/RIPK3-driven necroptosis (high levels of short isoform, c-FLIP$_S$) [50].

A central and complex role is taken by RIPK1, as it fulfills pro-survival and pro-death functions depending on the phosphorylation level, which is controlled by transforming growth factor β (TGF-β) activating kinase (TAK) [57]. The RHIM domains in RIPK1 and RIPK3 allow interaction with each other, as well as with other RHIM-containing proteins (ZBP1 or TRIF, for example) [61, 62].

RIPK1 phosphorylation at serine 25 and polyubiquitination favor the formation of pro-survival Complex I. Deubiquitination by CYLD or A20 followed by phosphorylation at serine 321 promote apoptosis (Complex IIa) independent of RIPK1 kinase function. In Complex IIb, however, TAK is absent, leaving RIPK1 unphosphorylated and triggering caspase 8 activation, dependent on RIPK1. Hyperphosphorylation of the RHIM domain by TAK and RIPK1 itself and polyubiquitination of RIPK1 by pellino E3 protein ligase 1 (PELI1) mediates RIPK1 dimerization and RHIM domain interaction with RIPK3. Subsequent phosphorylation of RIPK3 is considered to be a catalyst of MLKL recruitment, phosphorylation, and necrosome complex formation [57].

1.2.4 Oncolytic virus-induced apoptosis and necroptosis

Host cells have evolved to attain a vast set of defense mechanisms to protect themselves against viral infection. However, viruses co-evolved and developed numerous factors that counteract the host antiviral immunity or cell death signaling at any mechanistic level. While this has been the content of several reviews [59, 63, 66, 67], much less is known about the underlying cell death pathways in tumor cells in response to oncolytic virus infection. Tumor cells have acquired hundreds of mutations, some of which have gained the malignant cells features to resist cell death signaling, upregulate cell proliferation, and evade immune destruction [4]. Hence, oncolytic viruses encounter a unique cellular signature to establish infection and induce means of programmed cell death. However, considering the variability of tumor cell mutations, unique viral life cycles and oncolysis mechanisms, the elucidation of an underlying oncolytic death pathway becomes a comprehensive challenge for OV therapy development. Especially in the context of the engineered hybrid rVSV-NDV, the induced syncytial death pathway has not been characterized before and can so far only be predicted based on knowledge from the two parental viruses, VSV and NDV (summarized in **Table 1**).

Table 1. Cell death processes and ICD activated or inhibited by rVSV, rNDV, or rVSV-NDV in human cancer cell lines

Oncolytic vector	Cell death process	Key cell death mediators investigated	Outcome	Classic ICD marker	Tumor entity (cell line)	Ref.
VSV	Intrinsic apoptosis, autophagy	BAK, BAX, Bcl-2, Bcl-XL, MCL-1, Bid, Casp 3, LC-3B	Downregulation of MCL-1 by VSV contributes to apoptosis.	n.d.	HCC (Huh7, HepG2), lung cancer (A549)	[68]
VSV and VSV(MΔ51)	Intrinsic apoptosis, extrinsic apoptosis	FAS, Casp 3, 8 and 9, BH3-only proteins	VSV and VSV(MΔ51) induce intrinsic and extrinsic apoptosis. Defects in apoptotic signaling cause PDAC resistance to oncolysis.	n.d.	Pancreatic ductal adenocarcinoma	[69]
VSV(MΔ51)	Intrinsic apoptosis, extrinsic apoptosis	Bcl-XL, FAS, Casp 3	VSV(MΔ51) activates extrinsic apoptosis dependent on intrinsic apoptosis, even in presence of Bcl-XL overexpression.	n.d.	glioblastoma (U87)	[70]
NDV FMW strain	Apoptosis, autophagy, ER stress	MCL-1, Bcl-XL, PS exposure, PARP, LC-3, p62, eIF2a	NDV induces superior ICD upon STAT3 inhibition.	Hsp70, Hsp90, surface CRT, HMGB1, ATP	Prostate cancer (DU145, PC-3), melanoma (A375, C8161)	[71, 72]
NDV FMW strain	Apoptosis, autophagy	PS exposure, Casp3, PARP, LC-3B, ATG5	Autophagy dependent ICD induction by NDV in lung cancer. No contribution of necroptosis or apoptosis to ICD.	Hsp70, Hsp90, surface CRT, HMGB1, ATP	lung cancer (A549, H460)	[73]
NDV Herts 33 strain	Intrinsic apoptosis, extrinsic apoptosis, necroptosis	TNF, TRAIL upregulation, Casp 8, tBid, RIPK1 cleavage, p-MLKL,	NDV induces intrinsic and extrinsic apoptosis, which is promoted by RIPK1. RIPK1 recruits p-MLKL to stress granules, avoiding necroptosis.	n.d.	cervical cancer (HeLa)	[74]
NDV-Hitchner B1, NDV LaSota	Apoptosis	Bcl-XL, Casp 3	Enhanced syncytia formation in cells overexpressing anti-apoptotic Bcl-XL, but oncolysis is still mediated by apoptosis.	n.d.	lung cancer (A549)	[75]
NDV-Hitchner B1/FAS	Intrinsic apoptosis, extrinsic apoptosis	FAS, Casp 3, 8, and 9, PARP	NDV expressing FAS leads to higher and earlier activation of extrinsic and intrinsic apoptosis.	n.d.	HCC (Huh7), cervical cancer (HeLa), lung cancer (A549)	[76]
rVSV-NDV	n.d.	n.d.	Superior ICD induction by hybrid rVSV-NDV compared to parental viruses, VSV, and NDV.	Hsp70, Hsp90, surface CRT, HMGB1, ATP	HCC (Huh7)	[40]

Ref. (reference); n.d. (not defined); Casp (Caspase); LC-3B (microtubule associated protein 1 light chain 3 beta); ATG5 (autophagy-related gene 5); eIF2a (eukaryotic translation initiation factor 2A); PDAC (pancreatic ductal adenocarcinoma);

1.2.5 Immunogenic cell death

In addition to oncolysis, a major pillar in OV immunotherapy is the induction of a pro-inflammatory ICD, which awakens host immunity to fight cancer. ICD is initiated by surface exposure and release of a mixture of DAMPs, PAMPS, and TAAs from dying cells, which are sensed by PRRs on innate immune cells, like macrophages, natural killer (NK) cells, and DCs in the TME [7]. An essential step is to transmit the innate immune signal to T cells in the lymph node and unleash helper T cells (Th) and tumor-specific cytotoxic T lymphocytes (CTLs) that will home to the cancer site and carry out their effector functions. This is supported by the secretion of a panel of innate cytokines (TNF-α, IL-6, IL-12, IL-2, type I IFN) and T cell chemoattractants (CXCL9, CXCL10, CXCL11) to kindle an inflammatory environment surrounding the tumor [77]. However, cancer evolution has equipped malignant cells with various strategies to escape immune surveillance, for example, downregulation of MHC-I on tumor cells, upregulation of immune-dampening checkpoints, infiltration of immunosuppressor cells (myeloid-derived suppressor cells (MDSCs), regulatory T cells (T-reg), M2 macrophages) as well as production of high levels of anti-inflammatory and growth promoting cytokines (IL-10, TGF-β) [78]. All of this renders the TME as immunologically "*cold*" and impedes host anti-tumor immunity. Many OVs are equipped with an inherent feature to reverse the immunosuppressive environment by inducing ICD. Thus, a major focus in OV research is to explore and augment the ability of OVs to trigger the cancer immunity cycle and prime the body's own immune system in establishing short and long-term adaptive anti-cancer immunity (**Figure 6** A).

1.2.5.1 Essential markers of an immunogenic cell death

A set of the following DAMPs are typical markers that are used to identify cells undergoing ICD: surface exposure and release of calreticulin (CRT), the excretion of heat-shock proteins (Hsp70 and Hsp90) and high-mobility group box 1 protein (HMGB1), as well as quantification of extracellular ATP. Together with TAAs, type I IFN, and other factors, these DAMPs are sensed by PRRs on APCs and phagocytosing cells to bridge innate danger recognition and adaptive immunity (**Figure 6** B).

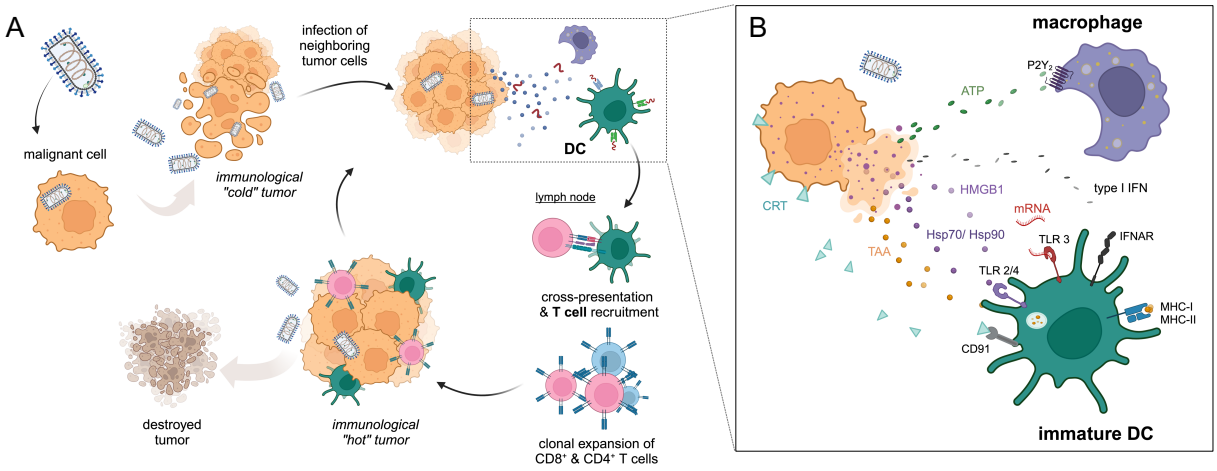

Figure 6. Oncolytic viruses trigger the cancer immunity cycle and stimulate intense immunogenic crosstalk between dying tumor cells and innate immune cells.

(**A**) Oncolytic viruses specifically infect tumor cells and elicit an innate immune response that is at first antiviral. Oncolysis of an often immunologically "*cold*" (low immune cell infiltration) tumor releases several DAMPs, PAMPs, and neoantigens to the TME. As early response to the virus, innate immune cells become activated and start infiltrating the tumor (not specifically shown here). DCs and macrophages sense the released DAMPs via specific PRRs (further specified in **B**) and migrate to tumor-draining lymph nodes, where they encounter naïve T cells. Upon cross-presentation, helper T cells and CTLs attain their effector function and home to primary and metastatic tumor sites. This twists the TME to a highly immune cell infiltrated "*hot*" tumor, which is targeted by the stimulated adaptive immune response. In (**B**): Interaction of a dying cancer cell with macrophages and DCs. Surface exposed CRT functions as an "*eat-me*" signal, while other released DAMPs (Hsp70, Hsp90, ATP, HMGB1) and cellular mRNA are typical "*find-me*" signals that serve to stimulate phagocytosis and antigen uptake. Released type I IFNs are typically sensed by TLRs and IFN-α receptor (IFNAR), potentiating the inflammatory innate response. NK cells also play a crucial role in innate antiviral as well as innate and adaptive anti-tumor responses. For simplicity of the Figure, NK cells are not shown. Figure created in BioRender.com under consultation of [7, 77, 79].

CRT is an ER-resident chaperone that supports protein folding, MHC-I assembly and maintains cellular Ca^{2+} homeostasis. CRT is a typical early ICD marker that, upon ER stress, trans-locates to the cell surface of dying cells, before the exposure of PS. On DCs, CRT is recognized by CD91 surface receptors, among many others, and simplifies phagocytosis of tumor antigens. In conditions of a strong lytic death, CRT is also released to the extracellular space, whereby it is debated whether soluble CRT can also fulfill opposite, immunosuppressive, roles [79-81].

Heat-shock proteins are molecular chaperones that are abundantly expressed in all cells and aid in protein (re-) folding or proteolysis. Concomitant to cell lysis, Hsp release is an alarming event that supports the innate response by upregulation of co-stimulatory signals on immature DCs as well as cytokine and chemokine secretion. Antigen cross-presentation to Th1 cells via MHC-I is stimulated, especially when Hsp-chaperoned peptides leave the dying cell and are recognized by endocytic receptors on APCs [82].

ATP excretion is generally considered to be a marker of dying cells. In ICD, several cellular stress pathways, including apoptosis, autophagy, endosomal exocytosis, and membrane permeabilization contribute to ATP release, but independently of HMBG1 release and CRT exposure.

ATP binds to purinergic $P2Y_2$ or $P2RX_7$ receptors on macrophages and DCs to elevate phagocytosis, activate the inflammasome, and stimulate T cells via released IL1-β [7, 83].

Another adjuvant component of ICD is the active excretion of HMGB1 from lytic cells and passive leakage from innate immune cells following their stimulation. HMBG1 is sensed by TLR4 and triggers DCs to vesicular antigen uptake. Interestingly, depending on its redox state, HMGB1 can increase chemokine and cytokine levels to recruit T cells, but in the presence of high levels of reactive oxygen species, fully oxidized HMGB1 loses its immune-stimulatory functions [84].

1.2.5.2 DC antigen cross-priming and anti-tumor cytotoxic T cell response

A functional evaluation of underlying ICD is obtained by *in vitro* or *in vivo* measurement of DC differentiation, activation, migration, and cross-priming of NK and T cells. DAMPs are recognized by numerous PRRs on DCs, leading to direct tumor antigen uptake and stimulation of DCs to migrate to tumor-draining lymph nodes and differentiate to mature DCs (detectable by upregulation of MHC-I, MHC-II, CD80, CD83, and CD86) [85]. In the lymph nodes, DCs cross-present processed tumor antigens via MHC class I receptors to naïve $CD8^+$ cytotoxic T cells, and via MHC-II to naïve $CD4^+$ helper T cells. Upregulation of co-stimulatory receptors on DCs (CD80, CD86) strengthens the crosstalk with Th1, Th2, Th17 cells, and further triggers the production of important differentiation cytokines (IL-12, type I IFN, IL1-β). In this way, $CD8^+$ CTLs undergo clonal expansion and home to the tumor site, where they recognize TAAs through antigen-specific T cell receptors and begin to produce IFN-γ for targeted cancer cell elimination (**Figure 6** A) [77, 86].

In vivo, myeloid or conventional DCs (cDC; $CD11c^+$, $CD123^-$) can be classified into two subtypes: cDC1 and cDC2. cDC1 ($CD141^+$, MHC-II ^{medium}) are specialized in cross-presenting foreign antigens, or neoantigens, or antigens from necrotic cells to naïve $CD8^+$ T cells, but also engage with Th1 cells to stimulate IL-12 production. The cDC2 subset ($CD1c^+$, MHC-II ^{high}, $CD11b^+$) is much more abundant than cDC1s and is primarily involved in Th cell activation via cross-presentation on MHC-II. A third class comprises plasmacytoid DCs (pDCs; MHC-II ^{low}, $CD11c^-$, $CD123^+$) that frequently respond to viral infections by secretion of high levels of type I IFN; however, additional roles in anti-tumor immunity and chemokine secretion are also described [85, 86]. In this study, the functional ICD characterization was limited to *in vitro* monitoring of differentiation and activation of DCs isolated from human peripheral blood mononuclear cells (PBMCs). These monocyte-derived DCs (moDCs) were differentiated to primarily cDC2 subsets (as there are only less than 0.05 % cDC1 in PBMCs) using GM-CSF and IL-4 [85] (see **Figure 46**).

1.2.5.3 Immunogenicity of rVSV-NDV

In contrast to apoptosis, necroptosis is commonly seen as the more immunogenic death, mainly because antigenic material and DAMPs are released from bursting necrotic cells, and RIPK1 and RIPK3 have been directly associated with pro-inflammatory gene expression. But, there has been a series of publications demonstrating that some established chemotherapies (anthracyclines or bortezomib), radiation, or photodynamic therapy can lead to an immunogenic type of apoptosis (reviewed in detail in [87]).

While the cell death pathway induced by rVSV-NDV is unknown, previous work established its immunogenicity in HCC and melanoma models, detecting essential DAMP release, DC activation, as well as cross-priming to cytotoxic T cells *in vitro* and *in vivo* [40-42]. Especially the demonstrated synergism of OVs in combination with immune-checkpoint inhibitors, highlights the huge potential OVs have on shaping immunogenicity. However, the mechanistic link between the immunogenic potential and the unique type of syncytial oncolysis is yet to be elucidated.

1.3 Model systems to decipher oncolytic virus-induced cell death

1.3.1 Human lung cancer as *in vitro* model system

This study primarily performed cell death characterizations in response to OV infection in two human non-small cell lung cancer (NSCLC) cell lines: A549 and H1437. Even though the mortality rate of lung cancer has been on a decline since 2000, at approximately 20 %, lung cancer still ranks at the top of cancer-related deaths in men and women in Europe [88]. Current treatment options range from surgery, radio- and chemotherapy to targeted treatment using kinase inhibitors or combination therapy with ICI [89]. However, depending on the tumor stage and time of diagnosis, the 5-year survival rate after diagnosis is prognosed at approximately 15 % in Germany [90]. Fortunately, more than 30 new therapies have been FDA-approved in the last decade for lung tumors, and their efficacy may improve patient survival [1]. Although there has been no OV therapy approved for lung cancer yet, numerous vectors are currently being investigated in phase I and II clinical trials for primary or metastatic lung carcinomas [91]. The therapeutic potential of the novel rVSV-NDV hybrid in human or murine lung cancer had not been explored and was therefore taken as a primary objective of this study.

1.3.2 Translation into mouse models of lung cancer

1.3.2.1 Intratracheal administration: an alternative OV delivery route for lung cancer

As opposed to many internal solid tumors, the lungs offer a unique opportunity for a directed, non-invasive loco-regional OV administration via the respiratory route, similar to drug delivery for chronic obstructive pulmonary disease (COPD), bronchial asthma, or acute lung injuries. The huge surface area and extensive vascularization of the respiratory endothelium can facilitate virus absorption and, thereby, limit dosages and side effects [92], compared to systemic injection. Even though intravenous (i.v.) treatment offers some advantage over the intratracheal (i.tr.) route in its simple clinical implementation, it still faces numerous challenges. Despite promising safety data, systemic OV delivery often presents challenges in efficacy. This could be explained by poor pharmacokinetics, addressable to the first-pass effect through the liver, dilution of the bioavailable OV dose in the circulation, and inactivation by neutralizing antibodies or complement in the blood [93]. For lung cancer treatment, OVs could thus be delivered by intratracheal administration, inhalation of aerosols, intranasally, or via intrapleural injection. Notwithstanding, as promising as that sounds, it also imposes numerous unsolved questions ranging from vector design, virus stability, requirement of adjuvants, pharmacokinetics, and antiviral immunity in the lung to oncolytic efficacy.

However, a recent phase I/II clinical study with oncolytic HSV-1 in lung mesothelioma patients demonstrated safety and had a promising treatment outcome using intrapleural OV delivery [94].

Superior treatment effects have been reported using intratracheal administration in mice, although the procedure is rather complex and delicate, depending on anesthesia, the insertion of a fine tube catheter into the mouse trachea, and the instillation of the OV suspension. Garbuzenko et al. demonstrated that liposome-coated doxorubicin led to better destruction of A549 lung cancer xenotransplants when given intratracheally than when the same drug was administered intravenously [95]. Another study confirmed that intratracheal influenza A virus administration yielded higher acute and better reproducible infections in mice than via the intranasal route [96]. In a genetically induced orthotopic lung cancer model in mice, Fukazawa et al. tested the intratracheal administration of adenoviral gene therapy and achieved superior tumor reduction in combination with exogenous pulmonary surfactant, compared to adenovirus alone. The effect was explained by ameliorated penetration of the surfactant-virus formulation into distant alveolar lung regions [97]. Pulmonary surfactant is an endogenous lipoprotein mixture with essential functions in lowering lung epithelial surface tension and enabling free gas exchange in the alveolar region [98]. Whether these observations are translatable to the oncolytic effects of rVSV-NDV remained to be seen, but the trends highlight the potential of employing alternative treatment routes in OV therapy development.

1.3.2.2 Two distinct models of murine lung cancer

In order to qualify rVSV-NDV for a potential local treatment of lung cancer, a proof-of-concept study in two models of murine lung cancer was employed and explored the feasibility of standard intravenous injection versus direct intratracheal OV delivery.

A frequently used model for orthotopic induction of murine lung adenocarcinoma was originally described by Jackson and colleagues [99-101]. Local, intratracheal administration of adenovirus expressing Cre recombinase (Ad-Cre) into *K-ras*$^{LSL\text{-}G12D/+}$*; p53*$^{fl/fl}$ (KP) mice induces spatiotemporal recombination events leading to the activation of the Kirsten rat sarcoma (KRAS) proto-oncogene, a common oncogenic driver in lung cancer, as well as deletion of the p53 tumor suppressor gene. Mice then develop multifocal lung tumors which histopathologically mimic all four stages of human NSCLC development (benign hyperplasia, atypical adenomatous hyperplasia, adenoma, adenocarcinoma) [99, 101]. A detailed description of the model is given in sections 2.2.6.3 and 3.3.2.

In an alternative model, syngeneic murine tumor cells (B16 melanoma or Lewis-lung carcinoma cells, LLC) were implanted via tail-vein injection and are described to engraft within 2 – 3 weeks in the mouse lungs [102-104]. These experimental metastasis models are more invasive than genetically induced models yet recapitulate multifocal lung cancers and are faster to generate than the genetic models. Details of the model are also further described later (2.2.6.4 and 3.3.2.2).

Overall, the second “chapter” of the thesis will show that translation into a suitable preclinical model is a major challenge in OV drug development. First steps to evaluate the efficacy of rVSV-NDV therapy in lung cancer were taken and a first realization of two distinct treatment routes in this model is provided.

1.4 Aim

The overarching goal of this doctoral thesis was to explore the therapeutic potential of the oncolytic hybrid virus rVSV-NDV in lung cancer and characterize its mechanism of oncolysis. The project was divided into two aims: (**1**) Deciphering the underlying cell death pathway(s) of syncytial oncolysis *in vitro* and (**2**) establishing a murine model of lung carcinoma suitable for testing two delivery routes of the OV therapy *in vivo*.

In recent years, rVSV-NDV has proven its therapeutic potential in an expanding portfolio of tumor entities and encompasses a unique mechanism of tumor cell killing via syncytia formation [46]. Cell death pathways in normal physiology and disease are widely characterized, but oncolytic virus-induced cancer cell death mechanisms are hitherto superficially studied, especially in the case of fusogenic, engineered vectors. Initial data using rVSV-NDV suggests that virus-mediated cancer cell-cell fusion triggers an immunogenic death [40-42]; however, an underlying cell death pathway has not been identified. A thorough characterization, however, can reveal relevant host or viral regulators of oncolysis that are worth targeting in OV combination therapies or that can improve viral vector design by expressing appropriate death-promoting transgenes. The main section of this work aims to decipher the cell death mechanism of syncytial oncolysis in human lung cancer cells *in vitro.* Moreover, it was aimed to elucidate a relationship between the level of fusogenicity and immunogenicity of dying cancer cells. Based on previous work, it was hypothesized that a higher rate of cell-cell fusion correlates with higher immunogenicity of tumor cell death.

In the second part of this work, rVSV-NDV was explored for its putative therapeutic potential in two mouse models of lung cancer. While systemic OV delivery is an important aim of oncolytic virotherapy development, lung tumors allow for a direct, loco-regional treatment via the respiratory route that could enhance treatment effects. Hence, another objective of the thesis was to study and optimize the therapeutic effects of rVSV-NDV in an established genetically induced mouse model of lung adenocarcinoma, as well as a model of orthotopically implanted lung cancer. Thereby, it was anticipated to achieve superior tumor reduction via the intratracheal treatment route, compared to intravenous injection of the OV.

The development of novel oncolytic viro-immunotherapies is a long-lasting process and warrants a thorough mechanistic understanding of the underlying molecular mechanism of action, but also a suitable animal model for successful transition from bench science into clinical studies. Anticipating the clinical translation of the engineered OV rVSV-NDV, this work approached two of many hurdles in clinical OV therapy development.

2 MATERIALS AND METHODS

2.1 Materials

2.1.1 Antibodies

Table 2. Primary and secondary antibodies

Antibody	Application	Manufacturer (catalog #)
Rabbit anti- Calreticulin (ER-marker)	Flow Cytometry	Abcam (#2907)
Mouse anti- human CD1a – Pacific Blue	Flow Cytometry	Biolegend (#300124)
Mouse anti- human CD1c (L161) – Pacific Blue	Flow Cytometry	Biolegend (#331507)
Mouse anti- human CD11c – APC clone 3.9	Flow Cytometry	Biolegend (#301613)
Mouse anti- human CD14 – PE-Cy7 (clone M5E2)	Flow Cytometry	BD Biosciences (#557742)
Mouse anti- human CD86 – PE	Flow Cytometry	Biolegend (#374206)
Mouse anti- human CD123 – FITC	Flow Cytometry	Biolegend (#306013)
Mouse anti- human CD141 (BDCA-3) – APC-Vio770	Flow Cytometry	Miltenyi Biotec (#130-113-315)
Mouse anti- human HLA-DR (MHC-I) – PerCP-Cy5.5	Flow Cytometry	Biolegend (#311420)
Mouse anti- human HLA-ABC (MHC-II) – BV-605	Flow Cytometry	Biolegend (#311432)
Mouse anti- β-Actin (clone AC-74)	Western Blot	Sigma Aldrich (#A2228)
Rabbit anti- Calreticulin (D3E6) XP®	Western Blot	Cell Signaling Technology (#12238)
Mouse anti- Caspase 3 (31A1067)	Western Blot	Santa Cruz Biotechnology (#56053)
Mouse anti- Caspase 8 (1C12)	Western Blot	Cell Signaling Technology (#9746)
Rabbit anti- Caspase 9	Western Blot	Cell Signaling Technology (#9502)
Rabbit anti- cleaved Caspase 9 (D315)	Western Blot	Cell Signaling Technology (#9505)
Rabbit anti- GAPDH (14C10)	Western Blot	Cell Signaling Technology (#2118)
Rabbit anti- HMGB1 (D3E5)	Western Blot	Cell Signaling Technology (#6893)
Mouse anti- HSP70 (3A3)	Western Blot	Santa Cruz Biotechnology (#32239)
Rabbit anti- HSP90	Western Blot	Cell Signaling Technology (#4874)
Rabbit anti- MLKL antibody [EPR17514]	Western Blot	Abcam (#184718)
Rabbit anti- MLKL (phospho S358) antibody [EPR9514]	Western Blot	Abcam (#187091)
Rabbit anti- PARP antibody	Western Blot	Cell Signaling Technology (#9542)
Rabbit anti- human phospho RipK1 (S166) (D1L3S)	Western Blot	Cell Signaling Technology (#65746)
Mouse anti- RIP (clone 38/RIP)	Western Blot	BD Transduction Labs (#610459)
Rabbit anti- RIPK3 (phospho S227) (EPR 9627)	Western Blot	Abcam (#209384)
Rabbit anti- human RIPK3 antibody	Western Blot	Abcam (#226297)
Horse anti- Mouse IgG, HRP-linked Antibody	Western Blot	Cell Signaling Technology (#7076)
Goat anti- Rabbit IgG, HRP-linked Antibody	Western Blot	Cell Signaling Technology (#7074)
Goat anti- Rabbit IgG H&L (Alexa Fluor® 488)	Flow Cytometry	Abcam (#150077)

2.1.2 Chemicals, reagents and kits

Table 3. Chemicals, media supplements and reagents

Item	Manufacturer (catalog #)
Alveofact (bovine pulmonary surfactant)	Lyomark Pharma (6559990)
Curosurf (porcine pulmonary surfactant)	Chiesi (10122-510-01)
Doxorubicine-HCl (Doxo)	Cayman Chemicals (15007)
FCCP (Carbonyl cyanide-*p*-trifluoromethoxyphenylhydrazone)	Cayman Chemicals (15218)
Hygromycin-B solution	Carl Roth (CP12.2)
LCL-161 (Smac mimetic)	Cayman Chemicals (22420)
MAX Efficiency™ Stbl2™ competent cells	Invitrogen (10268019)
Mitoxantrone – dihydrochloride (MTX)	Tocris Bio (4250)
Nano-Glo® Endurazine Live Cell Substrates	Promega (N2570)
Necrostatin-1 (Nec-1)	Sigma (N9037)
Necrosulfonamide (NSA)	Selleckchem (S8251)
One Shot™ Stbl3™ competent cells	Invitrogen (C737303)
Prostaglandin E2 (PGE_2)	Cayman Chemicals (14010)
Polybrene (Hexadimethrine bromide)	Tocris Bio (7711)
Polyethylenimin (PEI)	Thermo Fisher Scientific (040528.22)
Puromycin Dihydrochloride	Carl Roth (0240)
R848 (Resiquimod)	Invivogen (tlrl-r848)
Recombinant human GM-CSF	Biolegend (576302)
Recombinant human IL-4	Peprotech (200-04)
Recombinant human TNF-α	Peprotech (300-01A)
Recombinant IFN-γ	Peprotech (300-02)
Recombinant IL1-β	Peprotech (200-01B)
Rotiphorese-30 Gel (Acrylamide/Bis-acrylamide solution (29:1), 30 %)	Carl Roth (A124.2)
Staurosporine	Cayman Chemicals (81590)
Subcloning Efficiency™ DH5alpha™ Competent Ecoli cells	Invitrogen (18265017)
TMRE (Tetramethylrhodamine ethyl ester)	AAT Bioquest (ABD-22220)
zVAD-fmk (shortened zVAD)	AbMole BioScience (M31-43)

Table 4. Assay and reagent kits

Kits	Manufacturer (catalog #)
ATP Bioluminescence Assay Kit HS II	Roche (11699709001)
Caspase-Glo® 3/7 Assay system	Promega (G8091)
Caspase-Glo® 8 Assay system	Promega (G8201)
CellTiter-Glo® Luminescent Cell Viability assay	Promega (G7571)
Cytotox 96 Non-radioactive cytotoxicity assay	Promega (G1780)
DC™ Protein Assay	BioRad (5000113, 5000114)
HotStarTaq DNA Polymerase kit	Qiagen (203203)
InnuPrep™ RNA Mini kit	Analytik Jena (1440958)
OneStep RT-PCR kit	Qiagen (210212)
QIAex II gel purification kit	Qiagen (20021)
QIAfilter Plasmid DNA Midi kit	Qiagen (12245)
QIAprep Spin Miniprep kit	Qiagen (27106)
QIAquick PCR purification kit	Qiagen (28106)
Quick Ligation kit	New England BioLabs (NEB, M2200S)

2.1.3 Primer

Table 5. Forward and reverse primer sequences

Primer name	Application	Sequence 5' – 3'	Expected fragment [bp]
Myc_fwd	Mycoplasma PCR	GGCCAATGGGTGAGTAACACG	450-500
Myc_rev		GATAACGCTTGCGACCTAT	
NDV/F -5 (fwd)	PCR over NDV-F gene for validation of NDV/F_{3aa}(L289A) mutation; plasmid and plaque sequencing primer	ATGGGCTCCAGACCTTCTAC	1620
NDV/F -3 (rev)		TCACATTTTTGTAGTGGCTC	
NDV-HN (pme-5) fwd	RT-PCR to validate viral rescue of rVSV-NDV variants	TATCATGGACCGCGCCGTTAGCCAA	1720
NDV-HN (pac-3) rev		TTTAAACCTAGCCAGACCTGGCTTCTC	
VSV-L_111_rev	RT-PCR to validate viral rescue of GFP-containing rVSV-NDV variants (multiple cloning site)	AAGTACGTCATGCGCTCATC	1200 (with GFP), 470 (without insert)
VSV-NDV_6857HN_fwd		TAGAAACCACACCTTGCG	
VSV-P_fwd	RT-PCR to validate viral rescue of rVSV-NDV variants	TCTCGTCTGGATCAGGCGGTAGGA	675
VSV-P_rev		TCGTCCGTCACCTCCGACAGA	
Vaccinia_fwd	RT-PCR to validate absence of Vaccina Virus	ATGAACACGATTAACATCGC	2500
Vaccinia_rev		TTACGCGAACGCGAAGTCCG	

K-ras_wt_fwd	PCR for K-ras genotyping	CACCAGCTTCGGCTTCCTATT	270 (wt); 270/170 (het.)
K-ras_common_rev		AGCTAATGGCTCTCAAAGGAATGA	
K-rasG12D_mut_fwd		CCATGGCTTGAGTAAGTCTGC	
P53_fwd	PCR for p53fl/fl genotyping	GGTTAAACCCAGCTTGACCA	270 (wt); 270/390 (het.) 390 (homo.)
P53_rev		GGAGGCAGAGACAGTTGGAG	
U6_fwd	Fwd primer for sequencing of sgRNA containing plentiCRISPR v2	GAG GGC CTA TTT CCC ATG ATT CC	/
RIPK3_exon2_fwd	Primer for CRISPR/Cas9 knockout validation (flanking exon 2 of RIPK3)	CCAGCCTGATGTCGTGCGTCAA	450
RIPK3_exon2_rev		ATTCAGGCCCCAGAGCACAGTG	
RIPK3_exon6_fwd	Primer for CRISPR/Cas9 knockout validation (flanking exon 6 of RIPK3)	GGATCCTTAACCCCAGGTGCCCTT	460
RIPK3_exon6_rev		AGGGACAGCAGAGTGGAGTGCA	
MLKL_exon9_fwd	Primer for CRISPR/Cas9 knockout validation (flanking exon 9 of MLKL)	TCAAACTCCTCCAAGGACCACC	488
MLKL_exon9_rev		GCCACCAGCTTGCGGATCTTCT	
MLKL_exon2_fwd	Primer for CRISPR/Cas9 knockout validation (flanking exon 2 of MLKL)	TGGACCAGCTCTTCCCAGCTACA	436
MLKL_exon2_rev		ATCTCCCCATTAGCCTCCTCCAGG	

Abbreviations: fwd (forward); rev (reverse); het. (heterozygous); homo. (homozygous); wt (wildtype); bp (base pairs)

2.1.4 Appliances

Table 6. Laboratory appliances

Equipment	Manufacturer
AxioVert 40 CFL Fluorescent Microscope	Carl Zeiss
CytoFLEX S flow cytometer	Beckman Coulter
Gel Doc XR+ Documentation system	BioRad
GloMax® Discover microplate reader	Promega
JuLiBR (brightfield) imaging station	Nanoentec
LUNA-FL™ cell counter	Logos biosystems
Multiskan™ FC microplate Photometer	Thermo Fisher Scientific
NanoDrop™ Lite™	Thermo Fisher Scientific
nanoScan SPECT/CT	Mediso Medical Imaging Systems
Optima UX-L ultracentrifuge	Beckman Coulter
SW70Ti fixed angle bucket	Beckman Coulter
xCELLigence Real-Time Cell Analysis	Agilent

2.1.5 Software

Table 7. Software

Software	Developer
Benchling	Benchling Inc.
BioRender	BioRender.com
CHOPCHOP – CRISPR Genome Editing tool	University of Bergen [105]
FlowJo version 10.8	BD Biosciences
Illustrator CS5 version 15.0	Adobe Inc.
ImageJ (Fiji) version 2.1	Wayne Rasband (NIH)
ImageLab version 6.1	BioRad Laboratories Inc.
ITK-Snap version 4.0.1	University of Pennsylvania [106]
MacVector version 12.6	MacVector Inc.
Nucline™ 2.03 Nanoscan Software	Mediso
Photoshop CS5 version 12.0	Adobe Inc.
PRISM version 8	GraphPad Software Inc.
Excel, Powerpoint, Word	Microsoft Corp.

2.1.6 Buffer compositions

Table 8. Buffer compositions

Buffer	Composition
Cellular DNA isolation buffer	10 mM Tris-HCl (pH 7.5) in dH_2O 1 mM CaCl2 3 mM MgCl2 1 mM EDTA 1 % Triton-X 100 0.2 mg/mL Proteinase K (Qiagen), added fresh before use
Mouse DNA Isolation buffer	10 mM Tris-HCl (pH 8.3) in dH_2O 50 mM KCl 0.45 % (v/v) IGEPAL® 0.45 % (v/v) Tween-20 0.4 mg/mL Proteinase K (Qiagen), added fresh before use
Ponceau-S solution:	0.1 % (w/v) Ponceau-S tetrasodium salt in dH_2O 5 % (v/v) glacial acetic acid
Protein Lysis buffer (RIPA)	50 mM Tris-HCl (pH 7.4) in dH_2O 150 mM NaCl 0.1 % (w/v) SDS 1.0 % (w/v) Na-deoxycholate 1.0 % (v/v) Triton-X 100 protease + phosphatase inhibitors added fresh before use
Tris-buffered saline + Tween (TBS-T), 1X	20 mM Tris-HCl (pH 7.4) in dH_2O 150 mM NaCl 0.1 % (v/v) Tween-20
Western blot sample loading buffer (6x Laemmli)	375 mM Tris-HCl (pH 6,8) in dH_2O 50 % (v/v) glycerol 9 % (w/v) SDS 0.06 % (w/v) bromophenol blue 0.6 % (v/v) β-mercaptoethanol, added fresh before use
Western blot low-molecular weight sample loading buffer, 6X	300 mM Tris-HCl (pH 6.8) in dH_2O 50 % (v/v) glycerol 24.5 % (w/v) SDS 0.6 % (w/v) Coomassie Brilliant Blue
Western Blot low-molecular weight SDS PAGE running buffer, 1X	25 mM Tris-HCl (pH 8.3) in dH_2O 25 mM Tricine 0.05 % (w/v) SDS 0.25 g/L $NaHSO_3$, added fresh before use

Western Blot high-molecular weight SDS PAGE running buffer, 1X	25 mM Tris-HCl (pH 8.3) in dH_2O 25 mM Tricine 1 % (w/v) SDS 0.25 g/L $NaHSO_3$, added fresh before use
Western blot transfer buffer (Towbin), 1X	2.5 mM Tris-HCl (pH 8.3) in dH_2O 19.2 mM glycine 20 % (v/v) methanol 0.25 g/L $NaHSO_3$, added fresh before use
Western blot ECL solution	100 mM Tris HCl (pH 8.5) in dH_2O 0.2 mM *p*-coumaric acid 1.25 mM Luminol 0.03% (v/v) of 30 % H_2O_2 solution

Table 9. Western Blot gel recipes for separating and stacking gel

Recipe for 3 standard 13 x 9 cm gels; adapted and modified from [107].

	Acrylamide in gel	Rotiphorese ®-30 % (29:1) [mL]	2.5M Tris-HCl 0.3 % SDS buffer (pH 8.8) [mL]	dH_2O [mL]	APS [µL]	TEMED [µL]
Separating gel	7 %	4.6	11.2	3.8	200	20
	10 %	6.6	11.2	1.8	200	20
	12 %	8.0	10.0	1.8	200	20
	16 %	10.6	8.6	0.4	200	20
	Acrylamide in gel	Rotiphorese ®-30 % (29:1) [mL]	0.5 M Tris-HCl, 0.3 % SDS buffer (pH 6.8) [mL]	dH_2O [mL]	APS [µL]	TEMED [µL]
Stacking gel	4 %	2.4	3.8	11.5	200	20

2.2 Methods

2.2.1 Cell culture

All cell culture was performed in media without antibiotics and was routinely checked for mycoplasma contamination by standard PCR using HotStarTaq DNA polymerase (Qiagen) and the primer pair indicated in **Table 5**. All cell lines were maintained at 37°C, 5 % CO_2 in a humidified incubator. Cell lines were cryopreserved in 45 – 50 % culture media, 45 % fetal calf serum (FCS) and 5 – 10 % DMSO and stored in liquid nitrogen gas phase. An overview of the cell lines used in this study and their respective media is listed in **Table 10**. Cell counts and viability were measured on a LUNA-FL™ cell counter using 0.4 % trypan blue staining prior to seeding and infection to accurately adjust the multiplicity of infection (MOI).

Table 10. Cell lines and media composition

Cell line	Description	Media*
A549	Human alveolar basal epithelial lung adenocarcinoma (NSCLC)	DMEM/F-12 + 5 % FCS
AGE1.CR.pIX	Muscovy Duck embryonic retina cells	DMEM/F-12 + 5 % FCS
B16-OVA	Murine melanoma cell line expressing chicken ovalbumin antigen (OVA)	DMEM GlutaMAX™ + 10% FCS
BHK-21	Baby Hamster Kidney fibroblast cells	GMEM + 10 % FCS + 2 % tryptose-phosphate broth
H1437	Human broncho-epithelial lung adenocarcinoma (stage 1 NSCLC)	RPMI-1640 + 10 % FCS
HEK-293T	Human embryonic kidney cells expressing SV40 large T antigen	DMEM GlutaMAX™ + 10 % FCS
LLC1	Murine Lewis lung carcinoma	RPMI-1640 + 10 % FCS

*Base media obtained from Gibco, FCS (Serana)

2.2.2 Viruses

2.2.2.1 Viral vectors

rVSV: The recombinant VSV vector is based on the laboratory VSV Indiana strain (NCBI GenBank accession No. J02428) and was modified to express an enhanced green-fluorescent protein (eGFP) reporter gene (rVSV-GFP) [108]. VSV stocks were generated in adherent BHK-21 cells and purified by sucrose gradient as previously described [109].

rVSV-NDV/F_{3aa}(L289A) and rVSV-NDV/F_{3aa}: The recombinant VSV-NDV/F_{3aa}(L289A) vector (shortened name rVSV-NDV) is composed of an rVSV backbone wherein the surface glycoprotein (VSV-G) had been replaced by the hemagglutinin-neuraminidase (HN) and the modified fusion protein (F_{3aa}(L289A)) of recombinant NDV, originally described by Abdullahi et al. [40]. A multiple cloning site (AscI, KpnI, AvrII) was introduced between the HN and L gene for transgene insertion to create rVSV-NDV-GFP [41]. rVSV-NDV or rVSV-NDV-GFP were further modified in this study to generate rVSV-NDV/F_{3aa} and rVSV-NDV/F_{3aa}-GFP, as explained in section 2.2.2.2.

Vaccinia virus expressing T7 RNA polymerase: The modified vaccinia virus Ankara (MVA), Vtf7.3, is an attenuated vaccinia vector that expresses the RNA polymerase of bacteriophage T7 to enable transient recombinant gene expression under the control of the T7 promoter [110]. Vaccinia virus Vtf7.3 was amplified and purified from BHK-21 cells by centrifugation through a 30 % sucrose cushion, described in detail in [111]. VV was titrated on BHK-21 cells as described in 2.2.2.4.

2.2.2.2 Viral engineering of rVSV-NDV/F_{3aa} and rVSV-NDV/F_{3aa}-GFP

To modify the fusion protein of rVSV-NDV, the gene segment encoding for the F_{3aa} protein was excised from a plasmid vector of the Hitchner B1-strain of NDV (NDV-B1/F_{3aa}) (GenBank accession No. AF375823) and cloned into the rVSV-NDV backbone to replace the NDV-B1/F_{3aa}(L289A) protein. In detail, both vectors were generated in DH5alpha competent *E. coli* cells, purified by QIAfilter Plasmid DNA Midi kit (Qiagen). Plasmid DNA concentration was measured on a NanoDrop™ Lite™ spectrophotometer (Thermo Fisher Scientific), and 5 µg DNA was sequentially digested using SmaI (25U, 25°C) and NotI-HF (25U 37°C) restriction enzymes (NEB) for 1 h each. The resultant 810 bp fragment, named NDV-B1/F_{3aa} insert, and a backbone construct of rVSV-NDV (around 13 kb) were gel purified by QIAex II gel purification kit (Qiagen). F protein exchange was achieved by ligating the NDV-B1/F_{3aa} insert into the rVSV-NDV backbone using QuickLigase (NEB) for 15 minutes at an insert/vector ratio of 5:1 at 25°C, followed by transformation into MAX Efficiency™ Stbl2™ competent cells (Invitrogen). Successful cloning was confirmed by control digestion of the new vector, called rVSV-NDV/F_{3aa} (see **Figure 10**) using SmaI and NotI-HF and completed by Sanger sequencing using the primers listed in **Table 5**. Cloning of the rVSV-NDV/F_{3aa}-GFP vector was performed in a similar manner using the NDV-B1/F_{3aa} insert and rVSV-NDV-GFP as a backbone vector. Here, bacterial clones were additionally screened by colony PCR for the presence of the GFP reporter gene inside the multiple cloning site (mcs).

To generate infectious rVSV-NDV/F_{3aa} or rVSV-NDV/F_{3aa}-GFP virus, the following reverse genetics protocol was applied (**Figure 7**). BHK-21 cells were seeded in a 6-well plate at 8x 10^5 cells/well and infected the next day with VV expressing the T7 polymerase (Vtf7.3) at an MOI of 1.

After 1 h of infection at 37°C, BHK-21 cells were co-transfected with the following plasmids using Lipofectamine™-2000 (Invitrogen):

- the respective vector containing the full-length antigenomic cDNA of rVSV-NDV/F_{3aa} or rVSV-NDV/F_{3aa}-GFP (2 µg/well)
- the following helper plasmids providing structural genes necessary to generate the first viral particle driven by the T7 promoter:
    - pIRES-VSV-G (0.25 µg/well).
    - pCI-neo Maraba-N (1 µg/well)
    - pCI-neo Maraba-P (0.8 µg/well), and
    - pCI-neo Maraba-L (0.4 µg/well).

VV infection was controlled in a separate well transfected with a pIRES-GFP plasmid (pUC19-T7-IRES-eGFP, Addgene), and transfection efficiency was controlled in an uninfected well transfected with a GFP-control plasmid (pcDNA3-eGFP, Addgene), in which GFP is expressed under the ubiquitous CMV promoter.

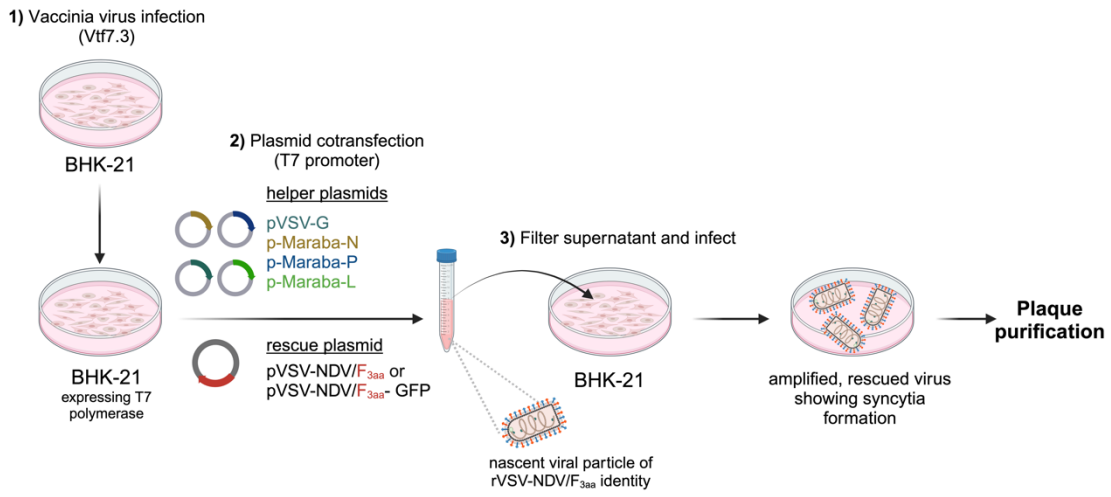

Figure 7. Reverse genetics system for the rescue of (-) RNA viruses.

Experimental workflow for the viral rescue and generation of nascent viral particles in BHK-21 cells exemplified for VSV-NDV/F_{3aa} and VSV-NDV/F_{3aa}-GFP. **1)** BHK-21 cells are first infected with Vtf7.3 and one hour later **2)** transfected with rescue and helper plasmids. Nascent viral particles are formed in BHK-21 cells and collected in the supernatant. **3)** Filtration and later plaque purification eliminate contaminant traces of VV and purify single clones of the rescued rVSV-NDV virus.

48 hours post transfection, cells were lysed by one freeze-thaw cycle, and the supernatant and lysate were cleared from cell debris and remaining VV by, first, centrifugation at 10000 x *g* for 5 min and subsequent filtration through a 0.22 µm filter. The cleared lysate containing the rescued virus was then transferred onto a fresh monolayer of confluent BHK-21 cells. In the following days, wells showing signs of syncytia formation were harvested and further purified from remaining VV by plaque purification as described previously but using BHK-21 cells [112]. Next, viral RNA from individual plaques of the rescued virus was isolated using InnuPrep™ RNA Mini Kit (Analytik Jena). The rescued viral plaques were validated by RT-PCR using Qiagen OneStep RT-PCR kit for:

1) the correct replacement of the fusion protein,

2) the absence of contaminant vaccinia virus,

3) the presence of the VSV backbone (VSV-P gene) and

4) for VSV-NDV/F_{3aa}-GFP: the presence of the GFP insert in the mcs

with the primers indicated in **Table 5** and the RT-PCR program listed in **Table 11**. Sanger sequencing further confirmed the correct insertion of the NDV-B1/F_{3aa} gene before large-scale virus production in AGE1.CR.pIX cells.

Table 11. RT-PCR program for validation of vaccina-free rescue of rVSV-NDV variants

Program	T [°C]	Hold time [min]	Cycles
cDNA synthesis	50	30	1
Denaturing	95	15	1
Amplification	95	1	
	50 / 55/ 57*	0.75	35x
	72	1	
Final elongation	72	10	1

*50°C Vaccinia primer, 55°C NDV-HN primer and GFP primer, 57°C VSV-P primer.
PCR products were purified using QIAquick PCR purification kit before analysis by Sanger sequencing.

2.2.2.3 rVSV-NDV virus production

For the production of rVSV-NDV and rVSV-NDV/F_{3aa} virus, AGE1.CR.pIX cells (ProBioGen) were seeded onto 15 cm^2 dishes and when reaching confluence, infected at an MOI of 0.0001 of the respective viruses in serum-free media. 48 hours post infection (hpi), culture supernatant (extracellular virus) was cleared (1000 x *g* at 4°C, 10 min) and directly subjected to ultracentrifugation.

Infected cells were lysed with 0.001 % Triton-X 100 in PBS, scraped, vortexed and sonicated for 3 min in a bath sonicator to release intracellular virus. Cellular debris were removed by centrifuging at 1000 x *g* at 4°C for 15 min. Intra- and extracellular harvests were pooled and ultracentrifuged at 65000 x *g* 4°C for 1 h to pellet virus (Beckman Coulter Optima UX-L; SW70Ti fixed angle bucket). The resulting viral pellets were pooled, passed through a 20*G* syringe needle and purified on a 60 - 30 - 10 % discontinuous sucrose gradient in PBS. The purified viral band was isolated and aliquoted for *in vitro* use. For *in vivo* applications, an additional ultracentrifugation run in PBS was performed to remove the remaining traces of sucrose, and the final viral pellet was resuspended in PBS. All viral stocks were stored at -80°C until use.

2.2.2.4 Virus titration

Viral titers in stocks or samples of rVSV, rVSV-NDV, or rVSV-NDV/F_{3aa} were quantified by the 50 % tissue culture infectious dose ($TCID_{50}$) method. In brief, confluent monolayers of AGE1.CR.pIX cells were infected with serially diluted samples (log_{10} increments) in technical quadruplicates. 72 hpi, infected wells were counted under the microscope to calculate the 50 % endpoint titer based on the Spearman and Kärber method [113], shown in the formula below. Viral titers are expressed as $TCID_{50}$/mL with a standard deviation of ± 0.3 log_{10} $TCID_{50}$/mL.

$$log_{10}\ 50\%\ endpoint\ dilution = -x + \frac{d}{2} - d\sum\frac{r}{n}$$

X is the highest dilution at which all wells are infected, d represents the log_{10} of the dilution factor (d = 1 for log_{10} serial dilutions). n is the total number of wells per dilution (n = 4 for quadruplicates) and r indicates the number of infected wells at dilution x+1.

2.2.4 *In vitro* studies

2.2.4.1 Viral growth curves and oncolysis measurement

Murine or human cancer cells were plated in either 6- or 12-well plates and incubated at 37°C overnight. The next day, when reaching 80 % confluency, cells were infected at various MOIs (further specified in the Results section). The infection was monitored on an Axiovert 40 CFL Fluorescent microscope (Zeiss) or using a brightfield cell imaging system (JuLI™ Br, NanoEntek). The infectious viral titer (see 2.2.2.4) and the virus-mediated cell cytotoxicity were measured from the supernatant at defined time points after infection. To quantify cytotoxicity as a measure for viral oncolysis, the amount of enzymatic lactate dehydrogenase (LDH) activity was measured from fresh supernatants using CytoTox96® Non-radioactive cytotoxicity assay following the manufacturer's protocol (Promega). Alternatively, cell viability was measured using the CellTiter-Glo® luminescent cell viability assay (Promega). Measurement for both assays were recorded on a GloMax® Discover microplate reader (Promega), and data was represented relative to uninfected controls.

2.2.4.2 Viral potency assay

As a measure for the oncolytic virus potency, cancer cells were infected with decreasing, serially diluted MOIs, and cell viability was measured using the CellTiter-Glo® Luminescent Cell Viability Assay (Promega). From the resulting dose–response curves, IC_{50} values were derived and interpreted as a readout for oncolytic potency. In brief, one day before infection, cancer cells were seeded in flat-bottom, white-walled 96-well plates at a density of 1×10^4 cells/well. Serial half-$\log_{10}$ dilutions of the virus sample were prepared in medium to a minimum of one virion per well (MOI 10^{-4}) in quadruplicates or left uninfected. 48 or 72 hpi, the medium was replaced with 50 µL of fresh culture medium and 50 µL of the lytic CellTiter-Glo® assay substrate, and luminescence was recorded using a microplate reader. The reduction of cell viability was expressed relative to uninfected control cells and plotted against the MOI. IC_{50} values were calculated using PRISM 8.0 (GraphPad).

2.2.4.3 Real-Time monitoring of viral-induced cell-cell fusion

To quantify the amount of cell-cell fusion elicited by the oncolytic virus, an assay based on a split luciferase was designed. CMV HaloTag-LgBiT and CMV HaloTag-HiBiT vectors were obtained from Promega based on a limited-user license agreement. The plasmid vectors were pre-amplified in DH5alpha *E. coli,* and 2 µg DNA was subsequently transfected into A549 and H1437 cells, respectively, using FuGene HD transfection reagent (3:1 ratio Fugene/DNA; Promega). After 2 days, transfected cell selection was started using 250 µg/mL (H1437) and

500 µg/mL (A549) hygromycin-B solution (Carl Roth) supplemented into the culture media. The respective hygromycin-B concentrations were previously determined based on kill curves performed in the same cell lines. After 2 to 4 weeks of selection, stably transfected cell lines were cryo-conserved, and every 3rd passage was performed in media containing hygromycin-B to maintain the stable gene expression.

For the fusion assay, LgBiT- expressing and HiBiT- expressing A549 or H1437 cells, respectively, were co-cultured in a 1:1 ratio in white 96-well plates at 1x 10^4 cells/well. The next day, cells were infected with oncolytic rVSV, rVSV-NDV, or rVSV-NDV/F_{3aa}, and a stable, cell-permeable luciferase substrate NanoGlo® Endurazine Live Cell Substrate (Promega) was added. Reduction of background signal was achieved by supplementing the media with DrkBiT peptide (Promega). Upon cell-cell fusion, LgBiT and HiBiT can interact to form an active NanoLuc® luciferase construct, and the luminescence signal generated can be quantified on a GloMax Discover system and is expressed as fold change cell fusion relative to untreated controls.

2.2.4.4 Real-Time monitoring of cell death

Cell death in Huh7 cells was monitored in real-time using an impedance-based xCELLigence Real-Time Cell Analysis (RTCA) system (Agilent). Huh7 cells were seeded onto special electrode-coated well plates (E-plate VIEW 16, Agilent), and 24 h later infected with increasing MOIs of either rVSV-NDV or rVSV-NDV/F_{3aa}. By continuously measuring the cellular impedance between the electrodes, a metric for the cellular viability can be derived. Virus-induced cell death was then expressed as loss in cellular impedance and expressed as % viability relative to untreated cells. Dose-response curves were plotted using PRISM 8.0 (GraphPad) and “time to 50 % oncolysis” (50 % viability) was extrapolated from the curves.

Alternatively, H1437 and A549 cell death was continuously measured using the RealTime-Glo™ Annexin V Apoptosis and Necrosis assay (Promega). Cells were seeded at 5x 10^3 cells/well in an opaque white 96-well plate and infected the next day or treated with control compounds as described in section 2.2.4.7. Immediately after cell treatment, the assay reagents were added as recommended by the manufacturer and kept present until the end of the experiment. In principle, PS exposure during early apoptosis was detected by Annexin V binding and, hence, complementation of a split luciferase, whereas late apoptotic/necrotic rupture of cell membranes enabled the entry of a DNA intercalating fluorescent dye. The resulting luminescence, and fluorescence at 485/525 nm (excitation/emission) wavelength were recorded “in real-time” by repetitive channeling of the plate between the incubator and the microplate reader.

2.2.4.5 Measurement of caspase activity

Caspase activity in infected cells was measured over time using Caspase-Glo® 3/7 Assay as well as Caspase-Glo® 8 Assay (Promega) following the manufacturer's instructions. Cells were seeded in white 96-well plates at 1x 10^4 cells/well, infected the next day, and the lytic assay substrate was added at the individual time points to read luminescence on a microplate reader as a measure of caspase activity.

2.2.4.6 Mitochondrial membrane permeabilization assay

MOMP was measured by staining mitochondria with a mitochondria-intercalating dye, tetramethylrhodamine ethyl ester (TMRE), and measuring the leakage of fluorescence signal from the mitochondria upon disintegration of the mitochondrial membrane. Cells were seeded at a density of 1x 10^4 cells/well in black 96-well plates. The next day, cells were infected at a series of MOIs, and 24 – 48 hpi, the mitochondria were stained with 500 nM TMRE for 30 min. Cells treated for 10 min with the decoupling agent FCCP (2 – 50 µM) were used as a positive control. Loss of fluorescence signal intensity was measured on a microplate reader at 530/580 nm (excitation/emission) wavelength and attributed to MOMP.

2.2.4.7 Pharmacological induction and manipulation of cell death

For the induction or inhibition of cell death pathways, the following pharmacological treatments were applied. Drug stock solutions were prepared in DMSO, ethyl acetate, or dH_2O and diluted to their final concentration using culture media. Unless otherwise indicated, the respective drug concentrations were taken from literature or pre-defined in titration assays measuring cell viability or death. Induction of apoptosis in human cancer cells was achieved by treatment with human TNF-α (500 ng/mL) and the Smac mimetic compound (LCL-161; 1 µM), named TS. Additional supplementation of TS with the pan-caspase inhibitor zVAD-fmk (shortened zVAD; 50 µM), named TSZ, was used to induce necroptosis, whereas zVAD alone was used to solely block the caspase branch of the apoptotic pathway. Necrostatin-1 (Nec-1, 10 µM) was used to specifically prevent the autophosphorylation of RIPK1, whereas necrosulfonamide (NSA, 1 µM) blocks MLKL tetramer polymerization downstream of RIPK3 activation and thereby prevents necroptosis [64, 65]. Mitoxantrone (MTX, 2 µM) or Doxorubicin (Doxo, 2 µM) were applied as positive controls for the induction of immunogenic cell death, whereas staurosporine (10 µM) served as broad spectrum positive control for an apoptotic death.

2.2.4.8 Generation of lentivirus for CRISPR/Cas9-mediated gene editing

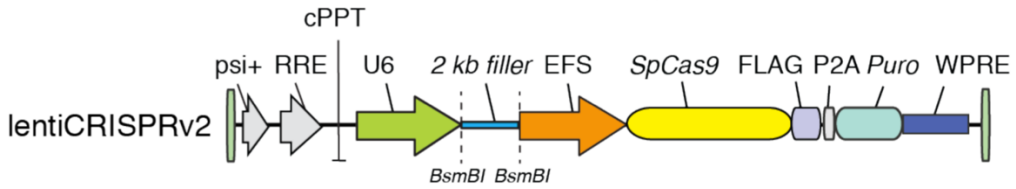

Figure 8. Schematic overview of the lentiviral CRISPR/Cas9 vector.

The plentiCRISPR v2 vector expresses the Cas9 under the control of the EF1a promoter and the sgRNA template will be expressed under the control of a U6 promoter. The vector features an ampicillin and puromycin resistance cassette. Upon linearization using the BsmBI restriction enzyme, sticky-end ligation will enable the replacement of the 2 kb filler sequence with the 20 nucleotide sequence that transcribes for the targeted sgRNA. Adapted from Addgene Lentiviral CRISPR toolbox [114] and originally described in [115, 116].

For gene knockout, the all-in-one CRISPR/Cas9 vector plentiCRISPR v2 (AddGene, # 52961) was used (**Figure 8**), originally described in [115, 116]. Target sequences were identified using the CHOPCHOP software tool [105], and oligonucleotides were obtained from Eurofins Genomics following the principle shown in **Figure 9**. For each human target gene (caspase 3, caspase 8, MLKL, RIPK1, and RIPK3), at least two distinct exons were targeted with a pool of three individual guide RNAs. Pooling the guides was performed to achieve maximized effects for gene deletion. Additionally, two non-target control sgRNAs (NTC) were generated. An overview of the targeted exons and sgRNAs is given in **Table 12**.

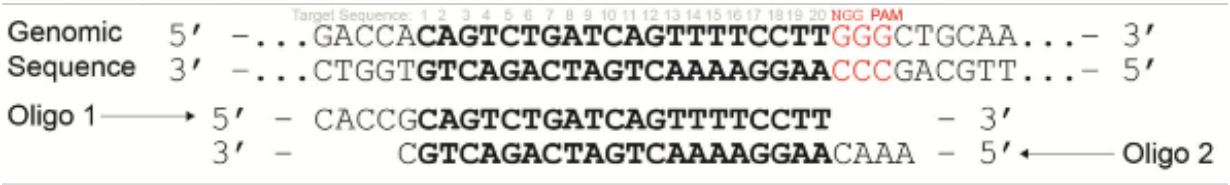

Figure 9. Example of CRISPR oligonucleotide design

The target sequence for the gene knockout is displayed in bold. Oligos are designed so that annealing will provide sticky ends that can ligate into the BsmBI-digested plentiCRISPR v2 vector. The protospacer adjacent motif (PAM) sequence, (NGG), is not included. Adapted from Addgene Lentiviral CRISPR toolbox and Shalem et al. [114] and originally described in [115, 116].

Initially, 10 µg of the plentiCRISPR v2 vector were digested using BsmBI-v2 (NEB) endonuclease at 55°C for 1 h, followed by gel purification of the linearized vector using QIAex II gel purification kit (Qiagen). 1 µL of complementary forward and reverse oligonucleotides were annealed in T4 ligation buffer at 95°C for 5 min, followed by a temperature ramp down to 20°C at 0.1°C /sec. Next, annealed oligos were diluted 1:1000 and pooled in a 1:1:1 ratio (three sgRNA per target). Target-specific lentiviral vectors were generated by sticky-end ligation using 50 ng of the linearized plentiCRISPR v2 vector and

1 µL of the prediluted oligo pool using T4 Ligase (NEB) for 1 h at room temperature, followed by transformation into One Shot™ Stbl3™ competent *E. coli* (Invitrogen). Transformed clones were picked, amplified, and plasmids were isolated by Mini-prep (QIAprep Spin Miniprep kit, Qiagen). Successful ligation of the sgRNA was validated by Sanger sequencing using a standard U6 forward primer (**Table 5**).

To produce lentivirus for gene editing, HEK-293T cells were transfected in a 12-well plate with 600 ng of the sgRNA containing plentiCRISPR v2 plasmid and 300 ng, and 150 ng, of the packaging plasmids psPAX2 (Addgene, #12260), and pMD2.G (Addgene, #12259), respectively, using 1 µg/µL polyethyleneimine (PEI, Thermo Fisher Scientific) in a 3:1 ratio of PEI/DNA in OptiMEM media (gibco). HEK-293T cells received fresh media 1 h prior to transfection and 6 h post transfection. Lentivirus was harvested from the supernatant of transfected cells on days 2 – 4 post transfection and pooled.

Table 12. Single guide RNA sequences and targeted exons for CRISPR/Cas9-mediated gene knockout

Gene target (human)	Ensembl #	sgRNA sequences 5' – 3'	target
Caspase 3	ENST00000308394	AGGAATGACATCTCGGTCTG	Exon 5
		ATGTCGATGCAGCAAACCTC	Exon 5
		GTCGCTTTGTGCCATGCTGA	Exon 8
Caspase 8	ENST00000673742	CCCTCAAGTTCCTGAGCCTG	Exon 2
		CGGGGATACTGTCTGATCAT	Exon 7
		CAAACGAGATATATCCCGGA	Exon 8
MLKL	ENST00000308807	TTGAAGCATATTATCACCCT	Exon 2
		GCATATTATCACCCTTGGCC	Exon 2
		TTAGCTTTGGAATCGTCCTC	Exon 9
RIPK1	ENST00000259808	GTGTTCCAGGATCGACCTTC	Exon 11
		TCTACTACATGGCGCCCGAG	Exon 5
		AGCACCTGAATGACGTCAAC	Exon 5
RIPK3	ENST00000216274	CCGCCCCCTTGGTGTCCATC	Exon 2
		CCTTGGTGTCCATCGAGGAA	Exon 2
		TCACTCGTGTACGAAGCAGT	Exon 6
NTC1 (from [115])	/	ACGGAGGCTAAGCGTCGCAA	/
NTC2 (from [115])	/	CGCTTCCGCGGCCCGTTCAA	/

2.2.4.9 Lentivirus-mediated target cell transduction for CRISPR/Cas9-mediated gene editing

Target cell lines, A549 and H1437, were transduced in 6-well plates using spin-infection and polybrene. When reaching 80 % confluency, cells were transduced with 500 µL of lentivirus supernatant using 10 µg/mL polybrene, and centrifuged for 90 min at 1000 x *g* at 37°C. The next day culture media was refreshed and 48 h after transduction, 5 µg/mL puromycin was added. Puromycin-resistant, stably transduced cells were further expanded and subsequently subjected to single cell clone isolation. Therefore, polyclonal cells were seeded at a low density onto 15 cm^2 dishes (approximately 1000 cells per dish) and incubated for 10-14 days (without puromycin) until outgrowth of single cell colonies was visible. Six clones per target gene were picked and transferred into 48-well plates and expanded until confirmation of the knockout status. Cells transduced with lentivirus encoding for NTC1 and NTC2 were prepared in a similar manner but used as a polyclonal cell population.

To validate gene knockouts, single cell clones were analyzed by Western Blot as described in section 2.2.4.10. Furthermore, DNA sequencing over the region of the respective targeted exons was performed to confirm successful gene deletions, as previously described [117]. In brief, DNA was isolated from cell pellets of the individual knockout clones using cellular DNA isolation buffer (**Table 8**) for 10 – 15 min at 57°C shaking, followed by heat-inactivation of proteinase K at 95°C 10 min. DNA was purified by standard isopropanol precipitation and PCR amplified using primers flanking the targeted exons (**Table 5** and **Table 13**). An aliquot of the PCR products was analyzed on a 2 % agarose gel and the remainder was purified using QIAquick PCR purification kit (Qiagen). Successful gene manipulation was confirmed by Sanger sequencing over the CRISPR-targeted exon.

Table 13. PCR program for validating the CRISPR knockout clones

Program	T [°C]	Hold time [min]	Cycles
Denaturing	95	15	1
Amplification	95	1	
	57 /61*	0,75	35x
	72	1	
Final elongation	72	10	1

*57°C for MLKL (exon 9); 61°C for RIPK3 (exon 2 and 6), MLKL (exon2)

B16-OVA cells with gene knockouts for caspase 3 and MLKL were obtained from and validated by Prof. Simon Heidegger (Department of Internal Medicine III, Klinikum rechts der Isar, TUM).

2.2.4.10 Western blot

Cell lines were seeded in 6-well plates, infected and harvested at the individual time points with trypsin/EDTA. Collected cell pellets were lysed for at least 15 min on ice with Radio Immunoprecipitation Assay (RIPA) protein lysis buffer (**Table 8**) supplemented with protease (cOmplete™ Protease inhibitor cocktail, Roche) and phosphatase inhibitors (PhosSTOP™ phosphatase inhibitor cocktail, Roche), called RIPA++. Complete cell lysis was accomplished by sonication (5 pulses, 15 sec, 25 % power, Sonopuls Ultrasound probe homogenizer (Bandelin)) prior to removal of cell debris at 16500 x *g*, 15 min, 4°C. Total protein content in cleared lysates was determined by DC™ Protein Assay (BioRad) against a 5 – 0.025 mg/mL standard curve of bovine serum albumin (BSA) in dH_2O. Absorbance at 720 nm was measured on a MultiSkan™ FC Photometer (Thermo Fisher Scientific). All samples were mixed with 6x protein loading dye (Laemmli, **Table 8**), denatured at 70°C for 10 min, and either stored at -20°C or directly analyzed.

20 µg of total protein was separated by sodium dodecyl sulfate – polyacrylamide gel electrophoresis (SDS-PAGE) on 7, 10, 12, or 16 % tricine gels. ROTI®-Mark TRICOLOR Protein marker (Carl Roth) served as molecular weight marker. Protein electrophoresis was performed at 80 V for 3 – 4 h. Tricine gel recipes, electrophoresis and transfer buffer compositions are given in **Table 8** and **Table 9**. Proteins were wet-transferred onto 0.2 µm nitrocellulose membranes (BioRad) for 45 – 90 min at 80 V, blocked in 5 % skim milk powder in TBS containing 0.1 % Tween-20 (TBS-T) for at least 1 h at RT and incubated with primary antibodies (**Table 2**) overnight at 4°C in 2.5 % BSA in TBS-T. The next day, membranes were washed at least 6x for 10 min using TBS-T. Secondary antibody linked to HRP (**Table 2**) incubation was done for at least 1 h at RT, followed by 6x washing the membranes with TBS-T for 10 min each. A self-made ECL substrate (**Table 8**) was used for Western Blot development, and the signal was detected with a Gel Doc XR+ Documentation system and ImageLab software (BioRad). Membranes were stripped using Restore™ Plus stripping buffer (Thermo Fisher Scientific), re-blocked with milk for at least 60 min and incubated with loading control antibodies against GAPDH (Glyceraldehyde 3-phosphate dehydrogenase) or β-Actin, or another primary antibody. Protein was quantified using densitometry within ImageLab software, accounting for background signal subtraction and expressing the protein intensity relative to the signal of the loading control. The obtained normalized volume intensities are compared relative to protein quantities in untreated samples and averaged over the biological replicates.

2.2.4.11 Measurement of extracellular ATP

Cells were seeded in 12-well plates at a density of 3x 10^5 cells/well and infected the next day at an MOI of 0.01 in serum-free media. MTX-treated cells were used as a positive control. Released ATP was quantified from fresh (non-frozen) culture supernatant samples at the individual time points with the ATP Bioluminescence Assay Kit HS II (Roche) and the luminescence signal was read on a microplate reader.

2.2.4.12 Quantification of extracellular ICD markers by Western blot

Released immunogenic cell death markers (Hsp70, Hsp90, extracellular Calreticulin and HMGB1) were detected and quantified from concentrated cell culture supernatants using Western blot. Cells were seeded and infected in phenol red-free and serum-free DMEM (gibco) supplemented with 2.5 mM glutamine in 6-well plates. Cells were infected at an MOI of 0.01, and at 24, 48, and 72 h after infection, the culture media was collected and precleared from cell debris by centrifugation at 1000 x *g,* 5 min, 4°C. Then, the supernatant was 30-fold concentrated at 4000 x *g*, for 30 – 45 min, 4°C using Amicon Ultra-2 centrifugal filters with a 10 kD cutoff (Merck). Concentrated supernatant was supplemented with protease- and phosphatase inhibitors, and protein content was measured using *DC*™ Protein assay (BioRad) as described above. Subsequently, 20 µg total protein was analyzed by SDS-PAGE and Western blotting. Whole-cell lysates collected at 24 h served as control. Western blot membranes were Ponceau-S stained (**Table 8**) and imaged to quantify the total protein. After de-staining the membrane, it was proceeded as described in section 2.2.4.10 using the antibodies indicated in **Table 2**. Protein was quantified relative to the total protein Ponceau-S staining using densitometry within ImageLab software.

2.2.4.13 Quantification of cell surface exposure of calreticulin

Cells were seeded in 12-well plates at a density of 3x 10^5 cells/well, infected the next day at different MOIs, and harvested after 24 h using Trypsin/EDTA. At least 1x 10^5 cells were transferred to a 96-well V-bottom FACS plate for cell surface staining of calreticulin, as previously described [118]. Briefly, cells were washed with PBS and first stained with Viobility 405/520 (1:300 in PBS; Miltenyi Biotec) on ice for 30 min, washed 1x with PBS, and thereafter stained with Rabbit-anti human Calreticulin antibody (Abcam; 1:250 in PBS) for at least 60 min. Primary staining was followed by a single wash with PBS and fixation of cells in 4 % PFA in dH_2O for 15 min on ice. After another three washing steps, cells were incubated with anti-Rabbit AlexaFluor-488 (Abcam, 1:250 in PBS) secondary antibody. Followed by washing 2x in PBS, cell surface exposure of Calreticulin was measured on a Cytoflex S flow cytometer, and data was analyzed using FlowJo software.

2.2.4.14 Generation of human DC from PBMCs

PBMCs were isolated from healthy human donors (female and male) and *in vitro* differentiated to dendritic cells using human IL-4 and human GM-CSF for 6 days. In brief, 50 mL whole blood was collected in heparinized tubes and 1:1 diluted with PBS, followed by isolation of white blood cells using a Ficoll gradient (Lymphoprep™, Stemcell Technologies) at 1000 x *g* for 30 min at RT (no brake). After two careful wash steps in PBS to remove platelets, cell debris were removed by passing through a 100 µm cell strainer. Next, using very-low endotoxin (VLE) RPMI media (gibco) containing 1.5 % human serum, 1.5x 10^7 PBMCs/well were left to adhere onto 6-well plates for 3 – 4 h at 37°C. The supernatant (containing T and B cells) was removed, and fresh VLE media with 580 U/mL human IL-4 (Peprotech) and 800 U/mL human GM-CSF (Biolegend) were added. On day 6 after isolation, dendritic cells were harvested by carefully scraping off the plate, and used for subsequent co-culture experiments.

2.2.4.15 Co-culture of human DC with oncolysate from OV-infected tumor cells and quantification of DC activation by flow cytometry

Oncolysates from oncolytic virus-infected tumor cells, A549 or H1437, were harvested at the time of maximum syncytia formation. In detail, cells were infected at an MOI of 0.01 in 12-well plates, and at 48 h (H1437) or 72 h (A549) post infection, cells were washed, scraped off the plate, and prior to freezing at -80°C, live virus in the oncolysate was UV-B inactivated for 5 min.

For the co-culture of oncolysate with dendritic cells, 100 µL of oncolysate was added to 1x 10^5 dendritic cells in a low-binding 96-well flat bottom plate. As additional controls, a fraction of the differentiated DCs was either left untreated or stimulated with an activation cocktail containing the following human cytokines: 2000 U/mL IL-1-β, 5000 U/mL IFN-γ, 1 µg/mL R848, 250 ng/mL PGE_2, 20 ng/mL TNF-α, 580 U/mL IL-4, and 800 U/mL GM-CSF. After 24 h of co-culture, or 48 h of cocktail stimulation, dendritic cells were transferred to a 96-well V-bottom FACS plate and stained as described in **Table 14** using 1:300 diluted Viobility™ 405/520 Fixable dye (Miltenyi Biotec) for live-dead discrimination. To specify the subtype of isolated and differentiated DCs, untreated cells were stained with an alternative panel, shown below. All antibodies were used at a 1:200 dilution in PBS. Cells were stained for 30 – 45 min at 4°C in the dark, followed by 3x washes with PBS. Next, dendritic cell activation was recorded on a Cytoflex S flow cytometer (Beckman Coulter), and data was analyzed using FlowJo software.

Table 14. Flow cytometry panel for PBMC-derived human dendritic cells

Antibody (anti-human)	Fluorophore	Laser	Emission bandpass filter (nm)	marker
Primary DC lineage/activation panel:				
CD1a	Pacific Blue	violet 405 nm	450/45	DC lineage
CD14	PerCP-Cy7	yellow 561 nm	780/60	DC lineage
CD141	APC-Vio 770	red 638 nm	712/25	DC lineage
CD86	PE	yellow 561 nm	585/42	DC activation
HLA-ABC (MHC-I)	PerCP-Cy5.5	blue 488 nm	690/50	DC activation
HLA-DR (MHC-II)	Brilliant Violet 605	violet 405 nm	610/20	DC activation
Viobility™	405/520 nm	violet 405 nm	525/40	Live-dead discrimination
Panel for DC subtype determination:				
CD11c	APC	red 638 nm	660/20	DC lineage
CD1c	Pacific Blue	violet 405 nm	450/45	DC lineage
CD123	FITC	blue 488 nm	525/40	DC lineage
CD141	APC-Vio 770	red 638 nm	712/25	DC lineage
CD14	PerCP-Cy7	yellow 561 nm	780/60	DC lineage
Viobility™	405/520 nm	violet 405 nm	525/40	Live-dead discrimination

2.2.6 *In vivo* studies

2.2.6.1 Ethics statement

All procedures involving animals were approved under ROB-55.2-2532.Vet_02-17-199 and performed in compliance with the guidelines of the Center for Preclinical Research (ZPF), Klinikum rechts der Isar, and the regional government (Regierung von Oberbayern, Munich, Germany). All animals were housed under pathogen-free, standard conditions and monitored daily for overall physical appearance and clinical symptoms. Animals were euthanized at humane endpoints using cervical dislocation under isoflurane anesthesia.

2.2.6.2 In vivo administration of oncolytic virus and dose finding

For intratracheal delivery, mice were anesthetized via intraperitoneal injection of Medetomidin-Midazolam-Fentanyl (MMF; 0.5/5.0/0.05 mg/kg body weight, prepared by the ZPF). At the stage of surgical anesthesia, mice were suspended by their front teeth on an inclined surface (120° angle, custom-made). Using a cold light source illuminating the chest and a tongue spatula (HWN-008-04, Hammacher Instruments), a blunted 20*G* needle equipped with a plastic catheter tube (Introcan 1.1 x 32 mm; 20*G*, B.Braun) was slowly inserted through the oral cavity into the mouse trachea just until the first bifurcation of the trachea. The blunted needle was removed and the catheter remained in the trachea, whereby correct positioning was controlled by measuring free breathing using an air-flow-meter (custom-made). For intratracheal drug delivery, 60 µL PBS, rVSV-NDV, or Ad-Cre virus diluted in PBS was slowly added into the inserted plastic catheter and taken up by inhalation. To achieve complete administration, remaining liquid in the catheter was carefully pushed into the lungs with an air-filled 1 mL syringe. The catheter was removed from the trachea and the mouse was relieved from the inclined surface and antagonized with Atipamezol-Flumazenil-Naloxon (2.5/0.5/1.2 mg/kg body weight, prepared by the ZPF) given subcutaneously. All mice were allowed a one-week resting period until the next intratracheal administration.

In order to define the maximum tolerated dose (MTD) of rVSV-NDV given intratracheally, healthy 9-14 week-old male and female *K-ras*$^{LSL\text{-}G12D/+}$*; p53*$^{fl/fl}$ (KP) mice (without Cre-recombination) were intratracheally administered with either 1x 10^6 or 1x 10^7 infectious virions ($TCID_{50}$) of rVSV-NDV in PBS. Since 1x 10^7 $TCID_{50}$/injection was previously determined as a safe dose by intravenous administration in mice, the dose study was performed by starting at this dose and lowering the dose upon observation of toxic effects. Blood was collected on day 1 and day 3 after virus injection (Microvette-200, Sarstedt) and centrifuged at 2000 x *g* 4°C for 5 min to obtain plasma, which was stored at -80°C until analysis of infectious virus titer by $TCID_{50}$ assay. Mice were monitored daily for virus-specific toxic effects and euthanized at

humane endpoints. In another experiment, formulations of rVSV-NDV with pulmonary surfactant Curosurf® (9 mg/mL) (Chiesi) were applied in a similar manner using decreasing doses of rVSV-NDV. To rule out negative effects of surfactants on rVSV-NDV replication and virus-mediated cytotoxicity, surfactant-virus preparations were tested *in vitro* in A549 cells. rVSV-NDV was pre-incubated with either 9 mg/mL Curosurf®, or 9 mg/mL Alveofact® (Lyomark) surfactant in PBS for 30 min on ice, followed by 30 min at room temperature, and then added to A549 cells for infection. Virus replication and cytotoxicity were measured as described in 2.2.4.1.

For intravenous delivery, mice were placed into a tail-first restrainer without anesthesia and slowly injected into the lateral tail vein with 150 µL PBS or rVSV-NDV in PBS. The MTD for intravenous injection of rVSV-NDV was already determined in previous studies to be at least 1x 10^7 $TCID_{50}$/injection.

2.2.6.3 Inducible model of murine lung adenocarcinoma

For the spontaneous generation of lung adenocarcinoma in mice, 9-14 week-old male and female KP mice were used (a kind gift from Prof. Philipp Jost). KP mice were genotyped with a standard primer set for the *KRAS* proto-oncogene and *p53* floxed allele (**Table 5**) using HotstarTaq DNA Polymerase (Qiagen). In brief, mouse ear punch biopsies were lysed overnight at 56°C using mouse DNA isolation buffer (**Table 8**). Proteinase K was inactivated the next day at 95°C for 10 min, and the crude DNA isolate was directly used for the genotyping PCR (**Table 15**).

Table 15. PCR program for KP mouse genotyping

Program	T [°C]	Hold time [min]	Cycles
Denaturing	95	15	1
Amplification	95	0,5	
	55 or 60*	0,75	35x
	72	1	
Final elongation	72	5	1

* (55°C for p53 PCR, 60°C for K-ras PCR)

KP mice were intratracheally instilled with 1x 10^5 or 5x 10^6 plaque-forming units (PFU) Adenovirus-5 expressing Cre recombinase (kindly provided by Dr. Martina Anton). For each animal, the Ad-Cre virus formulation in MEM media (1.8 mM Ca^{2+}; gibco) was complexed with an additional 10.2 mM $CaCl_2$ 20 min prior to injection.

The intratracheal instillation was performed as described in section 2.2.6.2, and mice were regularly scanned by µCT imaging of the lungs (see below) starting 8-12 weeks after Ad-Cre

injection and continued until the end of the experiment. Tumor-bearing animals were randomly distributed into treatment groups and received up to 6 weekly treatments of either PBS, or rVSV-NDV in PBS, by either of the treatment routes (intratracheally or intravenously). The survival study was terminated at predefined humane endpoints, and tumor pathology was analyzed upon necropsy.

2.2.6.4 Implantable model of murine lung cancer

For implantation of murine tumor cells, all cell lines were routinely checked for mycoplasma contamination inhouse, were passaged at least three times after thawing to assure regular cell growth, and were certified for transfer into the ZPF by the hygiene officer.

Ten week-old female C57BL/6-J mice (Janvier Labs) were implanted with either B16-OVA or LLC cells via the lateral tail vein. To determine the optimal cell count for implantation, 1x 10^5 and 2x 10^5 cells in 150 µL PBS per mouse were tested. Mice were monitored daily for peripheral tumor growth and off-target effects, and scanned weekly by lung µCT imaging (see below). At humane endpoints whole-body necropsy was performed to assess tumor distribution.

For the survival study, 2x 10^5 LLC cells were implanted intravenously and after 10-14 days, when tumors were detected by µCT imaging, mice were randomized into treatment groups and subjected to therapy. Tumor-bearing animals received multiple intratracheal administrations or intravenous injections of rVSV-NDV diluted in PBS or PBS control as specified in the Results section. The survival study was terminated at predefined humane endpoints and tumor pathology was analyzed upon necropsy.

2.2.6.5 Lung µCT scans

Animals were anesthetized using Isoflurane (5 %), and the lungs were imaged by small-animal computer tomography (CT) on a nanoScan SPECT/CT (Mediso Medical Imaging Systems). Isoflurane was maintained at a low level (2 %) after an initial induction at 5 %, and animal breathing was controlled at 35 – 80 breaths per minute throughout the acquisition process. CT scans were acquired using Nucline 2.03 Nanoscan Software and the following parameters: X-ray power of 35 kVp (peak kilo voltage), 670 µA; 720 projections; 450 ms exposure time, 1:4 binning. Tumors in the lung were detectable as white, spherical contrasting areas and had to be clearly visible in all three focal views (sagittal, coronal, axial). µCT image analysis was done using ITK-Snap software [106], as further specified in 3.3.2.1.

2.2.7 Statistical methods

All data was plotted and analyzed in PRISM version 8.0 (GraphPad). All *in vitro* experiments were performed in biological triplicates (n = 3, unless otherwise indicated), and mean values ± standard deviation (SD) were used for further analysis. For the comparison of two groups, a two-tailed Student's t-test was applied. One-way ANOVA with Tukey's or Dunnett's multiple comparisons test was performed for the analysis of more than two groups. Kaplan-Meier survival curves were analyzed by log rank test, and median survival times calculated using PRISM. P values smaller than 0.05 were considered to be statistically significant (*p ≤ 0.05, **p ≤ 0.01, ***p ≤ 0.001, ****p ≤ 0.0001, ns = non-significant).

3 RESULTS

3.1 Syncytia formation and oncolysis is coordinated by apoptosis and necroptosis regulators

3.1.1 Cloning, rescue and initial characterization of the new fusogenic OV variant, rVSV-NDV/F_{3aa}

The oncolytic virus hybrid rVSV-NDV has been previously described as a potent therapeutic vector that spreads in tumor cells via cell-cell fusion and induces an immunogenic destruction of cancer cells *in vitro* and *in vivo* [40-42]. The unique feature of forming syncytia with neighboring tumor cells can be attributed to the NDV surface proteins HN and F. However, the exact mechanism of syncytial cell death and whether modifications in cell fusion can be harnessed to boost immunogenicity are yet undiscovered.

A new variant of rVSV-NDV with an altered fusion capacity was generated by replacing its *hyperfusogenic* fusion protein rNDV/F_{3aa}(L289A) with rNDV/F_{3aa}. It was hypothesized that the new OV vector (named rVSV-NDV/F_{3aa}) would induce a slower cell-to-cell spread, which may lead to altered viral replication kinetics and syncytial immunogenicity. The genome sequences of the new vectors rVSV-NDV/F_{3aa}, and rVSV-NDV/F_{3aa}-GFP are shown in **Figure 10**.

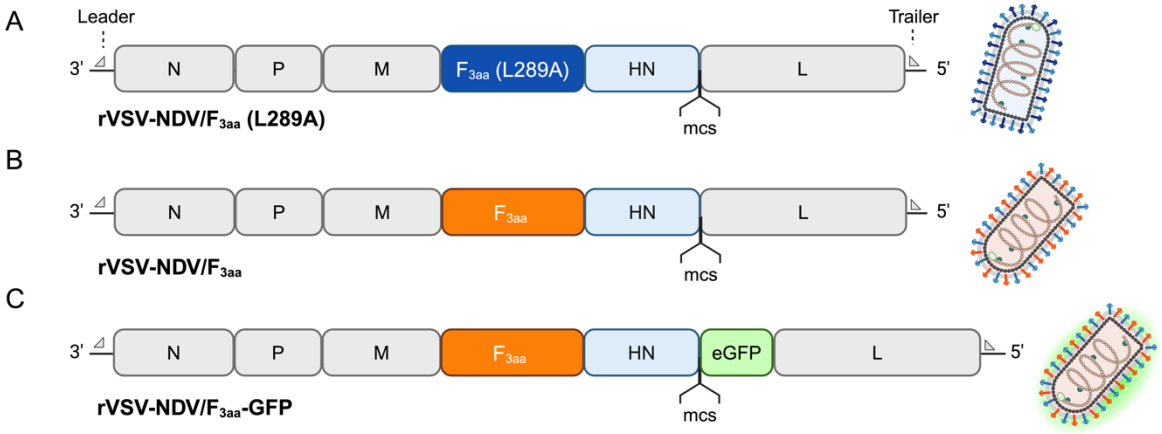

Figure 10. Viral genome sequence of the novel hybrid viruses rVSV-NDV/F_{3aa} and rVSV-NDV/F_{3aa}-GFP

(**A)** Viral genome sequence of rVSV-NDV/F_{3aa}(L289A) (referred to as rVSV-NDV). (**B**) Viral genome sequence of the fusogenic variant of rVSV-NDV, named rVSV-NDV/F_{3aa}, which was engineered in this study by reversing the fusion protein in rVSV-NDV/F_{3aa}(L289A) to rNDV/F_{3aa} in rVSV-NDV/F_{3aa}. The new vector thus contains the modified proteolytic cleavage site (F_{3aa}) but lacks the *hyperfusogenic* (L289A) modification in the fusion protein (**C**) An eGFP reporter gene was introduced into the mcs upstream of the L gene to obtain rVSV-NDV/F_{3aa}-GFP. Figure created in BioRender.com.

To generate rVSV-NDV/F_{3aa} and rVSV-NDV/F_{3aa}-GFP, an established cloning and viral rescue system was applied. A detailed overview of the cloning approach is shown in **Figure 11** A, exemplified for the pVSV-NDV/F_{3aa}-GFP vector. After digestion with SmaI and NotI, the F protein insert (obtained from pNDV-B1/F_{3aa}-GFP) and the linearized rVSV-NDV-GFP vector were gel purified (**Figure 11** B) and then ligated to generate bacterial clones expressing the pVSV-NDV/F_{3aa}-GFP vector. pVSV-NDV/F_{3aa} was cloned with the same approach (data not shown), sequence-validated, and used as a positive control for the diagnostic digestion of pVSV-NDV/F_{3aa}-GFP (**Figure 11** C). A colony PCR amplifying the transgene insert further confirmed the presence of the GFP reporter gene inside the new vector pVSV-NDV/F_{3aa}-GFP (**Figure 11** D). The amino acid substitution (A → L) at nucleotide position 865 – 867 of the F gene was then validated by Sanger sequencing (not shown), and plasmid DNA from selected clones was used for the viral rescue.

The reverse genetics virus rescue system (depicted in **Figure 7**) relies on infecting BHK-21 cells with an MVA variant (Vtf7.3), enabling transient T7 RNA polymerase expression. Subsequent co-transfection with the rescue plasmid containing the full-length virus genome (pVSV-NDV/F_{3aa}-GFP, for example) and structural helper plasmids allow the formation of nascent rVSV-NDV/F_{3aa}-GFP virus particles. After additional viral replication cycles, the structural helper proteins are replaced by surface proteins of rVSV-NDV/F_{3aa}-GFP and first observation of typical syncytial morphology and GFP transgene expression indicates successful rescue (**Figure 12** A). Vaccinia-free rVSV-NDV/F_{3aa} was obtained after one round of plaque purification, whereas rVSV-NDV/F_{3aa}-GFP required two filtration steps and an additional round of plaque purification (called "*sub-plaques*") to eventually eliminate contaminant VV, which was validated for the individual plaques and sub-plaques by RT-PCR (**Figure 12** B). GFP reporter gene expression and NH gene identity in the rescued viral plaques were confirmed by RT-PCR (**Figure 12** C and D). Similar to the validation of bacterial clones, successful F protein exchange in rVSV-NDV/F_{3aa} and rVSV-NDV/F_{3aa}-GFP were verified by RT-PCR and Sanger sequencing over the F gene (not shown).

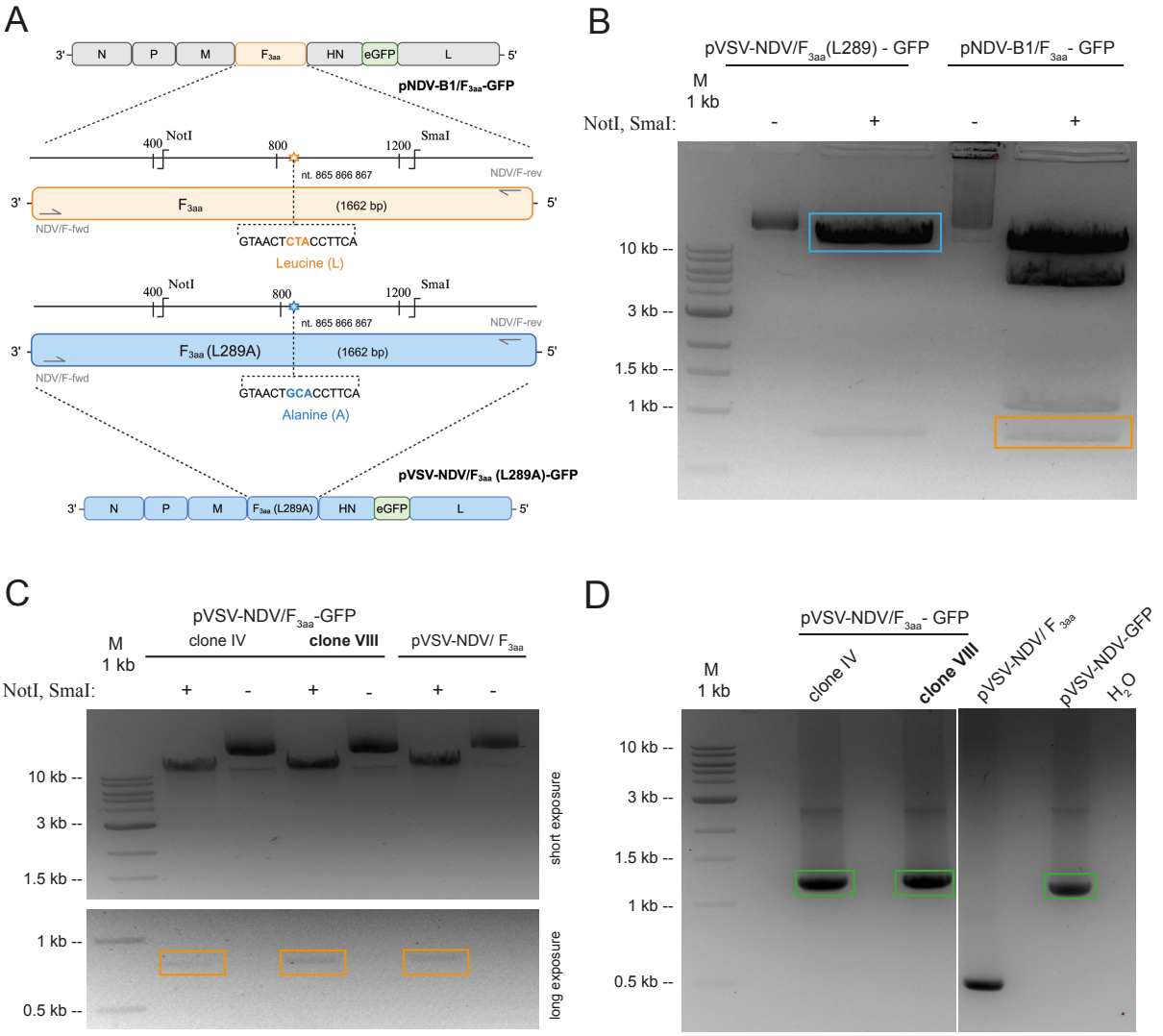

Figure 11. Cloning approach for the generation of pVSV-NDV/F_{3aa} and pVSV-NDV/F_{3aa}-GFP

The F protein modification strategy is exemplified for pVSV-NDV/F_{3aa}-GFP. (**A**) pNDV/F_{3aa}-GFP as donor plasmid and the F protein segment (in orange) are shown. CTA encodes for a Leucine at nucleotides 865-866-867 in the F protein. Below, the backbone plasmid of pVSV-NDV/F_{3aa}(L289A)-GFP (in blue) is visualized, and GCA encodes for an Alanine at nucleotides 865-866-867, previously characterized as *hyperfusogenic* F protein [40]. Restriction sites of NotI and SmaI, and binding sites of NDV/F-fwd and NDV/F-rev primers are indicated (**B**) Restriction enzyme digest with NotI and SmaI excised the individual F gene segments (810 bp) and enabled gel purification of the linearized pVSV-NDV/F_{3aa}(L289A)-GFP vector (devoid of the F_{3aa}(L289A) gene, blue rectangle) and the F_{3aa} insert (orange rectangle). (**C**) Subsequent ligation replaced the F_{3aa}(L289A) gene with the F_{3aa} gene, generating the new vectors pVSV-NDV/F_{3aa} or pVSV-NDV/F_{3aa}-GFP, respectively. A diagnostic digestion with NotI and SmaI confirmed the correct insertion of the 810 bp F gene segment (orange rectangles), exemplified for two bacterial clones, IV and VIII. (**D**) In the case of pVSV-NDV/F_{3aa}-GFP, an additional PCR over the multiple cloning site was performed to confirm the presence of the eGFP reporter gene (1200 bp). The clone that was chosen for subsequent viral rescue is marked in bold. M indicates the DNA size marker: 1 kb ladder (NEB); kb = kilobases, bp = base pairs.

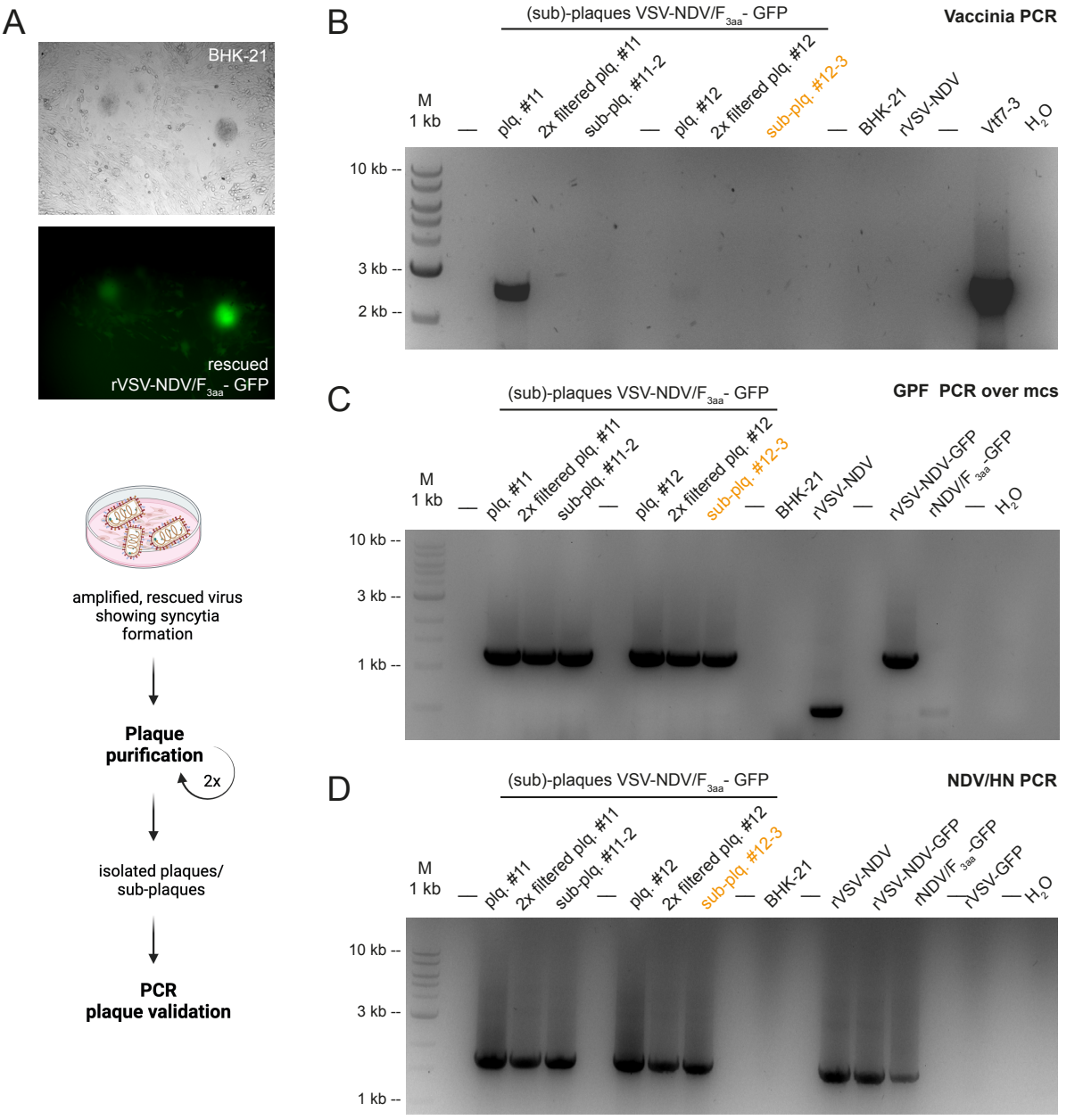

Figure 12. Plaque purification and PCR validation of the new rVSV-NDV/F_{3aa} or rVSV-NDV/F_{3aa}-GFP vector

(**A**) Successful rescue of nascent rVSV-NDV/F_{3aa} virus was confirmed by monitoring syncytia formation and, in the case of rVSV-NDV/F_{3aa}-GFP, GFP fluorescence, in infected BHK-21 cells. To eliminate contaminant vaccina virus, amplified rVSV-NDV/F_{3aa} or rVSV-NDV/F_{3aa}-GFP virus supernatants were filtered onto fresh BHK-21 cells for plaque purification and subsequent PCR plaque validation as shown in the workflow. (**B**) If necessary (exemplified for rVSV-NDV/F_{3aa}-GFP plaques), filtration and plaque purification had to be repeated until absence of VV Vtf7-3 was proven by RT-PCR. (**C**) RNA isolated from BHK-21 cells infected with the isolated plaque or sub-plaque was analyzed by RT-PCR over the HN gene and (**D**) the mcs to confirm the presence of the reporter gene. The sub-plaque chosen for rVSV-NDV/F_{3aa}-GFP Master bank production is highlighted in orange. M indicates the DNA size marker: 1 kb ladder (NEB); kb = kilobases, plq = plaque.

As rVSV-NDV/F_{3aa}(L289A) (subsequently referred to as rVSV-NDV) has shown rapid replication and a typical *hyperfusogenic* oncolysis in Huh7 hepatocellular carcinoma cells [40], it was questioned whether the new fusogenic variant rVSV-NDV/F_{3aa} is indeed modified in its fusion, replication, and killing kinetics.

Both viruses, rVSV-NDV and rVSV-NDV/F_{3aa}, induced sufficient cytotoxicity in Huh7 cells, measured by LDH release upon virus-mediated cell lysis. However, oncolysis was significantly delayed in the rVSV-NDV/F_{3aa} variant at 48 hpi (**Figure 13** A). This effect was corroborated by comparing syncytia formation and cytopathic effects (CPEs) under the microscope. rVSV-NDV/F_{3aa} displayed a dampened killing kinetic: Observation of first syncytia, syncytia growth, and final collapsing of the monolayer was much more delayed in rVSV-NDV/F_{3aa} compared to the *hyperfusogenic* variant (**Figure 13** B). In line with this, measurement of viral titers from the supernatant confirmed an MOI-dependent impairment in rVSV-NDV/F_{3aa} replication even though similar maximum titers were achieved (**Figure 13** C).

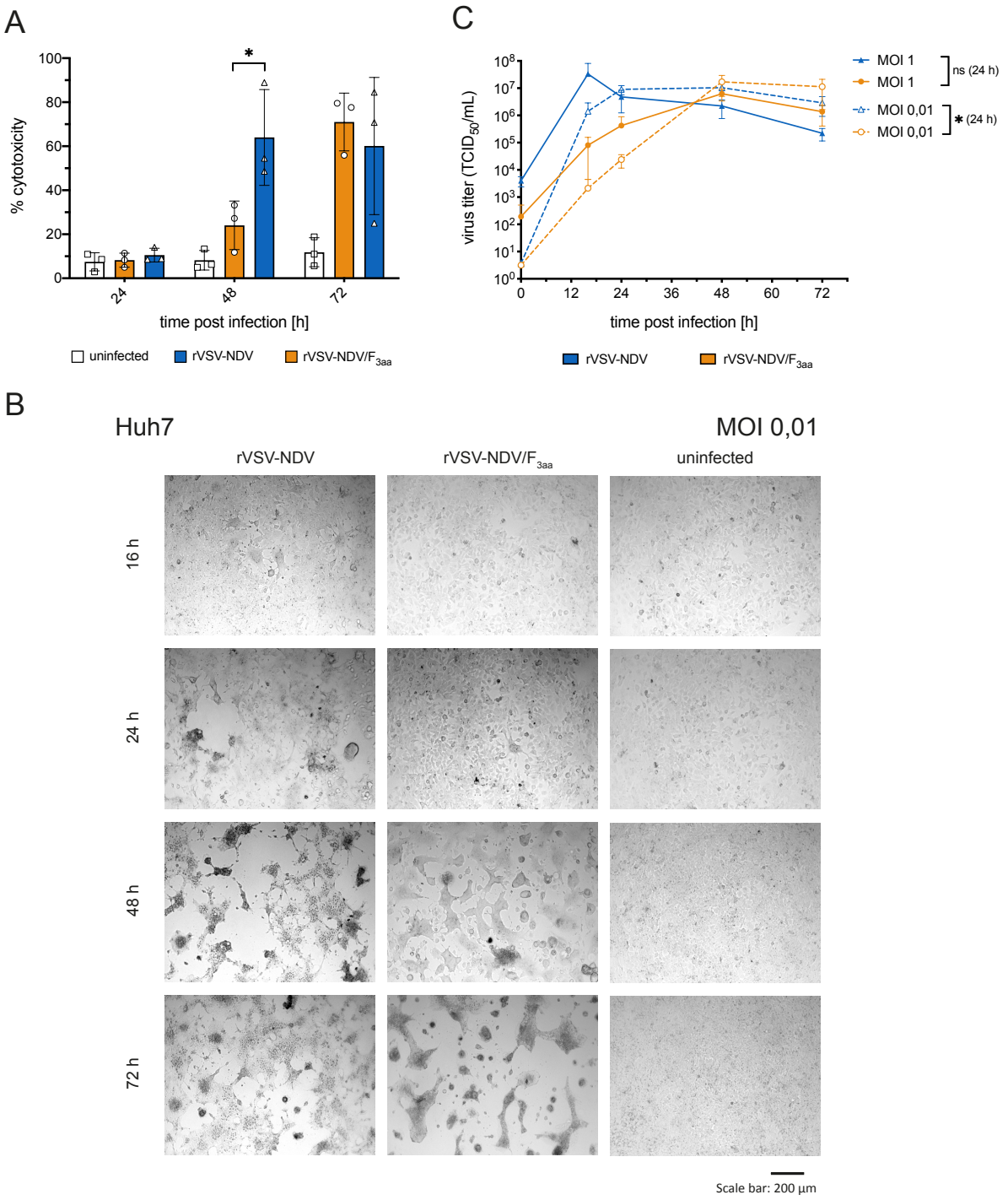

Figure 13. Characterization of rVSV-NDV/F_{3aa} in susceptible Huh7 cells

The new virus variant rVSV-NDV/F_{3aa} was characterized in Huh7 cells and compared to the existing rVSV-NDV variant. (**A**) The virus-mediated oncolysis was characterized by LDH release assay and is visualized for an MOI of 0.01. (**B**) Microscopy time course of the virus-induced cytopathic effect in Huh7 cells. Shown are brightfield images of one representative biological replicate at MOI 0.01. (**C**) Virus replication was monitored over time using two different MOIs (0.01 and 1). Graphs represent mean values ± SD of n = 3 independent experiments. One-way ANOVA with Tukey's multiple comparisons test was used to define statistical significance (ns = non-significant, *p ≤ 0.05).

To gain more detailed insight into the underlying syncytia formation and death differences between rVSV-NDV and rVSV-NDV/F_{3aa}, real-time monitoring of cell morphology was applied using an Xcelligence RTCA system. The Xcelligence machine uses special, electrode-coated well plates that measure the impedance between the electrodes. Impedance will increase with cell growth until confluency is reached, and with damage of the monolayer by, for example, oncolytic virus-mediated cell killing, impedance values will gradually decline in real-time. Here, Huh7 cells were infected at two MOIs with the respective virus, and impedance was measured until complete death was observed (**Figure 14**). Values were normalized to uninfected wells. Similar to the cytotoxicity data from the LDH release assay, impedance measurements indicated that rVSV-NDV induced faster cell killing in a dose-dependent fashion. From the median time to achieve 50 % cell killing (IC_{50} value), extrapolated from the impedance curves, it appears that the *hyperfusogenic* variant rVSV-NDV achieved a quicker initiation and progression of syncytial death in Huh7 cells than the rVSV-NDV/F_{3aa} variant. Consequently, rVSV-NDV/F_{3aa} was referred to as a "*non-hyperfusogenic*" version of rVSV-NDV, showing not only a delayed replication, but also a decelerated syncytia formation and destruction profile. Thus, with rVSV-NDV/F_{3aa}, a useful research tool was generated to further interrogate the underlying mechanisms of syncytial oncolysis.

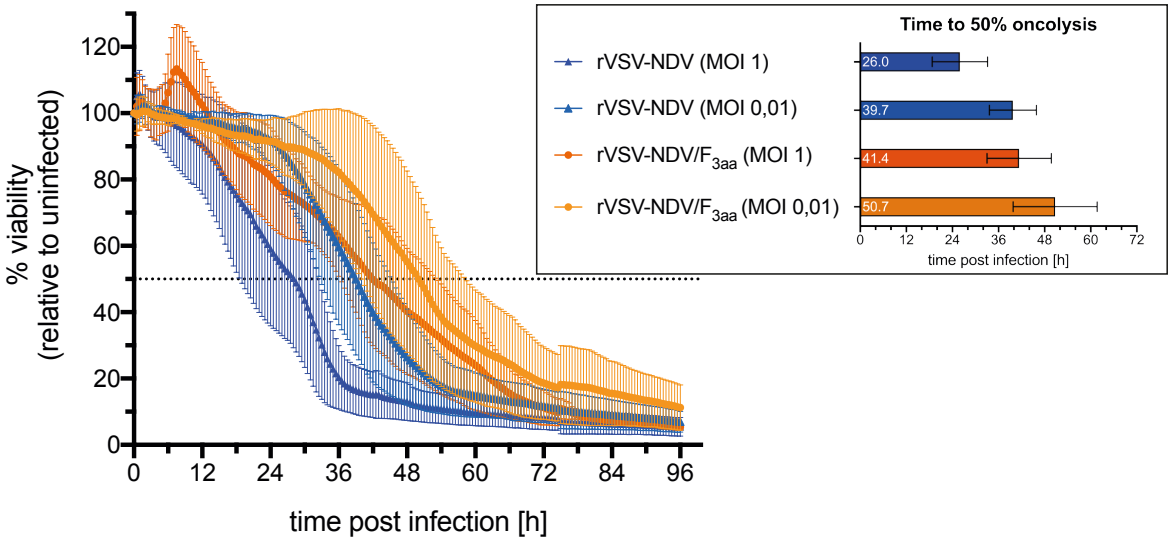

Figure 14. Real-time monitoring of virus-mediated cytopathic effects in Huh7 cells

Huh7 cells were infected at two MOIs (0.01 and 1) with either rVSV-NDV or rVSV-NDV/F_{3aa} and the cytopathic effect was measured in real-time by an Xcelligence RTCA system. Impedance values were normalized to the uninfected control and the time of infection and expressed as % viability (100 % at time 0 hpi). Shown are mean values ± SD of n = 4 independent experiments. Inset: The median time to achieve 50 % cell killing was calculated using non-linear regression in GraphPad PRISM, similar to calculating an IC_{50} value in a viral potency assay (section 2.2.4.2).

3.1.2 Characterization of fusogenicity in human lung cancer cells

In light of the overall project focus on establishing an OV therapy for lung cancer, the effects of the fusogenic OV variants were next investigated in human lung cancer cell lines. As the susceptibility of lung cancer cells to oncolytic rVSV-NDV had not been characterized previously, virus growth kinetics and oncolysis were determined in two selected human NSCLC cell lines: A549 and H1437 (**Figure 15**). To specify if the death pathway stimulation is particularly attributable to the fusion competent HN and F proteins, the parental rVSV wildtype virus was included here and in subsequent experiments as non-syncytia forming OV control.

Both NSCLC cell lines were susceptible to all three viruses tested, although some differences in titer progression were found. The typically rapid rVSV replication kinetic to high titers was more apparent in A549 cells than in H1437 cells. In the latter cell line, rVSV seemed to be slightly attenuated in its ability to quickly replicate, and the peak titer reached was more than 1-log lower than that achieved in A549 cells (**Figure 15** A and B). This was also reflected in cytotoxicity. While rVSV killed the entire A549 cell monolayer by 48 hpi, only around 70 % of the H1437 cells were eliminated by rVSV at the same time point. When comparing rVSV-NDV and rVSV-NDV/F_{3aa} replication and oncolysis, it became clear, that the above-mentioned fusogenicity effects seem to be a cell line-dependent observation. Even though virus replication in A549 cells still indicated a *non-hyperfusogenic* profile for rVSV-NDV/F_{3aa}, the effects on virus-induced cell lysis were surprising. Opposite to the observations in Huh7 cells, rVSV-NDV/F_{3aa} virus-induced cytotoxicity was stronger than the cytopathic effects from rVSV-NDV at 48 hpi. In contrast, in H1437 cells, no distinct differences between a *hyperfusogenic* rVSV-NDV and a *non-hyperfusogenic* rVSV-NDV/F_{3aa} replication or oncolysis characteristic could be observed. H1347 cells were more susceptible to killing by the fusogenic variants than by rVSV, but when rVSV-NDV and rVSV-NDV/F_{3aa} were compared, virus amplification, as well as cell lysis profiles, were similar (**Figure 15** C and D).

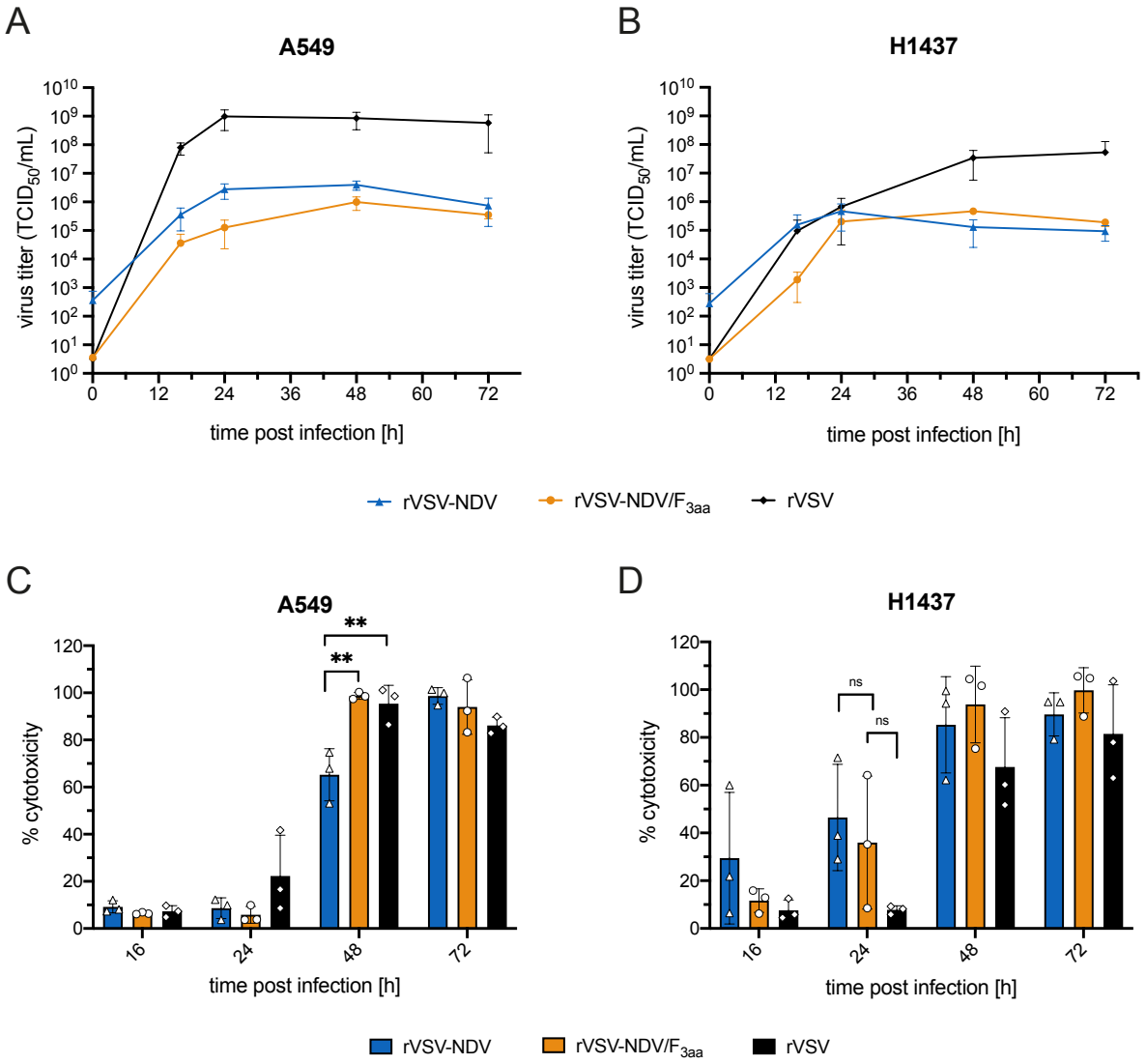

Figure 15. A549 and H1437 cell susceptibility to oncolytic virus replication and oncolysis

A549 and H1437 cells were infected with the three VSV-based oncolytic virus variants (rVSV-NDV, rVSV-NDV/F_{3aa}, or rVSV) at an MOI of 0.01. (**A** and **B**) Virus replication was monitored over time by $TCID_{50}$ assay from infectious supernatant. (**C** and **D**) Virus-mediated cell killing was measured by LDH assay. Shown are mean values ± SD of n = 3 independent experiments. Statistical significance was determined by One-way ANOVA with Tukey's multiple comparisons test (ns = non-significant, **p ≤ 0.01).

Fluorescence microscopy was applied to record the differences in cellular and syncytial morphology during infection (**Figure 16**). As expected, single cell rounding and no syncytia were observed for rVSV-infected A549 and H1437 cells, respectively. In A549, the entire monolayer seemed to be infected by rVSV and started rounding up by 16 hpi, whereas rVSV infection in H1437 cells spread more locally and much slower from discrete foci. These observations are consistent with the replication and cytotoxicity differences seen for rVSV-infected A549 and H1437 cells, and highlight the varying susceptibility of these two cell lines to rVSV.

Comparing rVSV-NDV and rVSV-NDV/F_{3aa}, cell line-specific CPEs and syncytial morphologies were observed. A549 cells, having a coherent monolayer of cells, formed wide-spanning syncytia with long protrusions upon infection with rVSV-NDV or rVSV-NDV/F_{3aa} and shapes that resembled a "*blur of color*" shape. Cell-cell fusions grew and eventually collapsed by shedding off the monolayer, but usually, a subset of uninfected and non-fused surrounding cells remained at 72 hpi. A complete destruction of the monolayer, like in Huh7 and H1437 cells, was thus visually not achieved in A549 cells, even though the LDH assay data might imply complete cytotoxicity. H1437 cells, growing in patches, also showed patch-like infection and syncytia spreading triggered by rVSV-NDV or rVSV-NDV/F_{3aa}. Within the first 24 hpi, cells started forming "*bubble-like"* syncytia of various sizes, although the expansion of syncytia was limited by the cell patches' boundaries and a seemingly quicker burst of syncytia compared to A549 cells. In general, close before losing membrane integrity and death, A549 and H1437 syncytia displayed signs of membrane blebbing and enlarged vacuole-like organelles. Slight but discernible morphologic differences in syncytia shape between rVSV-NDV/F_{3aa} and rVSV-NDV-infected H1437 cells were visible. A more classical, rounding CPE caused by rVSV-NDV contrasted to slightly more distinctive syncytia formed by rVSV-NDV/F_{3aa}. In A549 cells, syncytial morphology was mostly similar between those two variants. Overall, the infections in A549 and H1437 cells with the three OV variants not only demonstrated that lung cancer cells are susceptible to OV-mediated killing but also delineated unique differences in oncolysis kinetic and morphology.

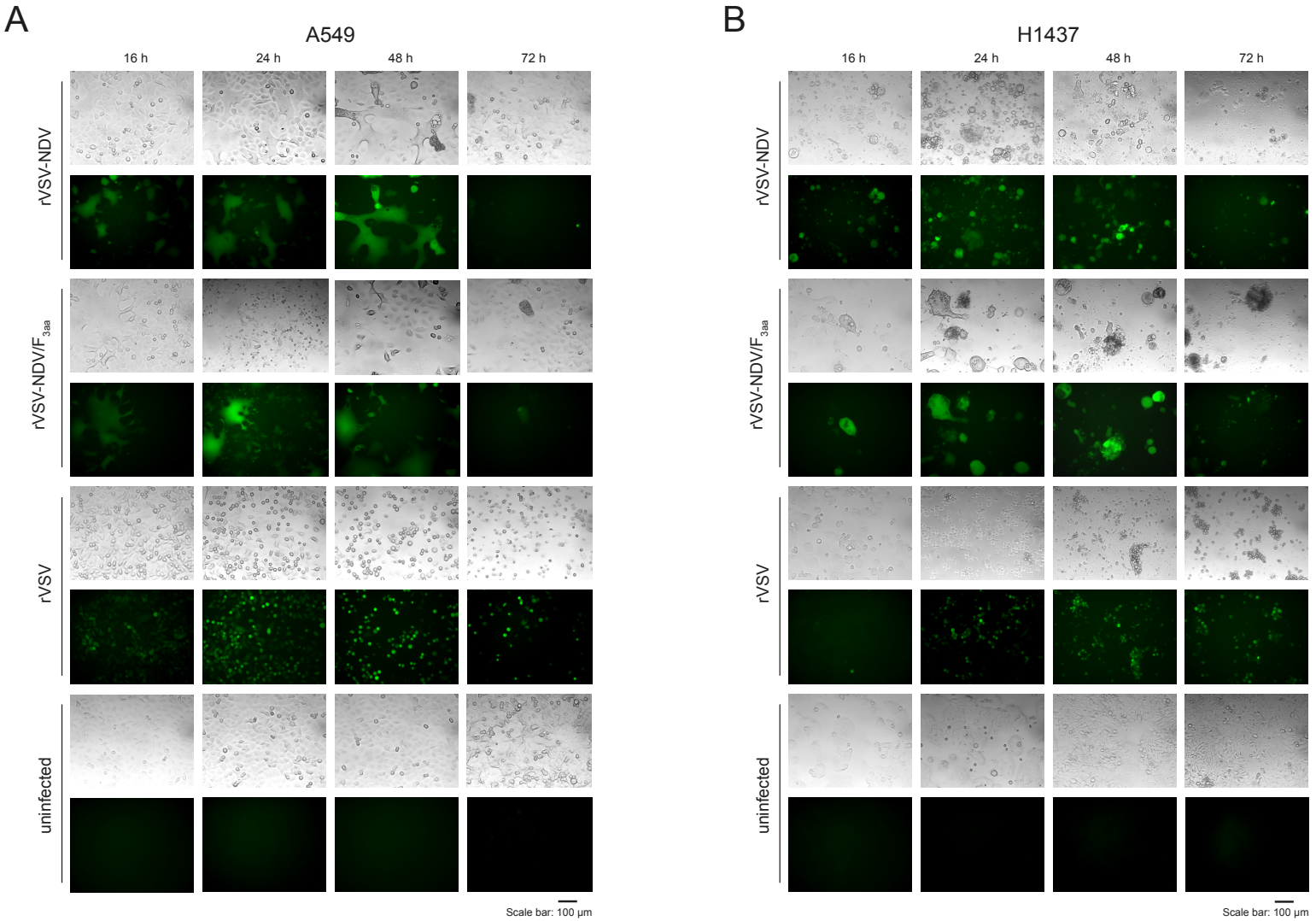

Figure 16. Fluorescence microscopy time course of oncolytic virus-mediated syncytia formation and cell killing

(**A**) A549 and (**B**) H1437 cells infected at an MOI of 0.01 were imaged at 16, 24, 48, and 72 hpi to record virus-induced cytopathic effects. GFP-expressing variants of the oncolytic viruses were used to simplify the delineation of the individual syncytia morphology. Shown are representative brightfield and fluorescent images of n = 3 biological replicates.

To further decipher the syncytia and oncolysis process of the viral variants, an assay that sensitively quantifies cell-to-cell fusion *in vitro* was developed based on commercially available plasmid constructs. Assays that involve fusion-dependent reporter gene expression, fluorescent dequenching on virus and host cell lipid membranes, or complementation of split reporter proteins have been described earlier to quantify fusion [119-121]. The oncolytic virus fusion assay described here utilized the NanoBiT® (NanoLuc® Binary Technology from Promega) system, which relies on the 19 kDa (kilodalton) catalytic subunit of the deep-sea luminous shrimp luciferase [122]. NanoLuc® luciferase was engineered and split into a 159 amino acid large fragment (called LgBiT) and a small, high-affinity subunit of 11 amino acids (called HiBiT), which can both be expressed from versatile plasmid vectors and transfected into eukaryotic cells. After high-affinity complementation with LgBiT (K_D = 700 pM) and addition of an optimized substrate, NanoLuc® produces very bright luminescence [123].

In this assay, LgBiT and HiBiT were stably expressed in separate cell populations (A549-LgBiT, A549-HiBiT, H1437-LgBiT and H1437-HiBiT) and co-cultured. Oncolytic virus-mediated cell-to-cell fusion would trigger cytoplasmic mixing, complementation of LgBiT and HiBiT and generate a luminescence signal proportional to the number of fused cells (**Figure 17**). A549 and H1437 cells were transfected with the corresponding LgBiT or HiBiT vector and maintained under hygromycin-B selection as described in 2.2.4.3. In scouting experiments, HiBiT and LgBiT subunits were co-transfected in the absence of viral infection to identify a suitable luciferase pro-substrate and evaluate the specificity of the real-time assay. This pre-experiment identified Endurazine™ as the preferable pro-substrate and confirmed that adding a cell-impermeable DrkBiT peptide to the media helped reduce unspecific background luminescence (data not shown). DrkBiT peptide was engineered as a competitive inhibitor to HiBiT with a much stronger affinity to LgBiT but complements to a non-functional luciferase [124]. During unspecific cell lysis, LgBiT and HiBiT subunits leak into the extracellular space and would result in luminescence that did not derive from fused cells. Adding DrkBiT, thus, guarantees that any detected luminescence signal can only result from intracellular NanoBiT® complexes and translates to cells that have undergone cell-to-cell fusion.

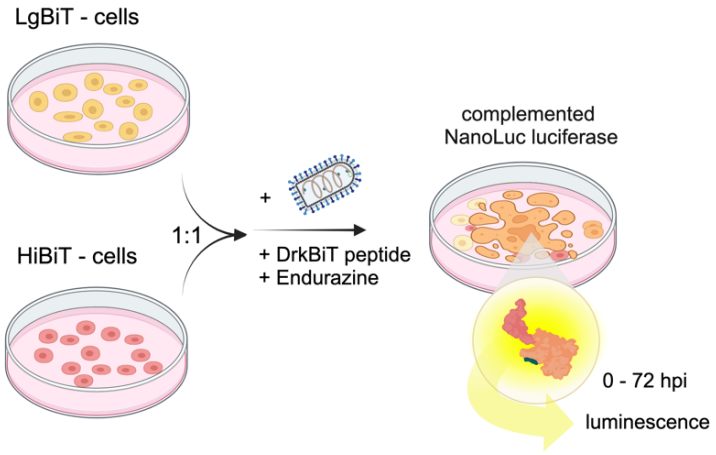

Figure 17. Schematic overview of the developed luminescence assay to monitor virus-mediated cell-cell fusion in real-time

A549 and H1437 cell lines expressing either of the split luciferase constructs (HiBiT or LgBiT) were separately generated by transient stable transfection. The co-culture of HiBiT with LgBiT-expressing cells in a 1:1 ratio is subsequently infected with the fusogenic viruses (rVSV-NDV, rVSV-NDV/F_{3aa}), or the non-fusogenic rVSV as control. Endurazine® is added as a stable, live-cell pro-substrate, and DrkBiT peptide is added to reduce background signal. The luminescence signal from the complemented luciferase (HiBiT + LgBiT) can be measured over the course of infection (in real-time) using a luminometer. Figure created with BioRender.com

Next, fusion assay performance was tested using the stably transfected LgBiT and HiBiT cell lines in a 1:1 co-culture ratio, followed by infection with the fusogenic and non-fusogenic virus variants and the addition of DrkBiT, and Endurazine™ pro-substrate. Relative luminescence units from A549 and H1437 cells were expressed as fold change relative to uninfected control cells. The fusion assay substantiates that only the fusogenic variants rVSV-NDV and rVSV-NDV/F_{3aa} were capable of inducing cell-to-cell fusion, evidenced by a several hundred-fold increase in fusion relative to rVSV infected or uninfected cells (**Figure 18** A and B). This highlights that the designed assay was suitable to recapitulate and quantify the degree of syncytia formation seen by fluorescence microscopy. A surprising observation was that the rVSV-NDV/F_{3aa} variant caused more eminent fusion in both cell lines than the *hyperfusogenic* rVSV-NDV. Cell-cell fusion events peaked earlier, and the cumulative fusion, taken from the area under the curve values (**Figure 18** C), was higher in rVSV-NDV/F_{3aa}, although significant differences between the fusogenic variants could only be obtained for A549 but not for H1437 cells.

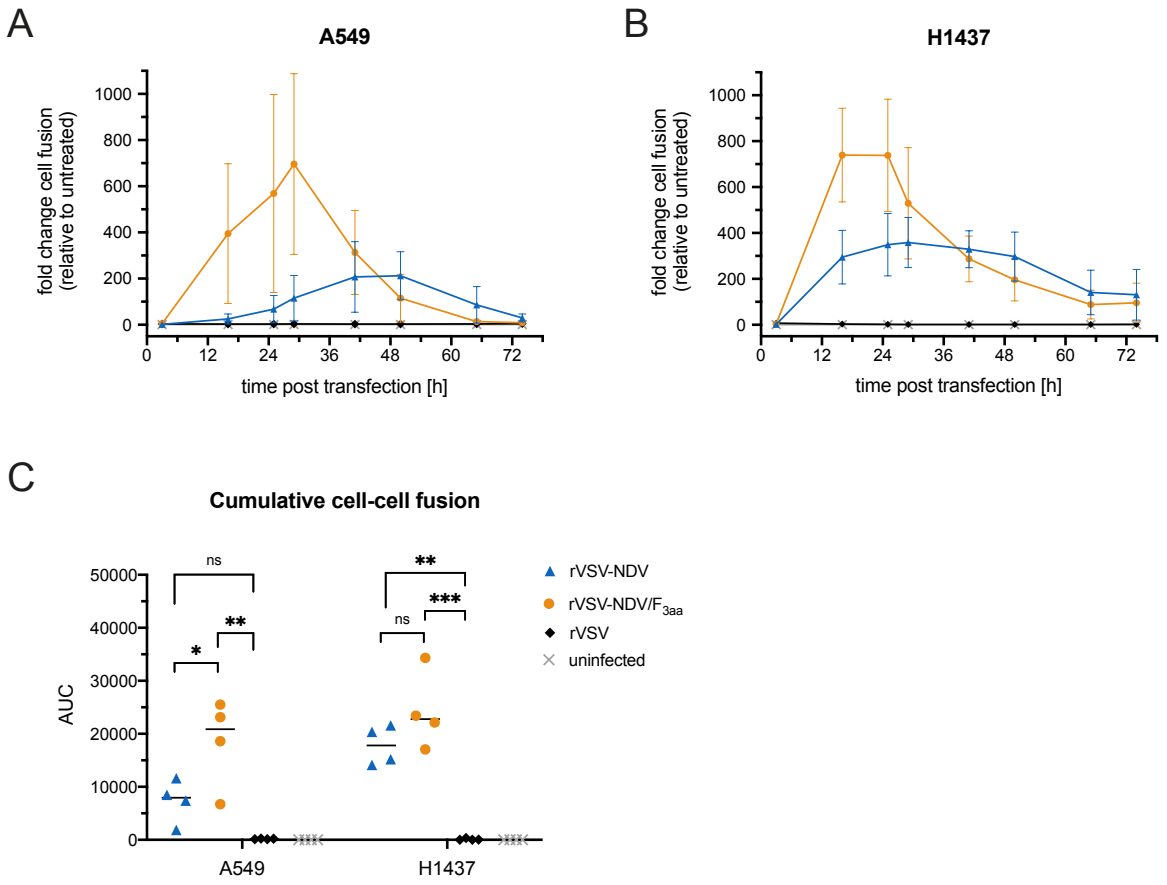

Figure 18. Real-time measurement of OV-mediated cell-cell fusion in A549 and H1437 cells

Stably transfected HiBiT and LgBiT cells were co-cultured and infected at an MOI of 0.01. Upon addition of the stable Endurazine™ live cell luciferase pro-substrate and DrkBiT peptide, virus-mediated cell-cell fusion was quantified in real-time by measuring the generated luminescence signal. Cell fusion in A549 (**A**) and H1437 cells (**B**) is expressed as fold-change relative to uninfected cells. The Figure legend is indicated in Figure (C). (**C**) As a measure of cumulative cell fusion, the area under the curve (AUC) was calculated (as previously described [125]) and plotted. Shown are mean values ± SD of n = 4 independent experiments. Statistical significance of cumulative fusion was calculated using One-way ANOVA with Tukey's multiple comparisons test (ns = non-significant; *p ≤ 0.05, **p ≤ 0.01, ***p ≤ 0.001)

With respect to the fusion data in A549 and H1437 cells, rVSV-NDV/F_{3aa} could no longer be termed *non-hyperfusogenic* and is subsequently just referred to as rVSV-NDV/F_{3aa}. As the fusion assay was not performed in Huh7 cells, it remains open if the *non-hyperfusogenic* phenotype is a sole cell line-specific observation. Nevertheless, the above data showed cell line- and virus-dependent, unique infection and syncytia kinetics, and the detected disparities between a fusogenic and a non-fusogenic death raised the question of the underlying cell death mechanism.

3.1.3 Cell-cell fusion causes a dynamic activation of apoptosis

Early during apoptosis, the cellular membrane lipid architecture changes by exposing PS from the inner to the outer leaflet, primarily functioning as an engulfment signal to phagocytosing cells [126]. Elevated PS exposure is also observed in the tumor microenvironment or upon viral infection and often functions as an immune dampening signal to sustain cancer cell growth or viral replication via the rapid removal of the apoptotic cells and subsequent secretion of anti-inflammatory cytokines by phagocytosing cells [127-129]. To gain a first insight into OV-activated cell death pathways, PS exposure and secondary necrosis were measured in a time course experiment using the RealTime-Glo® Annexin V Apoptosis and Necrosis assay. The applied assay utilizes a split luciferase bound to annexin V, which will complement and generate luminescence once annexin V binds PS. At the same time, loss of membrane integrity is detected by measuring the fluorescence signal generated from a DNA-intercalating dye (**Figure 19** A).

In A549 cells, before clear syncytia or CPE were apparent (until 24 hpi), the base level of PS exposure and measurable necrosis were low and consistent among the viruses. With progressing infection, increased PS exposure was observed sequentially for each virus (**Figure 19** B and C). rVSV activated a moderate PS exposure immediately followed by dominant membrane necrosis, similar to the complete cytotoxicity indicated by the LDH assay. Both events were induced much earlier than by either of the fusion-competent viruses. While the rVSV-NDV-mediated exposure of PS and secondary necrosis met the expectations of a slower progressing fusogenic death, rVSV-NDV/F_{3aa} performance in that assay was unexpected and did not correlate with the greater cumulative fusion potential described above. However, the assay confirmed the insufficient killing of A549 cells by rVSV-NDV and rVSV-NDV/F_{3aa}, taking into account that syncytia in A549 expand to some extent but then burst by necrosis, while surrounding cells remained uninfected.

A slightly opposite picture was seen with H1437 cells, which are less susceptible to rVSV than A549 cells. rVSV struggled to efficiently induce PS exposure in H1437 cells and only slowly but gradually caused membrane rupture through necrosis. In contrast, rVSV-NDV followed by rVSV-NDV/F_{3aa} translocated PS to the outer membrane simultaneous to the onset of syncytia formation (24 – 36 hpi) (**Figure 19** D and E). Against expectation, a peak in PS exposure for rVSV-NDV/F_{3aa} was reached 36 h later (at 72 hpi) than with the other fusogenic virus although the peak in rVSV-NDV/F_{3aa}-mediated necrosis was already obtained at 36 hpi. The necrosis profile of rVSV-NDV more realistically matched with the microscopically observed CPEs in H1437 cells.

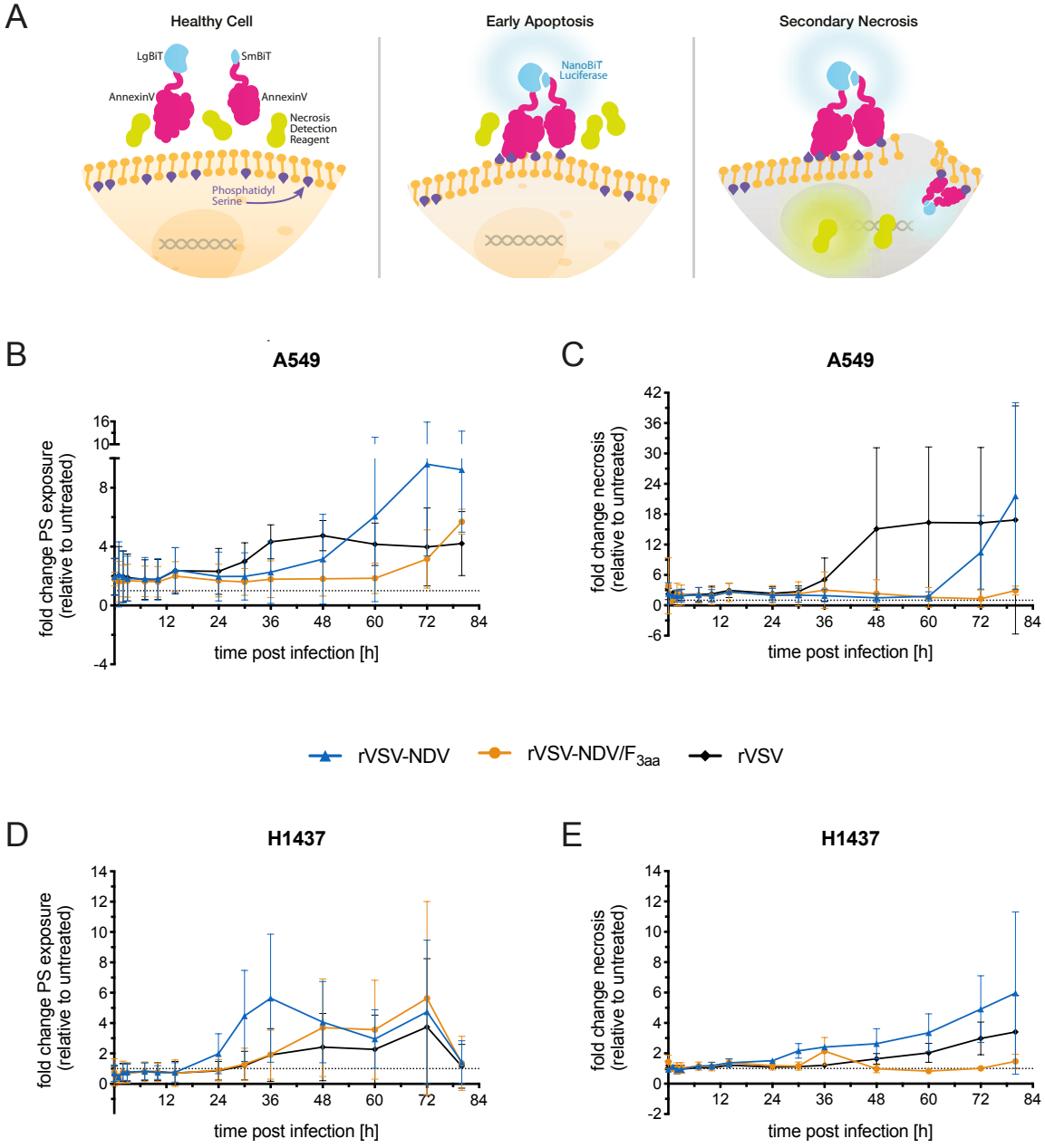

Figure 19. Real-time monitoring of virus-induced PS exposure and secondary necrosis in A549 and H1437 cells

(**A**) Assay principle of the RealTime-Glo Annexin V Apoptosis and Necrosis assay. In healthy cells, PS faces inside the intact lipid bilayer, preventing Annexin V binding and entry of the necroptosis detection reagent. During early apoptosis, the lipid bilayer architecture changes and PS is exposed externally, enabling binding of both, LgBiT Annexin V and SmBiT Annexin V. The proximity of LgBiT and SmBiT complement NanoLuc® luciferase and generates luminescence. Once membrane integrity is compromised, the necroptosis detection reagent enters the cell, and intercalation with DNA creates a fluorescent signal indicative of secondary necrosis. The scheme was adapted and cropped from the RealTime-Glo® Annexin V Apoptosis and Necrosis assay manual (with permission from Promega GmbH). (**B** and **D**) A549 and H1437 cells were infected with the respective virus variants at an MOI of 0.01, and phosphatidylserine exposure was monitored using the RealTime-Glo® Annexin V assay. (**C** and **E**) Membrane rupture, as a sign of cell necrosis, was measured in A549 and H1437 cells in real-time using the membrane-permeable, DNA-intercalating fluorescent substrate. Data is represented as fold change relative to untreated controls and shown as mean ± SD of n = 3 independent experiments.

Consequently, it was concluded that all virus variants triggered the exposure of PS on the outer lipid bilayer and thereby may have induced an apoptotic death program. PS exposure was not exclusive to fusogenic viruses, and in most cases, resembled the detected CPEs and susceptibilities of the individual cell lines to the viral variants. As PS exposure is just one, and not even an exclusive, hallmark of apoptosis, further markers had to be studied in conjunction with the OV-mediated syncytial death.

Once an oncolytic virus has entered and replicated inside a cell, an antiviral innate immune, and often intrinsic apoptotic, response is triggered to eliminate the invader [130]. For example, rNDV and rVSV infection were both reported to induce MOMP and release cytochrome C, indicative of intrinsic apoptosis [131, 132]. So, the extent to which the syncytial stage activates intrinsic apoptosis was investigated by looking at MOMP and caspase 9 activation. Both cell lines were infected at a range of MOIs and stained with TMRE, a mitochondria-specific dye, before measuring MOMP at time points where first syncytia were visible and before cell lysis was initiated. MOMP, mimicked by the uncoupling agent, FCCP (**Figure 20** C), or virus-mediated, then caused TMRE dye leakage to the cytoplasm, and thereby reducing fluorescence intensity.

In accordance with the higher susceptibility of A549 cells to rVSV infection, it was demonstrated that rVSV permeabilized mitochondria at lower viral doses than the fusogenic variants (**Figure 20** A). For example, with rVSV-NDV/F_{3aa}, only an MOI greater than 0.1 (log -1) was sufficient to trigger mitochondrial stress and outer membrane permeabilization. Interestingly, even though rVSV-NDV/F_{3aa} and rVSV-NDV efficiently killed H1437 cells, the ability to induce MOMP was more diminished with the rVSV-NDV/F_{3aa} variant (**Figure 20** B). rVSV-NDV showed dose-dependent leakage of the TMRE dye, whereas rVSV and rVSV-NDV/F_{3aa} only seemed to involve mitochondrial apoptosis at a high viral load.

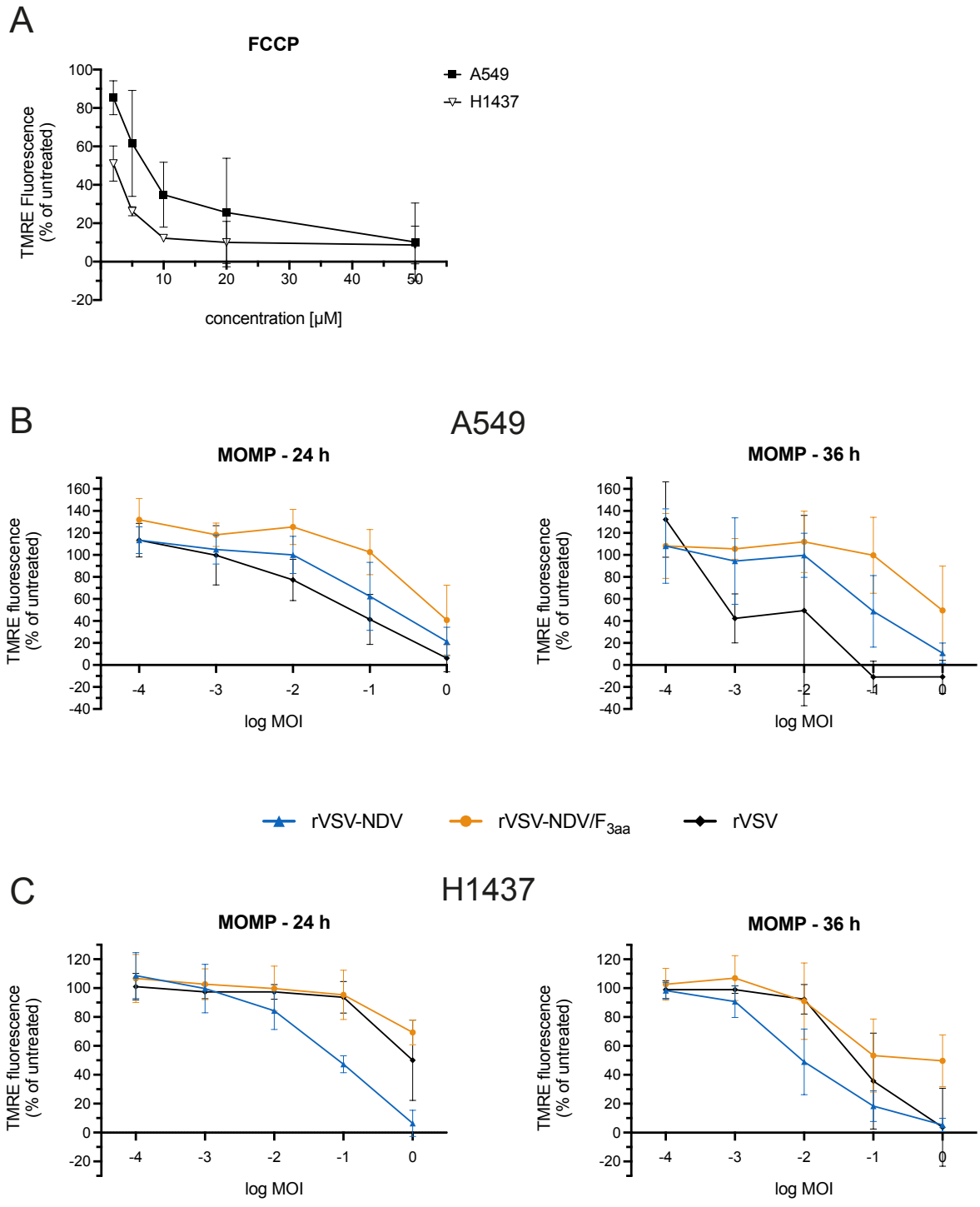

Figure 20. Characterization of MOMP in oncolytic virus-infected A549 and H1437 cells

Mitochondrial outer membrane permeabilization in A549 (**A**) and H1437 (**B**) cells was quantified in a range of different MOIs at 24 and 36 hpi using a fluorescent-based assay measuring the leakage of TMRE dye from compromised mitochondria. Values are expressed as % of TMRE fluorescence relative to untreated cells. (**C**) FCCP-treated cells were used as a positive control. Data is shown as mean values ± SD from n = 3 independent biological replicates.

Permeabilized mitochondria release Smac, mitochondrial DNA and cytochrome C into the cytoplasm. The latter then associates with Apaf-1 and dATP to oligomerize and form a large caspase 9 activating complex called the apoptosome [52]. Having seen moderate MOMP during oncolysis, it was questioned whether caspase 9 is activated and drives intrinsic apoptosis by cleaving downstream effector caspases.

Full-length and cleaved caspase 9 protein levels were detected by Western blot in a time course experiment from 8 – 24 hpi. To achieve thorough infection in that time span, A549 and H1437 cells were infected at an MOI of 1, and protein lysates were collected before cells succumbed to the infection. In A549 cells, although trends varied slightly between replicate experiments, no clear differences in protein expression of procaspase 9 and cleaved caspase 9 could be detected after the respective OV infections at any time point (representative blots and merged quantified data shown in **Figure 21** A). A reliable quantification of caspase 9 cleavage was skewed by unexpectedly high background levels of cleaved caspase 9 in untreated cells. Because the applied control conditions (TS, TSZ, or staurosporine) yielded a low level of caspase 9 cleavage as expected, it is possible that caspase 9 cleavage either happens later or does not play a role in the OV-mediated killing of A549 cells. Results from H1437 cells were more as expected. Not only were both cleavage isoforms (35 and 37 kDa) identified, but also a dynamic activation of caspase 9 was detectable from all virus variants (**Figure 21** B). Worth mentioning is a sudden 2.5-fold increase of rVSV-NDV/F_{3aa}-mediated caspase 9 activation from 16 to 24 hpi, whereas with rVSV-NDV, caspase 9 cleavage peaked at 16 hpi, and rVSV had a more moderate activation profile.

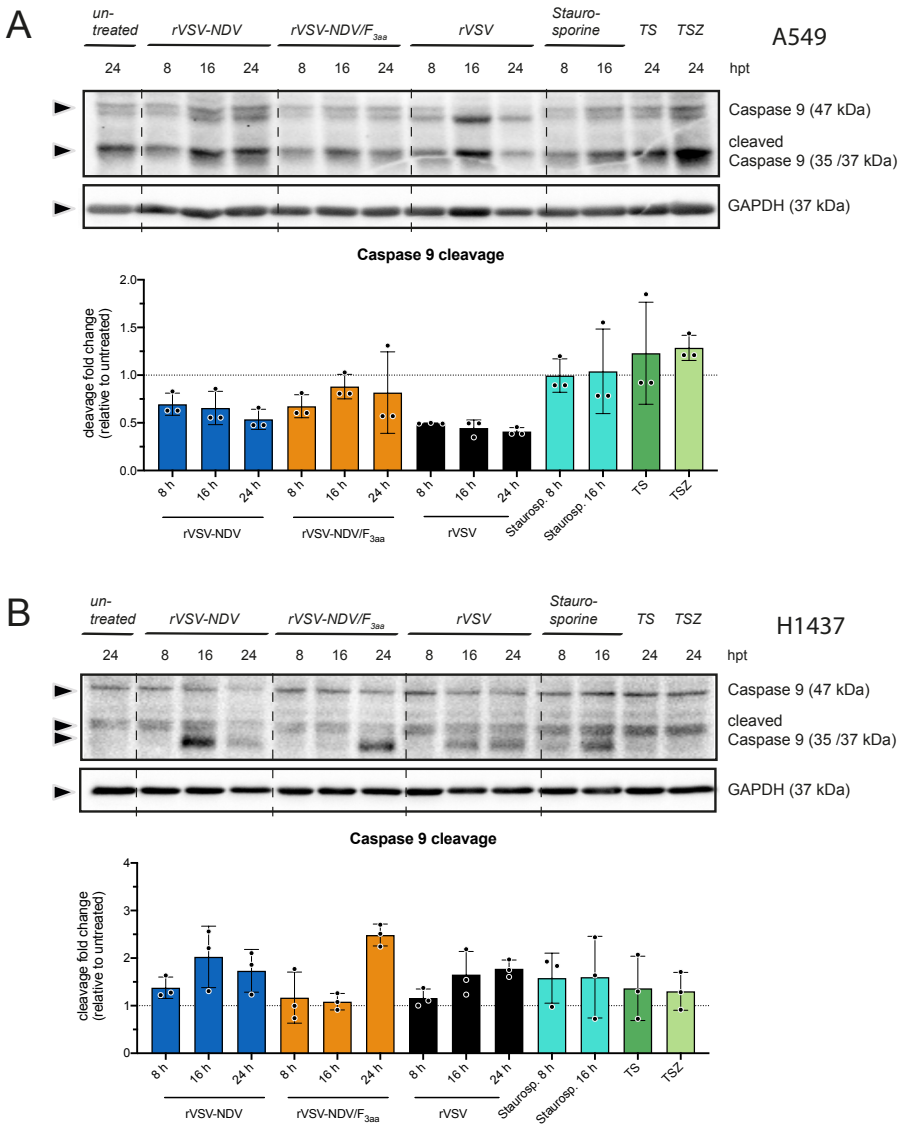

Figure 21. Characterization of caspase 9 activation in oncolytic virus-infected A549 and H1437 cells

Activation of intrinsic apoptosis caspase 9 was characterized in (**A**) A549 and (**B**) H1437 cells. After infection with the respective oncolytic virus variants at an MOI of 1, protein lysates were collected between 8 and 24 hpi. Expression of full-length (47 kDa) and cleaved caspase 9 (35/37 kDa) was determined by Western blot analysis using the corresponding antibodies listed in **Table 2**. One representative blot of the time course infection experiments compared to staurosporine, TS, or TSZ control treatment is shown. Protein levels were quantified on each blot relative to GAPDH expression and the ratio of cleaved caspase 9 over full-length caspase 9 is expressed as fold change relative to untreated cells in the bar chart below. Shown are mean ± SD values of n = 3 independent biological replicates. Arrow-heads on the left mark the quantified protein bands. Protein ladder: ROTI®-Mark TRICOLOR Protein marker (for simplicity not shown).

If rVSV-NDV- or rVSV-NDV/F_{3aa}-mediated cell killing relies on apoptosis, initiator caspase 8 and effector caspase 3 and 7 activation, next to PARP cleavage, should be detectable during the syncytial stage. These markers were investigated in follow-up experiments. It should be noted that, for both cell lines, the small active fragment of caspase 3 (17/19 kDa) could only be detected in one biological replicate, and active caspase 8 (18 kDa) was never detected with the anti-caspase 8 antibody, even though claimed by the manufacturer. Representative blots for those cleaved forms are shown in A and C of **Figure 22** and **Figure 23** but could not be reproduced. Alternatively, another cleavage isoform of caspase 3 (25 kDa fragment) and caspase 8 (42 kDa fragment) were repetitively detected and quantified from the Western blots. To complement the Western blot data, enzyme activity assays were performed to detect caspase 3/7 or caspase 8 cleavage activity (B and D of **Figure 22** and **Figure 23**).

In A549 cells, non-fusogenic rVSV caused early caspase 3 cleavage (25 kDa fragment), and moderate but accumulating caspase 3/7 activity until cells were dead at 48 hpi (**Figure 22**). In line with previous reports showing rVSV dependency on apoptosis [133, 134], rVSV mildly triggered the enzymatic activity of the upstream initiator caspase 8 prior to caspase 3 activity. Western blot and enzyme assay data also revealed that neither of the syncytia-forming viruses depended on caspase 8 activity in A549 cells. Yet, high caspase 3 and caspase 7 activity was eminent at time points where syncytia had developed and started to collapse (36 – 72 hpi).

In H1437 cells, Western blot-based quantification of the unconventional fragments of caspase 3 (25 kDa) or caspase 8 (42 kDa) provided more straightforward results and pointed to clear involvement of caspase 3 and caspase 8 cleavage during rVSV-, rVSV-NDV-, and rVSV-NDV/F_{3aa}-mediated death (**Figure 23**). Cleaved caspase 8 protein levels were higher in cells infected with the fusogenic variants, but this observation could not be supported by higher enzymatic caspase 8 activity. In general, the OV-mediated death signaling in H1437 cells involved slightly more caspase 8 activity than in A549 cells. The representative Western blot for active executioner caspase 3 (17/19 kDa), together with the detectable caspase 3/7 substrate cleavage measured by luminescence indicated that rVSV and rVSV-NDV certainly activated apoptosis. Surprisingly, effects were less pronounced using rVSV-NDV/F_{3aa}. Nevertheless, activation of caspase-mediated apoptosis may also be true for this variant, albeit with less certainty.

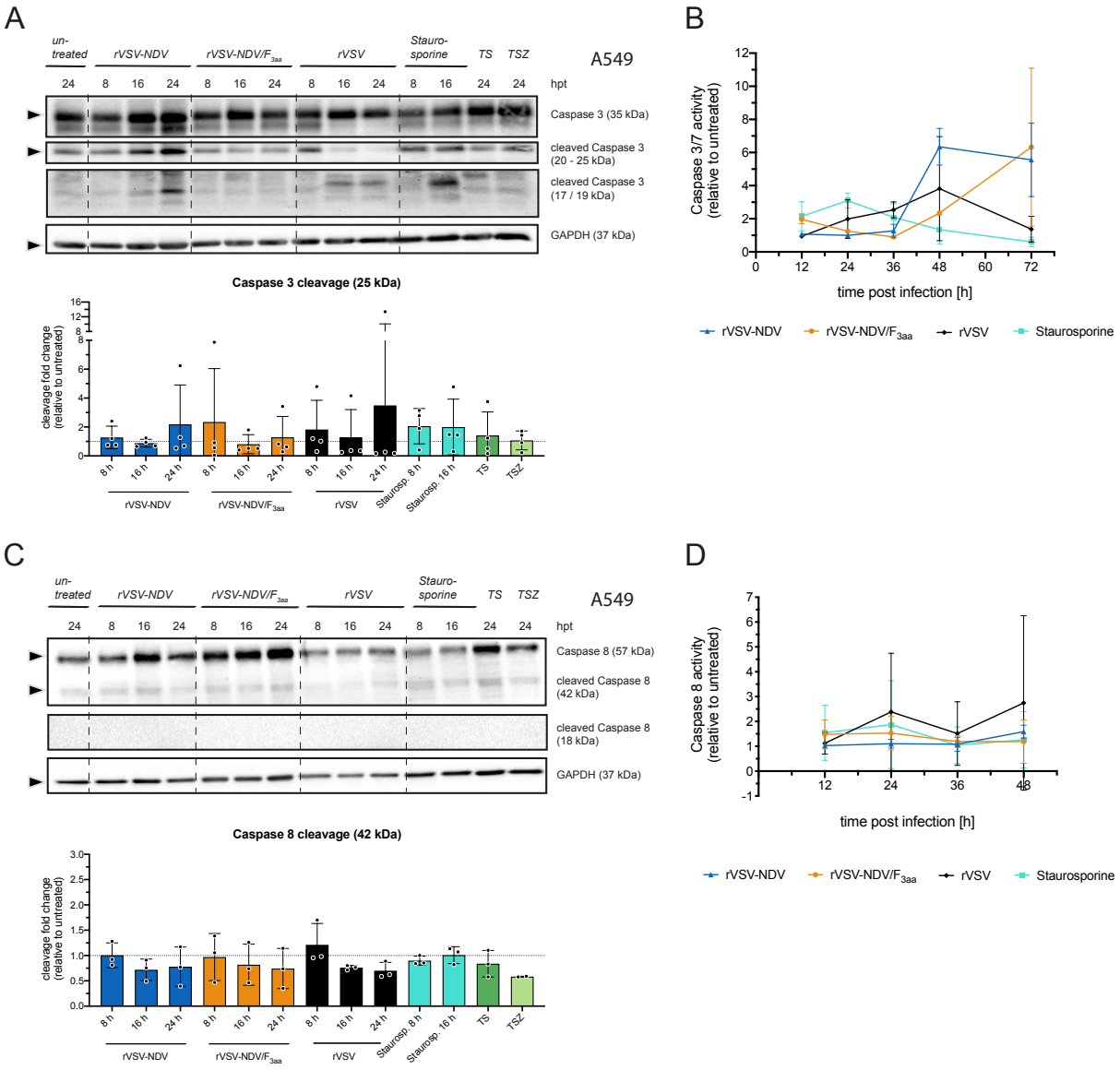

Figure 22. Characterization of caspase 3/7 and caspase 8 activity in oncolytic virus-infected A549 cells

(**A**) In a time course infection experiment in A549 cells, the protein level and cleavage of caspase 3 and caspase 8 were evaluated. A549 cells were infected at an MOI of 1, and protein lysates were collected between 8 and 24 hpi. Expression of full-length (35 kDa) and cleaved caspase 3 (25 and 17/19 kDa) was determined by Western blot analysis using the corresponding antibodies listed in **Table 2**. One representative blot of the time course infection experiments compared to staurosporine, TS, or TSZ control treatment is shown. Protein levels were quantified on each blot relative to GAPDH expression and the ratio of cleaved (25 kDa fragment) over full-length caspase 3 is expressed as fold change relative to untreated cells in the bar chart below. (**B**) Caspase 3 and 7 cleavage were measured over time by quantifying the caspase 3/7-specific conversion of the DEVD-aminoluciferin substrate and reading luminescence. Staurosporine- (10 µM) treated cells were used as a positive control. Data is expressed as fold change relative to untreated cells. (**C**) Expression of full-length (57 kDa) and cleaved caspase 8 (42 and 18 kDa) was determined by Western blot analysis using the corresponding antibodies listed in **Table 2**. One representative blot of the time course infection experiments compared to staurosporine, TS, or TSZ control treatment is shown. Protein levels were quantified on each blot relative to GAPDH expression and the ratio of cleaved (42 kDa fragment) over full-length caspase 8 is expressed as fold change relative to untreated cells in the bar chart below. (**D**) Caspase 8 enzyme activity was determined by reading the luminescence generated from a caspase 8-specific conversion of the LETD-aminoluciferin substrate. Staurosporine- (10 µM) treated cells were used as a positive control. Data in **A** - **D** is expressed as fold change relative to untreated cells and plotted as mean ± SD of n = 3 independent biological replicates. Arrow-heads on the left mark the quantified protein bands. Protein ladder: ROTI®-Mark TRICOLOR Protein marker (for simplicity not shown).

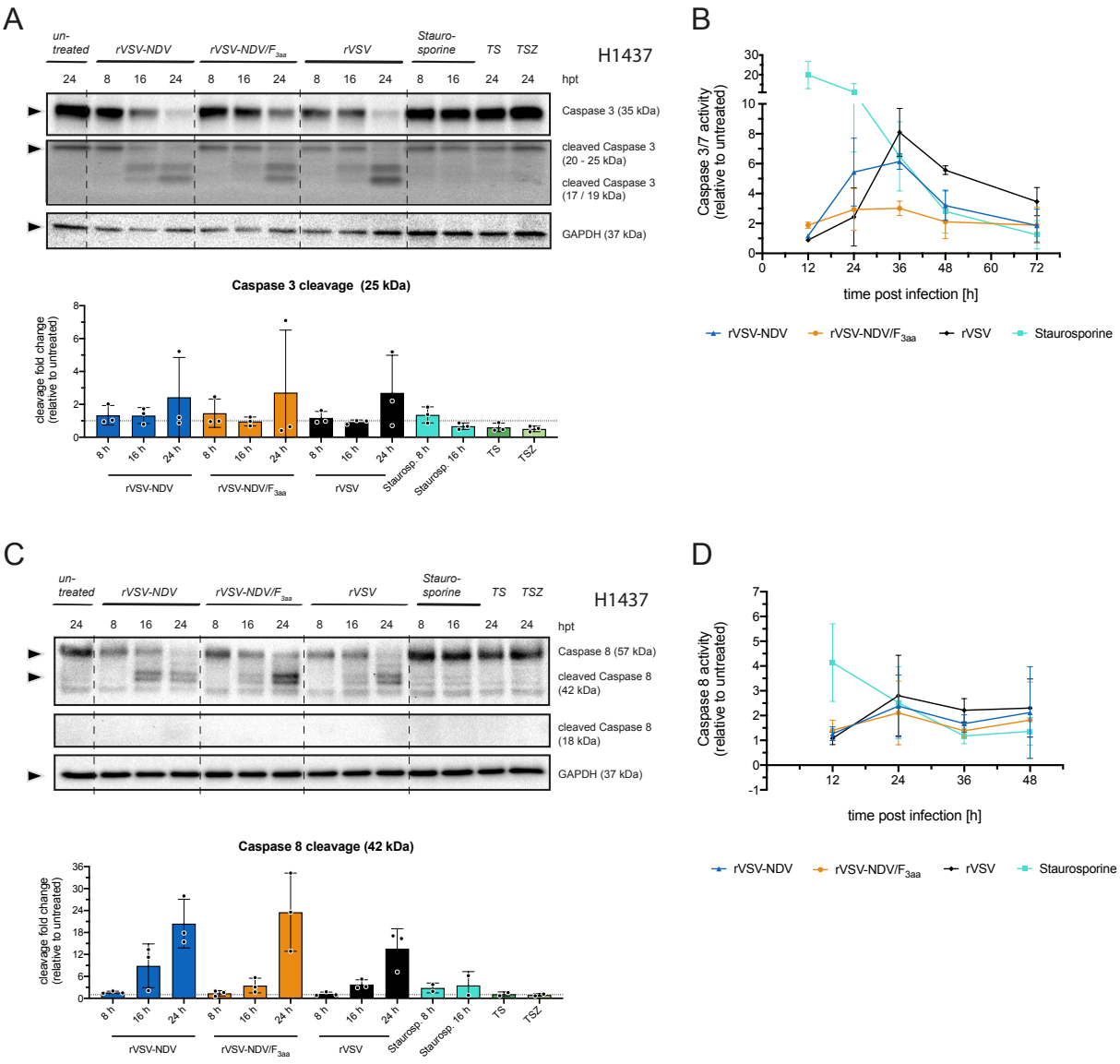

Figure 23. Characterization of caspase 3/7 and caspase 8 activity in oncolytic virus-infected H1437 cells

(**A**) In a time course infection experiment in H1437 cells, the protein level and cleavage of caspase 3 and caspase 8 were evaluated. H1437 cells were infected at an MOI of 1, and protein lysates were collected between 8 and 24 hpi. Expression of full-length (35 kDa) and cleaved caspase 3 (25 and 17/19 kDa) was determined by Western blot analysis using the corresponding antibodies listed in **Table 2**. One representative blot of the time course infection experiments compared to staurosporine, TS, or TSZ control treatment is shown. Protein levels were quantified on each blot relative to GAPDH expression and the ratio of cleaved (25 kDa fragment) over full-length caspase 3 is expressed as fold change relative to untreated cells in the bar chart below. (**B**) Caspase 3 and 7 cleavage were measured over time by quantifying the caspase 3/7-specific conversion of the DEVD-aminoluciferin substrate and reading luminescence. Staurosporine- (10 µM) treated cells were used as a positive control. Data is expressed as fold change relative to untreated cells. (**C**) Expression of full-length (57 kDa) and cleaved caspase 8 (42 and 18 kDa) was determined by Western blot analysis using the corresponding antibodies listed in **Table 2**. One representative blot of the time course infection experiments compared to staurosporine, TS, or TSZ control treatment is shown. Protein levels were quantified on each blot relative to GAPDH expression and the ratio of cleaved (42 kDa fragment) over full-length caspase 8 is expressed as fold change relative to untreated cells in the bar chart below. (**D**) Caspase 8 enzyme activity was determined by reading the luminescence generated from a caspase 8-specific conversion of the LETD-aminoluciferin substrate. Staurosporine- (10 µM) treated cells were used as a positive control. Data in **A** - **D** is expressed as fold change relative to untreated cells and plotted as mean ± SD of n = 3 independent biological replicates. Arrow-heads on the left mark the quantified protein bands. Protein ladder: ROTI®-Mark TRICOLOR Protein marker (for simplicity not shown).

To complement the results from above, it was further investigated whether activated executioner caspases also cleave one of many of their substrates, namely PARP. Quantification of cleaved PARP (89 kDa) by Western blot in A549 cells (**Figure 24** A) demonstrated that both of the fusogenic viruses caused moderate PARP cleavage starting in parallel to the observed syncytia stage, while rVSV stepwise increased PARP cleavage. A much higher magnitude of full-length to cleaved PARP conversion was evident in H1437 compared to A549, independent of the viral variants (**Figure 24** B).

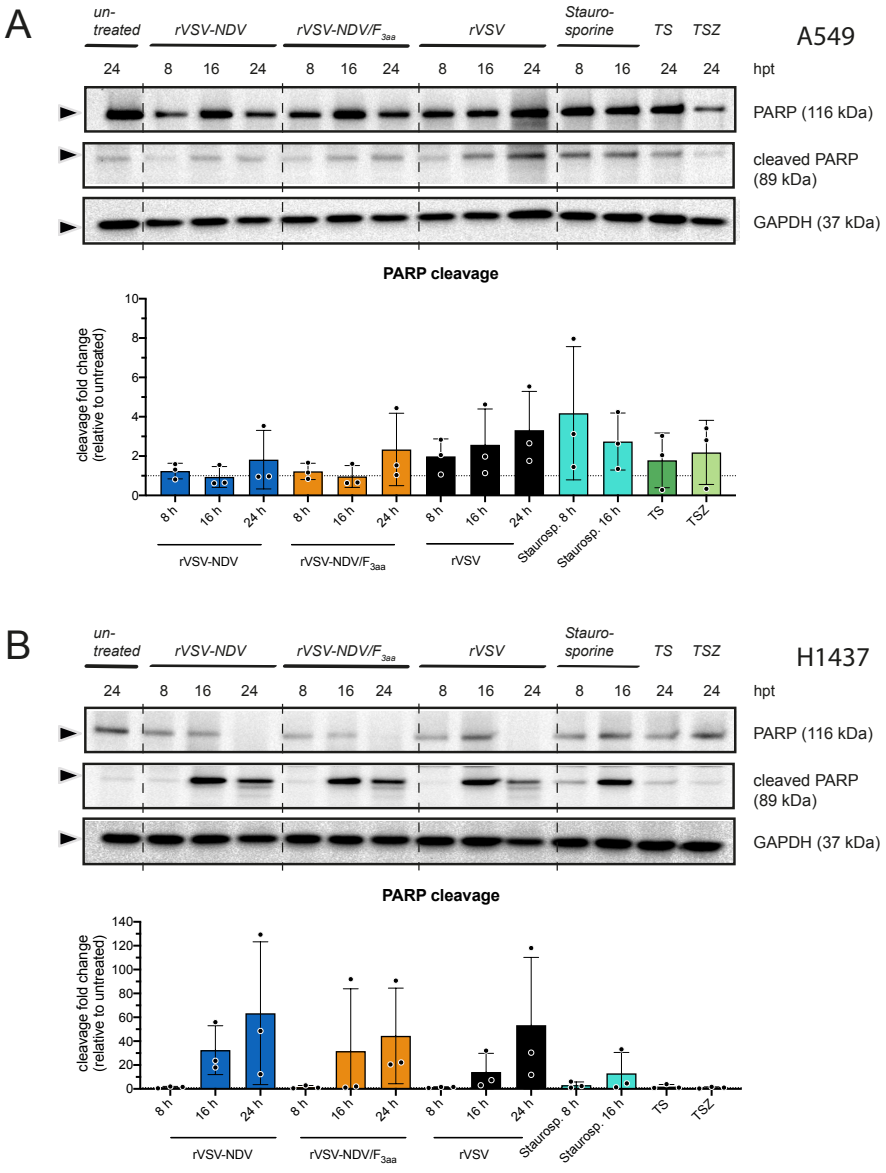

Figure 24. PARP cleavage quantified upon oncolytic virus infection in A549 and H1437 cells

In a time course infection experiment in A549 or H1437 cells, the protein level and cleavage of PARP were evaluated. (**A**) A549 and (**B**) H1437 cells were infected at an MOI of 1, and protein lysates were collected between 8 and 24 hpi. Expression of full-length (116 kDa) and cleaved PARP (89 kDa) was determined by Western blot analysis using the corresponding antibodies listed in **Table 2**. One representative blot of the time course infection experiments compared to staurosporine, TS, or TSZ control treatment is shown. Protein levels were quantified on each blot relative to GAPDH expression and the ratio of cleaved over full-length PARP is expressed as fold change relative to untreated cells in the bar chart below. Shown are mean ± SD values of n = 3 independent biological replicates. Arrow-heads on the left mark the quantified protein bands. Protein ladder: ROTI®-Mark TRICOLOR Protein marker (for simplicity not shown).

In summary, a dynamic activation of caspase-dependent apoptosis in a time-dependent fashion and with virus- and cell line-specific characteristics was observed. Notwithstanding, apoptosis induction was neither a unique feature of the syncytia forming rVSV-NDV, rVSV-NDV/F_{3aa} nor of fusion-incompetent rVSV. Upon viral entry, OVs are inevitably sensed by extrinsic pattern recognition receptors to activate antiviral signaling and production of death receptor ligands, leading to receptor-mediated extrinsic apoptosis. The latter activates initiator caspase 8 and consecutively the effector caspases 3 and 7. The detected MOMP and a moderate cleavage of caspase 9 may potentiate an apoptotic syncytial death via the intrinsic pathway.

To provoke the activated apoptotic pathway, infections were subsequently performed in combination with death-inducing or caspase-inhibiting stimulants, and cytotoxicity and viral replication were analyzed at 48 hpi (**Figure 25**). Infection in the presence of the pan-caspase inhibitor zVAD resulted in similar or even reduced cytotoxicity compared to the control, supporting the previously discovered caspase dependency of fusogenic and non-fusogenic viruses. Pretreatment of A549 or H1437 cells with an extrinsic death-receptor ligand, TNF-α, and Smac mimetic (TS) potentiated cytotoxicity in all conditions except for rVSV infection in H1437 cells. Moreover, a combination of TS and zVAD (TSZ) forced the cells to switch to another, caspase-independent, death with virus-specific observations: While rVSV stimulated a caspase-dependent death in A549, a TSZ-triggered necroptotic death predominated in rVSV-infected H1437 cells. TSZ and the fusogenic viruses further pushed cytotoxicity compared to control, showing that both cell lines were capable of activating a caspase-independent type of syncytial death. In this regard, especially H1437 cells seemed to favor a TSZ-triggered necroptotic pathway, whereas A549 cells were slightly more reluctant to necroptosis induction by TSZ. Having observed quite drastic effects on cytotoxicity, it was hypothesized that TS, TSZ, or zVAD treatment would also modulate virus replication, but none of the stimulants had an effect on $TCID_{50}$ values (**Figure 25** C and D).

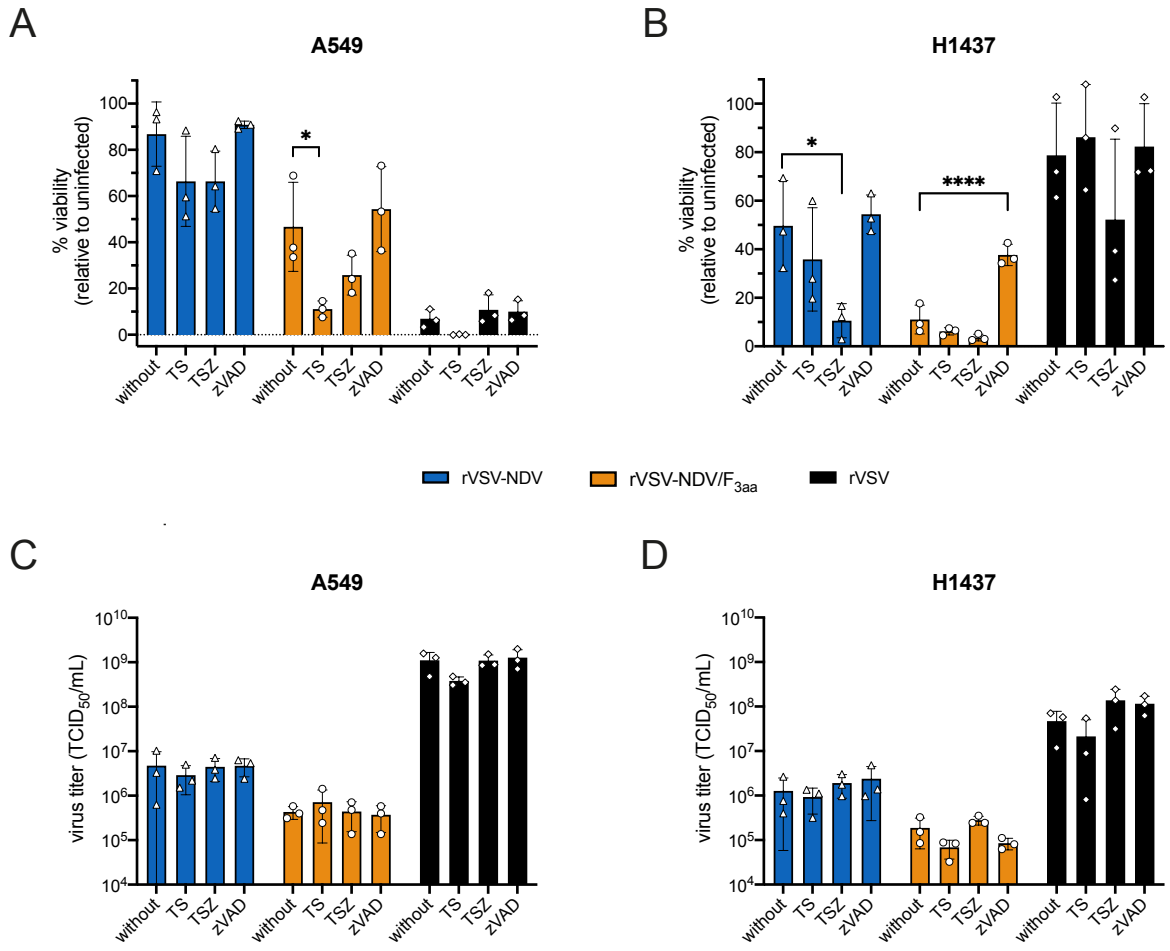

Figure 25. Oncolytic virus infection in A549 and H1437 cells in the presence of TS, TSZ, or zVAD

A549 and H1437 cells were pre-treated with TS, TSZ, or zVAD for 3 h and infected at an MOI of 0.01 in combination with the death-inducing treatments. (**A** and **B**) Cellular viability was measured at 48 hpi and expressed relative to untreated cells. (**C** and **D**) Virus replication was quantified from infectious supernatant by $TCID_{50}$ assay. Data is expressed as mean ± SD from n = 3 biological replicates. Statistical significance was calculated using one-way ANOVA with Dunnett's multiple comparisons test (*p ≤ 0.05, ****p ≤ 0.0001).

3.1.4 Syncytia formation and oncolysis also engage parts of necroptosis signaling

At this point, it had been established that rVSV-NDV and rVSV-NDV/F_{3aa}-mediated death encompasses caspase-dependent apoptotic signaling. But, infection in combination with TSZ already pointed to a possible switch and contribution of virus-induced necroptosis, a lytic and inflammatory type of programmed cell death. In a scenario where zVAD inhibits caspases (among them the initiator caspase 8), phosphorylation of RIPK1, RIPK3, and MLKL leads to assembly into necrosome complexes and the oligomerization and localization of p-MLKL to the plasma membrane eventually induces pore formation, a result of necroptotic death [63]. Consequently, lysates from the Western blot time course experiment were analyzed for the presence and phosphorylation of RIPK1, RIPK3, and MLKL.

In A549 cells (**Figure 26**), rising protein levels of phospho-MLKL were detected for all viruses starting at 16 hpi and peaking at 24 hpi. While rVSV-NDV and rVSV-NDV/F_{3aa} were still in the pre-death, syncytial stage, rVSV likely already had elicited an MLKL-controlled membrane rupture and necroptotic death. This is in line with the above-described necrosis data from the real-time fluorescent assay (**Figure 19**). Although fold changes to untreated cells were not high, low phosphorylation of RIPK1 and RIPK3 was recorded for the fusogenic variants and for rVSV earlier than the peaks of p-MLKL accumulation.

A very bright band of a potential RIPK3 isoform slightly above the defined 57 kDa RIPK3 band was exclusively detected in rVSV-infected cells (A549 and H1437). Whether this translates to a very strong involvement of RIPK3 in rVSV-activated necroptosis, or whether this might be an unspecific binding of the antibody to the rVSV-G protein (size: 57-65 kDa, [135]), or a cellular protein, could not be resolved. However, it is worth mentioning that even though H1437 cells are less susceptible to rVSV than A549, at 16 – 24 hpi a similar bright band was detectable, and that band also appeared in TS- and TSZ-treated H1437 cells (**Figure 27**). Western blots further revealed only marginal protein levels of p-RIPK1 and p-RIPK3 levels in OV-infected H1437 cells. Nevertheless, the viruses proceeded a death program with adequate levels of MLKL phosphorylation. Altogether, evidence was gained that indicated formation of the necrosome complex in A549 and H1437 by rVSV, rVSV-NDV and rVSV-NDV/F_{3aa}, to different degrees, albeit clarity of necroptotic-dominant signaling during the syncytial stage could not be provided. Either way, the results contradict reported data, where A549 and H1437 are often described as non-responding and reluctant to necroptotic stimuli by, for example, TSZ [136] (as further discussed in 4.1.1), and indicate that the OVs may be a more potent necroptosis stimulant than TSZ.

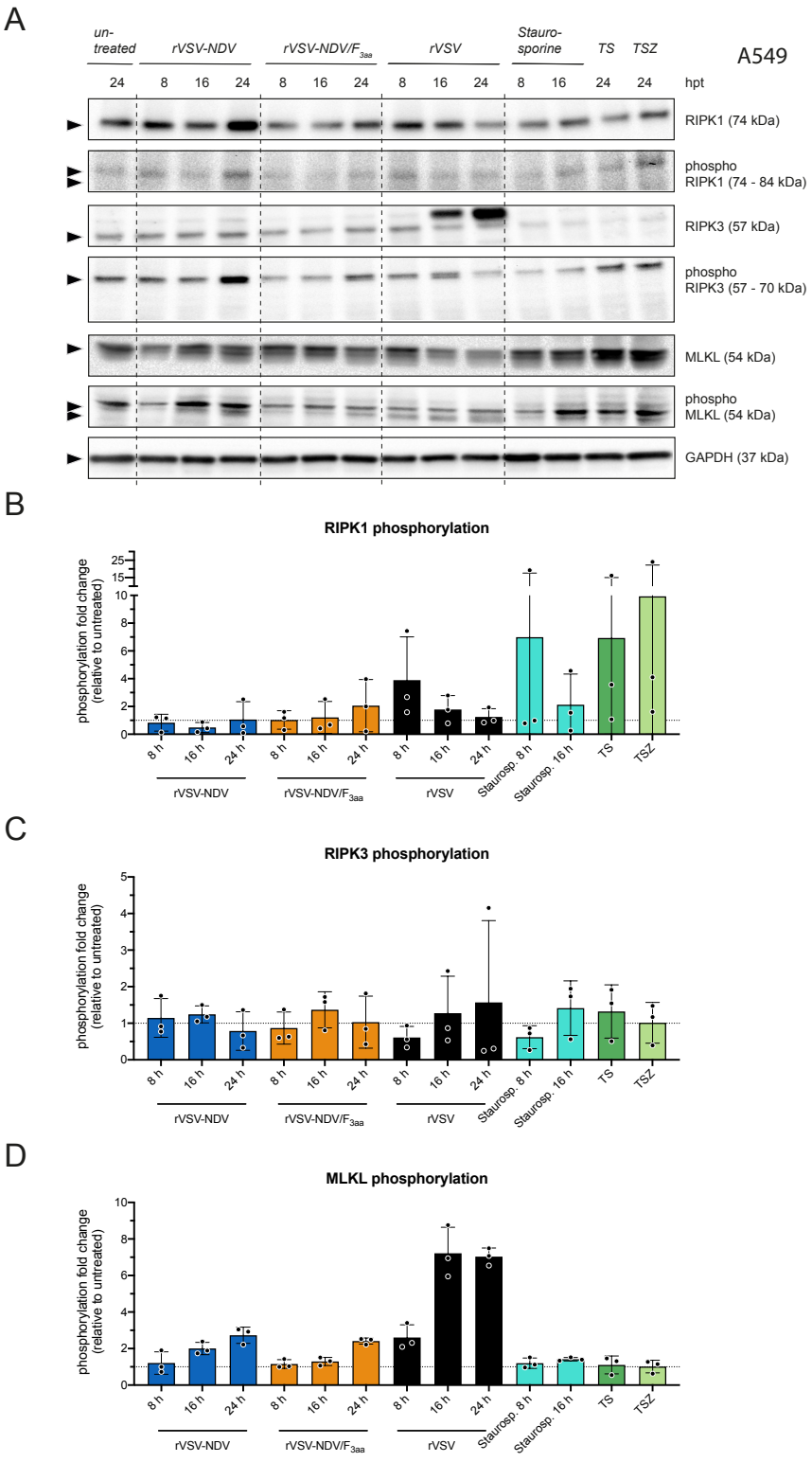

Figure 26. Western blot analysis of necrosome components RIPK1, RIPK3, and MLKL in OV-infected A549 cells.

In a time course infection experiment in A549 cells, the protein level and phosphorylation of necrosome components RIPK1, RIPK3, and MLKL were evaluated by Western blot analysis using the corresponding antibodies listed in **Table 2**. A549 cells were infected at an MOI of 1, and protein lysates were collected between 8 and 24 hpi. (**A**) For each marker, representative blots of the time course infection experiments compared to staurosporine, TS, or TSZ control treatment are shown. Protein expression was normalized to GAPDH and the ratios of phosphorylated over non-phosphorylated protein is quantified and plotted for (**B**) RIPK1, (**C**) RIPK3, and (**D**) MLKL as fold change relative to untreated cells. Data in **B** - **D** shows mean ± SD values from n = 3 independent biological replicates. Arrow-heads on the left mark the quantified protein bands. Protein ladder: ROTI®-Mark TRICOLOR Protein marker (for simplicity not shown).

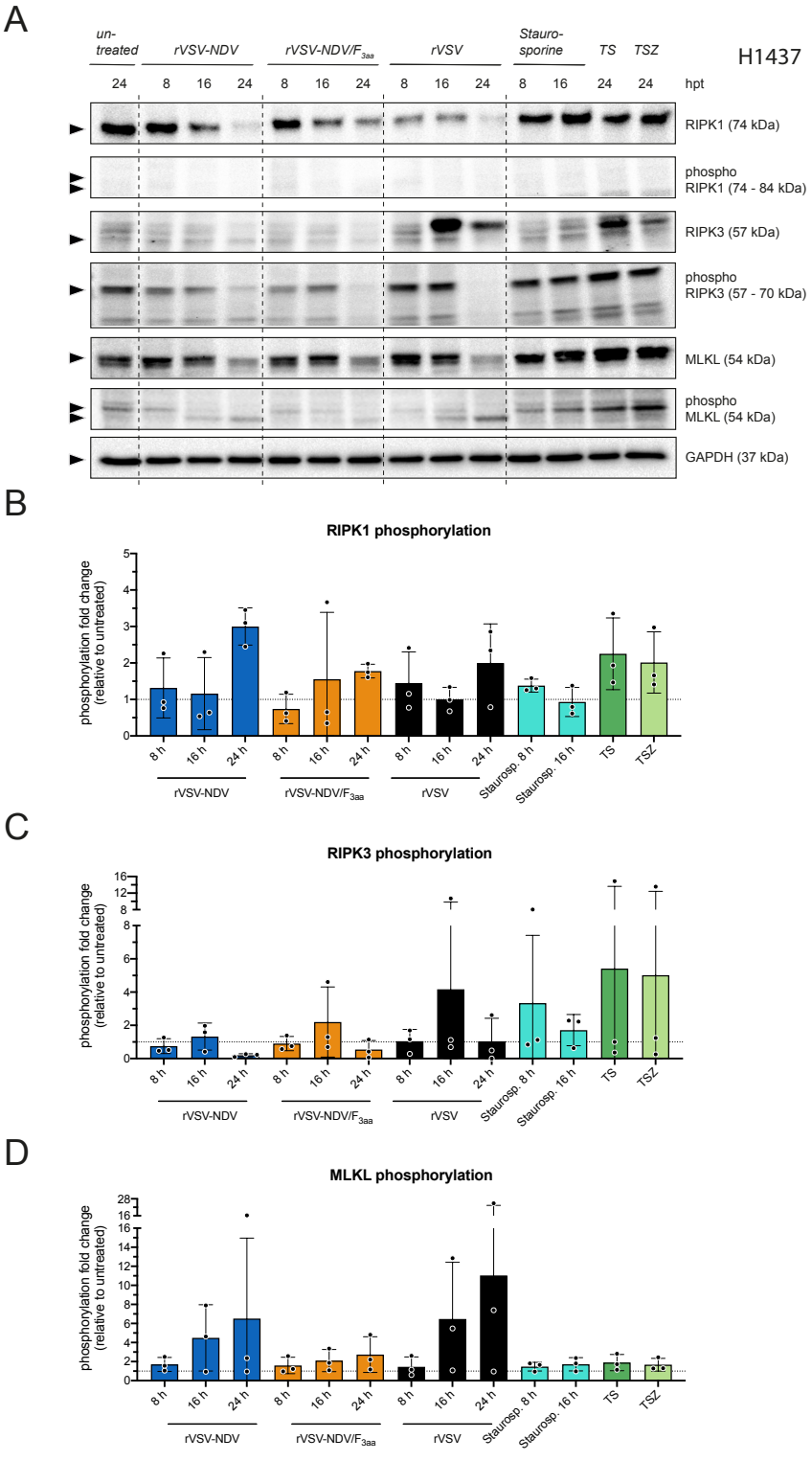

Figure 27. Western blot analysis of necrosome components RIPK1, RIPK3, and MLKL in OV-infected H1437 cells

In a time course infection experiment in H1437 cells, the protein level and phosphorylation of necrosome components RIPK1, RIPK3, and MLKL were evaluated by Western blot analysis using the corresponding antibodies listed in **Table 2**. H1437 cells were infected at an MOI of 1, and protein lysates were collected between 8 and 24 hpi. (**A**) For each marker, representative blots of the time course infection experiments compared to staurosporine, TS, or TSZ control treatment are shown. Protein expression was normalized to GAPDH and the ratios of phosphorylated over non-phosphorylated protein is quantified and plotted for (**B**) RIPK1, (**C**) RIPK3, and (**D**) MLKL as fold change relative to untreated cells. Data in **B** - **D** shows mean ± SD values from n = 3 independent biological replicates. Arrow-heads on the left mark the quantified protein bands. Protein ladder: ROTI®-Mark TRICOLOR Protein marker (for simplicity not shown).

To shed more light on the necroptosis susceptibility of A549 and H1437, in the absence of OV infection, a scouting experiment was performed using necroptosis-sensitive HT-29 cells as a control. Cells were monitored by brightfield microscopy and necroptotic protein expression was recorded by Western blot (**Figure 28**). HT-29 cells responded well to TSZ-induced necroptosis already at a low TNF-α concentration (20 ng/mL), not only with detectable RIPK1, RIPK3, and MLKL phosphorylation but also with apparent destruction of the cell monolayer, as previously reported [136, 137]. Addition of Nec-1, a RIPK1 inhibitor, increased RIPK1 levels, prevented its phosphorylation and overall diminished downstream RIPK3 and MLKL activation in HT-29 cells. Visually, Nec-1 treatment rescued cell viability of TSZ-induced HT-29 cells. Also, NSA, an MLKL-specific inhibitor, successfully blocked necroptosis in HT-29 cells on the protein level but could not prevent cell death. In contrast, in A549 and H1437 cells, TSZ could not induce measurable necroptosis induction, even with higher TNF-α concentrations (500 ng/mL) in TSZ. Microscopically, that trend was confirmed, as both of the cell lines remained viable upon TSZ supplementation. Accordingly, none of the inhibitor treatments, Nec-1 or NSA, had manipulating effects on the necroptosis pathway. However, while these chemicals failed to induce sufficient necroptosis in A549 and H1437 cells, the data from above was promising to assume that either of the oncolytic viruses could still induce the necroptosis pathway.

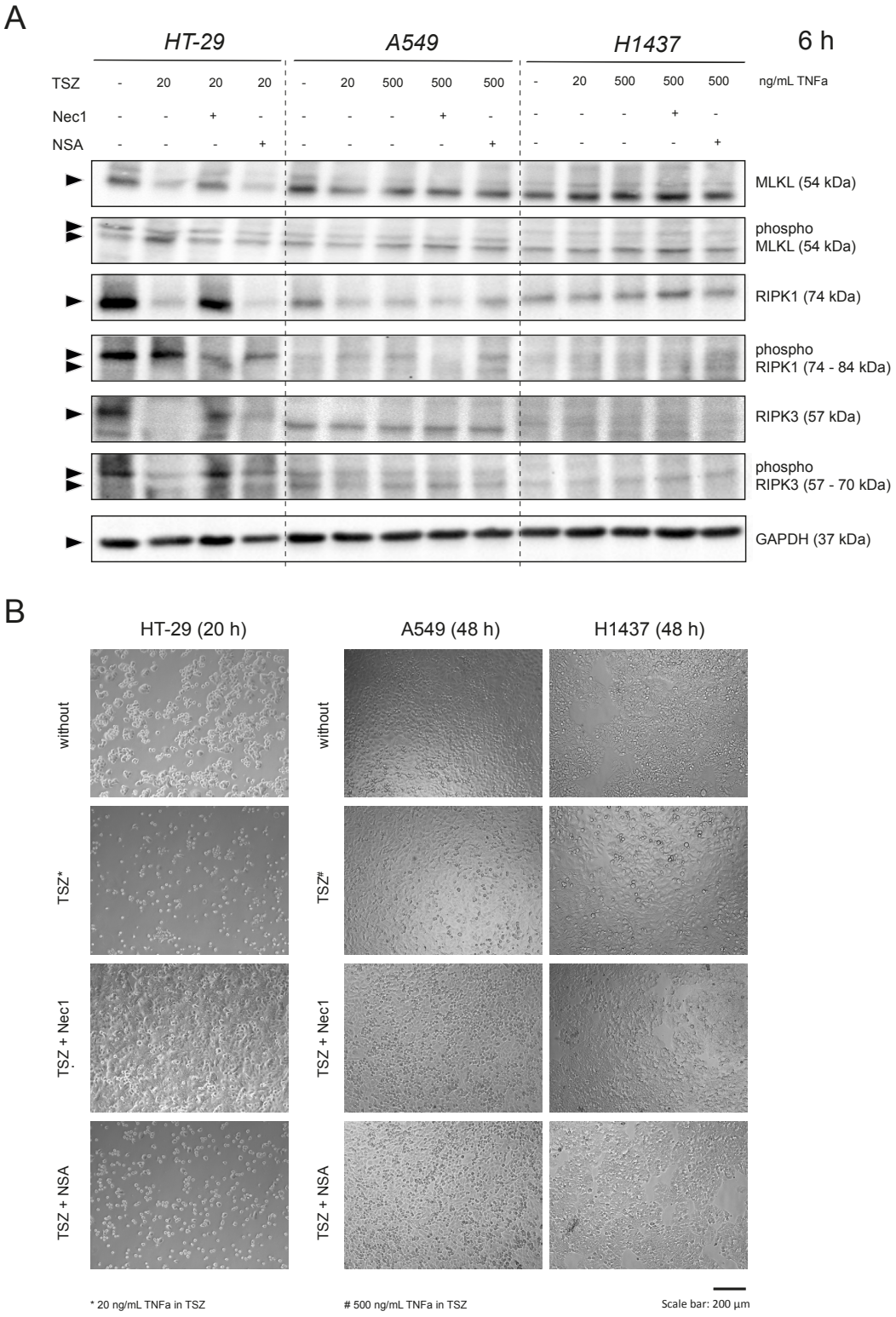

Figure 28. A549, H1437, and HT-29 cell susceptibility to necroptosis induction by TSZ and upon addition of necroptosis inhibitors

(**A**) A549, H1437, and HT-29 cells were treated with TNF-α, Smac mimetic LCL-161, and zVAD (TSZ) to induce necroptosis. Nec-1 was used to inhibit RIPK1 and NSA was added to block MLKL phosphorylation. Western blot analysis of necrosome components, using the corresponding antibodies listed in **Table 2**, is visualized for one representative biological replicate. Arrowheads on the left mark the expected protein bands. Protein ladder: ROTI®-Mark TRICOLOR Protein marker (for simplicity not shown). (**B**) Corresponding brightfield microscopy images of HT-29, A549, and H1437 cells after TSZ-mediated necroptosis induction, and addition of Nec-1 or NSA. Shown are representative images of n = 1 biological replicate.

Detection of subtle differences in protein levels by Western blot was challenging and subject to high inter-experimental variation. Therefore, another approach was undertaken in order to investigate whether OV infections in the presence of Nec-1 or NSA had a direct impact on cytotoxicity and virus titers (**Figure 29**). Unfortunately, neither of the necroptosis-inhibiting treatments yielded a measurable difference in cytotoxicity or virus replication compared to the control. This highlights that p-MLKL-mediated membrane rupture may take place but cannot be inhibited by NSA or Nec-1. Thus, an additional death regulator may control syncytia necrosis.

In conclusion, despite these ambiguous results and no striking differences between a fusion-competent and non-fusogenic virus, the data provides some evidence that, in addition to apoptosis, A549 and H1437 cells can trigger phosphorylation of RIPK1, RIPK3, and MLKL which might culminate in cell death via necroptosis.

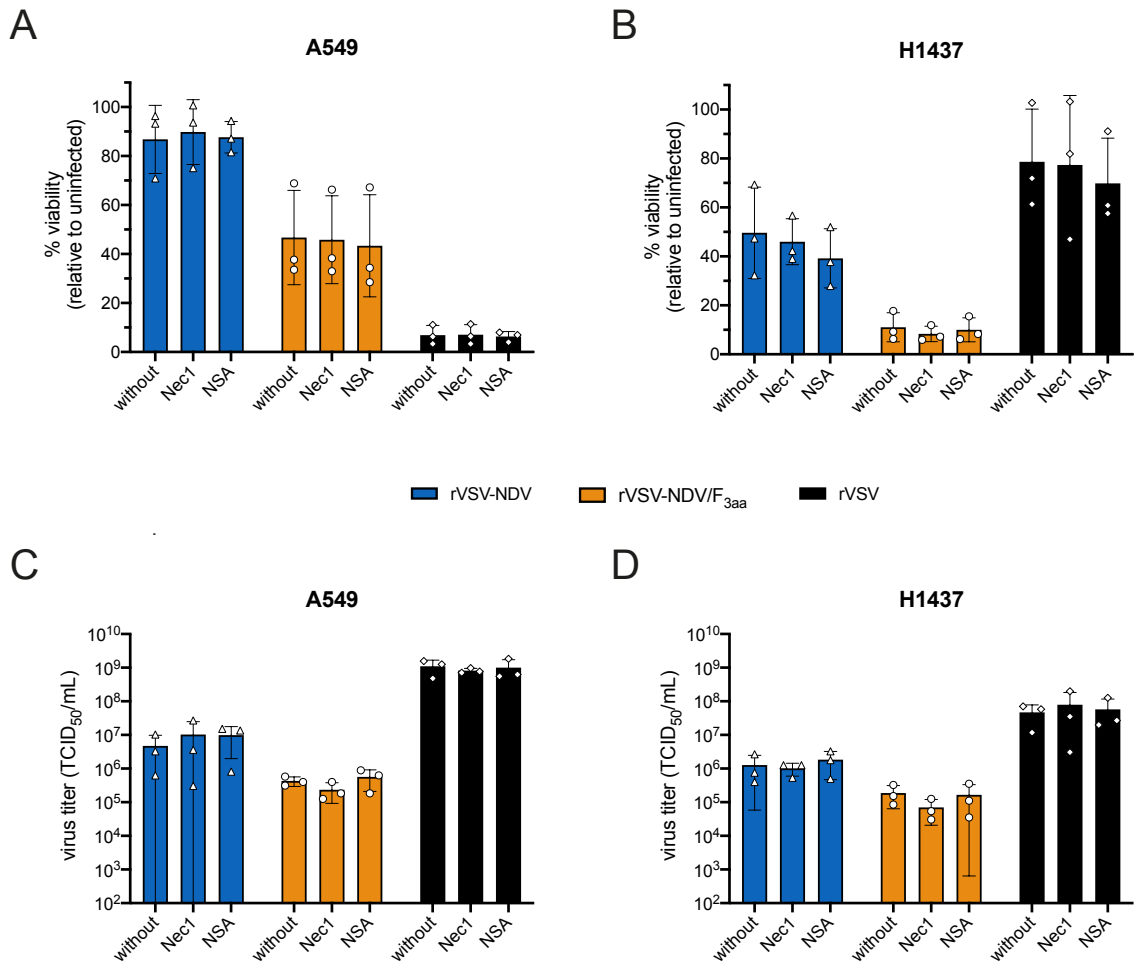

Figure 29. Oncolytic virus infection in A549 and H1437 cells in the presence of the necroptosis inhibitor Nec-1, or NSA

(**A**) A549 and (**B**) H1437 cells were pre-treated for 3 h with Nec-1 or NSA and infected at an MOI of 0.01 in the presence of the inhibitors. Cellular viability was measured at 48 hpi and expressed relative to untreated cells. (**C** and **D)** Virus replication was quantified from infectious supernatant by $TCID_{50}$ assay. Data is expressed as mean ± SD from n = 3 biological replicates.

3.1.5 Syncytial morphology and death can be altered by genetically manipulating the apoptosis or necroptosis pathway

Key regulators of apoptosis and necroptosis were knocked out using CRISPR/Cas9 in A549 and H1437 cells to further disentangle the complexity underlying a syncytial death. Single-cell knockout clones for caspase 3, caspase 8, RIPK1, RIPK3, and MLKL were generated as detailed in section 2.2.4.8, and successful gene deletion was validated by Western blot (**Figure 30**). Two polyclonal non-target control cell lines (NTCs) were generated for A549 and H1437 cells, respectively. The absence of detectable caspase 3, caspase 8, and RIPK1 could be clearly confirmed in both cell lines, but faint protein signals were obtained in the MLKL and RIPK3 knockout clones, respectively.

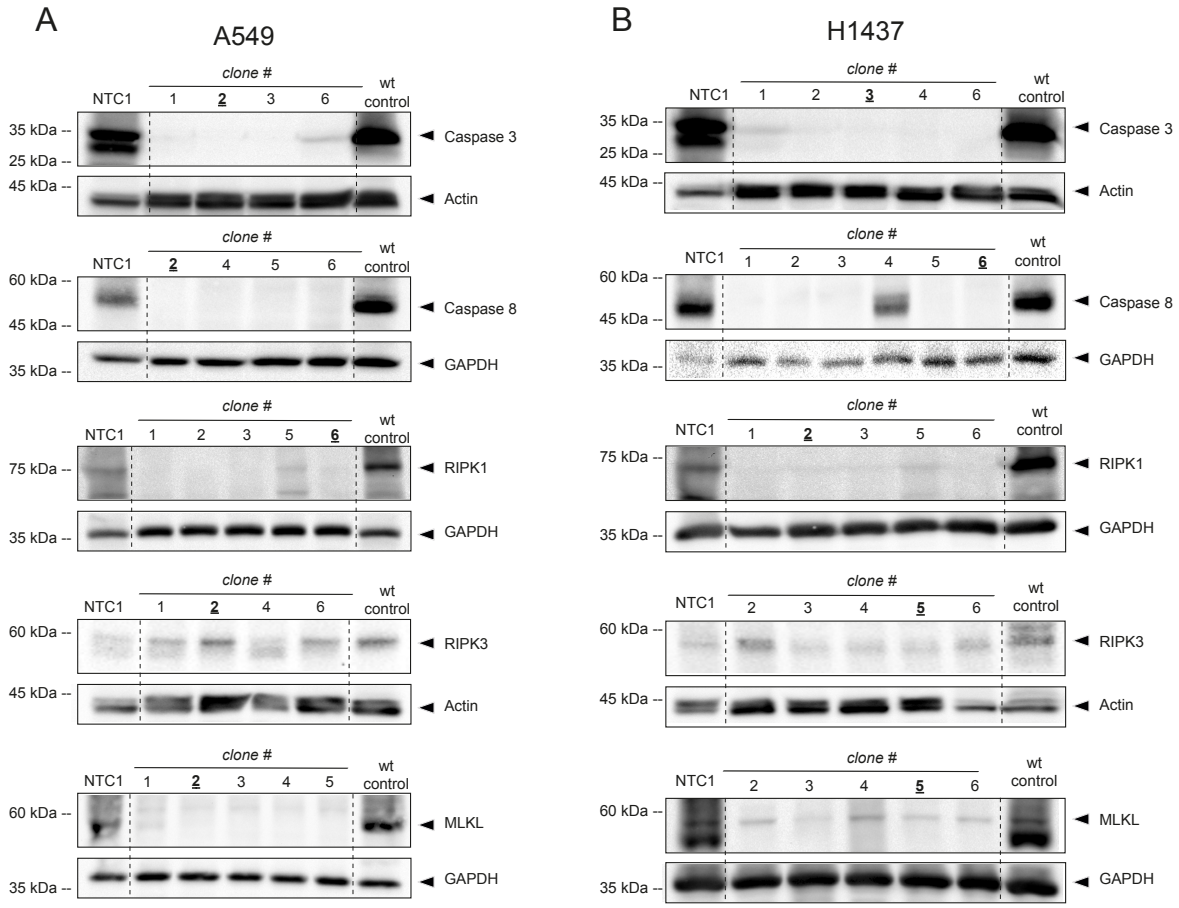

Figure 30. Western blot validation of CRISPR/Cas9 gene knockouts in A549 and H1437 single cell clones

Single-cell clones for each target gene were isolated under puromycin selection by limiting dilution and expanded. To validate successful gene knockout in (**A**) A549 and (**B**) H1437 cells, total protein was isolated from each knockout clone with RIPA buffer, followed by Western blot analysis using the corresponding antibodies listed in **Table 2**. Lysates from wildtype cells (wt control) and cells transduced with the NTC1 sgRNA were used as positive controls. The knockout clones that were chosen for subsequent experiments are underlined in bold. Shown are representative blots of n = 1 biological replicate. Arrow-heads on the left mark the expected protein bands. Protein ladder: ROTI®-Mark TRICOLOR Protein marker (for simplicity not shown).

To remediate the doubts, selected RIPK3 and MLKL knockout clones were validated by exon PCR, amplifying the CRISPR-targeted exons and subsequent Sanger sequencing to identify gene indels (insertion and deletions) in the exons. Distinct size differences of the PCR products between CRISPR knockout clones and NTCs or the appearance of additional smaller PCR amplicons already indicated the effectivity of the Cas9-mediated knockouts in A549 and H1437 cells (**Figure 31** A and B). Sequencing over the region of the CRISPR-targeted exon then clarified effective gene knockouts of RIPK3 and MLKL, respectively. An example alignment of the clonal sequences against the wildtype sequence for RIPK3 is visualized in **Figure 31** C for two A549 knockout clones for RIPK3 exon 2 and 6, respectively. Even though for some genes only one of two targeted exons was successfully hit, with the applied CRISPR/Cas9 knockout strategy, gene and protein perturbations in key regulators of the apoptosis and necroptosis death pathways were obtained in A549 and H1437 cells. Hence, the ability of the fusogenic and non-fusogenic viruses to replicate and trigger oncolysis in these knockout cells was tested by measuring viability and virus titers and recording changes in the CPEs using fluorescent microscopy.

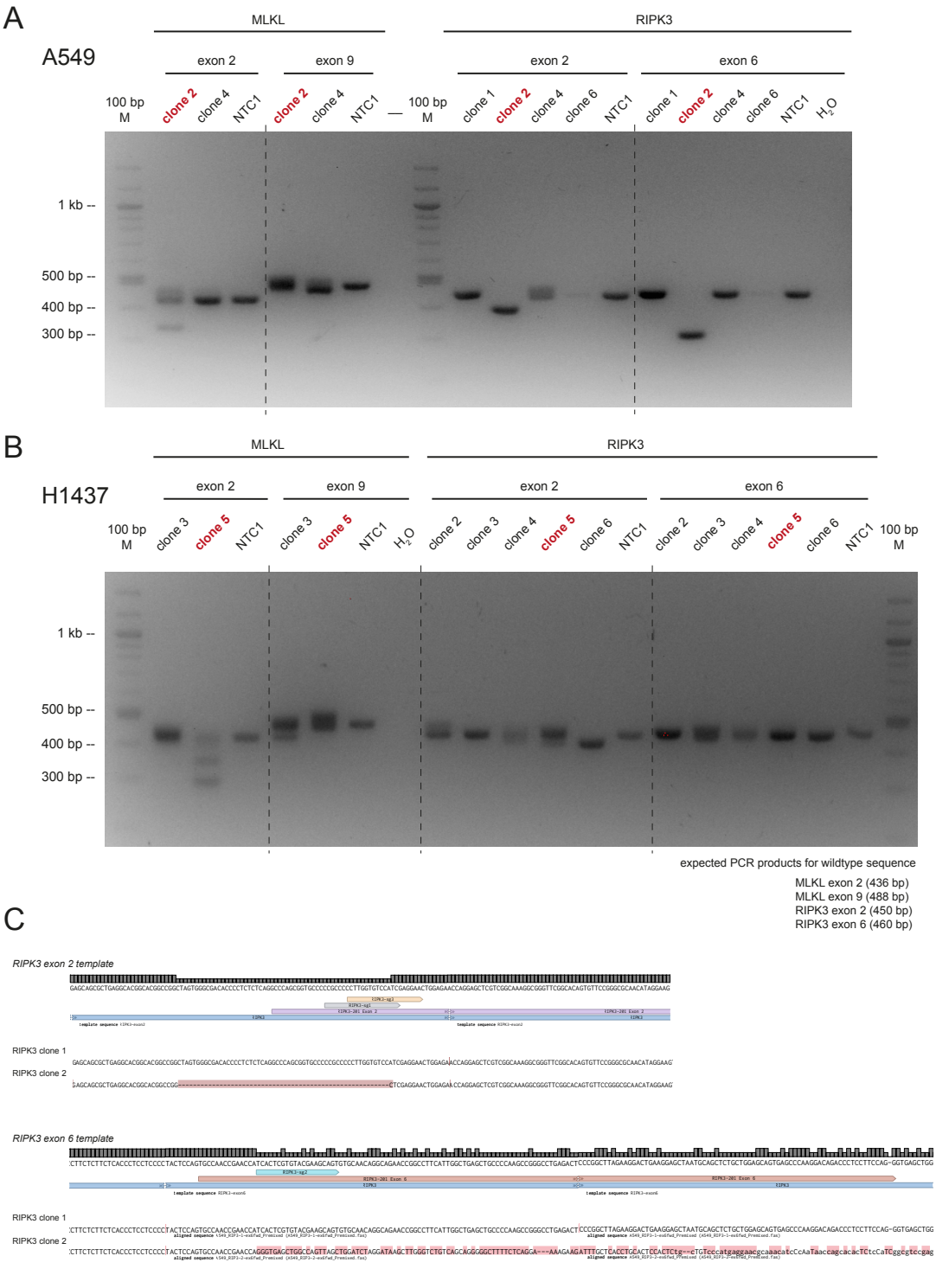

Figure 31. Exon PCR and sequencing validation of RIPK3$^{-/-}$ and MLKL$^{-/-}$ CRISPR/Cas9 gene knockouts in A549 and H1437 single-cell clones

Selected (**A**) A549 or (**B**) H1437 single cell clones were analyzed by PCR over the single-guide RNA-targeted exons and compared to wildtype or NTC1 cells. Unique primer pairs were designed to cover exon 2 or 6 of RIPK3 and exons 2 or 9 of MLKL. Expected PCR product sizes for the non-mutated exons are indicated in (B). Shown are representative agarose gels of n = 1 biological replicate. The knockout clones that were chosen for subsequent experiments are highlighted in bold red. M indicates the DNA size marker: 100 bp ladder (NEB); kb = kilobases, bp = base pairs. (**C**) Alignments from Sanger sequencing validation of the gene knockouts exemplified for A549 RIPK3 knockout clones 1 and 2, targeting exon 2 and 6, respectively. Sequencing alignments were analyzed with Benchling.com, similar to Liu et al [117]. sg1 and sg3 mark the single guide RNAs binding upstream of exon 2, and sg2 marks the single guide RNA binding exon 6 of RIPK3 gene. The dark red highlighted sections represent the gene mutations: base pair deletions and single nucleotide mismatches.

During a time course of 24 – 48 hpi, genetic deletion of caspase 3 or 8 in A549 cells infected with the fusogenic variants had no discernible effect on cellular viability compared to NTCs (**Figure 32** A). Solely viability at a later time of rVSV-NDV-mediated syncytia formation (72 hpi) appeared higher in the caspase 3 knockout line. Interestingly, viability of rVSV-infected A549 cells could be prolonged in both caspase knockouts, and especially in caspase $8^{-/-}$ cells, pointing to rVSV dependency on caspase-mediated apoptosis. In H1437 knockout cells, the following trends were observed: rVSV-NDV and rVSV-NDV/F_{3aa} depended on the presence of caspase 3, but less on the activity of caspase 8 to proceed their death program, which supports the idea of having both, apoptosis and necroptosis, pathways active in parallel (**Figure 32** B). A non-fusogenic death of H1437 cells by rVSV was characterized as primarily controlled by caspase 3.

Affected by the standard error of the $TCID_{50}$ method and unexpected variation between the two NTCs, no significant differences in rVSV-NDV, rVSV-NDV/F_{3aa} or rVSV virus titer were detectable from infected caspase 3 or caspase 8 knockouts of either, A549 or H1437 cells (**Figure 33**). This indicates that the OVs still maintain amplification and release of their virions independently of the two caspases and the altered death signaling.

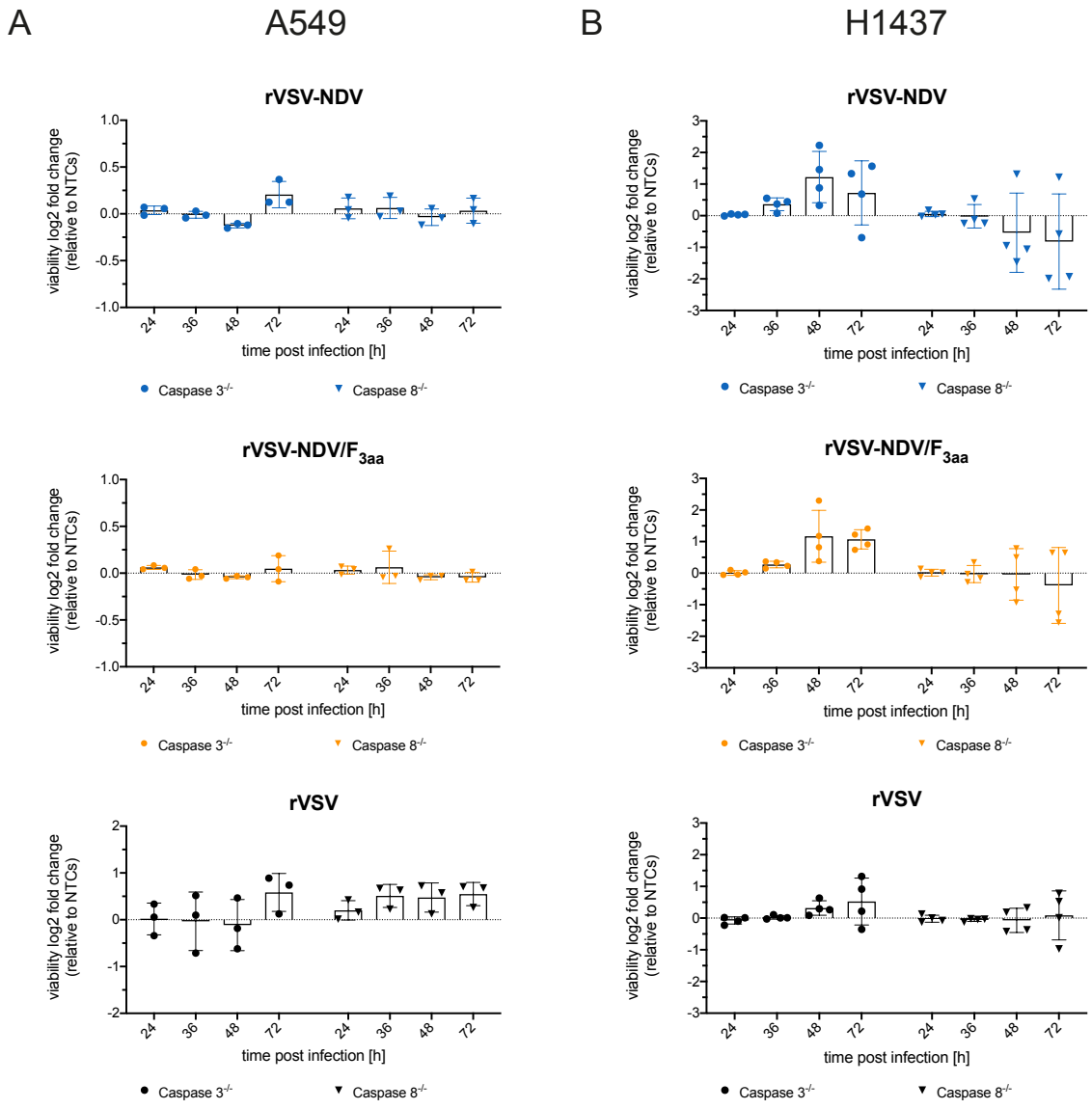

Figure 32. Log-2 fold change of cell viability in A549 and H1437 caspase 3 or caspase 8 knockout cells after OV infection

(**A**) A549 and (**B**) H1437 caspase 3 or caspase 8 knockout cells were infected at an MOI of 0.01, and changes in cell viability were measured by CellTiter-Glo® assay in a time course experiment. Viability data was normalized to untreated cells and then expressed as log-2 fold changes relative to the average of the NTCs. Plotted are mean ± SD values of n = 3 (A549) or n = 4 (H1437) independent biological replicates.

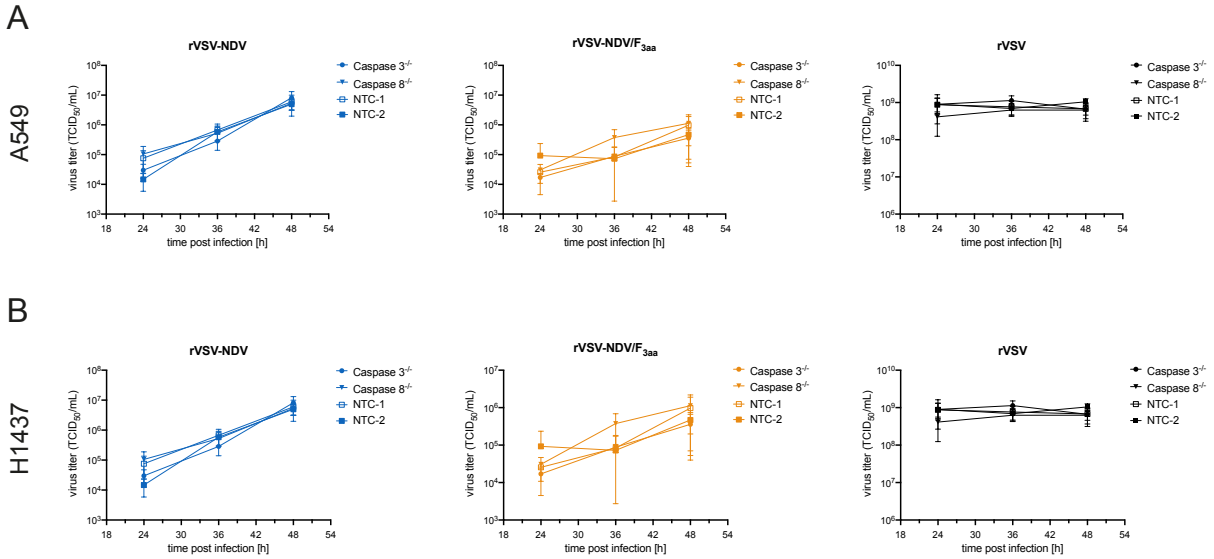

Figure 33. Time course of oncolytic virus replication in A549 and H1437 caspase 3 or caspase 8 knockout cell lines

(**A**) A549 and (**B**) H1437 caspase 3 or caspase 8 knockout cells were infected at an MOI of 0.01, and changes in viral replication were determined by measuring the extracellular virus concentration by $TCID_{50}$ assay. Virus concentrations were compared to the NTCs. Plotted are mean ± SD values of n = 3 independent biological replicates.

While the effects on replication were minimal, morphologic differences in virus-induced cytopathic effects are noteworthy. In both cell lines, the absence of caspase 3 resulted in a distinctive and longer persisting syncytial stage, apparent by enhanced virus-mediated GFP expression, and even caused rVSV-infected cells to form larger single cell rounding in A549 cells (**Figure 34**). In H1437 cells, with distinguishably weaker susceptibility to rVSV, the caspase 3 and caspase 8 knockout supported infection, apparent by earlier detection of GPF-positive cell islets. Syncytia formation was not completely abolished by caspase 8 deletion in H1437 cells, but resulted in smaller and more rapidly disappearing cell-cell fusions (**Figure 35**). This can be interpreted as a rapid switch of the death program to either intrinsic apoptosis or necroptosis and was also seen for non-fused, rVSV-infected cells.

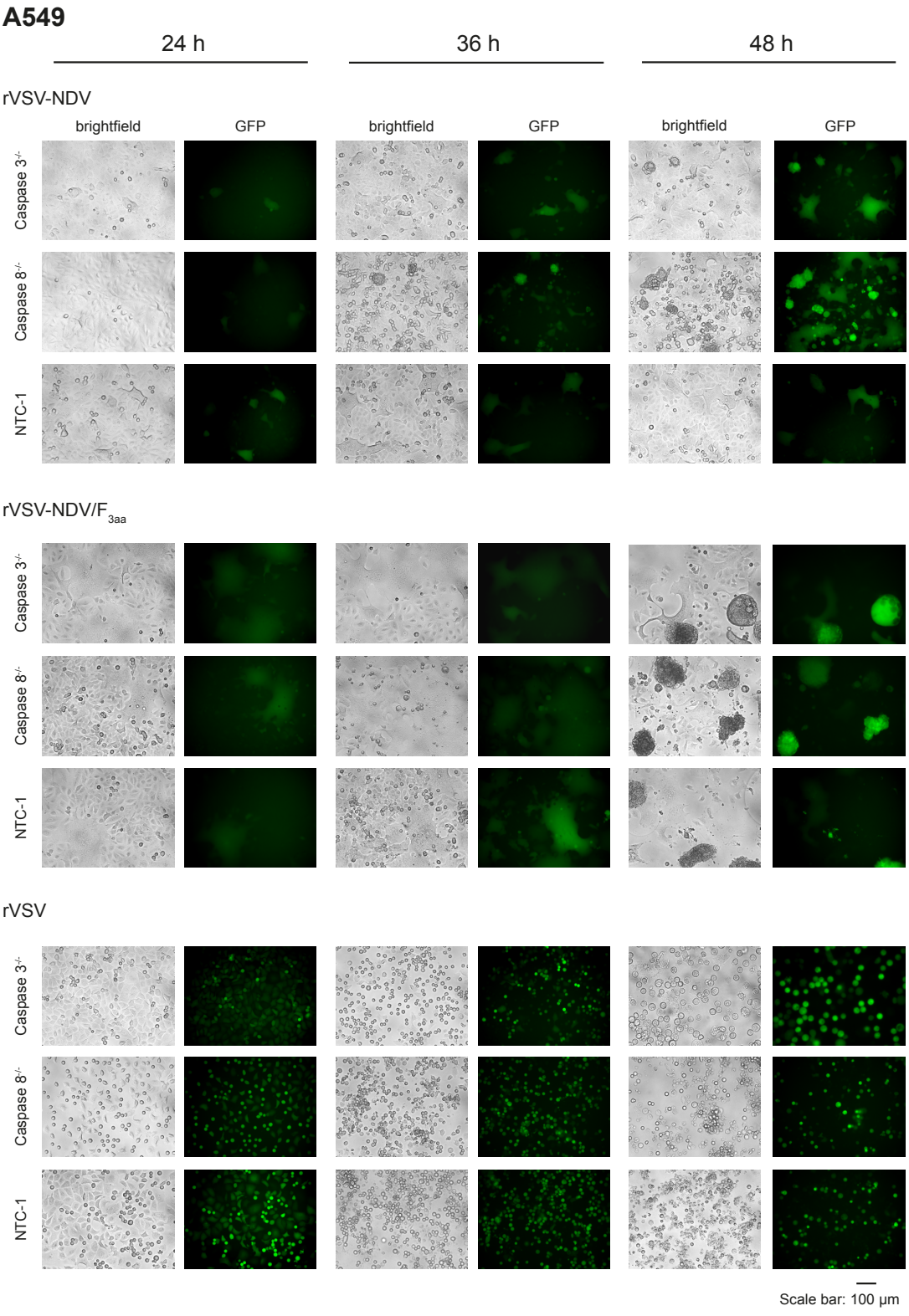

Figure 34. Fluorescent microscopy time course of OV-infected A549 caspase 3 or caspase 8 knockout cells

A549 caspase $3^{-/-}$ and caspase $8^{-/-}$ cells were infected at an MOI of 0.01 with GFP-expressing variants of the OVs, and cell morphology was monitored on a fluorescent microscope at 24, 36, and 48 hpi. Shown are representative brightfield and fluorescent images of n = 3 independent biological replicates. Images of the other NTC cell line (NTC-2) are shown in **Figure 38**.

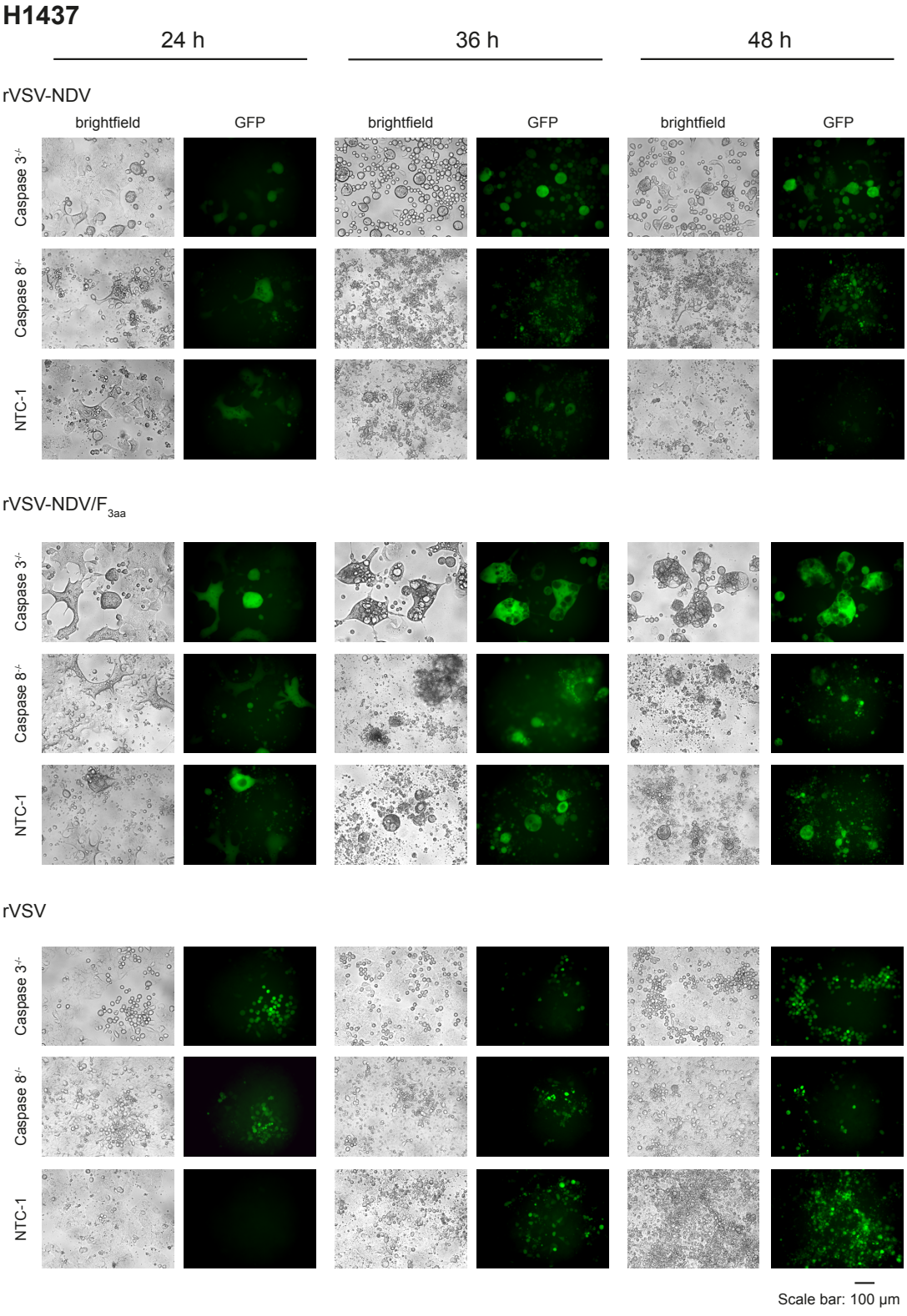

Figure 35. Fluorescent microscopy time course of OV-infected H1437 caspase 3 or caspase 8 knockout cells

H1437 caspase $3^{-/-}$ and caspase $8^{-/-}$ cells were infected at an MOI of 0.01 with GFP-expressing variants of the OVs, and cell morphology was monitored on a fluorescent microscope at 24, 36, and 48 hpi. Shown are representative brightfield and fluorescent images of n = 3 independent biological replicates. Images of the other NTC cell line (NTC-2) are shown in **Figure 39**.

Although the microscopic observations were not always mirrored in viability and $TCID_{50}$ readouts, experiments with caspase 3 and caspase 8 knockout lines indicated that all virus variants employ the cell's caspase machinery to induce oncolysis. However, to sustain particle release, cell lines encompass flexibility of alternating to caspase-independent cell death. Syncytia-forming rVSV-NDV and rVSV-NDV/F_{3aa}, that behaved much alike, may thus partly depend on the activity of caspase 8 to develop and maintain pronounced syncytia, while caspase 3 subsequently controls rupture of syncytia.

Based on these findings, the contribution of necroptosis to syncytia formation, maintenance, and death was next interrogated. To that end, RIPK1$^{-/-}$, RIPK3$^{-/-}$, and MLKL$^{-/-}$ cells of the A549 and H1437 background were generated, and OV infections were compared in these contexts. While genetic manipulation of necroptosis in A549 cells had a considerable effect on rVSV at all time points, the fusogenic viruses yielded variable trends only at specific time points. In A549 cells, perturbation of the necroptosis pathway boosted oncolysis of rVSV, especially in MLKL and RIPK3 knockout cells (**Figure 36** A), which indicates that involvement of the necrosome components, RIPK1, RIPK3, and MLKL, seems to be vastly irrelevant, or even counterproductive to oncolysis with non-fusogenic rVSV. As similar trends were detected in H1437 knockout cells (**Figure 36** B), the hypothesis of an rVSV-driven caspase-controlled death program is supported.

In contrast, a syncytial death by rVSV-NDV and rVSV-NDV/F_{3aa} was found to be dependent on the activity of RIPK1, RIPK3, and to a lesser extent on MLKL. Late in infection, when syncytia started to collapse, A549 and H1437 RIPK3$^{-/-}$ cells were more viable than the NTCs. As the same was true for H1437 RIPK1$^{-/-}$ cells, but opposing trends were observed in A549 RIPK1$^{-/-}$ cells, it can be deduced that H1437 cells required signaling of the RIP kinases to fulfill a necroptotic virus-mediated death. Thereby, MLKL is probably not the only factor in proceeding oncolysis by membrane poration; instead, the results in H1437 cells show a possible switch to another syncytia destroying pathway

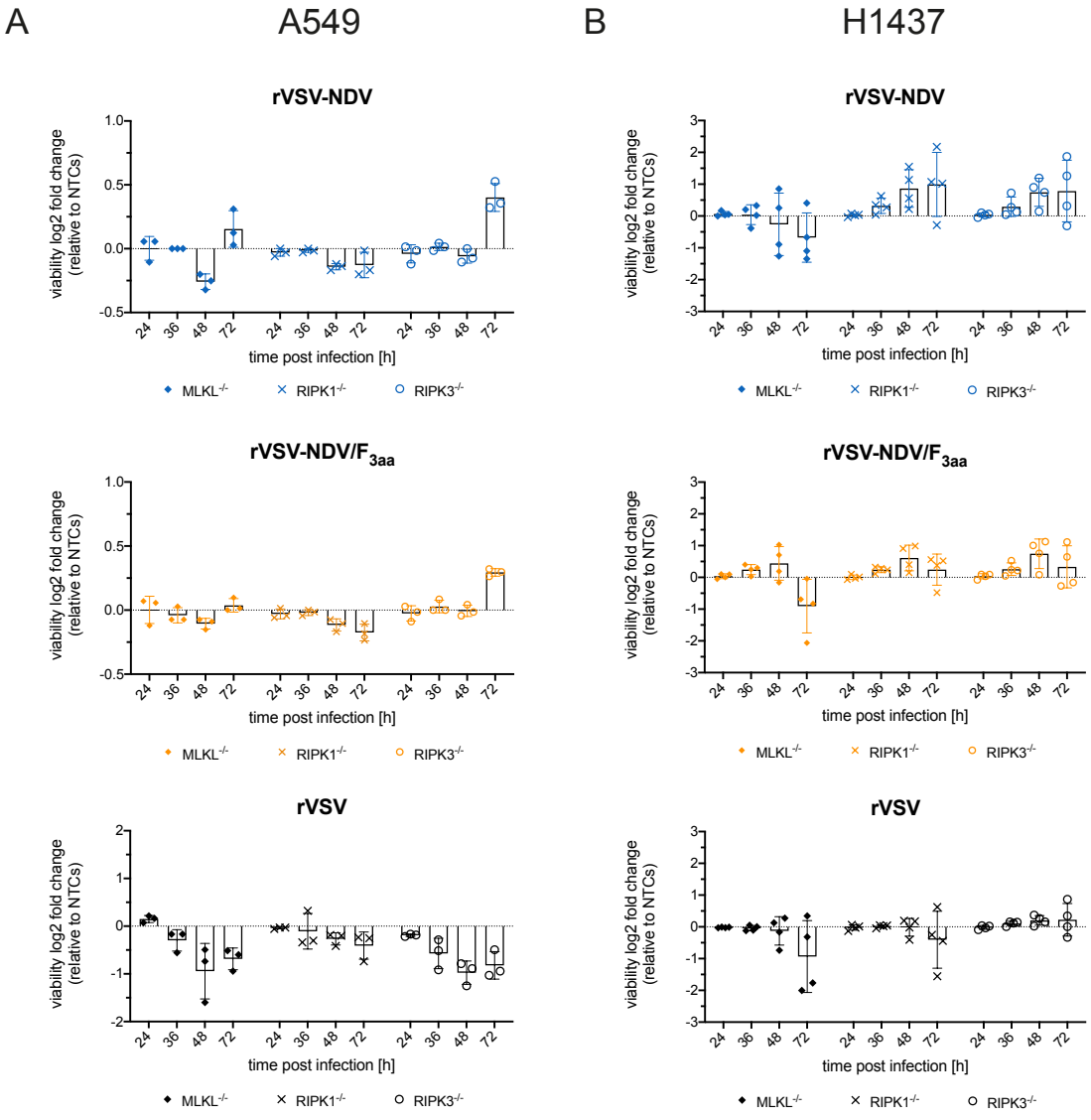

Figure 36. Log-2 fold change in cell viability in A549 and H1437 RIPK1, RIPK3, or MLKL knockout cells after OV infection

(**A**) A549 and (**B**) H1437 RIPK1$^{-/-}$, RIPK3$^{-/-}$ and MLKL$^{-/-}$ cells were infected at an MOI of 0.01, and changes in cell viability were measured by CellTiter-Glo® assay in a time course experiment. Viability data was normalized to untreated cells and then expressed as log-2-fold changes relative to the average of the NTCs. Plotted are mean ± SD values of n = 3 (A549) or n = 4 (H1437) biological replicates.

Investigating virus replication in the context of the necroptosis knockout cells, trends in A549 cells were mostly inconsistent between the NTCs and the biological replicates (**Figure 37** A). rVSV-NDV/F_{3aa} had a small but reproducible increase in titers in RIPK1$^{-/-}$ cells, while a slight reduction was quantifiable from RIPK3$^{-/-}$ cells, which matches with the trends seen in syncytia-mediated cytotoxicity described in previous sections. Masked by high variation in the $TCID_{50}$ values, RIPK1 and RIPK3 knockouts had no effect on rVSV-NDV replication. Because RIPK1 is ubiquitously involved in upstream apoptosis and necroptosis signaling, a clear conclusion cannot be made on its role during syncytial death.

The absence of MLKL had a highly variable influence on either of the tested viruses so that the trends seen in RIPK3$^{-/-}$ are not automatically attributable to a clear involvement of necroptosis in A549 syncytial death. Even though the viability data indicated an independence of rVSV oncolysis on necrosome components, a direct link to viral replication could not be drawn for A549 cells.

In H1437 cells (**Figure 37** B), RIPK1, RIPK3, and MLKL gene knockouts attained no clear trends on viral replication compared to the NTCs. Hence, necroptosis-mediated syncytial death and release of new virions in H1437 cells may just partly depend on functional RIPK1-RIPK3 interaction and downstream phosphorylation of MLKL by RIPK3. With the exception of a slight increase in early (24 hpi) rVSV replication in A549 and H1437 MLKL$^{-/-}$ cells, manipulation of either of the RIP-kinases had no significant effect on rVSV virus concentrations. The dynamic, sometimes time-point-dependent, effects of RIPK1, RIPK3, or MLKL knockouts highlight the complexity of the underlying death pathway leading to syncytial death. Nevertheless, the data has shown that death signaling in both cell lines can be altered and pushed in favor of either apoptosis, necroptosis, or another non-characterized death pathway.

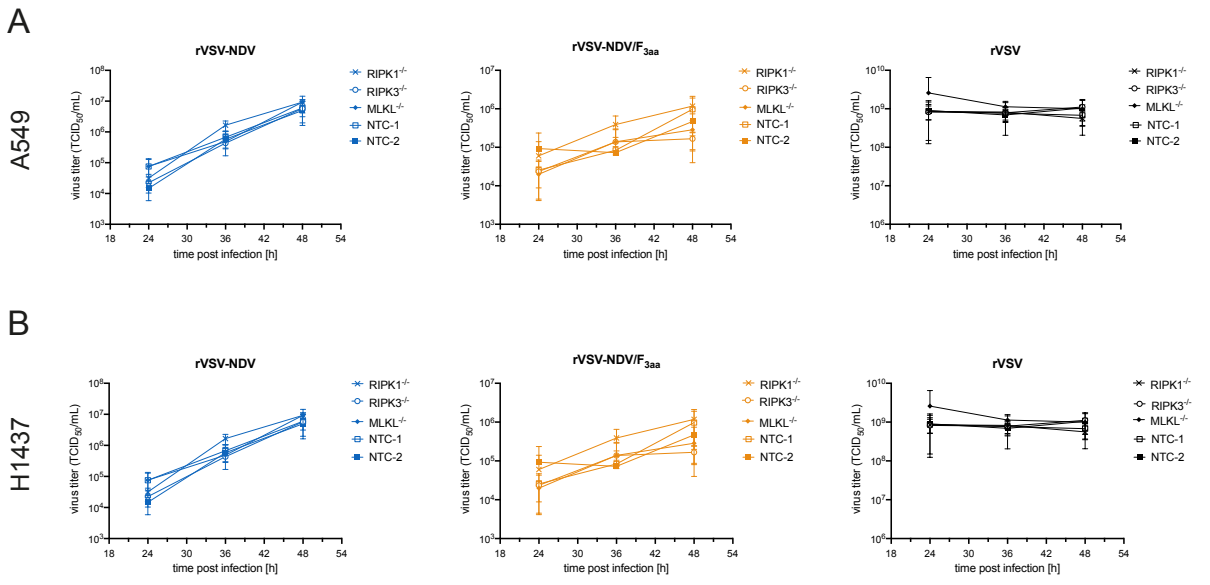

Figure 37. Time course of oncolytic virus replication in A549 and H1437 RIPK1, RIPK3, or MLKL knockout cell lines

(**A**) A549 and (**B**) H1437 RIPK1$^{-/-}$, RIPK3$^{-/-}$ and MLKL$^{-/-}$ cells were infected at an MOI of 0.01, and changes in viral replication were determined by measuring the extracellular virus concentration by $TCID_{50}$ assay. Virus concentrations were compared to the NTCs. Plotted are mean ± SD values of n = 3 independent biological replicates.

The question remained, whether RIPK1, RIPK3, or MLKL knockouts changed the syncytial phenotype and whether these morphologic differences could hint to the predominant death signaling. The quickest death progression among all virus variants was visually noticed in MLKL$^{-/-}$ A549 cells (**Figure 38**). rVSV-NDV and rVSV-NDV/F_{3aa} formed syncytia that were visually unlike the above-described "*blur of color*" phenotype, rather rapidly rounded up and burst in a "*bubbly*" phenotype, which resembled apoptotic bodies. NTC cells, as well as RIPK1 and RIPK3 knockout cells, showed a mixed phenotype of bursting cells and larger spanning syncytia with a rather faintly distributed GFP signal. rVSV-infected RIPK1 and RIPK3 knockouts had strong morphologic similarity to NTCs and; thus, further confirming that necroptosis is not the predominant cell death pathway utilized in rVSV-mediated oncolysis.

Similarly, in H1437 cells, syncytial death appeared to be most progressed in MLKL$^{-/-}$ and slower developing in RIPK3$^{-/-}$ background, whereas RIPK1$^{-/-}$ cells showed no discernable difference to NTC (**Figure 39**). Morphological abnormalities in syncytia expansion or lysis were not apparent. Trends in rVSV-infected H1437 knockout cells were alike with early detection of GFP-positive cells in MLKL$^{-/-}$ and a delayed advancement of cell death in the absence of RIPK3.

In conclusion, OV infection in RIPK1, RIPK3 or MLKL knockout cells maintained the virus-induced cell killing capability but altered fusogenicity, as evident by the morphological differences to NTCs. This likely triggered a dynamic but partial activation of necroptosis, in which syncytial death is ultimately overtaken by other, presumably apoptotic, death signaling routes. Taken together, a unique determinant of the syncytial death program could not be found, as the fusogenic OVs instead provoke a tight and intricate interplay of both apoptotic and necroptotic signaling. Beyond that, as the results demonstrate, both cell lines characteristically responded to the gene knockouts and individual virus infections.

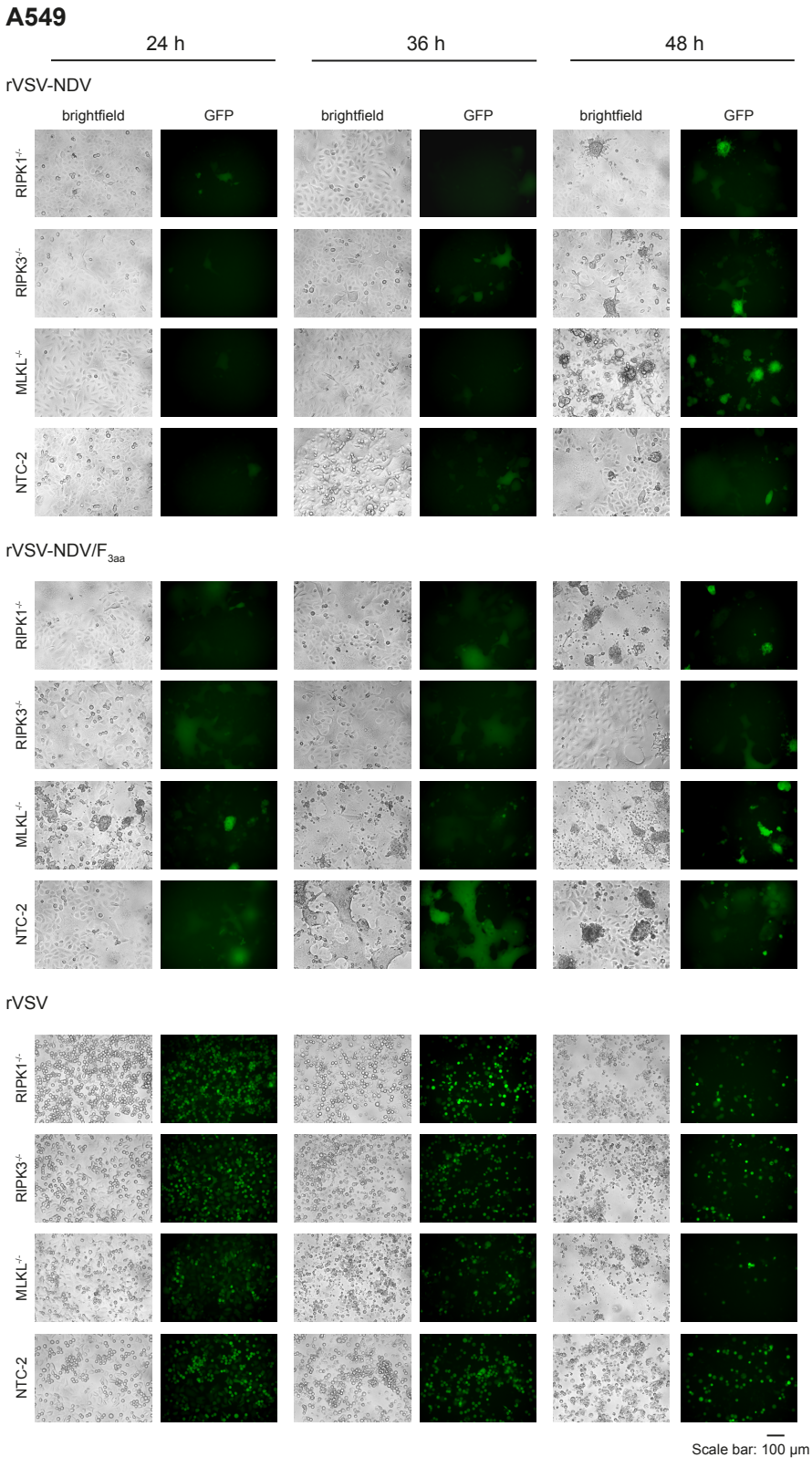

Figure 38. Fluorescent microscopy time course of OV-infected A549 RIPK1, RIPK3, or MLKL knockout cells

A549 RIPK1$^{-/-}$, RIPK3$^{-/-}$ and MLKL$^{-/-}$ cells were infected at an MOI of 0.01 with GFP-expressing variants of the OVs, and cell morphology was monitored on a fluorescent microscope at 24, 36, and 48 hpi. Shown are representative brightfield and fluorescent images of n = 3 independent biological replicates. Images of the other NTC cell line (NTC-1) are shown in **Figure 34**.

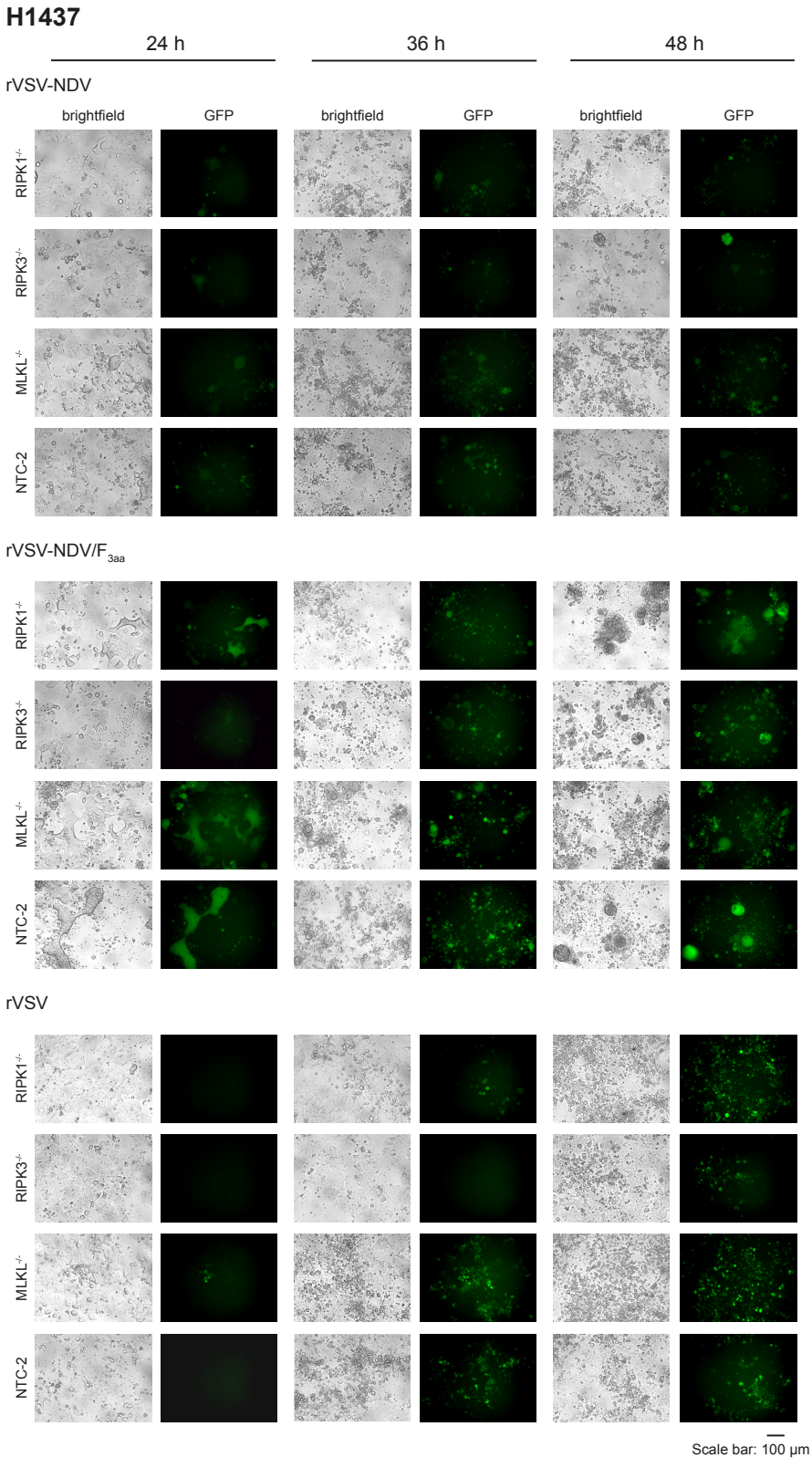

Figure 39. Fluorescent microscopy time course of OV-infected H1437 RIPK1, RIPK3, or MLKL knockout cells

H1437 RIPK1$^{-/-}$, RIPK3$^{-/-}$ and MLKL$^{-/-}$ cells were infected at an MOI of 0.01 with GFP-expressing variants of the OVs, and cell morphology was monitored on a fluorescent microscope at 24, 36, and 48 hpi. S Shown are representative brightfield and fluorescent images of n = 3 independent biological replicates. Images of the other NTC cell line (NTC-1) are shown in **Figure 35**.

In order to investigate the cell line-dependence of these effects further, similar infections were performed in murine B16-OVA caspase 3 and MLKL knockout cells and compared to B16-OVA wildtype cells, which have been previously characterized as highly susceptible to rVSV-NDV-mediated killing [41]. When these B16 knockout lines were infected with the respective virus variants, an intriguing and striking difference in syncytia morphology triggered by caspase 3 and MLKL knockouts was observed (**Figure 40** A). A wide-spanning syncytia network was induced by rVSV-NDV and rVSV-NDV/F_{3aa} in caspase $3^{-/-}$ cells, whereas in the absence of MLKL, B16 cells failed to form obvious syncytia and mainly died by rounding. As rVSV died by classical and indistinguishable cell rounding effects regardless of the knockout situation, the phenotypic observations were specific to the syncytia formation capability of the fusogenic variants. These effects were also reflected in the corresponding quantification of cytotoxicity, as determined by LDH assay. Wildtype B16 cells achieved approximately 75 % cell killing at 32 hpi, but in caspase $3^{-/-}$ cells, effective cell killing was abrogated in an MOI-dependent fashion (**Figure 40** B). Cytotoxicity in rVSV-infected cells was not significantly impaired by either caspase 3 or MLKL knockout. Moreover, the unique cell rounding in rVSV-NDV- and rVSV-NDV/F_{3aa}-infected B16 $MLKL^{-/-}$ cells did not correlate with a statistically significant increase in cytotoxicity.

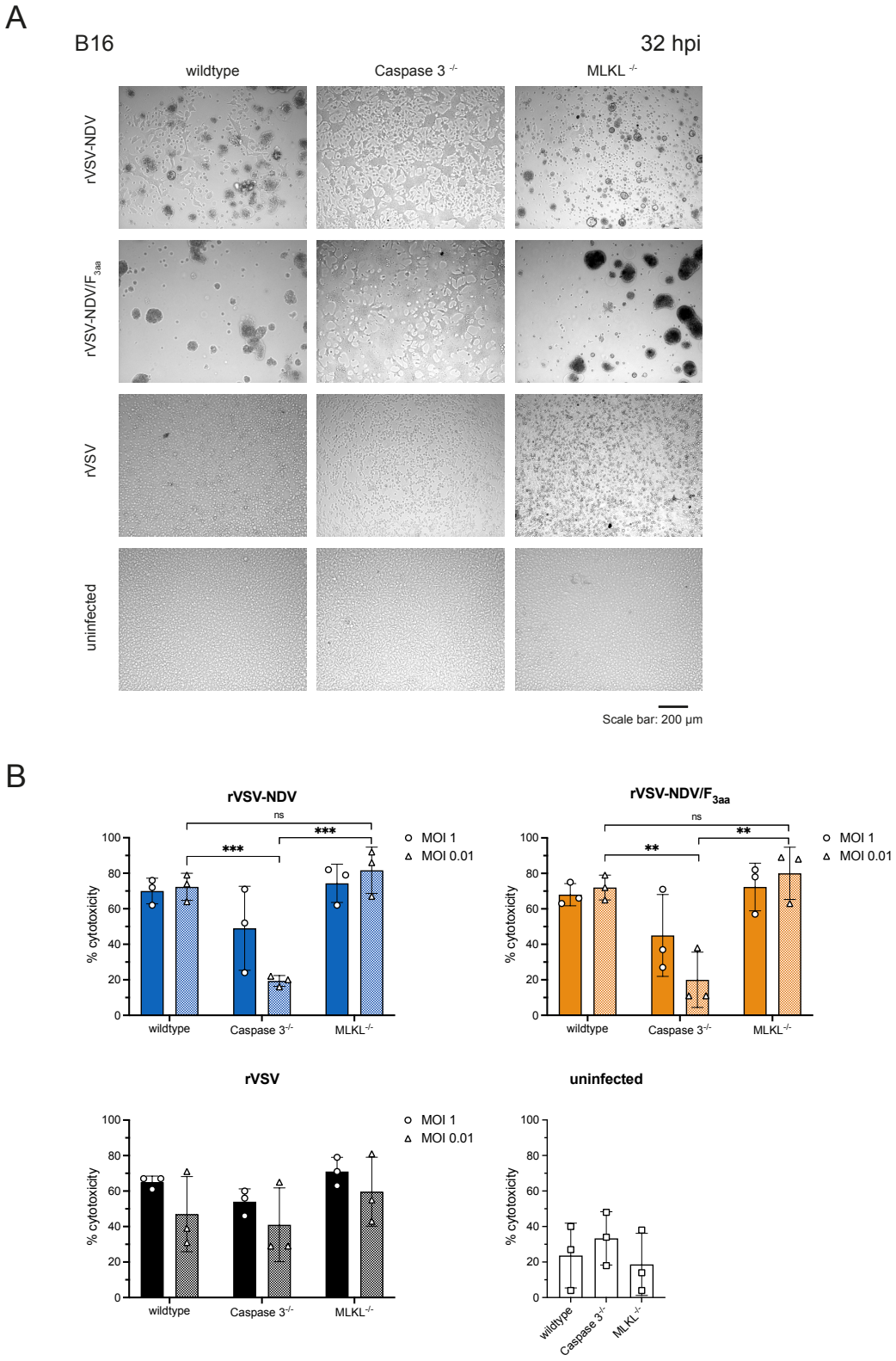

Figure 40. Oncolytic effects in murine B16 caspase 3 or MLKL knockout cells

(**A**) B16-OVA wildtype, caspase $3^{-/-}$, or $MLKL^{-/-}$ cells were infected with the OV variants at MOI of 0.01, and cytopathic effects were captured by microscopy at 32 hpi. (**B**) Cytotoxicity was measured using the LDH assay at 32 hpi and comparing OV infection at an MOI of 1 and 0,01. Shown are representative brightfield images and data from n = 3 independent biological replicates. Cytotoxicity values are expressed as mean ± SD % cytotoxicity, relative to the maximum release control (100 % cytotoxicity). Statistical significance was calculated using one-way ANOVA with Tukey's multiple comparisons test (ns = non-significant, **p ≤ 0.01, ***p ≤ 0.001).

The death process in B16 knockout lines was then further challenged by the addition of the pan-caspase inhibitor zVAD in a prototype experimental setup, with just using rVSV-NDV and monitoring infection by microscopy (**Figure 41**). The combination of genetic and pharmacological inhibition of caspase-mediated apoptosis revealed an even more pronounced network of syncytia that persisted until 72 hpi, a time point at which wildtype B16 cells (+ zVAD) or caspase $3^{-/-}$ cells (without inhibitor) were already dead. Interestingly, zVAD also slightly delayed the death kinetics of $MLKL^{-/-}$ cells. The underlying death process in rVSV-NDV-infected B16 cells, thus, likely involved both necroptotic and apoptotic signaling. Next to MLKL as a potential mediator of syncytial membrane pore formation, especially the executioner caspase 3, seemed to effectuate syncytia destruction; because otherwise, expanded syncytia, as seen in the B16 knockout cells, would not persist for such a long time.

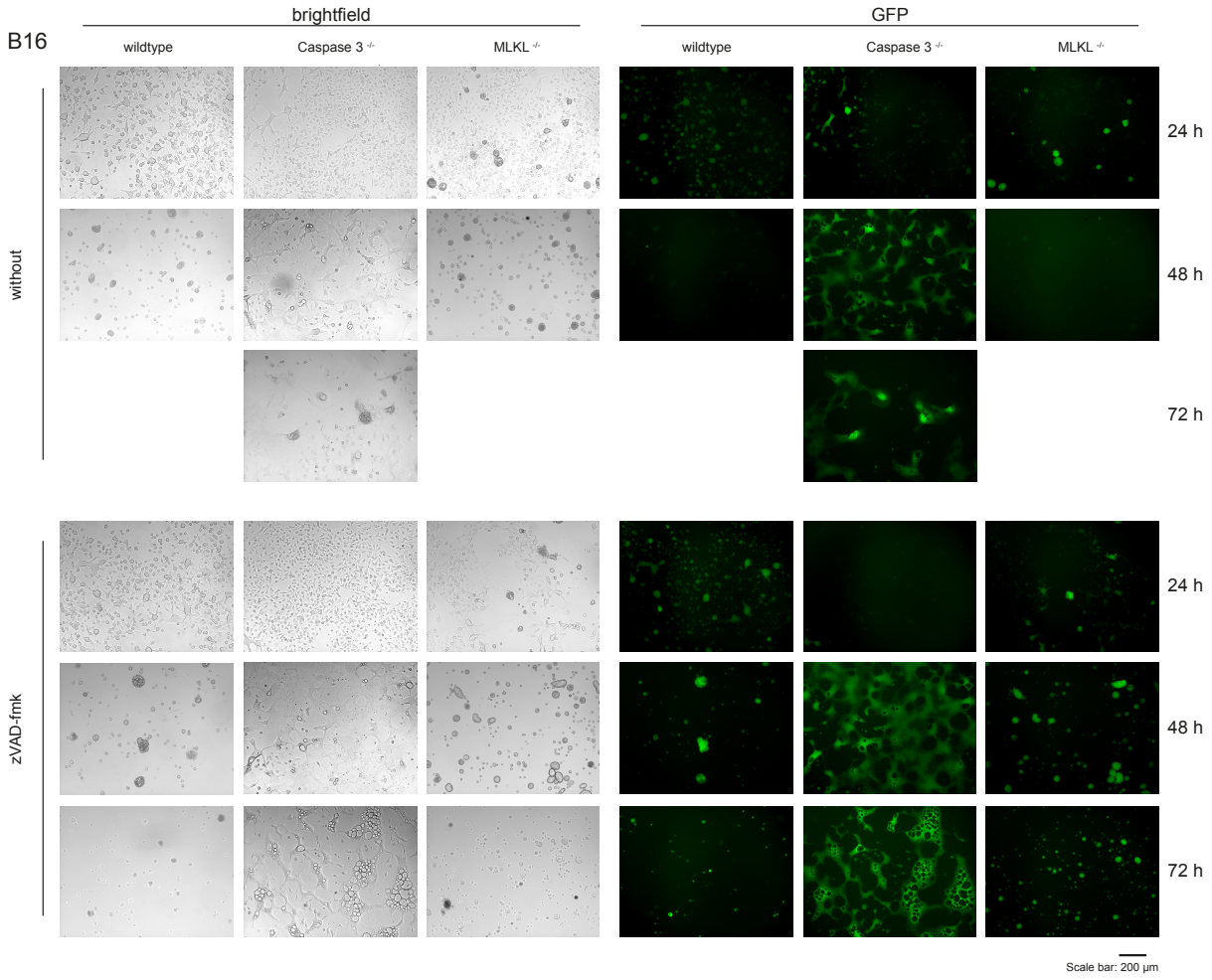

Figure 41. B16 caspase 3 or MLKL knockout cell infection in combination with pan-Caspase inhibition by zVAD

B16-OVA wildtype, caspase $3^{-/-}$, or $MLKL^{-/-}$ cells were infected with rVSV-NDV at an MOI of 0.01 and treated with pan-caspase inhibitor zVAD concomitant to infection. Cell killing was monitored by brightfield and fluorescent microscopy at 24, 48, and 72 hpi. Shown are representative images of n = 1 biological replicate. Images for wildtype and $MLKL^{-/-}$ cells at 72 hpi were not recorded in this scouting experiment because cells already had reached complete death at 48 hpi.

3.2 Fusogenic viruses are potent immunogenic cell death inducers

3.2.1 Oncolytic virus infection in A549 and H1437 cells triggered DAMP release

Besides the mechanistic complexity of syncytial cell death, which requires additional in-depth investigation of other cell death regulators, one key aspect of a promising OV therapy remains to be characterized: immunogenicity. In previous work in human HCC or murine melanoma, the hybrid virus rVSV-NDV already demonstrated great potential as an inducer of an immunogenic type of death [40-42]; however, an underlying mechanism could not yet be defined. Therefore, another aim of this project was to clarify whether the fusogenicity of rVSV-NDV or rVSV-NDV/F_{3aa} determines an effective immunogenic cell death.
ICD is identified by the release of DAMPs and TAAs from dying tumor cells, which are sensed *in vivo* by surrounding immune cells and elicit a strong, inflammatory anti-tumor immune response [79]. Initially, it was questioned to what extent OV-infected A549 and H1437 cells release immunogenic DAMPs, including Hsp70, Hsp90, HMGB1, extracellular ATP, as well as calreticulin, and whether differences arise between the fusogenic variants.
In a time course experiment, Western blot analysis of concentrated supernatants from infected cells was applied to quantify Hsp70, Hsp90, HMGB1, and extracellular calreticulin protein levels. With a strong magnitude of effect, A549 (**Figure 42**) and H1437 (**Figure 43**) cells effectively accumulated and released the ICD markers over the course of infection, much more than the MTX-treated control. However, even though the representative blots (in A) may indicate subtle differences, protein quantification relative to total protein was affected by inter-experimental variation, and hence, no significant differences between the virus variants could be obtained from the quantified DAMP signals; although, a general trend in A549 cells indicated an increase in DAMPs in response to infection with the fusogenic viruses.

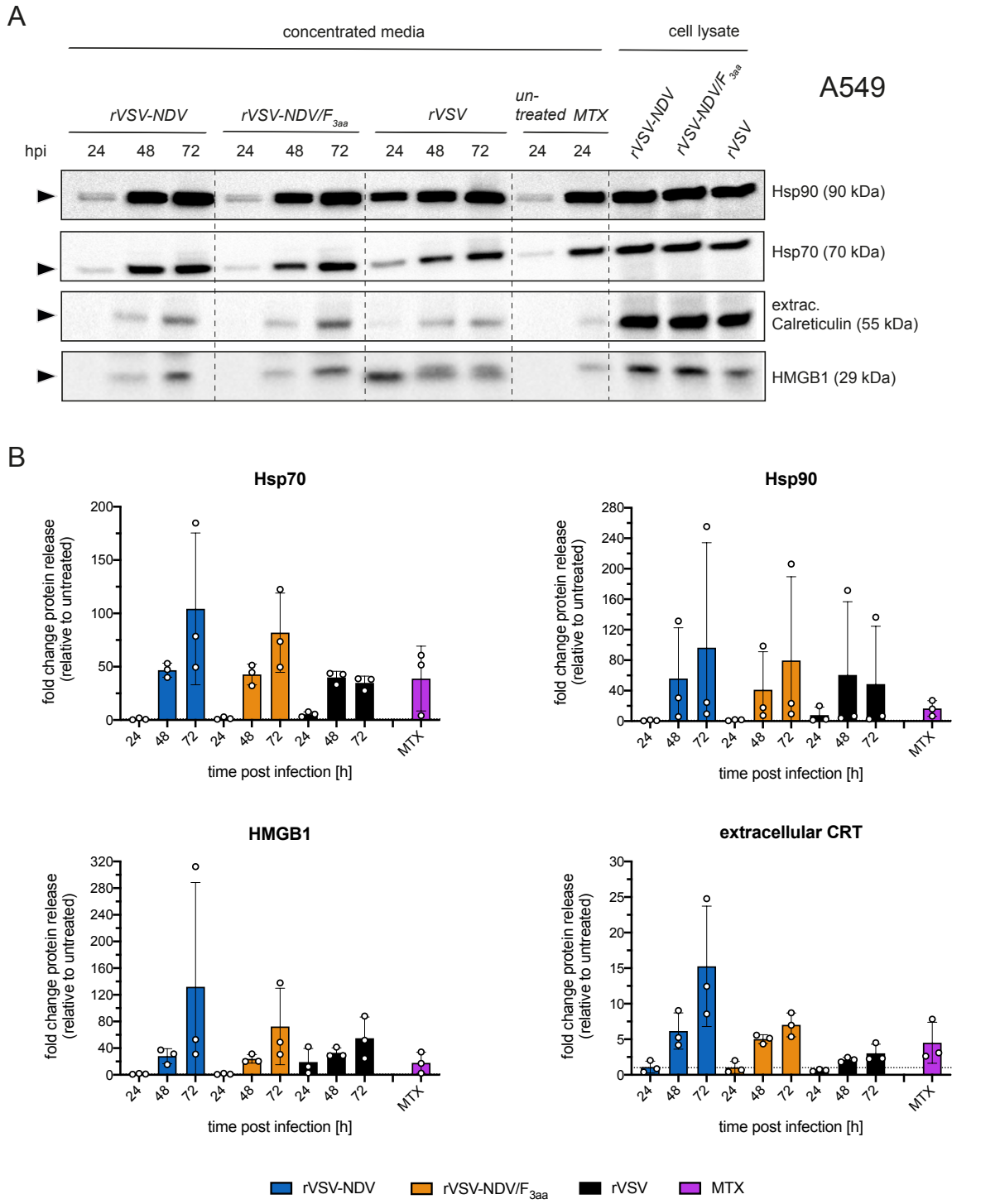

Figure 42. Western blot detection of released immunogenic cell death markers from supernatant of OV-infected A549 cells

A549 cells were infected at an MOI of 0.01, and protein from supernatants was concentrated at the respective time points and analyzed by Western blot for the expression of Hsp70, Hsp90, HMGB1, and released CRT using the corresponding antibodies listed in **Table 2**. (**A**) One representative blot of the time course infection experiments compared to MTX (2 µM) treatment as an ICD inducer control is shown. Arrow-heads on the left mark the quantified protein bands. Protein ladder: ROTI®-Mark TRICOLOR Protein marker (for simplicity not shown). (**B**) Hsp70, Hsp90, HMGB1, and released CRT protein bands were quantified relative to the Ponceau-S total protein staining (in each lane) and are expressed as protein release fold change relative to untreated cells. Shown are mean ± SD values of n = 3 independent biological replicates.

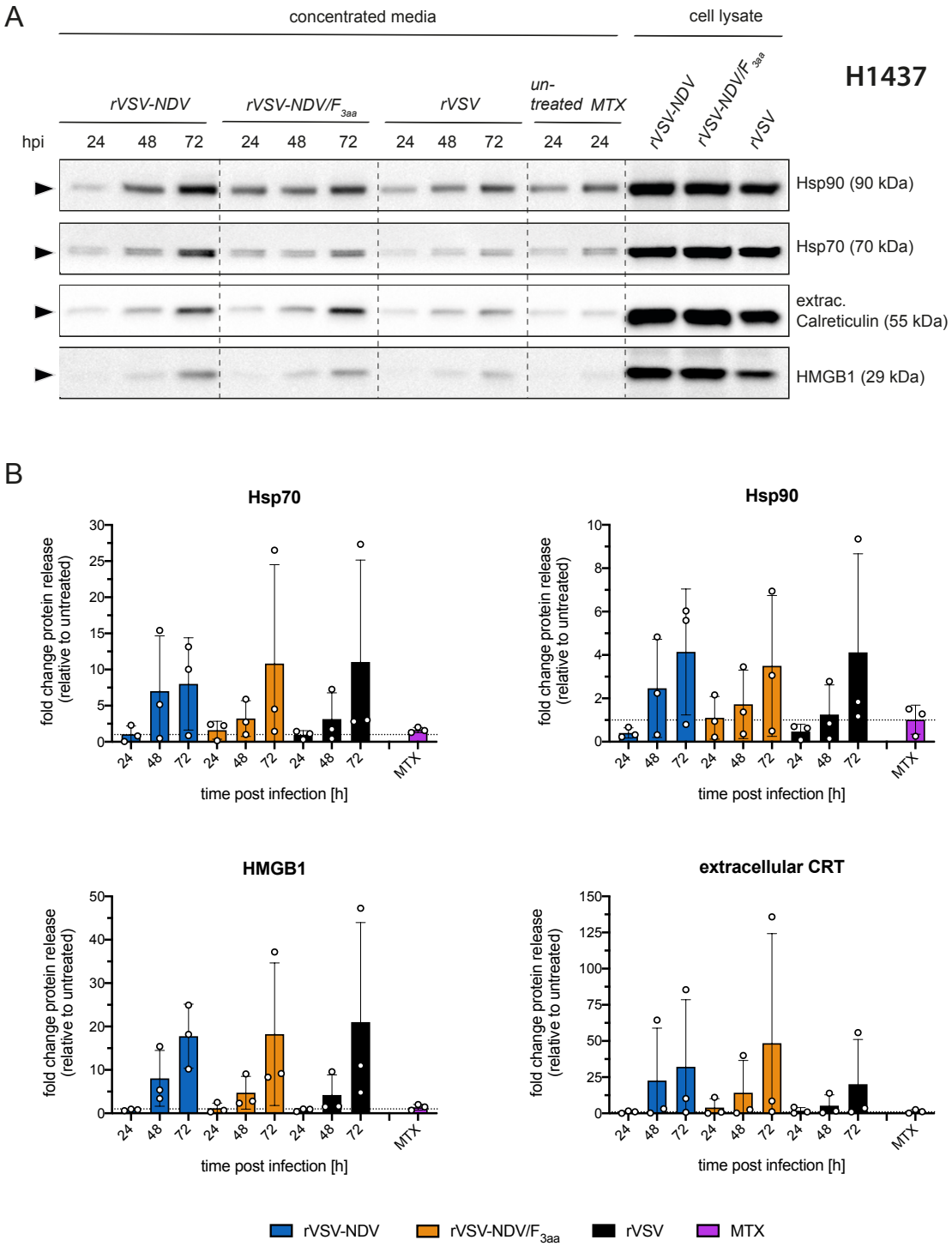

Figure 43. Western blot detection of released immunogenic cell death markers from supernatant of OV-infected H1437 cells

H1437 cells were infected at an MOI of 0.01, and protein from supernatants was concentrated at the respective time points and analyzed by Western blot for the expression of Hsp70, Hsp90, HMGB1, and released CRT using the corresponding antibodies listed in **Table 2**. (**A**) One representative blot of the time course infection experiments compared to MTX (2 µM) treatment as an ICD inducer control is shown. Arrow-heads on the left mark the quantified protein bands. Protein ladder: ROTI®-Mark TRICOLOR Protein marker (for simplicity not shown). (**B**) Hsp70, Hsp90, HMGB1, and released CRT protein bands were quantified relative to the Ponceau-S total protein staining (in each lane) and are expressed as protein release fold change relative to untreated cells. Shown are mean ± SD values of n = 3 independent biological replicates.

Release of CRT to the extracellular space as a marker for ICD has been reported in the context of apoptotic cell phagocytosis by macrophages [138]; however, much more commonly, CRT is described as being exposed from the ER compartment onto the cell surface of dying cells as a typical "*eat-me*" signal. Therefore, a protocol for the quantification of surface-exposed CRT by flow cytometry was designed, and the percentage of live, CRT-positive A549 or H1437 cells was determined (**Figure 44**). In both cell lines, the individual OVs triggered the surface translocation of CRT, whereby only the fusogenic variants did so in an MOI-dependent manner. In A549 cells, this might be attributable to the higher susceptibility to rVSV infection, meaning rVSV had already triggered saturation of CRT exposure, irrespective of the MOI. In contrast, A549 cells infected with the fusogenic variants exhibited a more gradual build-up of surface calreticulin. In H1437 cells, dose-responses of the fusogenic variants were less pronounced but at a higher viral input (MOI 0.1), the fusogenic variants rVSV-NDV and rVSV-NDV/F_{3aa} generated a presumably larger population of CRT exposing cells than rVSV; however, with no statistically significant difference.

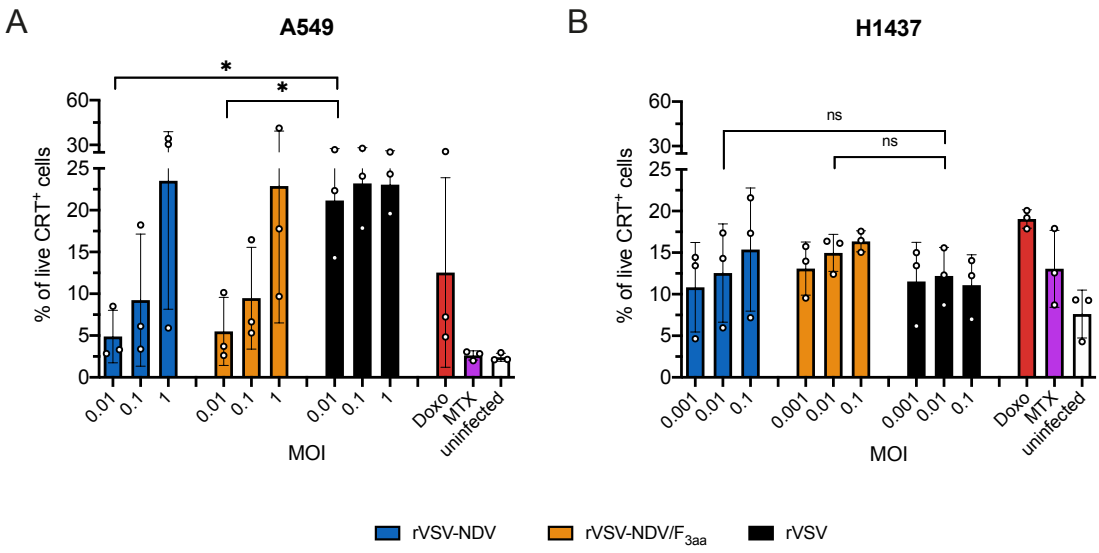

Figure 44. Flow cytometry-based quantification of calreticulin cell surface exposure in OV-infected A549 and H1437 cells

(**A**) A549 and (**B**) H1437 cells were infected with three MOIs of the particular OVs, and 24 hpi cells were harvested for indirect flow cytometry staining of human Calreticulin using the antibodies listed in **Table 2**. MTX (2 µM) or Doxo (2 µM) were used as positive controls. Data is calculated as % CRT positive cells among live cells and represented as mean ± SD of n = 3 independent biological replicates. Statistical significance was tested using one-way ANOVA with Tukey's multiple comparisons test (ns = non-significant, *p ≤ 0.05).

To complement the picture of induced ICD markers, the release of ATP from OV-infected cells was explored using the ATP Bioluminescence Assay Kit. In A549 cells (**Figure 45** A), detectable ATP concentrations were nearly 10 times lower than in H1437 cells (**Figure 45** B), but with a few exceptions, the ATP release kinetics fit with the infectibility of the respective cell lines and led to more ATP release than the ICD inducer MTX. While both of the syncytia-forming variants caused a maximum of extracellular ATP in H1437 cells at 48 hpi, with a trend

toward an increase compared to rVSV-infected cells, ATP values measured from rVSV-NDV/F_{3aa} infected A549 cells did not follow a pattern that would match with the level of syncytia formation and death at the respective time points. Despite these inexplicable trends, data from Western blot, flow cytometry, and titration of extracellular ATP provide substantial evidence that either of the oncolytic viruses is a potent ICD inducer by stimulating the release of DAMPs.

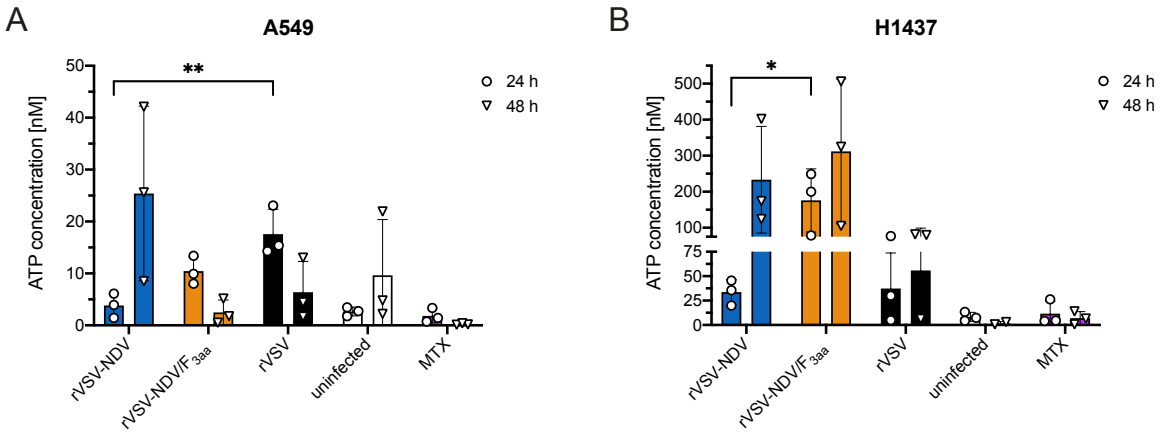

Figure 45. Extracellular ATP quantified from OV-infected A549 and H1437 cells

(**A**) A549 and (**B**) H1437 cells were infected with rVSV-NDV, rVSV-NDV/F_{3aa}, or rVSV at an MOI of 0.01 and at 24 and 48 hpi, released ATP was quantified from the supernatant using ATP Bioluminescent Assay Kit. MTX (2 µM) was used as a positive control, and ATP concentrations in nM were calculated from a log-log standard curve generated with the supplied ATP standard (std curve range 10 µM to 0.1 nM ATP). Plotted are mean ± SD values of n = 3 independent biological replicates. Statistical significance was tested using one-way ANOVA with Tukey's multiple comparisons test (*p ≤ 0.05, **p ≤ 0.01).

3.2.2 Oncolysate from fusion-competent OVs showed enhanced DC activation

To effectively stimulate an anti-tumor immune response, it not only requires a coordinated spatiotemporal release of DAMPs, it further demands the recruitment, antigen uptake, and maturation of antigen-presenting cells, which eventually present tumor antigen to cytotoxic immune cells [139]. The next logical step was to investigate, if the syncytial phenotype and the released ICD markers succeeded in stimulating naïve DCs to differentiate and mature into antigen-presenting DCs. To that end, PBMCs were isolated from healthy human donors and *in vitro* differentiated into DCs (as described in 2.2.4.14), followed by co-culture with oncolysate from A549 or H1437 cells (outlined in **Figure 46** A). Using a specific flow cytometry DC panel designed to characterize the two main DC subtypes (see **Table 14**), it was confirmed that the GM-CSF + IL-4 differentiation protocol primarily yielded cDC2 cell subsets ($CD14^-$, $CD123^-$, $CD11c^+$, $CD1c^+$, MHC-I ^{high}, MHC-II ^{high}, **Figure 46** B).

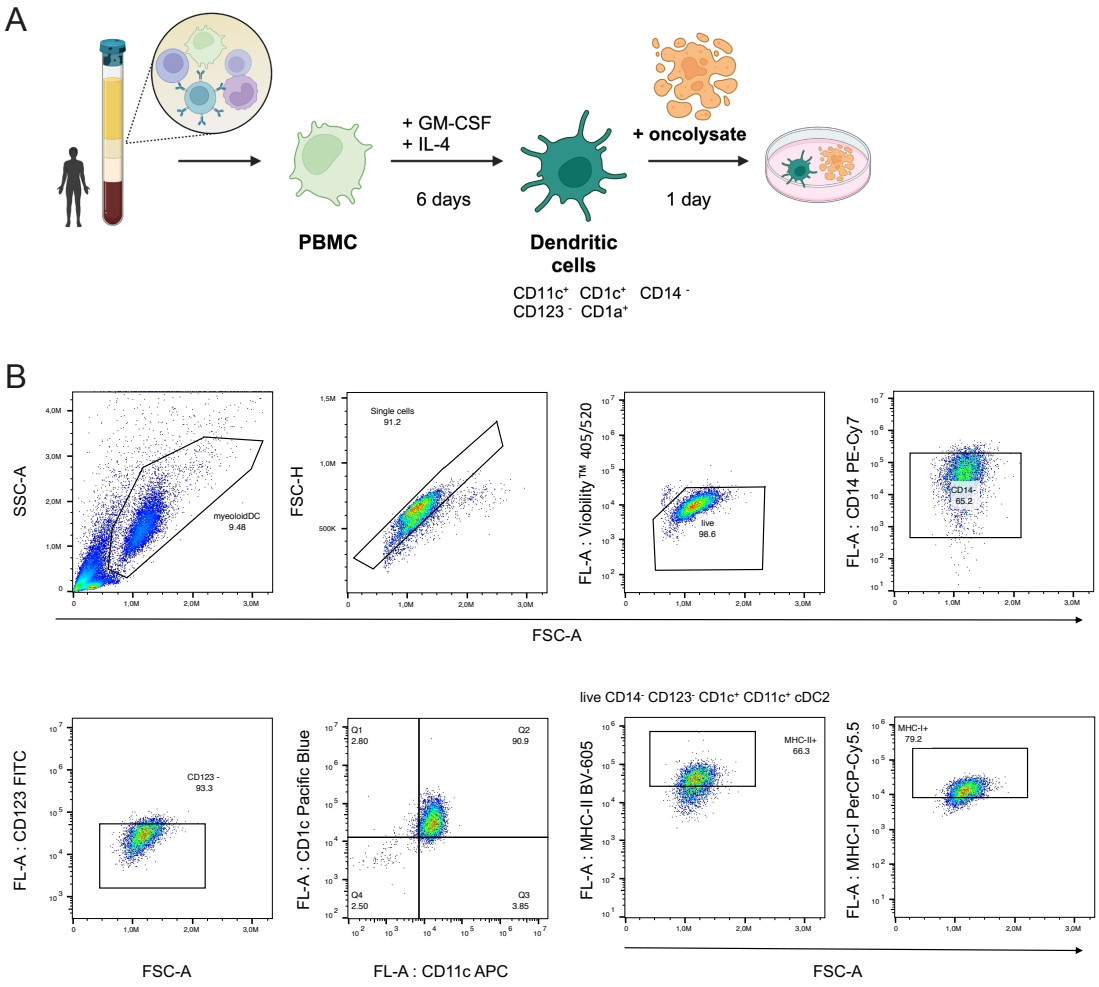

Figure 46. Isolation and subtype determination of human DCs from PBMC

(**A**) Workflow for human DC isolation from PBMCs and co-culture with oncolysates of A549 and H1437 cells. (**B**) Flow cytometry characterization of the cDC2 subtype after GM-CSF + IL-4 differentiation of human PBMCs. The gating strategy is exemplified for one donor. Shown are representative scatter plots from FlowJo. FSC-A = forward scatter area, SSC-A = sideward scatter area, FSC-H = forward scatter height, FL-A = fluorescence channel area. Figure (A) created with BioRender.com

Figure 47 A represents the gating strategy applied for the oncolysate-DC co-culture, exemplified for cocktail-treated DCs. Following 24 h of DC co-culture with oncolysates from A549 or H1437 cells, cDC2 activation status was determined according to the mean fluorescence intensity (MFI) values for CD86, MHC-I, and MHC-II (**Figure 47** B and C). DC co-culture with oncolysate from uninfected tumor cells yielded equally low activation as non-co-cultured and unstimulated DCs. As expected, the stimulation of (non-co-cultured) DCs with an activation cocktail led to an efficient activation, indicated by a significant increase in all activation markers investigated. Interestingly, oncolysates from both cell lines infected with the syncytia-competent viruses caused a significant upregulation of all activation markers; CD86, MHC-I, and MHC-II, in co-culture with DCs in comparison to uninfected controls. In contrast, infection of either tumor cell line with non-fusogenic rVSV failed to induce DC activity above those mediated by uninfected control cells.

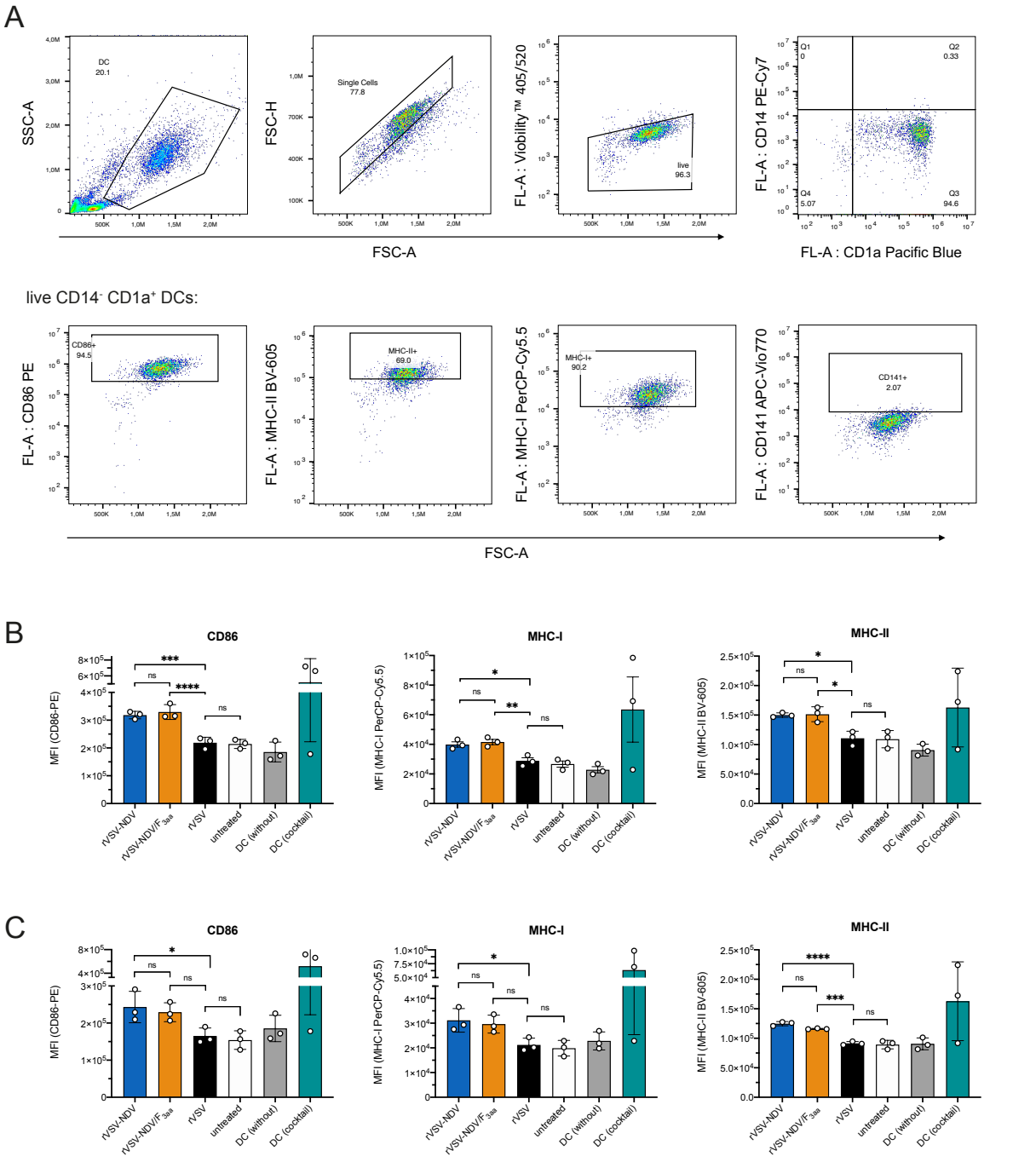

Figure 47. Human DC differentiation and activation upon co-culture with oncolysate from OV-infected A549 and H1437 cells.

In vitro differentiated human DCs were co-cultured with oncolysates of the fusogenic and non-fusogenic viruses and analyzed by flow cytometry using the DC activation panel, described in **Table 14**. (**A**) The applied gating strategy is exemplified for cocktail-treated control DCs from one donor. Gating in FlowJo was applied on live, $CD14^-$, $CD1a^+$ cells, characterized as cDC2 subtype, followed by gating for the DC activation status (CD86, MHC-I, and MHC-II). In this activation panel, CD141 was used to discriminate cDC2 ($CD141^-$) from cDC1 ($CD141^+$) subtype DCs. DC activation from oncolysate co-cultures of (**B**) A549 or (**C**) H1437 cells quantified by flow cytometry and expressed as mean fluorescence intensity (MFI) of CD86, MHC-I, and MHC-II, respectively. Cocktail-stimulated DCs (see 2.2.4.15) were used as a positive control. Represented are mean ± SD values of n = 3 individual healthy donors. Statistical significance was tested using one-way ANOVA with Tukey's multiple comparisons test (ns = non-significant, *p ≤ 0.05, **p ≤ 0.01, ***p ≤ 0.001, ****p ≤ 0.0001).

To summarize, it could be demonstrated that all OV variants mediated the production and release of key ICD markers Hsp70, Hsp90, CRT, and extracellular ATP in the tested lung cancer cell lines. Moreover, the functional readout employing human DCs demonstrated higher APC activation by the fusion-proficient viruses, rVSV-NDV and rVSV-NDV/F_{3aa}, than by rVSV, highlighting the great potential of fusogenic OVs have in augmenting an anti-cancer immunity.

It was also questioned whether the F protein modification in rVSV-NDV/F_{3aa} provokes another death pathway by manipulating the syncytia formation kinetics and whether this ameliorates immunogenicity. Overall, but depending on the cell line, rVSV-NDV/F_{3aa} displayed altered fusion kinetics and slightly changed syncytia morphology but to the depth of the investigation, not with a changed death mechanism. Even though the studied cell death pathways unveiled a high degree of complexity in how syncytial oncolysis is regulated and could not point out distinct differences between rVSV-NDV and rVSV-NDV/F_{3aa}, the data provides evidence that the fusogenic variants may be the better immune-activators among the tested OVs.

3.3 Establishment of a directed OV therapy in lung adenocarcinoma-bearing mice

Based on promising *in vitro* findings a translation into a suitable murine lung cancer model was justified. Tumor-reducing effects of the respective viral variants and their immunogenicity had not been previously tested in an *in vivo* setting. In a proof-of-concept survival study two distinct tumor models, the genetic *K-ras*$^{LSL\text{-}G12D/+}$*; p53*$^{fl/fl}$-induced lung adenocarcinoma, and tail vein implanted syngeneic murine LLC cells, were compared. Moreover, tumor reduction and survival benefits were investigated by exploring two different treatment routes for the oncolytic virus: localized treatment via intratracheal instillation of rVSV-NDV and systemic delivery by intravenous injection.

3.3.1 Reduced maximum tolerated dose using intratracheal administration of rVSV-NDV

Intravenous injection of rVSV-NDV at an MTD of 1x 10^7 $TCID_{50}$ per injection has previously demonstrated success in an inducible multifocal HCC model in AST mice [40], as well as in orthotopically implanted HCC and PDAC in syngeneic C57BL/6 mice (unpublished data). In the context of a "*new*" target tissue (lung) and a yet unexplored intratracheal virus delivery, the MTD of rVSV-NDV given intratracheally had to be determined in a dose escalation study. Fukazawa et al. reported the improved delivery of a therapeutic adenovirus to distant alveolar regions using pulmonary surfactant [97]. Consequently, it was hypothesized that surfactant could also improve rVSV-NDV intratracheal delivery, and formulations of rVSV-NDV and surfactant were included in the study.

Healthy, non-tumor-bearing C57BL/6 mice received a single injection of rVSV-NDV in PBS or rVSV-NDV in PBS containing surfactant via intratracheal instillation. The viral dose was gradually lowered starting from the intravenous safe and effective dose of 1x 10^7 $TCID_{50}$/injection. Over a two-week observation period, body weight loss, breathing defects, and virus-related cytopathic effects, such as signs of neurotoxicity or systemic inflammation, were monitored. A dose was considered to be safe when 3/3 or 5/6 mice survived the observation period without showing severe toxic symptoms (**Table 16**). 4 out of 5 intratracheally instilled mice did not tolerate the highest dose of rVSV-NDV (1x 10^7 $TCID_{50}$) in PBS (**Figure 48**). Within the first 3 to 5 days after injection, these mice rapidly lost body weight and showed signs of labored breathing and a hunched posture with clear indicators of pain. In turn, a ten-fold reduction of the dose (1x 10^6 $TCID_{50}$) was tolerated by 5 out of 6 mice and defined as the MTD in PBS for the intratracheal treatment. In general, mice injected with this dose more rapidly recovered from the virus application procedure, stably maintained their body weight and had no signs of pain or breathing difficulties.

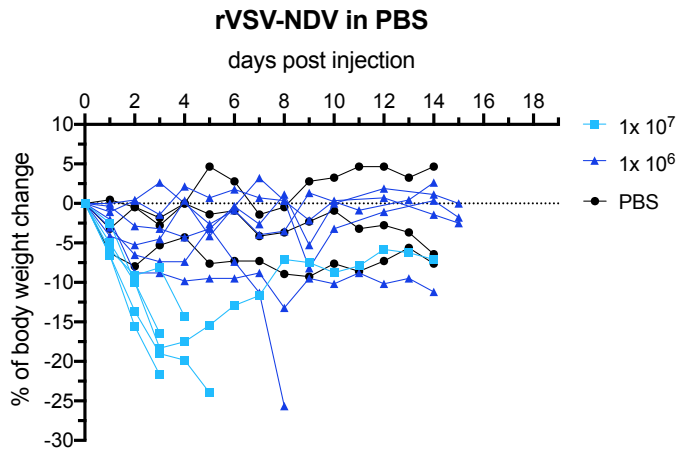

Figure 48. Percent body weight change during the dosing study of intratracheally applied rVSV-NDV in PBS

The body weight for each mouse was recorded over the two-week observation period and is expressed as % body weight change after one dose of intratracheal treatment (on day 0) with either rVSV-NDV at 1x 10^7 $TCID_{50}$/injection, or 1x 10^6 $TCID_{50}$/injection in PBS, or PBS alone.

It was hypothesized that a virus formulation with pulmonary surfactant could result in improved delivery and potentially enhanced treatment effects, but could also affect the tolerated virus load (MTD) in the lungs. Alveofact® and Curosurf® are naturally derived pulmonary surfactants consisting of polar lipids, phosphatidylcholine, and hydrophobic surfactant proteins SP-B and SP-C (product leaflet of Curosurf® and Alveofact®). Due to this lipid-rich nature, a damaging effect of the lipids on the viral envelope of rVSV-NDV was a risk. Therefore, prior to testing the virus-surfactant formulation in mice, virus infection, replication, and cell killing were monitored in susceptible A549 cells after rVSV-NDV pre-incubation in PBS containing 9 mg/mL surfactant (Curosurf® or Alveofact®) (**Figure 49**). No negative effects on virus replication were observed with either of the surfactant preparations. The formulation with Curosurf®, but not with Alveofact®, surfactant showed a dampened oncolysis in A549 despite similar viral replication kinetics compared with surfactant-free formulation. Nevertheless, due to the superior storage stability of Curosurf®, subsequent dosing experiments in mice were performed using rVSV-NDV dissolved in PBS containing 9 mg/mL Curosurf®.

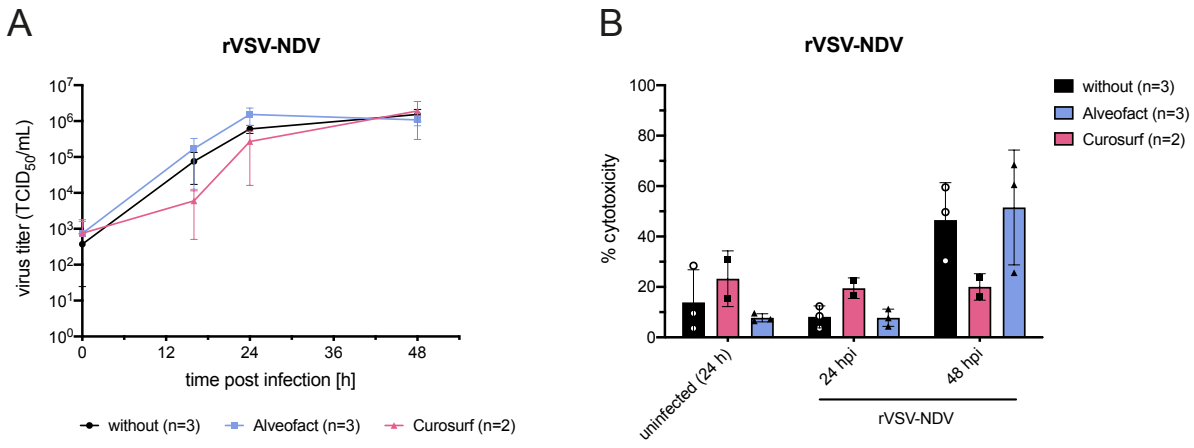

Figure 49. *In vitro* performance of rVSV-NDV surfactant formulations in A549 cells

(**A**) A549 cells were infected with rVSV-NDV in PBS, rVSV-NDV in PBS with 9 mg/mL Alveofact® or rVSV-NDV in PBS with 9 mg/mL Curosurf® at an MOI of 0,01, and virus replication and (**B**) virus-induced cytotoxicity (LDH-assay) were measured over time. Mean ± SD of n = 2 (Curosurf®) or n = 3 (Alveofact and without) independent biological replicates.

When the dosing experiment was repeated with a virus formulation in PBS containing 9 mg/mL Curosurf® surfactant to improve virus delivery to distant alveolar regions, a similar dose of 1x 10^6 $TCID_{50}$ and even a dose of 1x 10^5 $TCID_{50}$ was no longer tolerated (**Figure 50**). The majority of the treated mice displayed toxic effects, breathing difficulties and weight loss, and had to be euthanized early, while surfactant alone was well tolerated. Further reducing the viral dose, 5x 10^4 $TCID_{50}$/injection was determined to be a safe dose in 3 out of 3 injected mice (**Table 16**).

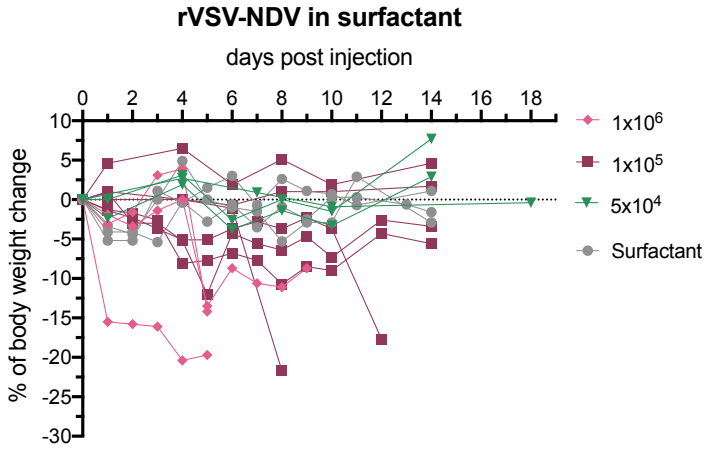

Figure 50. Percent body weight change during the dosing study of intratracheally applied rVSV-NDV in a formulation with Curosurf surfactant

The body weight for each mouse was recorded over the two-week observation period and expressed as % body weight change after one dose of intratracheal treatment (on day 0) with either 1x 10^6, 1x 10^5, or 5x 10^4 $TCID_{50}$ of rVSV-NDV in 9 mg/mL Curosurf ®, or 9 mg/mL Curosurf ® surfactant alone.

In conclusion, after a single intratracheal dose of rVSV-NDV, the tolerated viral load in the lungs was markedly reduced compared to an intravenous treatment. Co-administration of surfactant and rVSV-NDV surprisingly increased the adverse effects, thereby reducing the MTD, presumably due to an enhanced viral transduction efficiency in the lungs mediated by the surfactant. Infectious virus, however, was not detected in either of the blood plasma samples taken on day 1 or day 3, independent of the applied virus dose or presence of surfactant ($TCID_{50}$ results below detection limit; data not shown). During the subsequently performed survival study in lung tumor-bearing mice and treatment with rVSV-NDV in PBS, the safety of the intratracheal dose was corroborated by well-tolerated, repetitive (weekly) administration of 1x 10^6 $TCID_{50}$/injection without signs of toxicity, no weight losses and quick recovery of the mice. In light of the dampened oncolytic effect of rVSV-NDV and Curosurf® in A549 cells, and the much lower MTD in a surfactant formulation, a survival study with as low as 5x 10^4 $TCID_{50}$/injection with Curosurf® was not performed.

Table 16. Survival proportion of healthy mice intratracheally instilled with decreasing doses of rVSV-NDV

Treatment	total injected	survived
1,00E+07 rVSV-NDV in PBS	5	1
1,00E+06 rVSV-NDV in PBS	6	5
1,00E+06 rVSV-NDV in Surfactant	3	0
1,00E+05 rVSV-NDV in Surfactant	6	4
5,00E+04 rVSV-NDV in Surfactant	3	3
PBS	3	3
Curosurf® surfactant	3	3

3.3.2 Absence of survival benefits in two different models of murine lung adenocarcinoma

In a subsequent study, the therapeutic benefits of rVSV-NDV were investigated in two distinct models of murine lung carcinoma: an Ad-Cre-inducible model in KP mice and an implantable model using intravenously injected LLC cells. Both tumor models are reported in literature [99, 101, 103, 104, 140]; however, tumor development, side effects, detectability of lung lesions by µCT imaging, as well as tumor classifications for randomization to treatment groups had to be established for the anticipated survival study.

3.3.2.1 End-stage KP lung tumors are non-responsive to oncolytic rVSV-NDV treatment

Multifocal lung adenocarcinoma can be induced in KP mice by intratracheal instillation of Ad-Cre virus under MMF anesthesia. The Cre recombinase will excise the STOP cassette in front of the *KRAS* proto-oncogene, and eliminate the *p53* tumor suppressor gene (**Figure 51** A) by recombination at the *loxP* sites, allowing for tumorigenesis in the lungs. Usually after 3 days, Ad-Cre-induced KP mice recovered from the complex procedure and remained stable in body weight and overall health throughout the tumor growth phase. Initially, mice were scanned by µCT imaging at weeks 4, 8, 10, and 12 post induction; however, distinctive lung tumor lesions could not be detected. In fact, it was discovered that at an Ad-Cre dose of 1x 10^5 PFU/mouse, a minimum of 16 – 23 weeks is required to develop visible tumor lesions distributed in both or at least one of the lung lobes. Throughout the survival study, successive study groups were induced with a higher Ad-Cre dose to speed up tumor formation. Indeed, it was observed that 5x 10^6 PFU/injection accelerated tumor growth to 13 – 16 weeks. The time point after Ad-Cre induction was, therefore, not a defining criterion to start tumor treatment, and since uniformity of Ad-Cre distribution in lung lobes could not be guaranteed, the following inclusion criteria were determined based on the µCT scans. At least two of the criteria had to be met to be randomized for tumor treatment:

- Minimum 1–2 individual lesions in each lung lobe (simplified as right and left lobes)
- At least one individual lesion bigger than 2 mm^3
- Several (≥ 4 – 5) small-sized lesions of 0.5 - 1 mm^3
- Total tumor volume of ≥ 2 mm^3

All mice that received tumor treatment were devoid of symptoms and displayed normal breathing and fitness. Mice that did not fulfill the inclusion criteria by week 23 (1x 10^5 PFU Ad-Cre) or week 16 (5x 10^6 PFU Ad-Cre) were excluded from the study. Due to the stress of the intratracheal administration, only a weekly treatment schedule with either PBS or rVSV-NDV at the predefined MTD was applied and stopped after 6 doses. The same treatment regime was chosen for the intravenous treatment group (**Figure 51** B).

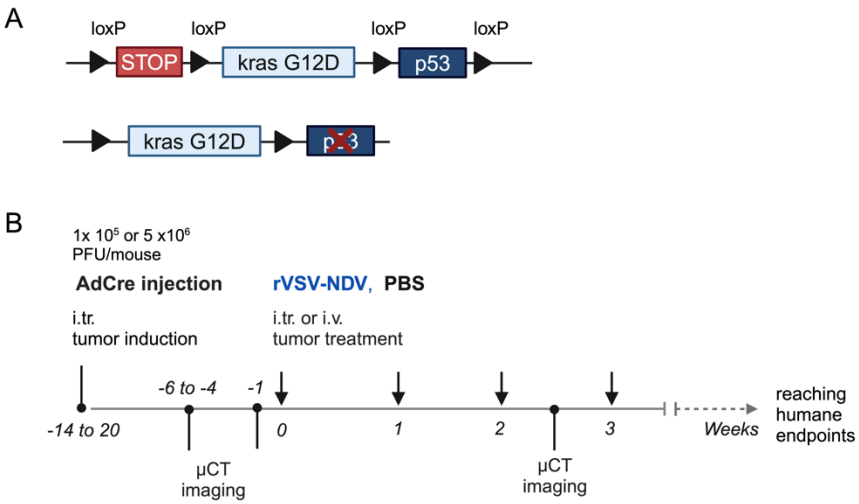

Figure 51. Adenovirus-Cre inducible model of *K-ras*$^{LSL-G12D/+}$; *p53*$^{fl/fl}$ lung cancer and OV treatment timeline

(**A**) Schematic representation of the genetic modification in KP mice upon adenovirus-mediated delivery of Cre recombinase for induction of tumor formation. (**B**) Representative timeline of the KP lung adenocarcinoma development from intratracheal Ad-Cre induction to oncolytic virus treatment. Upon confirmation of lung tumors by µCT and randomization, mice received weekly doses of rVSV-NDV or PBS (black arrows), given intratracheally (i.tr.) or intravenously (i.v.). LSL = loxP-STOP-loxP

Overall, it was noted that obvious symptoms were absent and mice showed minimal suffering, even at later tumor stages. As soon as the tumor load hindered normal breathing, the mice declined in overall condition and developed pain, which was apparent by reduced activity, isolation, exhaustion after handling, and reduced body weight. **Figure 52** shows the percentual change in individual body weights and the survival proportions after therapy beginning via the intratracheal or intravenous route.

Intratracheal administration of rVSV-NDV resulted in a median survival time of 84.5 days compared to 81 days in the PBS treatment group. After systemic treatment via tail vein injection, rVSV-NDV-receiving mice had a median survival time of 43.5 days, whereas PBS-treated animals had a median survival of 50 days. It has to be noted that all intravenously treated mice initially received a higher Ad-Cre dose and, therefore, tumor growth was accelerated, resulting in earlier death than mice from the intratracheal study groups. Regardless of this discrepancy, neither of the treatment routes yielded a significant survival benefit of the OV therapy over PBS control.

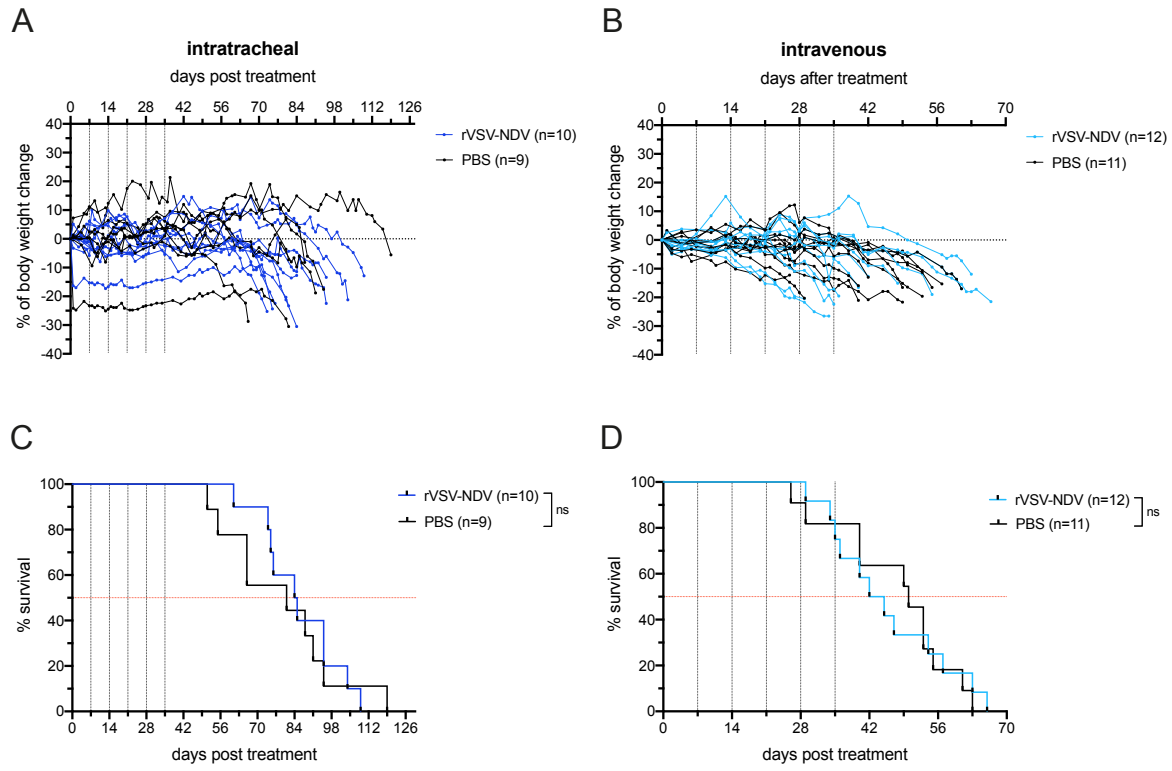

Figure 52. Body weight and Kaplan-Meier survival data of lung tumor-bearing KP mice upon start of intratracheal or intravenous therapy

(**A** and **B**) The body weight for each mouse was recorded over the survival period and expressed as % body weight change relative to the treatment start (day 0). Mice received 6 doses of PBS or rVSV-NDV at 1x 10^6 (intratracheal MTD, in **A**) or 1x 10^7 (intravenous MTD, in **B**) $TCID_{50}$/injection, given in weekly intervals (dashed vertical lines). (**C** and **D**) The Kaplan-Meier graphs show the survival proportions for each group (intratracheal treatment in **C**; intravenous treatment in **D**). Due to different Ad-Cre doses for lung tumor induction (1x 10^5 PFU/mouse in **A** and **C**; 5x 10^6 PFU/mouse in **B** and **D**), the overall survival time of PBS treated mice differed between the intratracheal and intravenous study group (further discussed in section 4.2.3). Median survival times were calculated from GraphPad PRISM and compared by a two-tailed unpaired t-test. (ns = non-significant). Group sizes are indicated in brackets.

Over the course of the survival study, mice were imaged by µCT to monitor tumor growth. Using ITK-Snap, distinct tumor lesions were manually marked in each anatomical section (sagittal, axial, and coronal view) to create a sum volume of left and right lobe tumors by the software. An analysis workflow and representative µCT images are displayed in **Figure 53** A-C. In contrast to the expectations, the number of quantifiable tumor lesions and the sum of left and right tumor volumes gradually increased after treatment regardless of the applied therapy (**Figure 53** E and F). Tumor load at late stages comprised multiple (> 6 – 10) individual big lesions in each lung lobes and spanned all cross-section planes. Frequently, tumor nodules also covered the entire chest, invading the ribcage (not shown) or formed a coherent tumor mass that was nearly indistinguishable from surrounding tissue in the µCT images and at necropsy (**Figure 53** D).

Taken together, neither intratracheal nor intravenous treatment with rVSV-NDV resulted in a significant survival prolongation or evidence of delayed tumor growth of orthotopic lung adenocarcinoma-bearing KP mice compared to the control groups. Instead, even though the treatments were repeated 6 times, mice eventually succumbed from end-stage tumors and the gradually accumulating tumor mass in the lungs.

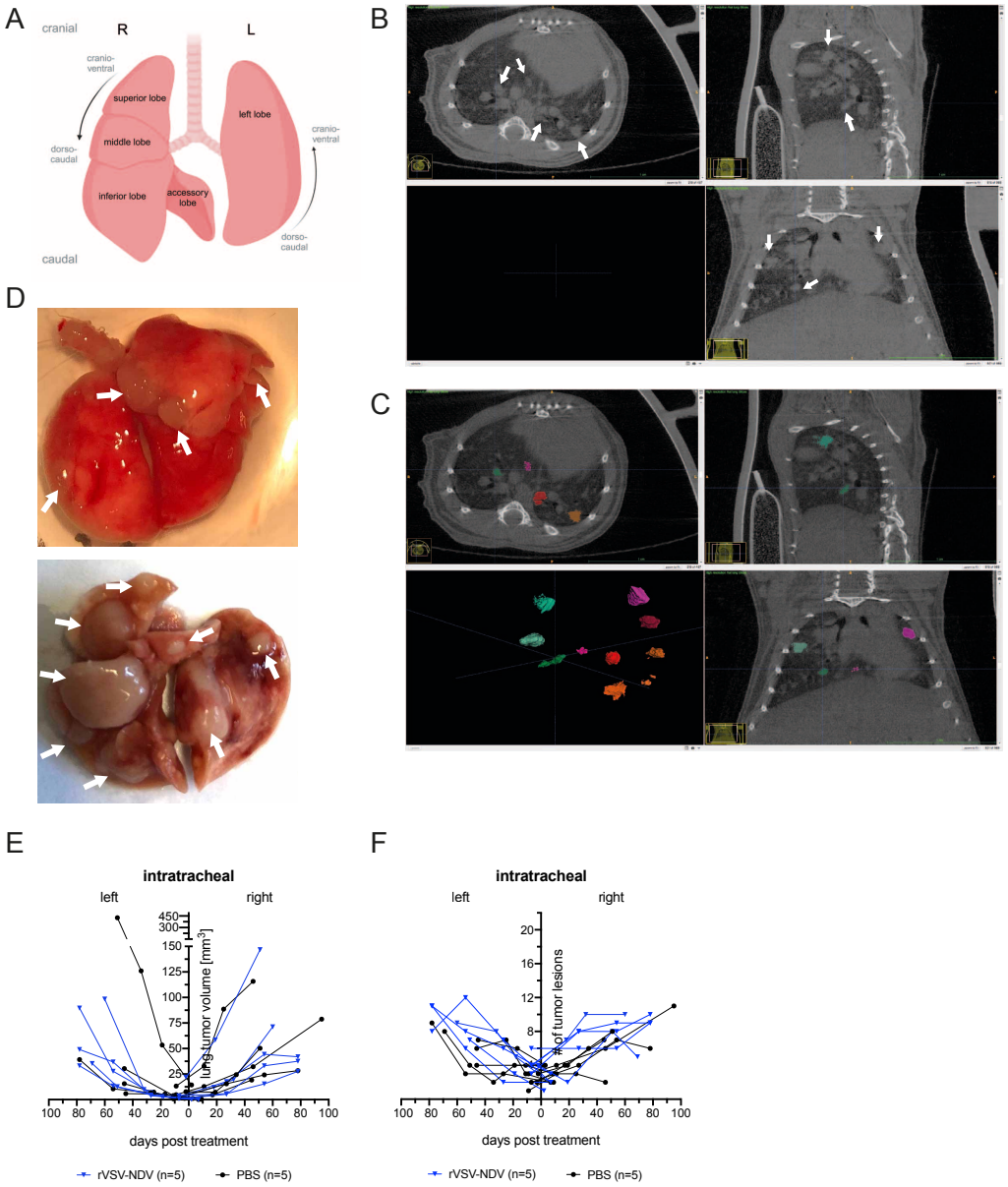

Figure 53. Lung tumor burden quantified from µCT images of intratracheally treated KP mice

(**A**) The mouse lung comprises four right and one left lung lobe, and tumor nodules are systemically quantified from dorso-caudal to cranio-ventral in the left and right lobes. (**B**) Tumors were marked in µCT scans pre and post treatment, and the tumor volume was quantified as exemplified for one representative mouse using ITK-Snap software. Individual lesions were manually detected (white arrows) in each anatomical section and lung lobes. (**C**) These nodules were colored and 3D-rendered. Volumetric pixels (= voxels) were quantified and transformed to tumor volumes in mm^3 (voxel size: 40 x 40 x 40 µm, voxels: 972 x 972 x 653, volume size: 40 x 40 x 27 mm). (**D**) For comparison, macroscopic lesions (white arrows) are shown on necropsy examples of KP mice with a medium (top image) and high (bottom image) lung tumor burden. (**E**) A representative set of 5 selected mice from each intratracheal treatment group (PBS or rVSV-NDV) was quantified at each imaging time point (one pre- and three scans post treatment) to plot the changes in left and right sum tumor volumes. (**F**) For the same mice as in (E), the number of distinguishable and quantifiable lesions in the left and right lobes is graphed.

3.3.2.2 Intravenously implanted LLC and B16-OVA cells grow invasively and are refractory to rVSV-NDV therapy

Due to the complexity of the inducible model described above, possibly contributing to the inability to determine a clear therapeutic effect, an alternative model of murine lung cancer was explored. Tail vein implanted syngeneic LLC cells are reported to primarily migrate to the lungs and develop orthotopic, fast-growing lung tumors within one to two weeks [103, 104]. Similarly, murine B16-OVA melanoma cells injected intravenously engraft primarily in the lungs and form heterotopic multifocal tumors, which are responsive to OVA-specific $CD8^+$ T cell-mediated tumor killing [102, 141]. Implementing either of these experimental metastasis models it was anticipated to achieve a faster and more uniform tumor growth and, to gain insights into *in vivo* oncolysis.

Before conducting *in vivo* experiments, LLC cells were screened for their susceptibility to rVSV-NDV infection and *in vitro* cell killing. rVSV-NDV efficiently replicated to high titers in LLC cells but instead required a higher starting MOI to induce sufficient oncolysis, as seen by an IC_{50} value of > MOI 0.1 (**Figure 54**). B16-OVA infectibility and efficiency *in vitro* as well as *in vivo* tumor cell killing by rVSV-NDV have already been successfully demonstrated [41]. Consequently, both cell lines were expected to be susceptible to infection and tumor cell destruction by rVSV-NDV once engrafted in the lungs of syngeneic mice.

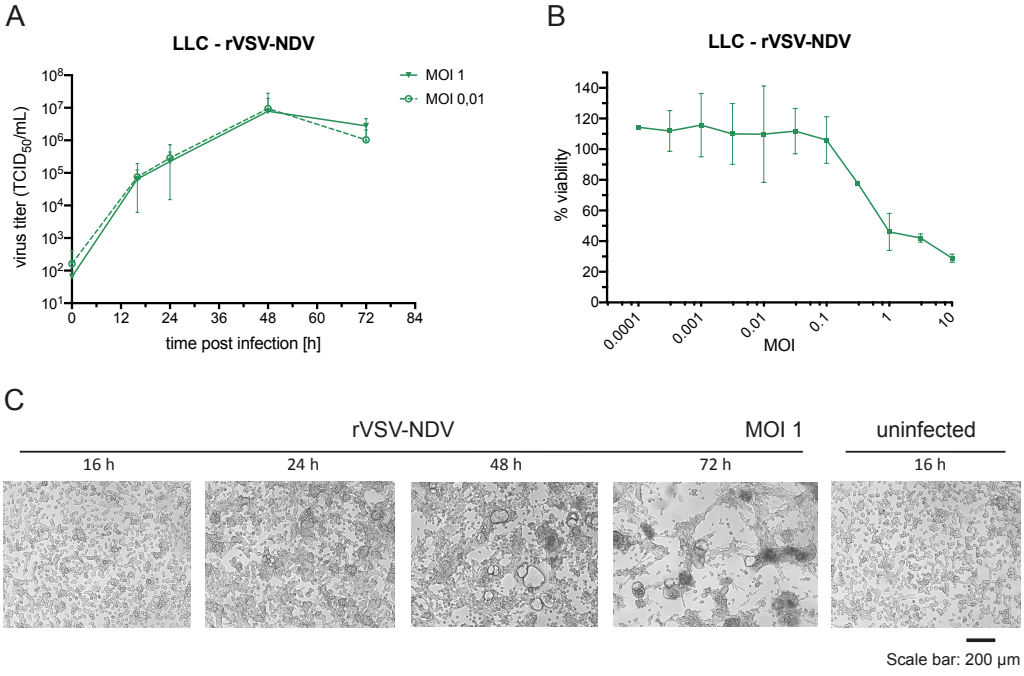

Figure 54. LLC cell *in vitro* susceptibility to rVSV-NDV infection

(**A**) LLC cells were infected at an MOI of 1 (n = 2) and 0.01 (n = 3), and virus replication was monitored by $TCID_{50}$ measurements from supernatants over time. (**B**) Viral potency in LLC cells was determined by measuring the reduction in cell viability over a range of MOIs, relative to untreated cells (n = 2). Mean values ± SD are shown in A and B. (**C**) Representative images of virus-mediated oncolysis at indicated time points in LLC cells infected at MOI 1, or uninfected at 16 hours.

To define a suitable cell number for implantation, healthy female C57BL/6 mice at ten weeks of age were injected with either 1x 10^5 or 2x 10^5 LLC cells or B16-OVA cells into the tail vein. To confirm tumor engraftment in the lungs, mice were imaged 10 days after implantation by µCT of the chest. Representative macroscopic and µCT images are shown in **Figure 55** A and B, and tumor lesions are marked with an arrow. Compared to the distinctive lesions seen in Ad-Cre induced KP mice, LLC- and B16-OVA-implanted lung tumors were much more difficult to delineate. Mostly independent of the injected dose, the B16-OVA metastasis model was very invasive and led to rapidly growing tumors in the lung but also cell engraftment in almost every organ of the mouse. Moreover, the condensed B16-OVA tumor mass in the lungs that also invaded the ribcage and trachea, masked a precise detection of individual lung tumor lesions by µCT. The majority of the tested mice had to be euthanized due to whole-body metastasis.

Even though off-target tumor engraftment, such as hip muscle and kidney, was also observed in LLC cell-implanted animals, LLC cells more successfully and reproducibly grew to defined lung tumor lesions. Injection of 2x 10^5 LLC cells led to an approximately 5 days quicker tumor development and more evenly distributed lesions in left and right lung lobes compared to the lower cell concentration. However, once the lung tumor mass affected normal breathing, mice quickly declined in fitness, lost body weight, and had breathing difficulties with gasping. Some mice additionally developed off-target tumors in other organs. **Figure 55** C shows a summary of the lung and metastatic tumor growth.

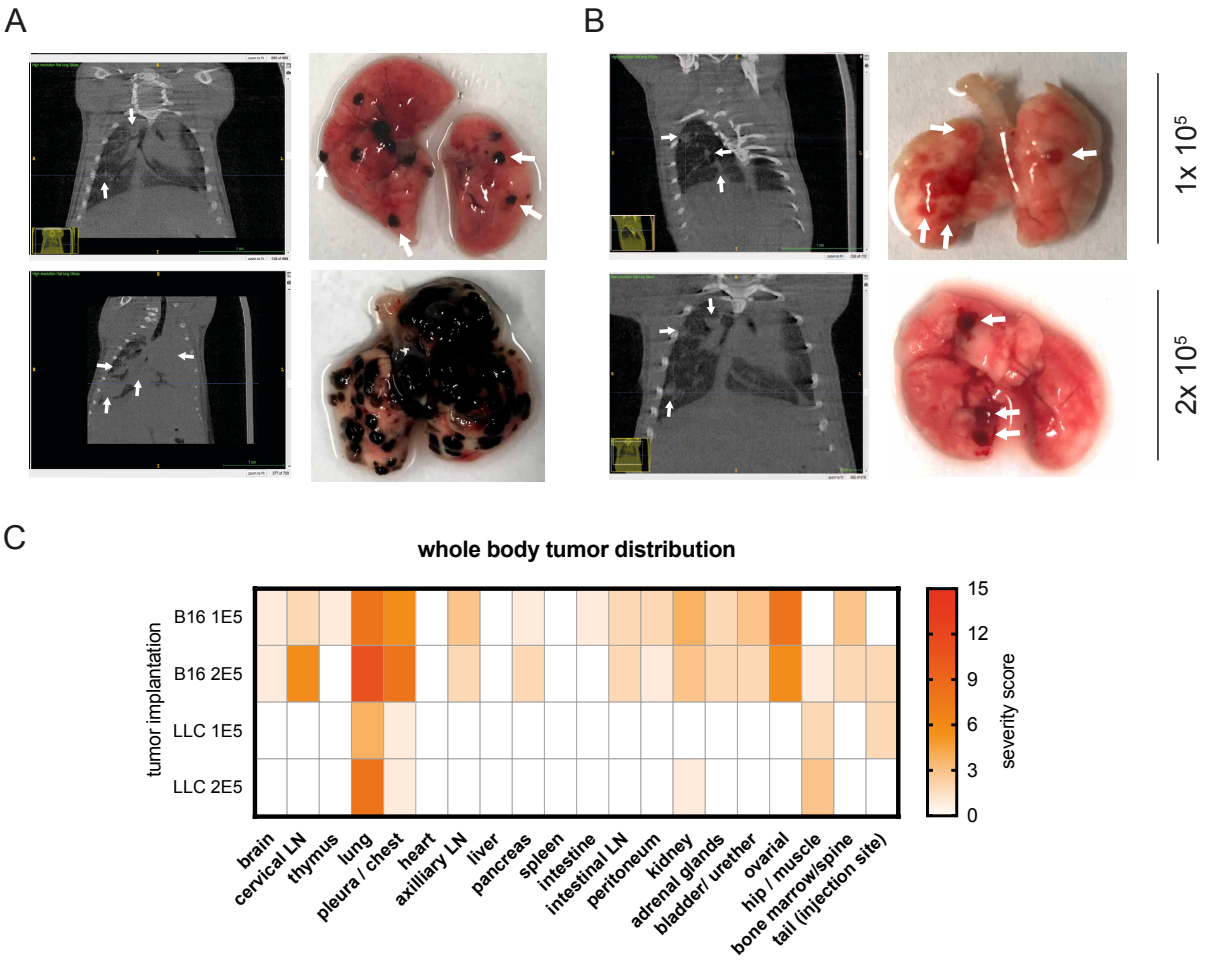

Figure 55. Tumor distribution in the implantable models of murine lung cancer

(**A**) and (**B**): Lung tumor lesions detected by µCT imaging and *ex vivo* necropsy in mice tail vein-implanted with (**A**) B16-OVA cells and (**B**) LLC cells. One representative mouse with a medium (1x 10^5 cells) and a high (2x 10^5 cells) tumor load is shown. White arrows mark some of the tumor lesions (**C**) At humane endpoints or latest 21 days post implantation, necropsy was performed to assess whole body tumor distribution and provide a severity score for each mouse and organ ranging from 0 - 3. A score of 0 represented healthy tissue with no detectable tumor, a score of 1 represented a low tumor load with a countable number of distinct small lesions, a score of 2 was given when tumor lesions were medium-sized or almost not countable in number, a score of 3 was given when the whole organ was covered in tumor mass. Considering 5 mice per group (B16-OVA 1x 10^5 cells implanted, B16-OVA 2x 10^5 cells implanted, LLC 1x 10^5 cells implanted, LLC 2x 10^5 cells implanted), the severity score for an implantation group ranged from 0 to 15. LN = lymph node.

Consequently, the subsequent survival study was conducted by implanting 2x 10^5 LLC cells and following the treatment schedule indicated in **Figure 56** A. As mentioned earlier, since µCT images from LLC tumors in the lungs on days 7- 14 were often inconclusive, treatment was started on day 14 for all study groups. *Ex vivo* necropsies at the humanized end points confirmed numerous small- to medium-sized lesions in both lung lobes and that successfully implanted LLC cells can eventually grow to a tumor phenotype that resembles the KP inducible tumors.

However, in this survival cohort it appeared that, regardless of the applied treatment, the majority of mice developed several LLC lesions in organs other than the lungs. The most frequent side effects, were massive tumor growth in the hip muscle, the spine, the ovaries, or the tail at the injection site. Unexpectedly, this was much more pronounced than in the previous experiment (**Figure 55** C). As these side effects were deleterious, painful for the animal, and affecting movement, these mice had to be euthanized and excluded from the dataset.

Hence, only a handful of mice devoid of off-target tumors remained for the intended tumor treatments, and a sufficient group size for testing the intratracheal treatment route was not achieved. Intravenous treatment with rVSV-NDV yielded a median survival time of 17.5 days compared to 19 days in the PBS control group, and mice most frequently suffered from strained breathing and rapid weight loss (**Figure 56** B and C). Necropsy revealed a similar tumor burden and lung weight in PBS- and virus-treated groups (data not shown). Due to the above-mentioned systemic tumor growth and the absence of significant survival benefits of rVSV-NDV in this implantable tumor model, no further animals were included in the study.

Consistent with the inducible lung adenocarcinoma model, no survival benefits of the OV therapy were achieved compared to the control, although with a group size of only 4 mice per group, definitive conclusions are not possible. Therefore, more detailed elucidation of the *in vivo* oncolysis and virus-mediated immune activation could unfortunately not be gained from the implantable tumor model, and the efficiency of an rVSV-NDV therapy targeting murine lung cancer remains questionable.

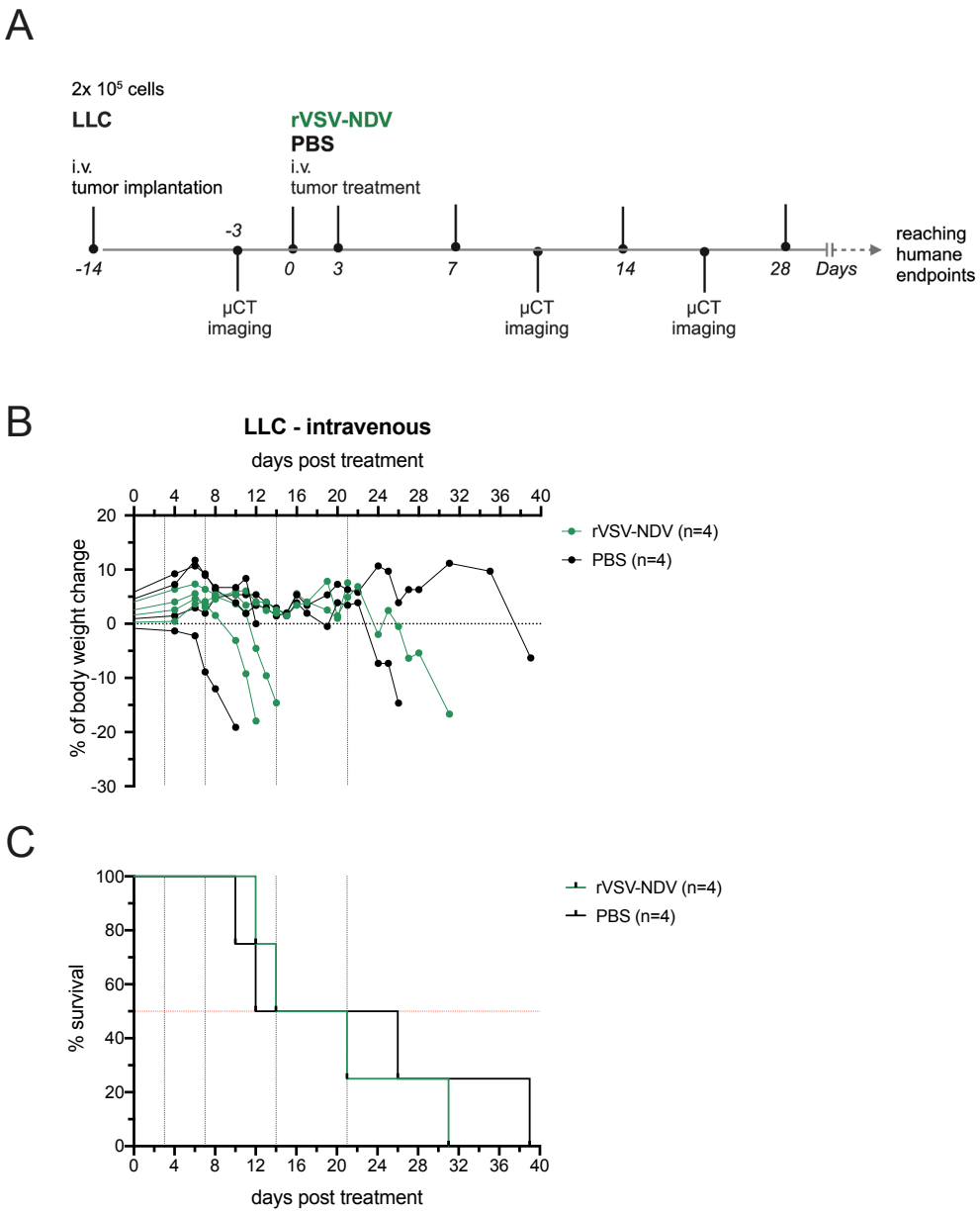

Figure 56. Body weight and Kaplan-Meier survival data of LLC lung tumor-bearing mice upon intravenous treatment with rVSV-NDV

(**A**) LLC cells were injected via tail vein, and lung tumor development was controlled by µCT imaging on day 10, followed by weekly intravenous PBS treatment or oncolytic rVSV-NDV therapy at a dose of 10^7 $TCID_{50}$/injection, starting on day 14 post implantation. Tumor growth was monitored weekly by non-invasive µCT imaging. (**B**) % change in body weight over the course of the tumor treatment reveals that weight loss is a critical parameter in tumor-bearing mice. Mice were euthanized at humane endpoints. (**C**) Survival proportions were plotted as Kaplan-Meier curve. Due to off-target tumor growth, only n = 4 mice per group (with LLC engraftment exclusively in the lungs) could be considered for the survival analysis.

4 DISCUSSION AND OUTLOOK

4.1 rVSV-NDV exhibits dynamic cell death regulation leading to immunogenic oncolysis

The present work sought to decipher the underlying cell death mechanism of the fusogenic hybrid OV, rVSV-NDV, in human lung cancer cell lines A549 and H1437. A potential link between fusogenicity and immunogenicity was studied by comparing syncytial oncolysis caused by two fusogenic variants of rVSV-NDV and the cytopathic effects induced by parental rVSV. Data revealed a dynamic and parallel activation of two well-defined programmed cell death pathways, apoptosis and necroptosis, mostly independent of the fusion capacity of the three tested OVs. Nevertheless, a particular role during syncytia destruction seems to be fulfilled by caspases and MLKL, as will be discussed in the following paragraphs. Promisingly, all OVs triggered the production and release of essential ICD markers, but with the indication of higher DAMP release from fusion-competent viruses, rVSV-NDV and rVSV-NDV/F_{3aa}, which culminated in better activation of cross-presenting DCs *in vitro*. Some ambiguity in the established data, cell line-, or virus-specific effects, as well as suggestions for future research approaches and pre-clinical implications, are discussed below.

4.1.1 Cell-line selection and variation

In the interpretation of the results generated in this work, it is crucial to note that the observed trends in apoptosis or necroptosis signaling are likely affected by cell line-specific effects, defined by the mutational profiles in A549 and H1437 cells. Furthermore, A549 and H1437 are differentially susceptible to infection with rVSV or either fusogenic variant and may elicit distinct antiviral responses.

Many cancer cell lines, among them A549 cells, have been listed as necroptosis-resistant. Since a loss in RIPK3 expression is usually causative for the irresponsiveness to TSZ- or 5-Aza-2′-deoxycytidine-induced necroptosis, only RIPK3 overexpression restores TSZ-induced killing [136, 137, 142, 143]. Data availability for H1437 susceptibility to necroptosis is very limited. Najafov and colleagues classified H1437 cells along with hundreds of other cancer cell lines as necroptosis-resistant using 20 ng/mL TNF-α in TSZ [136] but only measured death, and this study lacks mechanistic data showing, for example, the assembly of a necrosome complex. In contrast, using 100, 500, and 1000 ng/mL TNF-α in TSZ, a collaborating group at TUM succeeded in inducing dose-dependent necroptotic cell killing in H1437 cells and even rescued cell viability by addition of RIPK1 inhibitor Nec-1. However, A549 cells were also classified as necroptosis-reluctant based on this experiment

(unpublished data from Dr. Caterina Branca, former member in the department of Internal Medicine III at TUM; data not shown). Moreover, in contrast to literature indicating that RIPK3 is not detectable in A549 cells [142], analysis of necrosome components by Western blot revealed baseline expression levels and phosphorylation of RIPK1, RIPK3, and MLKL in A549 and H1437 cells in response to TSZ, albeit with an inconclusive pattern (see **Figure 28**). Despite conflicting data, two aspects corroborated the cell line decision for this project: First, it was hypothesized that while TSZ may be insufficient to break the necroptosis resistance, OV infection could still overcome it and activate necroptosis, potentially even in a death receptor-independent pathway. Secondly, with A549 cells being necroptosis-reluctant and H1437 cells being necroptosis-responsive, two functionally different cell lines were considered proper opposing tools for the OV cell death characterization. While the cell line choice may be a limitation of this study, the findings highlight the high degree of heterogeneity among tumor cells, necessitating a broader prospective death pathway analysis of rVSV-NDV-mediated oncolysis in an extended panel of cell lines and tumor indications, including, for example, highly necroptosis-sensitive HT-29 cells, or implementing additional knockout or overexpression models. Notwithstanding, the presented results clearly show a dynamic activation pattern of apoptosis and necroptosis in both A549 and H1437 cells, with effects that may be attributed to the respective OV but also to those inherent to the used cancer cell lines.

4.1.2 rVSV and rVSV-NDV: microscopically distinct oncolysis but similar in the engagement of intrinsic and extrinsic apoptosis

An underlying aim of this project was to clarify whether and how the unique type of syncytial cell death induced by rVSV-NDV differs from the well-defined cytopathic effect induced by rVSV. One feature that might have been conferred from the parental rVSV to the chimeric rVSV-NDV, is the ability to activate and manipulate apoptosis signaling [68-70, 144]. In this study, rVSV-infected A549 and H1437 cells phenotypically fulfilled a prototype apoptotic death program, showing single cell rounding and shrinkage before death [132]. However, the distinctly enlarged rVSV-NDV-induced cell-cell fusions are in strong morphologic contrast to the shrinking dynamic in apoptotic cells and appeared with a differential syncytial phenotype in A549 and H1437 cells, respectively. Even though end-stage syncytia displayed signs of membrane blebbing and enlarged vacuole-like organelles before losing plasma membrane integrity and death, a microscopy-based interpretation of the underlying death events was inconclusive. Future work would require high-resolution electron microscopy or immunofluorescence staining to visually distinguish rVSV-NDV-induced apoptotic events (chromatin condensation, membrane blebbing, and apoptotic bodies) from necroptotic organelle and cell swelling, vacuolization or plasma membrane disintegration [145, 146].

Kinetic differences in cell death are partly explicable by inherently different susceptibility of the two cell lines to rVSV and rVSV-NDV infection. Rapid replication and complete cell death mediated by rVSV infection in A549 cells is known to out-compete a protective antiviral response [147]. Consequently, an incomplete and slower rVSV-NDV infection of an A549 monolayer may result from an attained antiviral state in surrounding uninfected cells through paracrine signaling from infected cells that is achieved due to the slower kinetic of rVSV-NDV replication. A similar incomplete infection of an A549 monolayer and shedding (detachment from the monolayer) of infected syncytia had been previously described in oncolytic Respiratory syncytial virus (RSV) infection [148]. H1437 cells have not been previously reported in the context of oncolytic virus infection. To verify if a differential antiviral program in H1437 cells explains the reversed trends in susceptibility to rVSV and rVSV-NDV infection compared to A549 cells, measuring levels of antiviral sensors and cytokines by ELISA or RT-qPCR is suggested.

Similar to rVSV, rVSV-NDV also activated the intrinsic apoptosis machinery, evidenced by dose-dependent MOMP and moderate activation of caspase 9. However, observations were ambiguous and defined by the individual susceptibility of the respective cell lines to either virus. Owing to the higher susceptibility of A549 cells to rVSV, rVSV-NDV triggered less MOMP than rVSV, whereas opposing trends were observed in H1437 cells. At the investigated time points, caspase 9 activity was only detectable in H1437 cells infected with either rVSV or rVSV-NDV, indicating that intrinsic apoptosis was activated in these cells. Whether at a later time point, caspase 9 cleavage also occurs in A549 cells above the measured baseline activity, remains to be investigated. However, consecutive experiments collectively suggest that rVSV and, though to a minor degree, rVSV-NDV, also elicit the intrinsic apoptosis machinery in A549 cells (as further discussed below). Interestingly, similar kinetic variation and disagreement exist around intrinsic apoptosis activation by NDV. With reported virus strain and cell line dependency, NDV infection activates MOMP and caspase 9 either before [149], at the same time [76], or after [150, 151] parallel engagement of extrinsic apoptosis signaling via caspase 8. Researchers have previously associated rVSV with a strong contribution of the intrinsic MOMP – caspase 9 apoptosis axis during oncolysis [132] and identified several strategies of rVSV to down-regulate anti-apoptotic proteins of the Bcl-2 protein family, for example by proteolytically degrading Mcl-1 or cleaving Bcl-XL through preceding Bid cleavage and caspase 8 activation [68, 144]. Hence, these and the presented data affirm the notion that rVSV and pseudotyped rVSV-NDV likely activate similar signaling networks of the intrinsic and extrinsic apoptosis pathway to maintain oncolysis.

The following possibilities are proposed for explaining rVSV-NDV dependency on apoptosis in A549 cells. While rVSV triggered a model-type kinetic of initial caspase 8 activity followed by caspase 3/7 activation 24 h later, which agrees with data from literature [69], rVSV-NDV in contrast, did not activate caspase 8 in A549 cells, though it still caused effector caspase 3/7 cleavage. Thus, as further corroborated below, caspase 8 may be dispensable in rVSV-NDV infection in A549 cells. A realistic explanation is that another initiator caspase (9 or 10) cleaves effector caspases and the Western blot analysis did not capture the time point of caspase 9 activation between complete MOMP (24 hpi) and peak caspase 3 activation (48 hpi). Alternatively, rVSV-NDV may activate upstream mediator caspase 10 via recruitment to the DISC of TRAIL-R, which bridges receptor-mediated apoptosis to intrinsic apoptosis and MOMP via cleavage of Bid, or directly cleaves effector caspases 3 and 7 [152, 153].

Overall, the apoptotic scenario in H1437 cells appeared more straightforward. Both viruses, rVSV and rVSV-NDV, activate caspase 8 and caspase 3/7 in a strictly consecutive manner. Monitoring downstream effector caspase functions, the present results show moderate (A549) to high (H1437) rates of PARP cleavage in response to rVSV and rVSV-NDV infection. This is in line with literature on rVSV and rNDV infections, respectively [76, 154]. However, as the 89 kDa cleaved PARP fragment occurred even before caspase 3/7 activity peaked, it is plausible that also other caspases, such as caspase 1 or 4, as well as other PARP cleaving proteases, like cathepsin B and D, are triggered to cleave PARP and prevent DNA repair during OV-mediated apoptosis [155, 156]. By investigating additional initiator or effector caspases or apoptotic effector molecules, these uncertainties could be clarified in future experiments.

Taken together, the experimental evidence in H1437 cells and tendencies from A549 cells allow the assumption that a fusogenic death by rVSV-NDV triggers a parallel and timely controlled activation cascade of apoptotic caspases. Data from pharmacological perturbation in the apoptosis pathway and genetic deletion of caspase 3 or 8 by CRISPR/Cas9 further underpin this notion but also demonstrate that rVSV and rVSV-NDV can switch to a non-apoptotic death modality; however, non-fusogenic rVSV did so less efficiently.

4.1.3 PS exposure as apoptotic and non-apoptotic "*fuse-me*" signal

Consistent with the previously described time-dependent exposure of PS on rNDV- or rVSV-infected cells, followed by secondary necrosis [76, 157-159], rVSV-NDV similarly affected the flipping of PS to the outer syncytial membrane as early apoptotic "*eat-me*" signal to phagocytosing macrophages. However, there is growing evidence that non-apoptotic pathways also induce PS translocation. For example, Chen et al. described that antiviral IFN-γ induces PS exposure, with RIPK3 and MLKL being the executive factors in that pre-

necroptotic process [160]. Thus, the variable trends of PS exposure seen on H1437 and A549 cells can be explained by more than one pathway contributing to the exposure of PS. Correlating with the infectibility of the individual cell lines, rVSV-NDV-infected cells yielded slightly higher PS signals on their surface than rVSV-infected cells. A concept proposed by Whitlock and colleagues explains the non-apoptotic exposure of PS as a "*fuse-me*" signal to mark fusion-committed cells for coordinated membrane remodeling during syncytia formation [29]. Thus, it is possible that in addition to the classic early apoptotic signal, ectopic PS may promote syncytiogenesis of rVSV-NDV-infected cells. By using the herein presented fusion assay in combination with PS overexpression or blocking experiments by Annexin V or anti-PS antibodies, one could further investigate that hypothesis.

4.1.4 rVSV and rVSV-NDV can dynamically rework the underlying apoptotic program to maintain oncolysis

As mentioned in section 1.2.3, a series of molecular events, including low IAP levels, formation of complex II, proper RIPK1 phosphorylation and ubiquitination, and blocking of caspase 8 activity by c-FLIP are required to trigger a switch from apoptosis to necroptosis signaling [50]. However, for rVSV and rVSV-NDV, the mediator in this steady state death regulation remains elusive. In line with the above-described necroptosis reluctancy (A549) or sensitivity (H1437) of the cell lines investigated, both viruses could maintain their replication and lytic life cycle when caspases were inhibited by zVAD alone. With additional external death receptor stimulation (TNF-α) and IAP antagonism (Smac mimetic; TSZ); however, cell death mediated by rVSV and rVSV-NDV was promoted, indicating a presumable switch to necroptosis. Existing literature on either of the parental viruses support this idea. rNDV oncolysis of HuTu-80 duodenum carcinoma cells was delayed but not prevented by inhibitors targeting initiator or all caspases (zVAD) until at 48 hpi, a non-apoptotic death program prevailed [149]. A cooperative effect of extrinsic death receptor stimulation and caspase-mediated intrinsic and extrinsic apoptotic death by rNDV was also shown by Cuadrado-Castano and colleagues [76]. rNDV infection in combination with initiator caspase 8 or 9 inhibition could neither shift the apoptotic program to the contrary initiator caspase nor increase caspase 3 activity and rNDV oncolysis. However, rNDV expressing a human FAS receptor to facilitate overexpression of additional death receptors on infected cells subverted oncolysis to increased and earlier intrinsic and extrinsic apoptosis [76]. Similar to the added oncolytic effects in the presence of TS shown in the present study, it had been demonstrated that a TNF-α-producing rVSV mutant (rVSV(MΔ51)-TNF-α) in combination with IAP antagonism by LCL-161 significantly increased extrinsic apoptosis and effector caspase activity [161].

In necroptosis-sensitive H1437 cells, caspase 8 deletion by CRISPR/Cas9 did not reduce rVSV killing and therefore prompted a switch to either caspase 9-dependent intrinsic apoptosis, or necroptosis. In necroptosis-reluctant A549 cells, knockout of caspase 8, and to some extent caspase 3, however, led to enhanced cell viability in response to rVSV infection compared to the NTCs, and an unaltered apoptotic morphology highlighted the reliance of rVSV on the intrinsic arm of apoptosis. This is in line with a previous study, in which rVSV was shown to maintain viral replication and caspase 3-mediated cell killing in caspase $8^{-/-}$ murine embryonic fibroblasts; however, once caspase 9 was ablated, effector caspase activation was delayed [132]. Thus, these and the results presented here support two established characteristics. rVSV oncolysis strongly depends on intrinsic and extrinsic apoptosis, whereby caspase 8 functions as an amplifier in the pathway. Alternatively, rVSV may also recruit the involvement of non-apoptotic death programs when caspase 8 and other caspases are inhibited. That caspase 8 can also be dispensable for a fusogenic death of rVSV-NDV was demonstrated in both cellular backgrounds; however, with unique conclusions on the involving death pathway. Considering the difficulty of triggering necroptosis in A549 cells, fusogenic oncolysis was presumably proceeded by intrinsic apoptosis instead. In contrast, the capability of H1437 cells to engage necroptotic signaling after caspase 8 had been deleted, accelerated rVSV-NDV oncolysis and pointed to an involvement of an alternative syncytial death via necroptosis.

4.1.5 rVSV and rVSV-NDV engage necroptosis as an oncolytic alternative to apoptosis

It was established that under the respective cellular circumstances, next to intrinsic and extrinsic apoptosis, non-fusogenic rVSV and fusogenic rVSV-NDV also utilize a non-apoptotic death program. In the absence of zVAD or genetic caspase inactivation as necroptotic stimuli, yet time-dependent upregulation and phosphorylation of RIPK1, RIPK3, and MLKL in both human lung cancer cell lines were yielded from Western blot analysis, allowing the conclusion that rVSV and rVSV-NDV engage necroptosis for oncolysis.

rVSV infection in RIPK1, RIPK3, or MLKL knockout A549 cells markedly promoted apoptotic death progression rather than impairing oncolysis. While the same was true for H1437 $RIPK1^{-/-}$ and $MLKL^{-/-}$ cells, the absence of RIPK3 in H1437 cells slightly muted rVSV death. That supports the above-mentioned notion: rVSV primarily engages caspase-dependent apoptosis during cell killing [68-70, 144] but, provided that the cell line is responsive to necroptosis, rVSV also utilizes RIPK3-dependent necroptosis. Except for a study by Silva da Costa et al., in which the authors describe rVSV-induced MLKL phosphorylation when caspases are blocked by zVAD [162], literature reports in support of the theory of an rVSV-induced necroptosis are rare so far.

Interestingly, muted death of rVSV-NDV-infected RIPK1$^{-/-}$ H1437, and RIPK3$^{-/-}$ A549 and H1437 cells, suggests a dependency of the fusogenic death program on RIPK1 and RIPK3. But, upon knockout of the necroptosis executioner, MLKL, in the two human lung cancer cell lines and murine B16 cells, oncolysis and replication of rVSV-NDV or rVSV were unaltered compared to wildtype cells. Since pharmacological blocking of RIPK1 or MLKL could, however, neither impair non-fusogenic nor fusogenic death progression, a dependency on necroptosis during OV-mediated death seems to be unsubstantiated or complexly regulated. This is supported by the fact that RIPK1 and RIPK3 both have mutual regulatory roles and kinase-independent functions in non-necroptotic death pathways, including caspase 8-dependent apoptosis (extensively reviewed in [163]). During rNDV infection, RIPK1 induces necroptosis via RIPK3 and MLKL phosphorylation, but Liao et al. further identified a central regulatory role of RIPK1 by self-aggregating and recruiting p-MLKL to rNDV stress granules [74]. Although not investigated within the scope of this project, their findings propose an alternative regulatory mechanism during which RIPK1 counters necroptotic p-MLKL pore formation, which could also apply to rVSV-NDV syncytial death.

Moreover, another aspect worth considering in the context of mutual pathway regulation is the individual ubiquitination and phosphorylation status of RIPK1 and RIPK3, which determine interactions via RHIM domains and thereby define cell death and inflammatory outcomes. To date, it has not been demonstrated that rVSV or rNDV can activate necroptosis via RIPK3-ZBP1 or RIPK3-TRIF interaction, independent of RIPK1 and preceding death-receptor signaling (as mentioned in 1.2.2). While it is yet also unknown whether rVSV or rNDV express RHIM-containing proteins or produce Z-form DNA or RNA intermediates during their life cycle, both parental viruses induce type I IFN production in a first-line antiviral defense via TLR3-TRIF-mediated sensing [164, 165]. Provided that this branch of viral sensing and type I IFN signaling is not defective, rVSV and fusogenic hybrid rVSV-NDV could presumably induce TRIF-RIPK3 interaction and subsequently activate RIPK1-independent necroptosis of tumor cells. Further research in this direction would not only help uncover mechanisms of OV-induced death signaling but would also support the overall understanding of rVSV-NDV antiviral sensing pathways in tumor cells.

To simplify pathway discrimination, future experimental design should comprise knockout cell infections in the presence of external death receptor stimulation and specific inhibitors for the individual caspases, MLKL, RIPK1, or RIPK3 (such as GSK-840, among others mentioned in [57]). Combined with downstream proteomics analysis of effector molecules, this complete abrogation or induction of apoptosis or necroptosis can define their essentiality during fusogenic and non-fusogenic OV-mediated killing. Investigation of apoptosis and necroptosis regulators, other than the molecules characterized here, can further help in the identification of

an underlying pathway that dictates a syncytial cell death. Relevant molecules include, for example, monitoring of inflammatory and additional effector caspases, pro- and anti-apoptotic members of the BH3-only protein family, the caspase 8 regulator c-FLIP or detailed characterization of RIPK1, RIPK3, and MLKL phosphorylation and ubiquitination status. Though the presence and phosphorylation of the individual necroptosis regulators, RIPK1, RIPK3, and MLKL, were shown by Western blot analysis, follow-up experiments are needed in order to prove their assembly into the necrosome complex by co-immunoprecipitation, as previously demonstrated by other groups [166-168].

4.1.6 Deciphering the downstream mediator of syncytia destruction

As an end-stage of rVSV-NDV infection, lytic syncytial death was microscopically evident but the downstream event mediating syncytium disintegration was unknown:
Is it driven by effector caspases that activate apoptotic effector molecules, by necroptotic p-MLKL membrane pore formation or by another lytic pathway? A main aim of the project was to address this question.

4.1.6.1 phospho-MLKL syncytial membrane pores

Overall, the hitherto discussed results cautiously affirm that rVSV-NDV and rVSV trigger necroptosis as an alternate cellular demise pathway during which p-MLKL membrane pore formation may be accountable for the lytic nature of cell death. Data ambiguity and scope of the applied assays could not provide conclusive evidence that translocated p-MLKL oligomers indeed effectuated destruction of the syncytial membrane and should be analyzed in the future by immunofluorescence microscopy, as nicely demonstrated by Samson and coworkers [169]. Nevertheless, the results show that MLKL deletion by CRISPR/Cas9 or inhibition by NSA is immediately compensated for by amplifying alternative cell-disintegrating pathways, as detailed in the next section.

4.1.6.2 Caspase-activated lytic downstream effectors

Fusion-incompetent rVSV preferentially destroys A549 and H1437 tumor cells via apoptosis, but effector caspase 3 deletion forced cells to alternate to another non-apoptotic pathway, apparent by delayed oncolysis and enlarged cell rounding, which could be a sign of necroptotic swelling. This compares to a study by Hobbs et al., which identified caspase 3-dependent apoptotic shrinkage and infected cell detachment, while rVSV replication and a cell rounding phenotype were maintained in caspase 3 knockout cells [133]. Since it is also possible that caspase 3 activity is replaced by effector caspases 6 and 7, or that cells switch to necroptosis to induce death, additional mediators of these pathways should be confirmed by supporting Western blot analysis or enzyme activity assays in follow-up studies.

Strikingly, knockout of caspase 3 caused extended syncytiogenesis and delayed oncolysis in both human lung cancer cell lines and murine B16 cells. This unique effect could be phenotypically increased upon further caspase blockade with zVAD. Thus, rVSV-NDV syncytia destruction is likely orchestrated by caspase 3, and while absent or inhibited, cell-cell fusions continue to expand until an alternative membrane rupturing process takes over. Similar to the syncytia morphology of rVSV-NDV-infected A549 cells, RSV infection in A549 cells sheds off dying syncytia from infected monolayers in a caspase 3/7-dependent mechanism that can be prevented by zVAD [148]. Oncolysis of thyroid carcinoma cells by an engineered, fusogenic Sendai virus was also marked by caspase 3-dependent apoptosis, and addition of zVAD inhibited the cytotoxic effects [170]. Moreover, frNDV was also shown to activate caspase-mediated apoptosis [149, 151] but at the same time was found to maintain oncolysis in apoptosis-resistant cancer cells [75], and upon zVAD, but not Nec-1, treatment, rNDV-induced necroptosis could control syncytial death in parallel to apoptosis [171].

The concept of an apoptotic syncytial death is a mechanism that is also conserved in non-enveloped oncolytic, or distantly related syncytia forming, but non-oncolytic, viruses. Human immunodeficiency virus type-1 (HIV-1) envelope protein (env)-mediated cell-cell fusion of $CD4^+$ lymphocytes co-activates a pro-apoptotic program with DNA damage, mitotic catastrophe, and nuclear fusion. This apoptotic destruction was reported to limit the lifespan of HIV env-formed syncytia, and to strongly depend on mitochondrial and caspase function [172, 173]. Similarly, reovirus FAST fusion proteins build syncytia that remain intact and non-leaky for a long time until apoptotic pathways trigger death through loss of membrane stability [174]. Syncytial apoptosis thus describes a process that intends to maintain membrane integrity, allowing for syncytium expansion until caspases may orchestrate syncytial death.

4.1.6.3 Pyroptosis and PANoptosis

On the basis of the obtained results, the involvement of caspase 3 or p-MLKL in mediating the immunogenic syncytial death was not clearly elucidated. It is, therefore, plausible that alternative regulators may be involved. In recent years, pyroptosis has emerged as another regulated and inflammatory cell death mode. In pyroptosis, specialized PRRs (NOD-like receptor pyrin domain containing; NLRP1 and NLRP3) sense viral pathogens and associate with ASC adaptor proteins and pro-caspase 1 in a so-called inflammasome complex. The latter activates caspase 1 to cleave pro-inflammatory IL-1 and IL-18 and pyroptosis effector gasdermin (GSDM). N-terminal fragments of GSDM translocate to the plasma membrane and form membrane pores (described in detail in [63]). Fusion-competent rNDV induces the NLRP3 inflammasome and GSDM-D-controlled pyroptotic death, although at a cost of viral fitness and replication [175].

rVSV similarly depends on GSDM-E-mediated pyroptosis to shape a pro-inflammatory anti-tumor response. Lin et al. recently discovered that pyroptotic processes by rVSV even increased tumor infiltrations of CTLs and could synergize the oncolytic effects of rVSV with immune checkpoint blockade in tumor-bearing mice [176]. Interestingly, SARS-CoV2 virus also forms syncytia in infected epithelial cells, that have been recently shown to die via pyroptosis, but GSDM-E cleavage was dependent on preceding caspase 9 and caspase 3 activity. The authors further showed that GSDM-E knockouts, as well as zVAD treatment, both blocked syncytia destruction [177]. This would imply that, in addition to p-MLKL, caspase 3-activated members of the GSDM family could control rVSV-NDV syncytia disassembly in a pyroptotic fashion and explains why syncytia were able to spread in the absence of caspase 3.

Accordingly, follow-up investigations should implicate the involvement of pyroptosis signaling during rVSV-NDV syncytial death. As the fusogenic death activated multiple branches of apoptosis and necroptosis pathways, pyroptosis may act in concert with these activities. In fact, this combined death modality has been recently summarized under the term PANoptosis (pyroptosis + apoptosis + necroptosis, reviewed in detail in [178]) and could be a critical missing research link in deciphering rVSV-NDV induced oncolysis.

4.1.7 Modification of fusogenicity did not alter the underlying cell death program

Generation of the fusogenic variant, rVSV-NDV/F_{3aa}, was pursued with the aim of having a tool to interrogate whether modifying the degree of OV-induced fusogenicity affects the molecular signature and immunogenicity of the underlying cell death pathway(s). It was hypothesized that a reduction in the rate of syncytiogenesis via reversion of the L289A mutation to the wildtype amino acid in the rVSV-NDV/F_{3aa} construct could provide more time for viral replication and generation of immunogenic factors before syncytia collapse. As the results demonstrate, rVSV-NDV/F_{3aa} has a unique syncytia morphology but delayed fusogenicity, replication, and oncolysis were cell line-specific observations in Huh7 but less prominent in A549 or H1437 cells. The designed fusion assay revealed even higher fusogenicity from rVSV-NDV/F_{3aa} than from rVSV-NDV, which was surprising, as per literature, the L289A modification of the NDV/F protein has thus far been observed to confer a *hyperfusogenic* phenotype [37, 40].

With the reversal of the L289A mutation in the F protein of rVSV-NDV/F_{3aa}, dependency on the co-expression of HN and F protein on the cell surface to mediate syncytia formation was, in theory, enhanced [37, 38, 40]. According to Sergel et al., even if HN may be dispensable for fusion in the L289A-mutant setting, fusion efficiency increases when HN is present [37]. Cell-cell fusions involve well-coordinated membrane rearrangements (see **Figure 3**) during which the "*finding*" of a fusion partner is considered as the rate-limiting step, whereas the actual fusion and syncytium reorganization takes seconds to minutes [29]. Assuming that rVSV-NDV/F_{3aa} is more discriminative in merging with neighboring cells than rVSV-NDV, this would explain the relatively rapid formation and breakdown of rVSV-NDV syncytia in contrast to slowed-down syncytial spreading caused by rVSV-NDV/F_{3aa} in some cell lines. The higher degree of cell-cell fusion measured by the fusion assay in A549 and H1437 cells may then be interpreted as longer persistence of syncytia and not as faster cell-to-cell fusion itself. Phenotypic differences in fusogenicity between rVSV-NDV and rVSV-NDV/F_{3aa} could be explained by the necessity of establishing an individualized surface coverage of F and HN proteins on infected cells in order to efficiently trigger fusion with neighboring cells [25, 179]. For example, cell fusion rates and syncytia sizes of an rVSV chimera expressing MV F and HN were discovered to occur in direct correlation with the cell surface expression of MV attachment receptor CD46 [180]. Thus, rVSV-NDV and rVSV-NDV/F_{3aa} may also require unique host cell surface protein signatures to maintain their fusogenicity, which may not only explain cell line-specific differences in cell-cell fusion but also define the kinetic signature of the activated apoptosis and necroptosis death programs.

Throughout the cell death characterization, rVSV-NDV/F_{3aa} displayed a similar mechanism of apoptosis and necroptosis activation as rVSV-NDV but often did so to a lesser extent or in a delayed fashion, even though overall fusogenicity was generally higher. Consistent with data from rVSV-NDV, syncytial death mediated by rVSV-NDV/F_{3aa} could be temporally attenuated by zVAD or in caspase $3^{-/-}$ cells and potentiated upon additional extrinsic death receptor stimuli, which supports the theory of a caspase- or MLKL-mediated syncytial death. As some of the apoptotic or necroptotic effects were also seen for non-fusogenic rVSV, it is plausible to speculate that the cell death pathway regulation may be driven by an endogenous VSV gene that is shared by the rVSV-NDV vector (in example N, P, M, or L), despite the fusogenicity being mediated exclusively by the NDV envelope proteins expressed by the chimeric construct. Along similar lines, the impact of the fusion protein modification in rVSV-NDV/F_{3aa} on the underlying cell death pathway seemed to be secondary to effects on cell-cell fusion kinetics. In other words, some of apoptotic or necroptotic observations in response to rVSV-NDV/F_{3aa} infection may have been an indirect effect of altered fusion kinetics rather than directly mediated by the modified F protein. Nevertheless, further surface protein modifications or pharmacological compounds, like the hemifusion stage inhibitor, lysophosphatidylcholine [29], that completely abrogate or change fusogenicity of the hybrid OV, could be applied as future research tools to better draw a link between syncytial spreading and activated death pathways.

4.1.8 A fusogenic death exerts superior immunogenicity

OVs kill in a two-tiered attack on cancer cells, comprising a direct oncolytic effect that triggers cancer cell death and an indirect spark of inflammation in the TME to attract antigen-presenting and phagocytosing cells to an immune-deserted tumor and drive an adaptive immune response against additional tumor cells. An essential feature of ICD is to elicit expression of TAAs, and release a cocktail of immunogenic DAMPs and PAMPs through virus-mediated oncolysis, with the ultimate effect of triggering a broad anti-tumor immune response [7]. This research further attempted to decipher the immunogenicity of a fusogenic oncolytic viral death in human lung cancer cells by first investigating the classical ICD hallmarks (see **Figure 6** B). That a syncytial death has immune-stimulatory properties has been previously established [44], and our group demonstrated in Huh7 cells that fusogenic rVSV-NDV causes higher release of HMGB1, Hsp70, Hsp90, and ATP, in addition to exposure of CRT on the cell surface, compared to non-fusogenic rVSV [40]. The data presented here also demonstrate that both fusogenic variants, rVSV-NDV and rVSV-NDV/F_{3aa}, trigger ICD marker release and exposure in human lung cancer cells, although rVSV does as well to some extent.

Because the underlying death program of rVSV, rVSV-NDV, and rVSV-NDV/F_{3aa} was dynamically controlled by apoptosis and necroptosis in parallel, the immunogenicity of a syncytial death cannot be attributed to a single death pathway. Possibly, even other death modalities, like pyroptosis or autophagy, may play a determining role during ICD. Several studies have demonstrated a similar immunogenic outcome of high CRT exposure and elevated ICD marker excretion (Hsp70, Hsp90, ATP, and HMGB1) upon rNDV infection, but the underlying death pathways seem to be differentially defined by the respective cell line and cancer entity (see also **Table 1**). For example, related strains of rNDV were described to preferentially elicit an immunogenic type of necroptosis in glioma cells [171], induce immunogenic apoptosis in prostate cancer [72], trigger an apoptosis- and necroptosis-independent type of autophagy in lung cancer cells [73], and a multimodal death program in a melanoma cell background [71]. Likewise, another study reported that rVSV exhibits CRT surface translocation and release of HMGB1 and ATP to maintain an ICD in murine breast and ovarian cancer cells [181].

An Intriguing observation in this project was made in *in vitro* co-cultures of human DCs with oncolysates from infected A549 or H1437 cells. Only oncolysates infected with the fusogenic viruses efficiently matured DCs to a CD86 ^{high}, MHC-I ^{high}, and MHC-II ^{high} cross-presenting subtype in the established co-culture system. Previous results from our group showed immunogenic oncolysis of rVSV-NDV-infected B16-OVA cells leading to *in vitro* murine DC maturation into an antigen-presenting phenotype, marked by upregulation of CD86, CD80, MHC-I, and MHC-II on the DC surface [42], as well as *in vivo* evidence of this (unpublished data). Even though the presented data suggest that the death program of rVSV involves an immunogenic type of apoptosis and necroptosis, rapid disruption of single-infected cells seemed to generate slightly less antigenic and immune-stimulatory DAMPs compared to slower dying, fused tumor cells. In a study that parallels the presented data, Gauvrit and colleagues reported that oncolysates of MV-infected mesothelioma cells underwent an apoptotic syncytial death and efficiently stimulated DCs *in vitro* [182]. However, a mechanistic explanation for superior DC activation with syncytia-competent OVs remains unexplained. It can only be assumed that the net quantity and the immune-stimulatory nature of DAMPs and TAAs released from syncytia were better perceived by the APCs than the immunogenic material from rVSV-infected cells. Therefore, future research should refine the *in vitro* experimental system with model-antigen-expressing lung tumor cells to investigate efficient T cell cross-priming by antigen-loaded DCs. Secondary to this, one should elaborate on the cross-priming nature of DCs by demonstrating model antigen presentation via MHC-I and MHC-II and measuring T cell differentiation chemokines and cytokines, like IL-12, IL-1β and type I IFNs. Lastly, measurement of IFN-γ production and CTL-mediated cancer cytotoxicity could reveal whether the *in vitro* stimulated CTLs attained lung tumor specificity.

4.2 Hurdles to tackle for a successful *in vivo* translation

As efficient oncolysis and replication of rVSV-NDV in murine (**Figure 54**) and human (**Figure 15**) lung cancer cell lines was established in the first part of the project, the potential therapeutic effects of rVSV-NDV were investigated *in vivo* in orthotopic lung cancer. To that end, two distinct syngeneic murine models of orthotopic lung cancer were employed. Unfortunately, neither intratracheal instillation nor tail vein injection of rVSV-NDV prolonged the survival of KP mutant mice, and neither OV delivery route led to a noticeable reduction in lung tumor volumes. Secondary to this attempt, monitoring OV survival outcomes in alternate implantable models of orthotopic lung metastasis was impeded by numerous unexpected side effects, which complicated the continuation of the study. Even though both tumor models have been reported in literature [99, 101, 103, 183, 184] and were applied by colleagues at TUM, tumor growth kinetics, monitoring by lung µCT imaging, and an OV treatment schedule and delivery route had to be re-established. Especially since murine lung tumor models and the intratracheal administration of rVSV-NDV had not been previously applied by our group, the following sections will contextualize the findings and outline challenges faced in preclinical development of rVSV-NDV in this setting.

4.2.1 Facing the challenge of intratracheal oncolytic virus delivery

The respiratory tract is a constant entry port for airborne pathogens or allergens and, therefore, is safeguarded by a tightly regulated population of specialized airway epithelial cells forming a biophysical mucosal barrier along with lung-resident and recruited innate immune cells. PRRs sense viral respiratory infections and automatically evoke pro-inflammatory responses including expression of type I and III IFNs [185]. In this context, it was questioned, whether the established intravenous safe and effective dose of rVSV-NDV ($1x\ 10^7\ TCID_{50}$/injection) elicits strong inflammatory responses and adverse effects in the lung epithelium upon intratracheal OV delivery.

In healthy mice, a single intratracheal instillation with rVSV-NDV (in PBS) was indeed only tolerated at a reduced dose, defined as an intratracheal MTD of $1x\ 10^6\ TCID_{50}$ per administration (**Figure 48**). Although rVSV-NDV is not expected to replicate in healthy lung tissue, injected mice had a physiological threshold of the OV load in the lungs, above which the animals seemed to react strongly with high-grade local inflammation and acute antiviral immunity, which severely impeded mouse normal breathing and wellbeing. It is likely that the intratracheal bolus delivery may have overwhelmed the delicate balance of lung immunosurveillance and led to high focal doses [186] of OV triggering excessive IFN responses, similar to other acute respiratory infections, like SARS-CoV2 [187]. However, in this study, the evaluation of adverse effects was limited to physiological scoring parameters.

Hence, to characterize the antiviral pulmonary immune response, analysis of inflammatory cytokines and pulmonary innate immune cell activation would need to be analyzed. Especially when the immune cell signature changes during oncogenesis of KP lung tumors [188], OV recognition and resorption by the tumor and surrounding lung tissue can be impacted. Encouraging, repeated dosing with rVSV-NDV in weekly intervals at the intratracheal MTD was well tolerated by all tumor-bearing mice, even in conditions of high tumor burden. Thus, intratracheal delivery of rVSV-NDV is concluded a safe alternative to intravenous injection and allows repeated dosing, though at a reduced dose and at less frequent intervals, owing to the complexity of the delivery technique. Despite the reduced dose, it was speculated that tumor transduction efficiency could be enhanced by intratracheal delivery compared to the intravenous route, due to the direct, locoregional application, which is what motivated the continuation of these studies.

4.2.2 Facing the challenge of using surfactant as an adjuvant for pulmonary oncolytic virus delivery

It was hypothesized that pulmonary surfactant could function as an adjuvant carrier for the intratracheal delivery of rVSV-NDV and increase oncolysis in the KP murine lung cancer model. Despite the model study by Fukazawa et al., where an adenoviral gene therapy vector co-administered with pulmonary surfactant attained 10 times higher tumor reduction and deep alveolar penetration [97], the combination of surfactant with rVSV-NDV in the lung tumor models, however, was impeded by inauspicious results from *in vitro* proof-of-concept studies and preliminary dosing experiments.

In a formulation with Curosurf®, but not with Alveofact®, rVSV-NDV oncolytic potency was attenuated in A549 cells *in vitro* (**Figure 49**). Both are extracts of pulmonary surfactant from pigs or cattle, with a known yet variable composition, disclosed by the manufacturers. Major components of all surfactants are anionic phospholipids that have detergent-like functions and can solubilize viral lipid envelopes (extensively reviewed in [189]). Together with surfactant proteins, surfactant phospholipids can exert anti-inflammatory and antiviral roles against several enveloped respiratory viruses [190, 191]. Infection with enveloped rVSV-NDV depends on lipid membrane dynamics (**Figure 3**) and is presumably highly sensitive to surfactant, which may explain the dampened oncolysis seen with Curosurf® in A549 cells *in vitro*. Of note, despite these counteractive effects on rVSV-NDV replication, only Curosurf® was feasible for use in the *in vivo* studies, because of a suboptimal shelf life of Alveofact®.

A similar direct influence on infectibility and cell fusion could thus occur *in vivo* at the lung epithelial barrier and abrogate rVSV-NDV adsorption and access to the tumor site. In line with that and against expectations, during the intratracheal dose testing, a further 20-fold reduction in virus dose was necessary to maintain safety (intratracheal MTD in surfactant: 5x 10^4 $TCID_{50}$/administration, **Figure 50**). Albeit without additional experimental proof, it is hypothesized that Curosurf® surfactant improved rVSV-NDV tissue adsorption and uptake in distant alveolar regions, thereby shifting the physiological threshold of viral loads in the lung and causing toxic effects, similar to a high OV dose (1x 10^7 $TCID_{50}$/administration) in PBS. From a therapeutic perspective, deep tissue penetration could benefit tumor delivery and achieve cancer cell reduction [97] at a much lower rVSV-NDV dose. However, vice versa, a dose of 5x 10^4 $TCID_{50}$/administration might be below a virological threshold to establish infection and increases the risk of rapid viral clearance before initiation of oncolytic effects. Due to these underlying safety and efficacy concerns, surfactant-OV formulations were not further tested in tumor-bearing mice.

4.2.3 Facing the challenge of choosing an appropriate murine lung tumor model

Despite the intratracheal MTD limitation, the dosing experiments confirmed the technical feasibility of applying the novel OV treatment route in two orthotopic lung cancer models, and to compare its efficacy with standard intravenous injection. In genetically induced murine small-cell lung cancer, Kellish and colleagues reported that pulmonary delivery of an oncolytic myxoma virus yielded marked tumor reduction and survival prolongation due to cancer-specific replication and OV-mediated immune cell recruitment to the tumor [192]. Inspired by this work, rVSV-NDV oncolytic effects were evaluated in the well-described model of Ad-Cre-inducible KRAS mutant, p53 deleted lung adenocarcinoma in mice [99, 101].

Tumor formation in genetically driven models temporally correlates with the applied Ad-Cre dose for induction, and at 2.5x 10^7 PFU/mouse, multiple adenocarcinoma nodules are obtained after 8-12 weeks, and median survival of KP lung tumor-bearing mice is described as approximately 76 days post induction [101, 188, 192, 193]. In this study, KP lung tumors were initially induced with an intratracheal Ad-Cre dose of 1x 10^5 PFU/mouse, followed by increasing the dose to 5x 10^6 PFU/mouse in another cohort to speed up tumor growth. Since corresponding histopathology of tumorigenesis was not performed, unifying µCT-based criteria were established to assess oncogenesis, control for varying tumorigenesis due to different Ad-Cre doses for induction, and to randomize mice to therapy based on an equal starting tumor burden. A comparison with existing µCT and histology data from a similar KP model [194], led to the conclusion that tumors were at an adenocarcinoma stage when they fulfilled the defined inclusion criteria (section 3.3.2.1).

Collectively, the applied KP model generated heterogenous multifocal lung tumors in mice that were suitable for evaluating rVSV-NDV oncolytic effects. A direct comparison of survival benefits achieved from intratracheal versus intravenous OV treatment was unfortunately complicated by the fact that each group received distinct starting Ad-Cre doses for tumor induction. Nevertheless, comparison within the respective groups (PBS vs. rVSV-NDV in PBS) revealed that neither intravenous nor intratracheal rVSV-NDV treatment could achieve a significant survival benefit over PBS control (**Figure 52**). Reasons for this poor efficacy are manifold:

First and foremost, this model, although clinically relevant, is highly aggressive and presents a substantial degree of heterogeneity; therefore, would require very large treatment groups in order to obtain statistically meaningful findings. Furthermore, due to limitations in resolution and detection limit of the µCT, it is likely that treatment was initiated at an advanced stage in which KP lung tumors were already rapidly invading the pulmonary air sacs and intrapleural space, thereby limiting the window for induction of sufficient therapeutic responses.

The weekly dose of rVSV-NDV or the dosing schedule was not optimized and may not have been sufficient to impact heterogeneity and the checkless pace of KP tumor growth, as monitored by µCT (**Figure 53**). Hence, an earlier treatment onset at a lower starting tumor load could have led to superior survival outcomes upon OV treatment. As the immune cell composition in KP lung adenocarcinomas evolves with increasing malignancy [188], an earlier OV treatment can effectively impact immunogenicity by inducing an *in-situ* vaccination effect to prime anti-cancer immunity [6]. However, since tumors are hardly detectable by µCT imaging below 1 mm^3 [183], correlating histopathology or *ex vivo* necropsy would be required to better pinpoint an earlier therapy beginning.

Another possible explanation is the insufficient tumor targeting and penetration achieved by the applied intratracheal injection of rVSV-NDV. Other than the mechanical control (air-flow-meter) for the correct insertion of the tracheal catheter, it can only be assumed that the applied virus evenly distributes to all lobes and reaches the tumor site. It is thus possible that before reaching the TME, endogenous surfactant, innate antiviral immunity, or cilial movement of the lung epithelia already actively prevented uptake of the OV in the lungs [98, 185, 189].

Lastly, the presented data do not yet provide information on the OV-triggered antiviral and anti-cancer immunogenicity. Whether existing inflammatory cells or cytokine expression in the lungs inhibited efficient virus replication and spread, or the absence of an efficient rVSV-NDV-mediated anti-tumor immune response in the KP model was a confounding factor for the missing survival benefits, cannot be determined from the obtained data. In this regard, the last section (4.3.2) suggests an alternative murine model that could better address these questions.

In a second approach, it was questioned whether rVSV-NDV would prolong the survival of mice in another orthotopic implantation model of lung cancer. The main objective was to achieve fast-growing, reproducible tumors in the lungs by tail vein injection of B16-OVA or LLC cells, and attempt an early therapy onset with rVSV-NDV by either intravenous injection or intratracheal administration. However, reliable survival data were not obtained from either of these models, as extensive off-target tumor engraftment was prevalent (**Figure 55**). Even though B16-OVA and LLC cells were both administered at cell concentrations lower or equal to those reported in literature [104, 184, 195], distribution and invasiveness of cancer cell engraftment to organs other than the lungs have not been previously reported in such a degree [195], especially not for LLC cells. Additionally, µCT imaging was not sufficiently sensitive to accurately detect B16-OVA or LLC nodules in the lungs at early growth stages. Considering the fast tumor progression, defining a plausible treatment window for initiating the OV therapy before mice reached end-point criteria was challenging.

In conclusion, although the presented data set for this model is incomplete, the preliminary results suffice to conclude that the implantable “experimental metastasis” model requires further optimization in order to allow for meaningful results in therapeutic studies.

The LLC lung tumor model has been early described as notoriously non-immunogenic [196], and model-antigen-expressing LLC-OVA cells were reported to fail in eliciting an antigen-specific T cell response during ICI therapy [197]. Notwithstanding, this lack of immunogenicity in lung tumors may be overcome by OVs, referring to the great potential of reprogramming the TME to an immune-infiltrated “*hot*” TME through the immunogenic OV-mediated killing. In an ICI therapy-resistant lung cancer model, Masemann et al. demonstrated such a synergistic anti-tumor effect with enhanced immune-mediated tumor destruction by using an oncolytic infuenza A virus variant in combination with B7-H3 ICI therapy [198]. In conclusion, with an appropriate lung tumor model and OV delivery route, exploring similar potential synergistic effects using rVSV-NDV in combination with ICI therapy remains a promising future research approach.

4.3 Future perspectives

4.3.1 Deciphering the mode of syncytial death to arm rVSV-NDV in future next-generation vectors

rVSV-NDV is a promising hybrid vector for oncolytic virotherapy of cancer. However, the cytotoxic phenomenon of tumor syncytia development and death is mechanistically and immunologically still poorly characterized. Syncytia formation is a tightly regulated process of cellular intermixing and dramatic rearrangements of the cellular architecture [29]. Syncytial death, however, has been described as an amorphous but immunogenic event [44]. Some of the complexity of the syncytial cell death mediated by rVSV-NDV was unraveled in this study, demonstrating that oncolysis by rVSV-NDV and the fusogenic variant rVSV-NDV/F_{3aa} involves parallel apoptotic and necroptotic signaling cues that culminate in ICD. Certainly, at this stage, studies of the engagement of additional death pathways, like pyroptosis and autophagy, are warranted to close unknown mechanistic links and identify druggable regulators.

Translational OV research is open to a theoretically unlimited range of targetable solid cancer entities with unique genetic signatures and individual TMEs. This inevitably makes investigating oncolytic cell death, antiviral, and anti-tumoral mechanistic pathways, a tedious empirical process. On the upside, however, this can uncover novel opportunities to tailor OV therapy through combinations with approved anti-cancer agents or the design of OV vectors expressing immune- or cell death-stimulating payloads that are individualized for the cancer.

As previously mentioned, combination of apoptosis-promoting Smac mimetics with an rVSV-based oncolytic vector expressing TNF-α, rVSV(MΔ51)-TNF-α, is a promising strategy to synergize classic oncolytic effects with enhancing cancer cell apoptosis [161]. With regard to the preclinical development of rVSV-NDV, a potential combination of LCL-161 with a recently cloned rVSV-NDV variant armed to express murine TNF-α (rVSV-NDV-m-TNF-α) can be a valuable therapeutic option. Research with this new vector is still underway and would require a thorough characterization of the synergism and underlying death pathway. Other research approaches pursue encoding of TRAIL or Beclin-1 as therapeutic transgenes, in order to boost the inherent oncolytic death stimulation with additional cancer cell apoptosis and autophagy [199, 200]. Alternatively, necroptosis stimulation by OV-encoded payloads can also result in therapeutic benefits. For instance, elevated neoantigen release and induction of a potent anti-tumor immune response through immunogenic necroptosis was achieved by a recombinant vaccinia virus vector engineered to express MLKL [201].

Thus, once crucial mediators of the rVSV-NDV-mediated syncytial cancer cell death are identified, next-generation vectors can be designed by arming rVSV-NDV with transgenes that specifically drive an immunogenic type of cell death inside the tumor.

However, the immunological crux of OV immunotherapy is to establish a fine balance between innate antiviral and the desired anti-tumoral immunity. Especially in the *in vivo* setting, innate immunity and potentially a pre-existing humoral immunity to the viral vectors presents a major challenge to OV therapy and becomes a considerable limitation to the effectiveness of repetitive dosing [6]. In similar lines, a better understanding of the underlying death, antiviral, and anti-tumoral mechanisms can help to skew the immunological effects in favor of a long-lasting anti-tumor immunity. The portfolio of putative transgenes thereby ranges from TAAs, ICIs, bi-specific T cell engagers (BiTes), or immunoreactive cytokines, and many others (as detailed in [202]). Current strategies pursued by our group include the development of rVSV-NDV expressing IL-12, IL-15, TNF-α, soluble versions of the immune checkpoint PD-1 or a short-chain variable fragment antibody against PD-1 (PD-1_{scFv}), many of which already show promising therapeutic potential in cell culture and animal models.

4.3.2 Prerequisites for studying rVSV-NDV therapeutic effects in murine lung tumors

One profound limitation of the *in vivo* study was the heterogeneity and unsuitability of the applied tumor models. The yet undefined treatment schedule for murine lung cancer and a somewhat "*blind*" intratracheal application is considered another weakness of the approach. Alternative approaches and solutions to some of the outlined hurdles in the preclinical development of an rVSV-NDV therapy in lung cancer are suggested.

Achieving systemic OV drug delivery, as opposed to intratumoral injection, bears one of the biggest challenges in development. It broadens the therapeutic spectrum to metastatic tumors, but uncontrolled biodistribution, potential sequestration in the liver and spleen, and dilution and neutralization effects in the blood, render effective dosing of a replicating vector a major limitation [93]. One approach to overcome this, is to optimize vector drug delivery by packaging of OVs as cargo inside carrier cells, such as autologous immune cells [203], using specialized OV formulations, re-targeting through vector engineering or using alternative routes of administration. With respect to limited experience in rVSV-NDV targeting to the lung, one should scrutinize rVSV-NDV pharmacokinetics in the respiratory tract of healthy and tumor-bearing mice. That includes an in-depth analysis of the effect of individual surfactant components on the viral envelope, investigation of rVSV-NDV interaction with lung-resident immune cells, as well as defining a suitable adjuvant formulation that improves OV lung delivery.

As a first step, one could quantify intratumoral virus content at an early time-point after treatment, in order to discriminate between uptake and replication (or both), as the major challenge in this setting. Additionally, it would be important to characterize cytokine expression and immune cell signatures in the lung, before versus after treatment, in order to investigate potential barriers to, as well as opportunities for an effective rVSV-NDV-based therapeutic approach.

In this study, longitudinal µCT-based evaluation and quantification of lung tumors was done by manually drawing regions of interest (tumor nodules) in each anatomical plane, which was laborious and slow. The risk of intra-analyst variation or inaccuracy in volumetric quantification increases with high tumor burden and large group sizes. Therefore, future studies should implement machine-based learning algorithms for an unbiased, fast, and automated µCT-based tumor analysis. Additionally, there is a need for greater tumor detection sensitivity, especially in the preclinical setting where even extremely small tumors can mean a short prognosis in a 20-gram mouse. Impressive and rapidly growing knowledge is already available in the field and has proven its superior accuracy and speed in quantification of large cohorts of NSCLC-bearing mice compared to manual segmentation [204, 205]. Through additional correlation of image-based quantification with classical histopathology and necropsy, group randomization and immediate therapy monitoring could be refined.

An essential step in OV therapy development is to translate *in vitro* observations into a predictive, immunocompetent animal tumor model that best mimics a therapeutic scenario in humans. In addition to allograft or xenograft implantation models, which rely on a highly artificial immune-deficient setting, numerous genetically induced lung cancer models are available for recapitulating human lung cancer in mice [206]. However, even the well-known genetically induced KP model is considered reluctantly responsive in research investigating immunotherapies [193]. As mentioned above, through an OV-mediated immunogenic type of cancer cell death and inflammation, this poor immunogenicity could be reconverted to an immune-infiltrated lung TME. Because KP tumors sparsely express neoantigens and tumor-specific T cell responses are a rare event, Fitzgerald and colleagues recently proposed the KP-NINJA mouse model as an immunogenic alternative to the classical KP model [193]. The KP-NINJA (inversion inducible joined neoantigen) model features an inducible *in vivo* switch for *de novo* neoantigen production from KP lung tumors, which attracts antigen-specific $CD8^+$ T cells to the tumor. Furthermore, the authors demonstrated that adenocarcinoma cell lines from the KP-NINJA model attained responsiveness to ICI therapy [193]. Thus, in addition to some of the above-described aspects, implementing the KP-NINJA model could highly benefit the future preclinical translation of rVSV-NDV immunotherapy into mouse lung cancer.

5 APPENDIX

5.1 List of Abbreviations

Ad-Cre	*adenovirus expressing Cre recombinase*
Apaf-1	*apoptotic peptidase activating factor 1*
APCs	*antigen presenting immune cells*
Bcl	*B-cell lymphoma*
BID	*BH3-only interacting domain death agonist*
c-FLIP	*FLICE-like inhibitory protein*
cIAP	*cellular inhibitor of apoptosis*
CPEs	*cytopathic effects*
CRT	*calreticulin*
CT	*computer tomography*
CTLs	*cytotoxic T lymphocytes*
CYLD	*cylindromatosis deubiquitinase*
DAMPs	*danger-associated molecular patterns*
DC	*dendritic cell*
DISC	*death-inducing signaling complex*
Doxo	*doxorubicin*
eGFP	(*enhanced) green fluorescent protein*
F	*fusion protein*
GAPDH	*glyceraldehyde 3-phosphate dehydrogenase*
GM-CSF	*granulocyte-macrophage colony-stimulating factor*
HCC	*hepatocellular carcinoma*
HMGB1	*high-mobility group box 1 protein*
HN	*hemagglutinin neuraminidase*
hpi	*hours post infection*
Hsp	*heat-shock proteins*
i.tr.	*intratracheal*
i.v.	*intravenous*
ICD	*immunogenic cell death*
ICI	*immune checkpoint inhibitor*
IFN	*interferon*
IL	*interleukin*
kDa	*kilodalton*
KP	*K-ras LSL-G12D/+; p53fl/fl mice*
KRAS	*Kirsten rat sarcoma*

LDH	*lactate dehydrogenase*
LLC	*Lewis-lung carcinoma*
Mcl-1	*induced myeloid leukemia cell differentiation protein-1*
mcs	*multiple cloning site*
MHC	*major histocompatibility complex*
MLKL	*mixed-lineage kinase domain-like*
MMF	*Medetomidin-Midazolam-Fentanyl*
MOI	*multiplicity of infection*
MOMP	*mitochondrial outer membrane permeabilization*
MTD	*maximum tolerated dose*
MTX	*mitoxantrone*
MV	*Measles virus*
MVA	*Modified Vaccinia Virus Ankara*
NDV	*Newcastle disease virus*
Nec-1	*necrostatin-1*
NSA	*necrosulfonamide*
NSCLC	*non-small cell lung cancer*
NTC	*non-target control*
OV	*oncolytic virus*
OVA	*chicken ovalbumin antigen*
PAMPs	*pathogen-associated molecular patterns*
PARP	*poly-(ADP-ribose) polymerase*
PBMCs	*peripheral blood mononuclear cells*
PDAC	*pancreatic ductal adenocarcinoma*
PFU	*plaque forming units*
PRRs	*pattern recognition receptors*
PS	*phosphatidylserine*
r	*recombinant*
RHIM	*RIP homotypic interaction motif*
RIPK	*receptor-interacting protein kinase*
RLR	*retinoic-acid-inducible gene like receptor*
RSV	*Respiratory syncytial virus*
SD	*standard deviation*
SMAC	*second mitochondrial activator of a caspases*
TAA	*tumor-associated antigen*
$TCID_{50}$	*50 % Tissue Culture Infectious Dose*
TLR	*toll-like receptor*

TME	*tumor microenvironment*
TNF	*tumor necrosis factor*
TRAIL	*TNF-related apoptosis-inducing ligand*
TRIF	*TIR-domain-containing adapter-inducing IFN-beta*
VSV	*Vesicular stomatitis virus*
VV	*Vaccinia virus*
ZBP1	*Z-DNA binding protein 1*

5.3 List of Figures

5.4 List of Tables

6 REFERENCES

1. Scott, E.C., et al., *Trends in the approval of cancer therapies by the FDA in the twenty-first century.* Nature Reviews Drug Discovery, 2023. **22**(8): p. 625-640.
2. Zhang, Y. and Z. Zhang, *The history and advances in cancer immunotherapy: understanding the characteristics of tumor-infiltrating immune cells and their therapeutic implications.* Cellular & Molecular Immunology, 2020. **17**(8): p. 807-821.
3. Russell, L., et al., *Oncolytic Viruses: Priming Time for Cancer Immunotherapy.* BioDrugs, 2019. **33**(5): p. 485-501.
4. Hanahan, D. and R.A. Weinberg, *Hallmarks of cancer: the next generation.* Cell, 2011. **144**(5): p. 646-74.
5. Engeland, C.E. and J.C. Bell, *Introduction to Oncolytic Virotherapy*, in *Oncolytic Viruses*, C.E. Engeland, Editor. 2020, Springer New York: New York, NY. p. 1-6.
6. Shalhout, S.Z., et al., *Therapy with oncolytic viruses: progress and challenges.* Nat Rev Clin Oncol, 2023. **20**(3): p. 160-177.
7. Palanivelu, L., C.H. Liu, and L.T. Lin, *Immunogenic cell death: The cornerstone of oncolytic viro-immunotherapy.* Front Immunol, 2022. **13**: p. 1038226.
8. Kelly, E. and S.J. Russell, *History of Oncolytic Viruses: Genesis to Genetic Engineering.* Molecular Therapy, 2007. **15**(4): p. 651-659.
9. Garber, K., *China Approves World's First Oncolytic Virus Therapy For Cancer Treatment.* JNCI: Journal of the National Cancer Institute, 2006. **98**(5): p. 298-300.
10. Greig, S.L., *Talimogene Laherparepvec: First Global Approval.* Drugs, 2016. **76**(1): p. 147-54.
11. MacLachlan, N.J. and E.J. Dubovi, *Chapter 18 - Rhabdoviridae*, in *Fenner's Veterinary Virology (Fifth Edition)*. 2017, Academic Press: Boston. p. 357-372.
12. Acheson, N.H., D. Kolakofsky, and C. Richardson, *Fundamentals of Molecular Virology - Chapter 15 Paramyxoviruses and Rhabdoviruses*. Vol. 2. 2012, Wiley.
13. Finkelshtein, D., et al., *LDL receptor and its family members serve as the cellular receptors for vesicular stomatitis virus.* Proc Natl Acad Sci U S A, 2013. **110**(18): p. 7306-11.
14. Hastie, E., et al., *Understanding and altering cell tropism of vesicular stomatitis virus.* Virus Res, 2013. **176**(1-2): p. 16-32.
15. Pikor, L.A., J.C. Bell, and J.-S. Diallo, *Oncolytic Viruses: Exploiting Cancer's Deal with the Devil.* Trends in Cancer, 2015. **1**(4): p. 266-277.
16. Stojdl, D.F., et al., *VSV strains with defects in their ability to shutdown innate immunity are potent systemic anti-cancer agents.* Cancer Cell, 2003. **4**(4): p. 263-275.

17. Wu, L., et al., *rVSV(M Delta 51)-M3 is an effective and safe oncolytic virus for cancer therapy.* Hum Gene Ther, 2008. **19**(6): p. 635-47.
18. Naik, S., et al., *Engineering VSV-IFN-NIS for the Treatment of Multiple Myeloma.* Blood, 2009. **114**(22): p. 378-378.
19. Zhang, L., et al., *Safety Studies in Tumor and Non-Tumor-Bearing Mice in Support of Clinical Trials Using Oncolytic VSV-IFNβ-NIS.* Hum Gene Ther Clin Dev, 2016. **27**(3): p. 111-22.
20. McGarrah, P.W., et al., *Phase 1/2 trial of vesicular stomatitis virus expressing human interferon-β and NIS (VSV-IFNβ-NIS), with pembrolizumab, in patients with neuroendocrine carcinoma.* Journal of Clinical Oncology, 2023. **41**(4_suppl): p. TPS657-TPS657.
21. Johnson, J.E., et al., *Neurovirulence properties of recombinant vesicular stomatitis virus vectors in non-human primates.* Virology, 2007. **360**(1): p. 36-49.
22. Shinozaki, K., et al., *Prophylactic alpha interferon treatment increases the therapeutic index of oncolytic vesicular stomatitis virus virotherapy for advanced hepatocellular carcinoma in immune-competent rats.* J Virol, 2005. **79**(21): p. 13705-13.
23. MacLachlan, N.J. and E.J. Dubovi, *Chapter 17 - Paramyxoviridae and Pneumoviridae*, in *Fenner's Veterinary Virology (Fifth Edition)*. 2017, Academic Press: Boston. p. 327-356.
24. Schirrmacher, V., *Molecular Mechanisms of Anti-Neoplastic and Immune Stimulatory Properties of Oncolytic Newcastle Disease Virus.* Biomedicines, 2022. **10**(3): p. 562.
25. Chang, A. and R.E. Dutch, *Paramyxovirus fusion and entry: multiple paths to a common end.* Viruses, 2012. **4**(4): p. 613-36.
26. Lozada, C., et al., *Identification and Characteristics of Fusion Peptides Derived From Enveloped Viruses.* Front Chem, 2021. **9**: p. 689006.
27. Burton, C., M.Y. Bartee, and E. Bartee, *Impact of Induced Syncytia Formation on the Oncolytic Potential of Myxoma Virus.* Oncolytic Virother, 2019. **8**: p. 57-69.
28. Park, M.S., et al., *Engineered viral vaccine constructs with dual specificity: avian influenza and Newcastle disease.* Proc Natl Acad Sci U S A, 2006. **103**(21): p. 8203-8.
29. Whitlock, J.M. and L.V. Chernomordik, *Flagging fusion: Phosphatidylserine signaling in cell-cell fusion.* J Biol Chem, 2021. **296**: p. 100411.
30. Pecora, A.L., et al., *Phase I trial of intravenous administration of PV701, an oncolytic virus, in patients with advanced solid cancers.* J Clin Oncol, 2002. **20**(9): p. 2251-66.
31. Buijs, P.R., et al., *Oncolytic viruses: From bench to bedside with a focus on safety.* Hum Vaccin Immunother, 2015. **11**(7): p. 1573-84.
32. Sinkovics, J.G. and J.C. Horvath, *Newcastle disease virus (NDV): brief history of its oncolytic strains.* J Clin Virol, 2000. **16**(1): p. 1-15.

33. Zamarin, D., et al., *Localized oncolytic virotherapy overcomes systemic tumor resistance to immune checkpoint blockade immunotherapy.* Sci Transl Med, 2014. **6**(226): p. 226ra32.
34. Clinicaltrials.gov, *A Study of MEDI9253 in Combination With Durvalumab in Select Solid Tumors, NCT04613492*. 2023, AstraZeneca: https://clinicaltrials.gov/study/NCT04613492.
35. Muik, A., et al., *Pseudotyping vesicular stomatitis virus with lymphocytic choriomeningitis virus glycoproteins enhances infectivity for glioma cells and minimizes neurotropism.* J Virol, 2011. **85**(11): p. 5679-84.
36. Porosnicu, M., et al., *Phase I study of VSV-GP (BI 1831169) as monotherapy or combined with ezabenlimab in advanced and refractory solid tumors.* Future Oncol, 2022. **18**(24): p. 2627-2638.
37. Sergel, T.A., L.W. McGinnes, and T.G. Morrison, *A single amino acid change in the Newcastle disease virus fusion protein alters the requirement for HN protein in fusion.* J Virol, 2000. **74**(11): p. 5101-7.
38. Li, J., et al., *Decreased dependence on receptor recognition for the fusion promotion activity of L289A-mutated newcastle disease virus fusion protein correlates with a monoclonal antibody-detected conformational change.* J Virol, 2005. **79**(2): p. 1180-90.
39. Altomonte, J., et al., *Engineered newcastle disease virus as an improved oncolytic agent against hepatocellular carcinoma.* Mol Ther, 2010. **18**(2): p. 275-84.
40. Abdullahi, S., et al., *A Novel Chimeric Oncolytic Virus Vector for Improved Safety and Efficacy as a Platform for the Treatment of Hepatocellular Carcinoma.* J Virol, 2018. **92**(23).
41. Krabbe, T., et al., *Adoptive T Cell Therapy Is Complemented by Oncolytic Virotherapy with Fusogenic VSV-NDV in Combination Treatment of Murine Melanoma.* Cancers (Basel), 2021. **13**(5).
42. Marek, J., et al., *Oncolytic virotherapy with chimeric VSV-NDV synergistically supports RIG-I-dependent checkpoint inhibitor immunotherapy.* Mol Ther Oncolytics, 2023. **30**: p. 117-131.
43. Fu, X. and X. Zhang, *Potent systemic antitumor activity from an oncolytic herpes simplex virus of syncytial phenotype.* Cancer Res, 2002. **62**(8): p. 2306-12.
44. Bateman, A.R., et al., *Viral fusogenic membrane glycoproteins kill solid tumor cells by nonapoptotic mechanisms that promote cross presentation of tumor antigens by dendritic cells.* Cancer Res, 2002. **62**(22): p. 6566-78.
45. Burton, C. and E. Bartee, *Syncytia Formation in Oncolytic Virotherapy.* Mol Ther Oncolytics, 2019. **15**: p. 131-139.

46. Krabbe, T. and J. Altomonte, *Fusogenic Viruses in Oncolytic Immunotherapy.* Cancers (Basel), 2018. **10**(7).
47. Ma, J., et al., *Characterization of virus-mediated immunogenic cancer cell death and the consequences for oncolytic virus-based immunotherapy of cancer.* Cell Death Dis, 2020. **11**(1): p. 48.
48. Vandenabeele, P., et al., *Molecular mechanisms of necroptosis: an ordered cellular explosion.* Nat Rev Mol Cell Biol, 2010. **11**(10): p. 700-14.
49. Bedoui, S., M.J. Herold, and A. Strasser, *Emerging connectivity of programmed cell death pathways and its physiological implications.* Nat Rev Mol Cell Biol, 2020. **21**(11): p. 678-695.
50. Van den Berghe, T., et al., *Molecular crosstalk between apoptosis, necroptosis, and survival signaling.* Mol Cell Oncol, 2015. **2**(4): p. e975093.
51. Vitale, I., et al., *Apoptotic cell death in disease-Current understanding of the NCCD 2023.* Cell Death Differ, 2023. **30**(5): p. 1097-1154.
52. Bock, F.J. and S.W.G. Tait, *Mitochondria as multifaceted regulators of cell death.* Nat Rev Mol Cell Biol, 2020. **21**(2): p. 85-100.
53. Cetraro, P., et al., *A Review of the Current Impact of Inhibitors of Apoptosis Proteins and Their Repression in Cancer.* Cancers (Basel), 2022. **14**(7).
54. Monier, B. and M. Suzanne, *Orchestration of Force Generation and Nuclear Collapse in Apoptotic Cells.* Int J Mol Sci, 2021. **22**(19).
55. Dondelinger, Y., et al., *Poly-ubiquitination in TNFR1-mediated necroptosis.* Cell Mol Life Sci, 2016. **73**(11-12): p. 2165-76.
56. Čopič, A., T. Dieudonné, and G. Lenoir, *Phosphatidylserine transport in cell life and death.* Curr Opin Cell Biol, 2023. **83**: p. 102192.
57. Chen, J., et al., *Molecular Insights into the Mechanism of Necroptosis: The Necrosome As a Potential Therapeutic Target.* Cells, 2019. **8**(12).
58. Vandenabeele, P., G. Bultynck, and S.N. Savvides, *Pore-forming proteins as drivers of membrane permeabilization in cell death pathways.* Nat Rev Mol Cell Biol, 2023. **24**(5): p. 312-333.
59. Mocarski, E.S., H. Guo, and W.J. Kaiser, *Necroptosis: The Trojan horse in cell autonomous antiviral host defense.* Virology, 2015. **479-480**: p. 160-6.
60. Orzalli, M.H. and J.C. Kagan, *Apoptosis and Necroptosis as Host Defense Strategies to Prevent Viral Infection.* Trends Cell Biol, 2017. **27**(11): p. 800-809.
61. Chen, X.Y., et al., *ZBP1-Mediated Necroptosis: Mechanisms and Therapeutic Implications.* Molecules, 2022. **28**(1).
62. Kaiser, W.J., et al., *Toll-like receptor 3-mediated necrosis via TRIF, RIP3, and MLKL.* J Biol Chem, 2013. **288**(43): p. 31268-79.

63. Verdonck, S., et al., *Viral manipulation of host cell necroptosis and pyroptosis.* Trends Microbiol, 2022. **30**(6): p. 593-605.
64. Cao, L. and W. Mu, *Necrostatin-1 and necroptosis inhibition: Pathophysiology and therapeutic implications.* Pharmacol Res, 2021. **163**: p. 105297.
65. Johnston, A. and Z. Wang, *Necroptosis: MLKL Polymerization.* J Nat Sci, 2018. **4**(7).
66. Rex, D.A.B., T.S. Keshava Prasad, and R.K. Kandasamy, *Revisiting Regulated Cell Death Responses in Viral Infections.* Int J Mol Sci, 2022. **23**(13).
67. Nailwal, H. and F.K. Chan, *Necroptosis in anti-viral inflammation.* Cell Death Differ, 2019. **26**(1): p. 4-13.
68. Schache, P., et al., *VSV virotherapy improves chemotherapy by triggering apoptosis due to proteasomal degradation of Mcl-1.* Gene Ther, 2009. **16**(7): p. 849-61.
69. Felt, S.A., M.J. Moerdyk-Schauwecker, and V.Z. Grdzelishvili, *Induction of apoptosis in pancreatic cancer cells by vesicular stomatitis virus.* Virology, 2015. **474**: p. 163-73.
70. Cary, Z.D., M.C. Willingham, and D.S. Lyles, *Oncolytic vesicular stomatitis virus induces apoptosis in U87 glioblastoma cells by a type II death receptor mechanism and induces cell death and tumor clearance in vivo.* J Virol, 2011. **85**(12): p. 5708-17.
71. Shao, X., et al., *STAT3 Contributes To Oncolytic Newcastle Disease Virus-Induced Immunogenic Cell Death in Melanoma Cells.* Front Oncol, 2019. **9**: p. 436.
72. Wang, X., et al., *Targeting STAT3 enhances NDV-induced immunogenic cell death in prostate cancer cells.* J Cell Mol Med, 2020. **24**(7): p. 4286-4297.
73. Ye, T., et al., *Oncolytic Newcastle disease virus induces autophagy-dependent immunogenic cell death in lung cancer cells.* Am J Cancer Res, 2018. **8**(8): p. 1514-1527.
74. Liao, Y., et al., *RIP1 is a central signaling protein in regulation of TNF-α/TRAIL mediated apoptosis and necroptosis during Newcastle disease virus infection.* Oncotarget, 2017. **8**(26): p. 43201-43217.
75. Mansour, M., P. Palese, and D. Zamarin, *Oncolytic specificity of Newcastle disease virus is mediated by selectivity for apoptosis-resistant cells.* J Virol, 2011. **85**(12): p. 6015-23.
76. Cuadrado-Castano, S., et al., *Enhancement of the proapoptotic properties of newcastle disease virus promotes tumor remission in syngeneic murine cancer models.* Mol Cancer Ther, 2015. **14**(5): p. 1247-58.
77. Chen, Daniel S. and I. Mellman, *Oncology Meets Immunology: The Cancer-Immunity Cycle.* Immunity, 2013. **39**(1): p. 1-10.
78. Galluzzi, L., et al., *Immunogenic cell death in cancer and infectious disease.* Nat Rev Immunol, 2017. **17**(2): p. 97-111.
79. Ahmed, A. and S.W.G. Tait, *Targeting immunogenic cell death in cancer.* Mol Oncol, 2020. **14**(12): p. 2994-3006.

80. Kepp, O., et al., *Surface-exposed and soluble calreticulin: conflicting biomarkers for cancer prognosis.* Oncoimmunology, 2020. **9**(1): p. 1792037.
81. Obeid, M., et al., *Calreticulin exposure dictates the immunogenicity of cancer cell death.* Nat Med, 2007. **13**(1): p. 54-61.
82. Binder, R.J., R. Vatner, and P. Srivastava, *The heat-shock protein receptors: some answers and more questions.* Tissue Antigens, 2004. **64**(4): p. 442-51.
83. Martins, I., et al., *Molecular mechanisms of ATP secretion during immunogenic cell death.* Cell Death Differ, 2014. **21**(1): p. 79-91.
84. Tang, D., T.R. Billiar, and M.T. Lotze, *A Janus tale of two active high mobility group box 1 (HMGB1) redox states.* Mol Med, 2012. **18**(1): p. 1360-2.
85. Rhodes, J.W., et al., *Human Dendritic Cell Subsets, Ontogeny, and Impact on HIV Infection.* Frontiers in Immunology, 2019. **10**.
86. Noubade, R., S. Majri-Morrison, and K.V. Tarbell, *Beyond cDC1: Emerging Roles of DC Crosstalk in Cancer Immunity.* Front Immunol, 2019. **10**: p. 1014.
87. Messmer, M.N., A.G. Snyder, and A. Oberst, *Comparing the effects of different cell death programs in tumor progression and immunotherapy.* Cell Death Differ, 2019. **26**(1): p. 115-129.
88. Malvezzi, M., et al., *European cancer mortality predictions for the year 2023 with focus on lung cancer.* Ann Oncol, 2023. **34**(4): p. 410-419.
89. Petrella, F., et al., *Stage III Non-Small-Cell Lung Cancer: An Overview of Treatment Options.* Curr Oncol, 2023. **30**(3): p. 3160-3175.
90. European-Cancer-Information-System, *ECIS Lung Cancer Burden in EU-27*. 2021, https://ecis.jrc.ec.europa.eu/pdf/factsheets/Lung_cancer_en-July_2021.pdf: European Union.
91. Li, Z., et al., *Lung cancer and oncolytic virotherapy--enemy's enemy.* Transl Oncol, 2023. **27**: p. 101563.
92. Zhang, Y.B., et al., *A Review of Non-Invasive Drug Delivery through Respiratory Routes.* Pharmaceutics, 2022. **14**(9).
93. Hill, C. and R. Carlisle, *Achieving systemic delivery of oncolytic viruses.* Expert Opin Drug Deliv, 2019. **16**(6): p. 607-620.
94. Danson, S.J., et al., *Oncolytic herpesvirus therapy for mesothelioma – A phase I/IIa trial of intrapleural administration of HSV1716.* Lung Cancer, 2020. **150**: p. 145-151.
95. Garbuzenko, O.B., et al., *Intratracheal Versus Intravenous Liposomal Delivery of siRNA, Antisense Oligonucleotides and Anticancer Drug.* Pharmaceutical Research, 2009. **26**(2): p. 382-394.

96. Morales-Nebreda, L., et al., *Intratracheal administration of influenza virus is superior to intranasal administration as a model of acute lung injury.* J Virol Methods, 2014. **209**: p. 116-20.
97. Fukazawa, T., et al., *Targeting KRAS mutation-bearing lung cancer in vivo by pulmonary surfactant-adenovirus-mediated gene transfer.* Anticancer Res, 2010. **30**(12): p. 4925-35.
98. Numata, M. and D.R. Voelker, *Anti-inflammatory and anti-viral actions of anionic pulmonary surfactant phospholipids.* Biochim Biophys Acta Mol Cell Biol Lipids, 2022. **1867**(6): p. 159139.
99. Jackson, E.L., et al., *The differential effects of mutant p53 alleles on advanced murine lung cancer.* Cancer Res, 2005. **65**(22): p. 10280-8.
100. Jackson, E.L., et al., *Analysis of lung tumor initiation and progression using conditional expression of oncogenic K-ras.* Genes Dev, 2001. **15**(24): p. 3243-8.
101. DuPage, M., A.L. Dooley, and T. Jacks, *Conditional mouse lung cancer models using adenoviral or lentiviral delivery of Cre recombinase.* Nat Protoc, 2009. **4**(7): p. 1064-72.
102. Timmons, J.J., S. Cohessy, and E.T. Wong, *Injection of Syngeneic Murine Melanoma Cells to Determine Their Metastatic Potential in the Lungs.* J Vis Exp, 2016(111).
103. Liu, P., et al., *In Vivo Imaging of Orthotopic Lung Cancer Models in Mice.* Methods Mol Biol, 2021. **2279**: p. 199-212.
104. Kim, K.J., et al., *STAT3 activation in endothelial cells is important for tumor metastasis via increased cell adhesion molecule expression.* Oncogene, 2017. **36**.
105. Labun, K., et al., *CHOPCHOP v2: a web tool for the next generation of CRISPR genome engineering.* Nucleic Acids Res, 2016. **44**(W1): p. W272-6.
106. Yushkevich, P.A., et al., *User-guided 3D active contour segmentation of anatomical structures: significantly improved efficiency and reliability.* Neuroimage, 2006. **31**(3): p. 1116-28.
107. Haider, S.R., H.J. Reid, and B.L. Sharp, *Tricine-SDS-PAGE.* Methods Mol Biol, 2012. **869**: p. 81-91.
108. Ebert, O., et al., *Oncolytic vesicular stomatitis virus for treatment of orthotopic hepatocellular carcinoma in immune-competent rats.* Cancer Res, 2003. **63**(13): p. 3605-11.
109. Altomonte, J., et al., *Synergistic antitumor effects of transarterial viroembolization for multifocal hepatocellular carcinoma in rats.* Hepatology, 2008. **48**(6): p. 1864-73.
110. Fuerst, T.R., et al., *Eukaryotic transient-expression system based on recombinant vaccinia virus that synthesizes bacteriophage T7 RNA polymerase.* Proc Natl Acad Sci U S A, 1986. **83**(21): p. 8122-6.

111. Kremer, M., et al., *Easy and Efficient Protocols for Working with Recombinant Vaccinia Virus MVA*, in *Vaccinia Virus and Poxvirology: Methods and Protocols*, S.N. Isaacs, Editor. 2012, Humana Press: Totowa, NJ. p. 59-92.
112. Abdelmageed, A.A. and M.C. Ferran, *The Propagation, Quantification, and Storage of Vesicular Stomatitis Virus.* Curr Protoc Microbiol, 2020. **58**(1): p. e110.
113. Hierholzer, J.C. and R.A. Killington, *Virus isolation and quantitation.* Virology Methods Manual, 1996: p. 25-46.
114. Zhang-Laboratory, *Addgene Lentiviral CRISPR Toolbox.* https://media.addgene.org/data/plasmids/52/52961/52961-attachment_B3xTwla0bkYD.pdf, 2014(24.02.2024).
115. Sanjana, N.E., O. Shalem, and F. Zhang, *Improved vectors and genome-wide libraries for CRISPR screening.* Nature Methods, 2014. **11**(8): p. 783-784.
116. Shalem, O., et al., *Genome-scale CRISPR-Cas9 knockout screening in human cells.* Science, 2014. **343**(6166): p. 84-87.
117. Liu, X., et al., *Key roles of necroptotic factors in promoting tumor growth.* Oncotarget, 2016. **7**(16): p. 22219-33.
118. Liu, P., et al., *Quantitation of calreticulin exposure associated with immunogenic cell death.* Methods Enzymol, 2020. **632**: p. 1-13.
119. Arbuzova, A., et al., *On the validity of lipid dequenching assays for estimating virus fusion kinetics.* Biochim Biophys Acta, 1994. **1190**(2): p. 360-6.
120. Nussbaum, O., C.C. Broder, and E.A. Berger, *Fusogenic mechanisms of enveloped-virus glycoproteins analyzed by a novel recombinant vaccinia virus-based assay quantitating cell fusion-dependent reporter gene activation.* Journal of virology, 1994. **68**(9): p. 5411-5422.
121. Kondo, N., et al., *Conformational changes of the HIV-1 envelope protein during membrane fusion are inhibited by the replacement of its membrane-spanning domain.* J Biol Chem, 2010. **285**(19): p. 14681-8.
122. Hall, M.P., et al., *Engineered luciferase reporter from a deep sea shrimp utilizing a novel imidazopyrazinone substrate.* ACS Chem Biol, 2012. **7**(11): p. 1848-57.
123. Schwinn, M.K., et al., *CRISPR-Mediated Tagging of Endogenous Proteins with a Luminescent Peptide.* ACS Chem Biol, 2018. **13**(2): p. 467-474.
124. Dixon, A.S., et al., *Activation of bioluminescence by structural complementation*. 2014, Promega Corp: US-patent US9797889B2.
125. Jessie, B. and H.M. Dobrovolny, *The role of syncytia during viral infections.* Journal of Theoretical Biology, 2021. **525**: p. 110749.

126. Fadok, V.A., et al., *Loss of phospholipid asymmetry and surface exposure of phosphatidylserine is required for phagocytosis of apoptotic cells by macrophages and fibroblasts.* J Biol Chem, 2001. **276**(2): p. 1071-7.
127. Dai, B., et al., *Preclinical Evaluation of Sequential Combination of Oncolytic Adenovirus Delta-24-RGD and Phosphatidylserine-Targeting Antibody in Pancreatic Ductal Adenocarcinoma.* Mol Cancer Ther, 2017. **16**(4): p. 662-670.
128. Amara, A. and J. Mercer, *Viral apoptotic mimicry.* Nat Rev Microbiol, 2015. **13**(8): p. 461-9.
129. Chang, W., et al., *Targeting phosphatidylserine for Cancer therapy: prospects and challenges.* Theranostics, 2020. **10**(20): p. 9214-9229.
130. Neumann, S., et al., *How do viruses control mitochondria-mediated apoptosis?* Virus Res, 2015. **209**: p. 45-55.
131. Morla, S., A. Kumar, and S. Kumar, *Newcastle disease virus mediated apoptosis and migration inhibition of human oral cancer cells: A probable role of β-catenin and matrix metalloproteinase-7.* Scientific Reports, 2019. **9**(1): p. 10882.
132. Sharif-Askari, E., et al., *Bax-dependent mitochondrial membrane permeabilization enhances IRF3-mediated innate immune response during VSV infection.* Virology, 2007. **365**(1): p. 20-33.
133. Hobbs, J.A., G. Hommel-Berrey, and Z. Brahmi, *Requirement of caspase-3 for efficient apoptosis induction and caspase-7 activation but not viral replication or cell rounding in cells infected with vesicular stomatitis virus.* Hum Immunol, 2003. **64**(1): p. 82-92.
134. Gaddy, D.F. and D.S. Lyles, *Vesicular stomatitis viruses expressing wild-type or mutant M proteins activate apoptosis through distinct pathways.* J Virol, 2005. **79**(7): p. 4170-9.
135. Mathieu, M.E., et al., *Folding, unfolding, and refolding of the vesicular stomatitis virus glycoprotein.* Biochemistry, 1996. **35**(13): p. 4084-93.
136. Najafov, A., et al., *BRAF and AXL oncogenes drive RIPK3 expression loss in cancer.* PLoS Biol, 2018. **16**(8): p. e2005756.
137. Koo, G.B., et al., *Methylation-dependent loss of RIP3 expression in cancer represses programmed necrosis in response to chemotherapeutics.* Cell Res, 2015. **25**(6): p. 707-25.
138. Osman, R., et al., *Calreticulin Release at an Early Stage of Death Modulates the Clearance by Macrophages of Apoptotic Cells.* Frontiers in Immunology, 2017. **8**.
139. Galluzzi, L., et al., *Consensus guidelines for the definition, detection and interpretation of immunogenic cell death.* J Immunother Cancer, 2020. **8**(1).
140. Zhao, M., et al., *Efficacy against lung metastasis with a tumor-targeting mutant of Salmonella typhimurium in immunocompetent mice.* Cell Cycle, 2012. **11**(1): p. 187-93.

141. Garcia-Hernandez Mde, L., et al., *Adoptive transfer of tumor-specific Tc17 effector T cells controls the growth of B16 melanoma in mice.* J Immunol, 2010. **184**(8): p. 4215-27.
142. Moriwaki, K., et al., *Differential roles of RIPK1 and RIPK3 in TNF-induced necroptosis and chemotherapeutic agent-induced cell death.* Cell Death Dis, 2015. **6**(2): p. e1636.
143. Yang, C., et al., *Regulation of RIP3 by the transcription factor Sp1 and the epigenetic regulator UHRF1 modulates cancer cell necroptosis.* Cell Death & Disease, 2017. **8**(10): p. e3084-e3084.
144. Pearce, A.F. and D.S. Lyles, *Vesicular stomatitis virus induces apoptosis primarily through Bak rather than Bax by inactivating Mcl-1 and Bcl-XL.* J Virol, 2009. **83**(18): p. 9102-12.
145. Burattini, S. and E. Falcieri, *Analysis of cell death by electron microscopy.* Methods Mol Biol, 2013. **1004**: p. 77-89.
146. Golla, N., L.J. Hong, and I. Chefetz, *Visualization of Necroptotic Cell Death through Transmission Electron Microscopy.* Methods Mol Biol, 2021. **2255**: p. 135-147.
147. Voigt, E.A., A. Swick, and J. Yin, *Rapid induction and persistence of paracrine-induced cellular antiviral states arrest viral infection spread in A549 cells.* Virology, 2016. **496**: p. 59-66.
148. Eckardt-Michel, J., et al., *The fusion protein of respiratory syncytial virus triggers p53-dependent apoptosis.* J Virol, 2008. **82**(7): p. 3236-49.
149. Elankumaran, S., D. Rockemann, and S.K. Samal, *Newcastle disease virus exerts oncolysis by both intrinsic and extrinsic caspase-dependent pathways of cell death.* J Virol, 2006. **80**(15): p. 7522-34.
150. Meng, S., et al., *Newcastle disease virus induces apoptosis in cisplatin-resistant human lung adenocarcinoma A549 cells in vitro and in vivo.* Cancer Lett, 2012. **317**(1): p. 56-64.
151. Ravindra, P.V., et al., *Time course of Newcastle disease virus-induced apoptotic pathways.* Virus Res, 2009. **144**(1-2): p. 350-4.
152. Ibraheem, K., et al., *TRAF3/p38-JNK Signalling Crosstalk with Intracellular-TRAIL/Caspase-10-Induced Apoptosis Accelerates ROS-Driven Cancer Cell-Specific Death by CD40.* Cells, 2022. **11**(20).
153. Wachmann, K., et al., *Activation and Specificity of Human Caspase-10.* Biochemistry, 2010. **49**(38): p. 8307-8315.
154. Olagnier, D., et al., *Activation of Nrf2 Signaling Augments Vesicular Stomatitis Virus Oncolysis via Autophagy-Driven Suppression of Antiviral Immunity.* Mol Ther, 2017. **25**(8): p. 1900-1916.

155. Margolin, N., et al., *Substrate and Inhibitor Specificity of Interleukin-1β-converting Enzyme and Related Caspases *.* Journal of Biological Chemistry, 1997. **272**(11): p. 7223-7228.
156. Gobeil, S., et al., *Characterization of the necrotic cleavage of poly(ADP-ribose) polymerase (PARP-1): implication of lysosomal proteases.* Cell Death Differ, 2001. **8**(6): p. 588-94.
157. Mozaffari Nejad, A.S., et al., *Oncolytic effects of Hitchner B1 strain of newcastle disease virus against cervical cancer cell proliferation is mediated by the increased expression of cytochrome C, autophagy and apoptotic pathways.* Microb Pathog, 2020. **147**: p. 104438.
158. Ginting, T.E., et al., *Antiviral interferons induced by Newcastle disease virus (NDV) drive a tumor-selective apoptosis.* Sci Rep, 2019. **9**(1): p. 15160.
159. Zhao, X., et al., *Evaluation of vesicular stomatitis virus mutant as an oncolytic agent against prostate cancer.* Int J Clin Exp Med, 2014. **7**(5): p. 1204-13.
160. Chen, J., et al., *Interferon-γ induces the cell surface exposure of phosphatidylserine by activating the protein MLKL in the absence of caspase-8 activity.* J Biol Chem, 2019. **294**(32): p. 11994-12006.
161. Beug, S.T., et al., *Combination of IAP Antagonists and TNF-α-Armed Oncolytic Viruses Induce Tumor Vascular Shutdown and Tumor Regression.* Mol Ther Oncolytics, 2018. **10**: p. 28-39.
162. da Costa, L.S., et al., *RNA viruses promote activation of the NLRP3 inflammasome through cytopathogenic effect-induced potassium efflux.* Cell Death Dis, 2019. **10**(5): p. 346.
163. Wegner, K.W., D. Saleh, and A. Degterev, *Complex Pathologic Roles of RIPK1 and RIPK3: Moving Beyond Necroptosis.* Trends Pharmacol Sci, 2017. **38**(3): p. 202-225.
164. Biswas, N., et al., *The ubiquitin-like protein PLIC-1 or ubiquilin 1 inhibits TLR3-Trif signaling.* PLoS One, 2011. **6**(6): p. e21153.
165. Gao, D., et al., *TLR3 controls constitutive IFN-β antiviral immunity in human fibroblasts and cortical neurons.* J Clin Invest, 2021. **131**(1).
166. Dondelinger, Y., et al., *MK2 phosphorylation of RIPK1 regulates TNF-mediated cell death.* Nat Cell Biol, 2017. **19**(10): p. 1237-1247.
167. Siokas, I., et al., *Immunoprecipitation Strategies to Isolate RIPK1/RIPK3 Complexes in Mouse Macrophages.* Curr Protoc, 2021. **1**(6): p. e156.
168. Simoes Eugénio, M., et al., *TRIM21, a New Component of the TRAIL-Induced Endogenous Necrosome Complex.* Front Mol Biosci, 2021. **8**: p. 645134.
169. Samson, A.L., et al., *MLKL trafficking and accumulation at the plasma membrane control the kinetics and threshold for necroptosis.* Nat Commun, 2020. **11**(1): p. 3151.

170. Miyagawa, Y., et al., *Induction of cell fusion/apoptosis in anaplastic thyroid carcinoma in orthotopic mouse model by urokinase-specific oncolytic Sendai virus.* Head Neck, 2019. **41**(9): p. 2873-2882.
171. Koks, C.A., et al., *Newcastle disease virotherapy induces long-term survival and tumor-specific immune memory in orthotopic glioma through the induction of immunogenic cell death.* Int J Cancer, 2015. **136**(5): p. E313-25.
172. Ohnimus, H., M. Heinkelein, and C. Jassoy, *Apoptotic cell death upon contact of CD4+ T lymphocytes with HIV glycoprotein-expressing cells is mediated by caspases but bypasses CD95 (Fas/Apo-1) and TNF receptor 1.* J Immunol, 1997. **159**(11): p. 5246-52.
173. Perfettini, J.L., et al., *53BP1 represses mitotic catastrophe in syncytia elicited by the HIV-1 envelope.* Cell Death Differ, 2010. **17**(5): p. 811-20.
174. Salsman, J., et al., *Extensive syncytium formation mediated by the reovirus FAST proteins triggers apoptosis-induced membrane instability.* J Virol, 2005. **79**(13): p. 8090-100.
175. Wang, B., et al., *Newcastle disease virus infection induces activation of the NLRP3 inflammasome.* Virology, 2016. **496**: p. 90-96.
176. Lin, J., et al., *Vesicular stomatitis virus sensitizes immunologically cold tumors to checkpoint blockade by inducing pyroptosis.* Biochim Biophys Acta Mol Basis Dis, 2022. **1868**(12): p. 166538.
177. Ma, H., et al., *Pyroptosis of syncytia formed by fusion of SARS-CoV-2 spike and ACE2-expressing cells.* Cell Discov, 2021. **7**(1): p. 73.
178. Zhu, P., et al., *Advances in mechanism and regulation of PANoptosis: Prospects in disease treatment.* Front Immunol, 2023. **14**: p. 1120034.
179. Rangaswamy, U.S., et al., *Newcastle Disease Virus Establishes Persistent Infection in Tumor Cells In Vitro: Contribution of the Cleavage Site of Fusion Protein and Second Sialic Acid Binding Site of Hemagglutinin-Neuraminidase.* J Virol, 2017. **91**(16).
180. Ayala-Breton, C., et al., *Faster replication and higher expression levels of viral glycoproteins give the vesicular stomatitis virus/measles virus hybrid VSV-FH a growth advantage over measles virus.* J Virol, 2014. **88**(15): p. 8332-9.
181. Gebremeskel, S., et al., *Natural killer T cell immunotherapy combined with oncolytic vesicular stomatitis virus or reovirus treatments differentially increases survival in mouse models of ovarian and breast cancer metastasis.* J Immunother Cancer, 2021. **9**(3).
182. Gauvrit, A., et al., *Measles virus induces oncolysis of mesothelioma cells and allows dendritic cells to cross-prime tumor-specific CD8 response.* Cancer Res, 2008. **68**(12): p. 4882-92.
183. Kirsch, D.G., et al., *Imaging primary lung cancers in mice to study radiation biology.* Int J Radiat Oncol Biol Phys, 2010. **76**(4): p. 973-7.

184. Ma, X., et al., *Integrin-Targeted Hybrid Fluorescence Molecular Tomography/X-ray Computed Tomography for Imaging Tumor Progression and Early Response in Non-Small Cell Lung Cancer.* Neoplasia, 2017. **19**(1): p. 8-16.
185. Harker, J.A. and C.M. Lloyd, *Overlapping and distinct features of viral and allergen immunity in the human lung.* Immunity, 2021. **54**(4): p. 617-631.
186. Driscoll, K.E., et al., *Intratracheal instillation as an exposure technique for the evaluation of respiratory tract toxicity: uses and limitations.* Toxicol Sci, 2000. **55**(1): p. 24-35.
187. Major, J., et al., *Type I and III interferons disrupt lung epithelial repair during recovery from viral infection.* Science, 2020. **369**(6504): p. 712-717.
188. Busch, S.E., et al., *Lung Cancer Subtypes Generate Unique Immune Responses.* J Immunol, 2016. **197**(11): p. 4493-4503.
189. Simon, M., et al., *Surfactants - Compounds for inactivation of SARS-CoV-2 and other enveloped viruses.* Curr Opin Colloid Interface Sci, 2021. **55**: p. 101479.
190. Numata, M., et al., *Phosphatidylglycerol provides short-term prophylaxis against respiratory syncytial virus infection.* J Lipid Res, 2013. **54**(8): p. 2133-2143.
191. Numata, M., et al., *Pulmonary surfactant lipids inhibit infections with the pandemic H1N1 influenza virus in several animal models.* J Biol Chem, 2020. **295**(6): p. 1704-1715.
192. Kellish, P., et al., *Oncolytic virotherapy for small-cell lung cancer induces immune infiltration and prolongs survival.* J Clin Invest, 2019. **129**(6): p. 2279-2292.
193. Fitzgerald, B., et al., *A mouse model for the study of anti-tumor T cell responses in Kras-driven lung adenocarcinoma.* Cell Rep Methods, 2021. **1**(5).
194. Haines, B.B., et al., *A quantitative volumetric micro-computed tomography method to analyze lung tumors in genetically engineered mouse models.* Neoplasia, 2009. **11**(1): p. 39-47.
195. Winkelmann, C.T., et al., *Microimaging characterization of a B16-F10 melanoma metastasis mouse model.* Mol Imaging, 2006. **5**(2): p. 105-14.
196. Treves, A.J., I.R. Cohen, and M. Feldman, *A syngeneic metastatic tumor model in mice: the natural immune response of the host and its manipulation.* Isr J Med Sci, 1976. **12**(4-5): p. 369-84.
197. Damme, H.V., et al., *Therapeutic depletion of CCR8⁺ tumor-infiltrating regulatory T cells elicits antitumor immunity and synergizes with anti-PD-1 therapy.* Journal for ImmunoTherapy of Cancer, 2021. **9**(2): p. e001749.
198. Masemann, D., et al., *Synergistic anti-tumor efficacy of oncolytic influenza viruses and B7-H3 immune- checkpoint inhibitors against IC-resistant lung cancers.* Oncoimmunology, 2021. **10**(1): p. 1885778.
199. Cao, X., et al., *Cancer targeting Gene-Viro-Therapy of liver carcinoma by dual-regulated oncolytic adenovirus armed with TRAIL gene.* Gene Ther, 2011. **18**(8): p. 765-77.

200. Lei, W., et al., *Enhancing therapeutic efficacy of oncolytic vaccinia virus armed with Beclin-1, an autophagic Gene in leukemia and myeloma.* Biomed Pharmacother, 2020. **125**: p. 110030.
201. Van Hoecke, L., et al., *Recombinant viruses delivering the necroptosis mediator MLKL induce a potent antitumor immunity in mice.* Oncoimmunology, 2020. **9**(1): p. 1802968.
202. Feola, S., et al., *Oncolytic ImmunoViroTherapy: A long history of crosstalk between viruses and immune system for cancer treatment.* Pharmacol Ther, 2022. **236**: p. 108103.
203. Reale, A., A. Calistri, and J. Altomonte, *Giving Oncolytic Viruses a Free Ride: Carrier Cells for Oncolytic Virotherapy.* Pharmaceutics, 2021. **13**(12).
204. Montgomery, M.K., et al., *Mouse lung automated segmentation tool for quantifying lung tumors after micro-computed tomography.* PLoS One, 2021. **16**(6): p. e0252950.
205. van de Worp, W., et al., *Deep Learning Based Automated Orthotopic Lung Tumor Segmentation in Whole-Body Mouse CT-Scans.* Cancers (Basel), 2021. **13**(18).
206. Kellar, A., C. Egan, and D. Morris, *Preclinical Murine Models for Lung Cancer: Clinical Trial Applications.* Biomed Res Int, 2015. **2015**: p. 621324.

ACKNOWLEDGEMENT

First and foremost, I want to express my gratitude to Jennifer, my "Doktormutter", for the inspiring working environment in your lab over the last years and the diverse projects I have been working on. I have always had your full support, and you have helped me gain broad experience and become an individual scientist! Your optimism truly rubbed off on me and helped me see through rocky and daunting phases of my projects. Thank you for always having your door open for a chat, a cup of coffee, or asking for your scientific input.

My special gratitude is addressed to my Thesis Committee, Prof. Philipp Jost and Adjunct Prof. OIiver Ebert, for the supporting and constructive meetings and for giving your guidance on the conceptualization of my projects.

I want to express my special thanks to my lab buddy, Alex. We've not only shared the long struggle of doing a Ph.D. together, we've also become close friends, and I look back to numerous inspiring and motivating conversations with you! Thanks for your help in the lab, constant empathy, and encouragement; I really value your realistic view of things.

My gratefulness goes to Teresa and Vicky. You've always been very supportive role models and inspiring colleagues, willing to share your time and expertise. You made it a pleasure working in the same office, celebrate a coffee break or talk about life (outside the lab)!

I want to thank Janina for onboarding me with my animal experiments. Thank you, and Sophie, for your unsolicited help in busy animal work. I would like to appreciate Sonja and Lorenz, for helping each other at any time during lab work and with FACS or animal experiments. Cecilia, I also want to thank you for your offhand support during the dendritic cell experiments.

Thank you, Franzi and Giulia, for spreading your optimism and positivity during my last year. Having a chit-chat with you made the final phase much more enjoyable.

Petra, I would like to express my thankfulness for your technical support and positivity, and for having pulled the strings in the background to keep the lab running.

In the spirit of the "Friday beer club": Alex, Vicky, Lorenz, Martin, Alex J., and all occasional members, thanks folks! After a busy week, having a word and some banter over a beer was always a great contrast.

All former and current colleagues I haven't mentioned yet, you all have contributed to a lively day-to-day working atmosphere and countless lunch chit-chat.

I would also like to thank Kivanc for your unsophisticated support in intravenous injections in mice and all the colleagues and friends I met in the surrounding departments during the last few years.

From my heart, I want to express my gratefulness for the support and love I receive from my family. My dear parents and sister, you've always believed in and encouraged me throughout my path. Coming home has always been an atmosphere of relaxation and a relief from day-to-day work!

Thank you!